MECHANISM OF ADIPONECTIN-MEDIATED PREVENTION OF CARDIOMETABOLIC DISEASES AND THERAPEUTIC POTENTIAL

JIALING TANG

A DISSERTATION SUBMITTED TO THE FACULTY OF GRADUATE STUDIES IN PARTIAL FULFILLMENT OF THE REQUIREMENTS FOR THE DEGREE OF

Doctor of Philosophy

GRADUATE PROGRAM IN BIOLOGY

YORK UNIVERSITY

TORONTO, ONTARIO

MARCH 2026

Abstract

Myocardial ischemia-reperfusion (IR) injury remains a major contributor to cardiomyocyte loss and heart failure progression despite advances in revascularization. Adiponectin, a cardioprotective adipokine reduced in cardiovascular disease and obesity, has well-recognized benefits, yet the mechanisms underlying adiponectin receptor–mediated protection during IR injury remain incompletely defined. This thesis investigates the multi-layered cardioprotective actions of ALY688, a synthetic adiponectin receptor agonist, with a focus on extracellular vesicle (EV)-mediated communication, metabolic organellar coupling, and autophagy regulation.

Four integrated studies employed complementary *in vivo* (rat and mouse myocardial infarction models) and in vitro (H9c2 cardiomyocytes and human iPSC-derived cardiomyocytes) approaches. Mechanistic interrogation utilized CRISPR-mediated gene editing, mass spectrometry-based proteomics, lipidomic profiling, real-time autophagy flux assays, and advanced imaging techniques including fluorescence molecular tomography and cryo-electron microscopy.

Study 1 demonstrated that ALY688 reduces infarct size and preserves cardiac function through dual mechanisms: direct cardiomyocyte protection, characterized by reduced oxidative stress, restored autophagy flux, and attenuated apoptosis, and Rab8a-dependent EV biogenesis. Genetic ablation of Rab8a abolished EV-mediated cardioprotection, identifying Rab8a as a critical regulator. Study 2 showed that ALY688 reprograms EV cargo toward cardioprotective phenotypes, enriching EVs with adiponectin, metabolic enzymes, and autophagy-related proteins. Systemic delivery of ALY688-derived EVs reduced infarct size, improved cardiac function, and normalized mitochondrial dynamics in both lean and obese mice, supporting the therapeutic potential of EV-based strategies. Study 3 uncovered a previously unrecognized role for Rab8a in maintaining lipid droplet–mitochondria coupling, essential for long-chain fatty acid utilization during ischemic stress. Hypoxia-reoxygenation suppressed Rab8a, disrupting metabolic coupling and promoting lipotoxicity, whereas ALY688 preserved Rab8a via AMPK-dependent signaling, restoring metabolic homeostasis in a Rab8a-dependent manner. Study 4 demonstrated that adiponectin deficiency exacerbates ischemia-induced cardiac dysfunction through impaired autophagy flux. CRISPR-mediated ATG7 deletion confirmed autophagy as mechanistically essential for adiponectin-mediated cytoprotection.

This thesis identifies adiponectin receptor signaling as a hierarchically organized cardioprotective network integrating direct cellular signaling, Rab8a-dependent EV biogenesis and cargo remodeling, preservation of lipid droplet-mitochondria metabolic coupling, and context-dependent autophagy regulation. Rab8a emerges as a central hub linking vesicular trafficking with metabolic resilience. These findings support the development of ALY688 and EV-based modalities as multi-mechanistic therapies for acute myocardial infarction and heart failure prevention.

Table of Contents

Acknowledgement

I am deeply grateful to my supervisor, Dr. Gary Sweeney, for his exceptional mentorship, guidance, and unwavering support throughout my doctoral training. His scientific rigor, thoughtful advice, and constant encouragement were central to my development as an independent researcher, and I sincerely appreciate his dedication to helping me succeed.

I would like to thank my PhD program advisor, Dr. Chun Peng, and Dr. Scott Kelly for their continued support during my doctoral studies. Having witnessed my progress from start to finish, they provided valuable feedback and insightful suggestions during evaluations that greatly strengthened my academic growth. I am also sincerely grateful to Dr. Tara Haas, Dr. Peter Backx, and Dr. Jason Dyck for agreeing to serve as my doctoral defense examiners and for dedicating their time and expertise to the evaluation of this work.

My sincere appreciation goes to Dr. Erfei Song and Dr. Dewei Ye for their strong encouragement and support in facilitating my transition into Dr. Sweeney's laboratory. Their confidence in me played an important role in shaping my doctoral path.

I also gratefully acknowledge all collaborators who generously contributed their expertise to this work, including Dr. Erin Mulvihill, Dr. Mireille Ouimet, Dr. Dylan Burger, Dr. Ali Sater, Dr. Renke Li, and Dr. Aimin Xu. Their collaboration significantly enriched this research.

I would like to express my deepest gratitude to Dr. Longmei Li, who first introduced me to wet lab research and guided my earliest steps into the scientific world. Her mentorship and encouragement were pivotal in shaping my decision to pursue graduate studies. Her resilience, dedication, and strength as a scientist and physician continue to inspire me, and I am truly grateful for the foundation she helped me build.

I am thankful to our lab manager and research associate, Hyekyoung Sung, whose professional expertise and genuine kindness created a supportive and welcoming laboratory environment. Her assistance extended well beyond research, offering both practical and personal support throughout my PhD journey.

I am fortunate to have worked alongside wonderful lab members, including Yubin Lei, Wing Yan Chung, Khang Nguyen, Dr. Sungji Cho, Eddie Tam, Patricia Reboucas, Photsathorn Haetanurak, Saher Ahmed, Yue Qu, Divya Shah, Tori Gosse, Celena-Dell-Mendia, and Dr. Justin Greig, whose collegiality, teamwork, and friendship made the laboratory a stimulating and supportive place to work.

I am profoundly grateful to my family, both biological and chosen, for their unconditional love, patience, and encouragement throughout my life and academic training. Their support sustained me through challenges and successes alike.

Finally, I would like to acknowledge myself for perseverance, resilience, and growth throughout this demanding journey. Completing this PhD has been a transformative experience, and I am proud of the dedication and determination that brought me here.

List of Table

Table 1.1 Current therapeutic approaches for cardiometabolic diseases 15
Table 1.2 Source of EVs and their actions on cardiometabolic diseases 23
Table 2.1 Summary of Echocardiography parameters of rat undergone sham and I/R surgery ... 65
Table 2.2 Top 22 significantly expressed proteins and functions in serum EV proteomics analysis 67
Table 3.1 Summary of Echocardiography parameters of mice undergone sham and MI 123
Table 3.2 Overlapping proteins in the between HFD sham ALY vs HFD sham PBS and SC sham ALY vs SC sham PBS 125
Table 3.3 Overlapping proteins in the between HFD MI ALY vs HFD MI PBS and SC MI ALY vs SC MI PBS 127
Table 3.4 Sequence of primers 138
Table 4.1 Sequence of primers 183

List of Figure

List of abbreviation

8-OHdG – 8-hydroxydeoxyguanosine

ACC – Acetyl-CoA carboxylase

ACE – Angiotensin-converting enzyme

ACEi – Angiotensin-converting enzyme inhibitor

ACS – Acute coronary syndrome

Ad-KO – Adiponectin knockout

AdipoR1 – Adiponectin receptor 1

AdipoR2 – Adiponectin receptor 2

ADSC – Adipose-derived stem cell

AGE – Advanced glycation end-product

AKO – ATG7 knockout

AMPK – Adenosine monophosphate-activated protein kinase

ANP – Atrial natriuretic peptide

ARB – Angiotensin receptor blocker

ARNI – Angiotensin receptor-neprilysin inhibitor

ATGL – Adipose triglyceride lipase

ATG – Autophagy-related gene

ATP – Adenosine triphosphate

BAT – Brown adipose tissue

Baf – Bafilomycin

BAX – BCL2-associated X protein

BCA – Bicinchoninic acid assay

BCL2 – B-cell lymphoma 2

cAMP – Cyclic adenosine monophosphate

Cat-B – Cathepsin B

CDC – Cardiosphere-derived cell

Cer – Ceramide

cGAS-STING – Cyclic GMP-AMP synthase - stimulator of interferon genes

cGMP – Cyclic guanosine monophosphate

CM – Conditioned medium

CPC – Cardiac progenitor cell

CPT-1b – Carnitine palmitoyltransferase-1b

CQ – Chloroquine

CRISPR – Clustered regularly interspaced short palindromic repeats

CRP – C-reactive protein

CRT – Cardiac resynchronization therapy

CV – Cardiovascular

CVD – Cardiovascular disease

DAG – Diacylglycerol

DAMP – Danger-associated molecular pattern

DAPI – 4',6-diamidino-2-phenylindole

DES – Drug-eluting stent

DGAT – Diacylglycerol acyltransferase

DiR – 1,1'-dioctadecyl-3,3,3',3'-tetramethylindotricarbocyanine iodide

DR – DapRed

Drp1 – Dynamin-related protein 1

ECM – Extracellular matrix

EDTA – Ethylenediaminetetraacetic acid

EF – Ejection fraction

eNOS – Endothelial nitric oxide synthase

ER – Endoplasmic reticulum

ESCRT – Endosomal sorting complexes required for transport

ETC – Electron transport chain

EV – Extracellular vesicle

$FADH_2$ – Flavin adenine dinucleotide (reduced form)

FCCP – Carbonyl cyanide p-trifluoromethoxyphenylhydrazone

FFA – Free fatty acid

FGF – Fibroblast growth factor

FMT – Fluorescence molecular tomography

FS – Fractional shortening

FUNDC1 – FUN14 domain-containing 1

GAPDH – Glyceraldehyde 3-phosphate dehydrogenase

GLUT4 – Glucose transporter type 4

GLP-1 – Glucagon-like peptide-1

GMP – Good manufacturing practice

GO – Gene ontology

GPI – Glycosylphosphatidylinositol

GPx – Glutathione peroxidase

GRP78 – 78 kDa glucose-regulated protein

gRNA – Guide RNA

HE – Hematoxylin and eosin

HF – Heart failure

HFD – High-fat diet

HFpEF – Heart failure with preserved ejection fraction

HFrEF – Heart failure with reduced ejection fraction

HIF-1α – Hypoxia-inducible factor 1-alpha

HR – Hypoxia-reoxygenation

HSL – Hormone-sensitive lipase

HSP – Heat shock protein

ICAM-1 – Intercellular adhesion molecule 1

IFN – Interferon

IL – Interleukin

iNOS – Inducible nitric oxide synthase

iPSC – Induced pluripotent stem cell

iPSC-CM – Induced pluripotent stem cell-derived cardiomyocyte

IR – Ischemia-reperfusion

IRI – Ischemia-reperfusion injury

IRS-1 – Insulin receptor substrate 1

JNK – c-Jun N-terminal kinase

KEGG – Kyoto Encyclopedia of Genes and Genomes

LAD – Left anterior descending (coronary artery)

LAL – Lysosomal acid lipase

LALi – Lysosomal acid lipase inhibitor

LC – Liquid chromatography

LC3 – Microtubule-associated protein 1A/1B-light chain 3

LCFA – Long-chain fatty acid

LD – Lipid droplet

LDH – Lactate dehydrogenase

LDL – Low-density lipoprotein

LDL-C – Low-density lipoprotein cholesterol

lncRNA – Long non-coding RNA

LPS – Lipopolysaccharide

LV – Left ventricular

LVEF – Left ventricular ejection fraction

MACE – Major adverse cardiovascular events

MAPK – Mitogen-activated protein kinase

MCP-1 – Monocyte chemoattractant protein-1

MCS – Membrane contact site

MFI – Mean fluorescence intensity

MFN – Mitofusin

MGL – Monoacylglycerol lipase

MI – Myocardial infarction

miRNA – MicroRNA

MISEV – Minimal Information for Studies of Extracellular Vesicles

MLKL – Mixed lineage kinase domain-like protein

MMP – Matrix metalloproteinase

mPTP – Mitochondrial permeability transition pore

MR – MagicRed

MRM – Multiple reaction monitoring

mRNA – Messenger RNA

MS – Mass spectrometry

MSC – Mesenchymal stem cell

mtDNA – Mitochondrial DNA

mtROS – Mitochondrial reactive oxygen species

mTOR – Mechanistic target of rapamycin

MVB – Multivesicular body

NADH – Nicotinamide adenine dinucleotide (reduced form)

NADPH – Nicotinamide adenine dinucleotide phosphate (reduced form)

NF-κB – Nuclear factor kappa B

NLRP3 – NOD-like receptor family pyrin domain containing 3

NO – Nitric oxide

Nox – NADPH oxidase

NRF2 – Nuclear factor erythroid 2-related factor 2

NTA – Nanoparticle tracking analysis

O_2 – Oxygen

OCR – Oxygen consumption rate

OPA1 – Optic atrophy 1

ox-LDL – Oxidized low-density lipoprotein

OXPHOS – Oxidative phosphorylation

p38 MAPK – p38 mitogen-activated protein kinase

p62 – Sequestosome 1

PAGE – Polyacrylamide gel electrophoresis

PBS – Phosphate-buffered saline

PCA – Principal component analysis

PCI – Percutaneous coronary intervention

PCSK9 – Proprotein convertase subtilisin/kexin type 9

PDGF – Platelet-derived growth factor

PET – Positron emission tomography

PGC-1α – Peroxisome proliferator-activated receptor gamma coactivator 1-alpha

PGK1 – Phosphoglycerate kinase 1

PI – Propidium iodide

PI3K – Phosphoinositide 3-kinase

PINK1 – PTEN-induced kinase 1

PKA – Protein kinase A

PKC – Protein kinase C

PKM – Pyruvate kinase M

PLIN – Perilipin

PLS-DA – Partial least squares discriminant analysis

PPAR – Peroxisome proliferator-activated receptor

PVDF – Polyvinylidene fluoride

qPCR – Quantitative polymerase chain reaction

RAAS – Renin-angiotensin-aldosterone system

RAGE – Receptor for advanced glycation end products

RIPK – Receptor-interacting serine/threonine-protein kinase

RKO – Rab8a knockout

RNA – Ribonucleic acid

ROS – Reactive oxygen species

Ros-PLIN – Rosella-PLIN

RT-PCR – Reverse transcription polymerase chain reaction

SC – Standard chow

SDH – Succinate dehydrogenase

SDS – Sodium dodecyl sulfate

SEC – Size-exclusion chromatography

SEM – Scanning electron microscopy / Standard error of the mean

SERCA2 – Sarco/endoplasmic reticulum Ca^{2+}-ATPase 2

SGLT2 – Sodium-glucose cotransporter-2

siRNA – Small interfering RNA

SIRT1 – Sirtuin 1

SMA – Smooth muscle actin

SNS – Sympathetic nervous system

SOD – Superoxide dismutase

SPECT – Single-photon emission computed tomography

STEMI – ST-elevation myocardial infarction

TAG – Triacylglycerol

TF-LC3 – Tandem fluorescent LC3

TFEB – Transcription factor EB

TGF-β – Transforming growth factor-beta

TLR4 – Toll-like receptor 4

TMAO – Trimethylamine N-oxide

TNF-α – Tumor necrosis factor-alpha

Tom20 – Translocase of outer mitochondrial membrane 20

TSC – Tuberous sclerosis complex

TUNEL – Terminal deoxynucleotidyl transferase dUTP nick end labeling

T2DM – Type 2 diabetes mellitus

ULK1 – Unc-51 like autophagy activating kinase 1

VCAM-1 – Vascular cell adhesion molecule 1

VDAC – Voltage-dependent anion channel

VEGF – Vascular endothelial growth factor

VLDL – Very low-density lipoprotein

WAT – White adipose tissue

WT – Wild-type

1. Chapter 1 Literature review

1.1 Cardiometabolic diseases and pathophysiological mechanisms

1.1.1 Definition and brief introduction to various cardiometabolic diseases

1.1.1.1 Definition and epidemiology

Cardiometabolic diseases represent a spectrum of interconnected pathological conditions that significantly contribute to global morbidity and mortality (1). These disorders share common pathophysiological mechanisms, including chronic inflammation, oxidative stress, and metabolic dysfunction, which collectively contribute to cardiovascular complications and metabolic dysregulation (2).

1.1.1.2 Shared risk factors

Cardiometabolic diseases share modifiable and non-modifiable risk factors. Non-modifiable factors include age, sex, genetics, and ethnicity, while modifiable factors include obesity, inactivity, poor diet, smoking, alcohol, and psychosocial stress (3, 4). Obesity, particularly visceral fat, drives insulin resistance, dyslipidemia, hypertension, and inflammation, closely linking it to Type 2 Diabetes Mellitus (T2DM) and cardiovascular complications (5). Visceral obesity fosters a chronic inflammatory milieu characterized by macrophage infiltration into adipose tissue, releasing pro-inflammatory cytokines including TNF-α, interleukin-6, and interleukin-1β that systemically impair insulin signaling through JNK and NF-κB pathway activation (6). Hypertension frequently precedes heart failure, promoting cardiac remodeling and diastolic dysfunction (7). Insulin resistance and dysglycemia impair glucose uptake while enhancing lipolysis, leading to hyperglycemia, elevated free fatty acids, endothelial dysfunction (8), and atherosclerosis (9). Dyslipidemia, including elevated low-density lipoprotein (LDL), triglycerides, remnant lipoproteins, and small dense LDL, contributes to plaque formation and instability (10, 11).

1.1.1.3 Common pathophysiological features

Cardiometabolic diseases share chronic inflammation, oxidative stress, endothelial dysfunction, metabolic dysfunction, and neurohormonal activation (12).

Obesity-induced adipose inflammation initiates a pathologic cascade that impairs cardiac function through multiple mechanisms (13). Obesity-induced adipose inflammation elevates IL-6, TNF-α,

and C-reactive protein (CRP), promoting insulin resistance, endothelial dysfunction, and atherosclerosis, with elevated inflammatory markers especially notable in obese HFpEF (14, 15).

In obesity, infiltration of macrophages into visceral adipose tissue results in chronic activation of pro-inflammatory transcription factors, particularly NF-κB, which orchestrates the production of a broad array of inflammatory mediators (16, 17). These inflammatory cytokines impair insulin signaling through activation of JNK and IκB kinase pathways, creating a self-perpetuating cycle of metabolic dysfunction (18). Furthermore, adipose tissue from obese individuals exhibits dysregulated secretion of adipokines, with elevated leptin and resistin levels contributing to systemic inflammation and myocardial dysfunction (19).

Excess reactive oxygen species (ROS) are tightly coupled to inflammation. They are a major source of cardiac and vascular injury (20). In diabetic cardiomyopathy, impaired insulin signaling forces excessive fatty acid oxidation. This leads to mitochondrial uncoupling. The result is abundant ROS production. ROS causes lipid peroxidation, protein nitrosylation, and cardiomyocyte death (21). During ischemia-reperfusion, mitochondrial dysfunction drives further ROS generation. This opens the mitochondrial permeability transition pore (mPTP). mPTP opening leads to mitochondrial swelling and cell death. In cardiac surgery, NADPH oxidase activity is the strongest predictor of postoperative atrial fibrillation. ROS also activates NF-κB, NRF2, and MAPK signaling (22). These pathways amplify inflammation and promote apoptosis. In obesity, adipose tissue generates excess ROS, which impairs local vasodilation and microvascular function (23). Notably, a combination of oleuropein, hydroxytyrosol, and oleocanthal activated Nrf2 signaling showed upregulated of superoxide dismutase 2 (SOD2) and catalase (CAT) enzyme expression, which reduced infarct size in mice with metabolic syndrome (24).

Endothelial dysfunction, which is characterized by reduced nitric oxide (NO) bioavailability, increased vascular permeability, and upregulation of adhesion molecules, represents a central mechanism linking inflammation and oxidative stress to structural cardiovascular disease (25). In atherosclerosis, disturbed hemodynamic shear stress at arterial branch points and bifurcations promotes endothelial activation and facilitates the adhesion and transendothelial migration of monocytes and neutrophils into the subintimal space (26). This process leads to foam cell accumulation, cytokine secretion, and phenotypic switching of vascular smooth muscle cells,

thereby advancing plaque development (27, 28). Pro inflammatory macrophage subtypes, including IL-1β positive and CCR2 positive populations, predominate in carotid lesions, whereas more homeostatic and anti-inflammatory phenotypes are observed in femoral artery plaques (29).

Metabolic dysregulation is a core feature of the cardiometabolic dysfunction, linking obesity, insulin resistance, type 2 diabetes, and heart failure (30). In the diabetic heart, impaired insulin signaling produces metabolic inflexibility, with cardiomyocytes unable to utilize glucose and exclusively dependent on fatty acid oxidation (31). The resulting excess intracellular lipid accumulation drives lipotoxicity through the accumulation of ceramides, diacylglycerols, and acylcarnitines, which activate protein kinase C isoforms, promote mitochondrial dysfunction, endoplasmic reticulum stress, and cardiomyocyte apoptosis (32). Advanced glycation end-products (AGEs), generated by hyperglycemia, crosslink extracellular matrix proteins, activate RAGE signaling via NF-κB and MAPK pathways, and stimulate TGF-β mediated fibrosis, collectively contributing to diastolic dysfunction and left ventricular stiffness (33). In ischemia, nutrient deprivation and hypoxia activate the integrated stress response (ISR) via upstream kinases including PERK, GCN2, leading to phosphorylation of eIF2α, global suppression of protein translation, and preferential synthesis of stress-adaptive proteins, representing a conserved adaptive response to ischemic metabolic crisis (34, 35). In obesity, myocardial steatosis reflects the inability of cardiac myocytes to handle excess lipid uptake, exceeding their oxidative capacity and generating toxic metabolites and ROS (36).

Neurohormonal dysregulation also extends to electrical remodeling and arrhythmogenesis. Sustained SNS and RAAS activation inhibit the slow component of the delayed rectifier potassium current (IKs). Reductions in IKs prolong action potential duration (APD). This prolongs the QT interval and increases the risk of ventricular arrhythmias (37) (38). Sustained β-adrenergic stimulation reduces IKs through Epac (exchange protein directly activated by cAMP)- and CaMKII-dependent pathways (39). Angiotensin II inhibits IKs via PKCε-mediated phosphorylation of KCNQ1 (40). These neurohormonal effects on ion channels are a key mechanism linking RAAS and SNS activation to sudden cardiac death, which accounts for up to 40% of mortality in severe heart failure (41). Patients with acute myocardial infarction (AMI), especially those with comorbid chronic kidney disease (CKD), neurohormonal dysregulation is amplified. Reduced glomerular filtration rate is associated with higher circulating aldosterone and ACE activity (42). Elevated aldosterone in AMI patients correlates with increased infarct size and

promotes post-infarction neovascular remodeling. Patients with higher aldosterone on admission have greater in-hospital mortality (43).

Natriuretic peptides, particularly atrial natriuretic peptide (ANP) and B-type natriuretic peptide (BNP) normally counter-regulate RAAS by inducing vasodilation and promoting renal sodium excretion. However, peripheral resistance to natriuretic peptides develops in heart failure. RAAS activity remains unopposed (44, 45). This creates a cycle of persistent vasoconstriction, volume overload, and worsening left ventricle remodeling. The angiotensin receptor-neprilysin inhibitor (ARNI) sacubitril/valsartan corrects this imbalance (46). Pharmacological antagonism of neurohormonal systems forms the foundation of heart failure therapy. β-Blockers, ACE inhibitors, ARBs, and mineralocorticoid receptor antagonists each target distinct components of the neurohormonal axis. They reduce myocyte loss, attenuate fibrosis, promote reverse left ventricle remodeling, and improve survival (47, 48).

1.1.2 Myocardial ischemia and reperfusion injury

Myocardial ischemia-reperfusion injury (IRI) is a key pathological process in cardiometabolic disease, especially during acute coronary syndromes. While reperfusion restores blood flow after MI, it paradoxically triggers metabolic and inflammatory cascades that extend myocardial damage. Understanding these mechanisms is critical for targeted therapy (49).

1.1.2.1 Cardiomyocyte cell death (apoptosis, necrosis, necroptosis, and ferroptosis)

Cardiomyocyte loss, which is also termed lethal reperfusion injury, is a form of cell death that is aconsequence of reperfusion. The loss of cardiomyocytes is the basic factor that induces irreversibleinjury. Cardiomyocyte loss can not only induce acute injury by increasing infarct size, which may account for 50% of the total injury (50), but also cause long-term injury by contributing to cardiac remodeling and heart failure. However, it takes a long time to unravel the forms of cell deaths that mediate myocardial I/R injury and their mechanisms. For decades, apoptosis and necrosis were considered to be the only two types of cell death. They were the first recognized cell death modes involved in myocardial I/R injury (51, 52). In recent years, several forms of regulated cell death that are distinct from apoptosis have been reported. This led to the discovery of ferroptosis, necroptosis, and pyroptosis (53-55).

Apoptosis is a programmed form of cell death characterized by chromatin condensation, nuclear fragmentation, and formation of apoptotic bodies. It proceeds without membrane rupture or

organelle swelling (56). It is executed by caspase-3 and caspase-7, which are activated through both intrinsic (mitochondrial) and extrinsic (death receptor) pathways (56). Apoptosis does not trigger an inflammatory response. It is activated in the ischemic myocardium and continues throughout the reperfusion phase (57, 58). Classical necrosis is characterized by nuclear disintegration, cytoplasmic membrane rupture, and organelle dilation (59). It is triggered by oxidative stress and cytosolic calcium overload. It relies on cyclophilin D (CypD)-dependent mitochondrial permeability transition pore (mPTP) opening (60). This form of cell death is highly inflammatory. Rupture of the plasma membrane releases intracellular contents and activates immune cascades. mPTP opening also underpins a more regulated subtype known as MPT-driven necrosis. Inhibiting mPTP opening with cyclosporin A has been shown to exert cardioprotective effects(61) (62). Necroptosis is a regulated form of necrotic cell death. It is defined by formation of the necrosome and phosphorylation of receptor-interacting protein kinase 3 (RIP3 (63)). Under conditions of reduced caspase-8 activity, RIP1 binds RIP3 through a shared RHIM domain. This complex activates mixed lineage kinase domain-like pseudokinase (MLKL). Phosphorylated MLKL oligomerizes and translocates to the plasma membrane, causing membrane rupture. In cardiomyocytes, RIP3 also phosphorylates CaMKII, which opens the mPTP and amplifies cell death (64) (65). In IR-injured cardiac tissue, total phosphorylated RIP1 and RIP3 levels are elevated (66). Necroptosis mainly occurs in the late reperfusion phase and persists for weeks after myocardial infarction. Inhibition of RIP1 with necrostatin-1 (Nec-1) reduces infarct size and prevents adverse remodeling at 28 days (67). Necroptotic signals are also upregulated in left ventricular samples from patients with heart failure (68). Ferroptosis is an iron-dependent form of regulated cell death driven by lipid peroxidation. It targets phospholipids with polyunsaturated acyl tails, primarily arachidonic acid-containing phosphatidylethanolamine (AA-PE) (69). ROS generated through the Fenton reaction and iron-dependent lipoxygenases (LOX) oxidize these lipids into toxic hydroperoxides. The primary defense pathway is the system Xc-/GSH/GPX4 axis, which detoxifies lipid hydroperoxides (69). During IR, GPX4 activity and SLC7A11 expression are both reduced, impairing this protective mechanism. Ischemia triggers primary lipid peroxidation via ALOX15, serving as a priming signal (70). Iron overload, which raised from ferritinophagy, heme degradation, and transferrin receptor activation plays a central role(71). Clinically, iron chelation with deferoxamine before PPCI reduces oxidative stress. In patients undergoing coronary artery bypass grafting (CABG) (72).

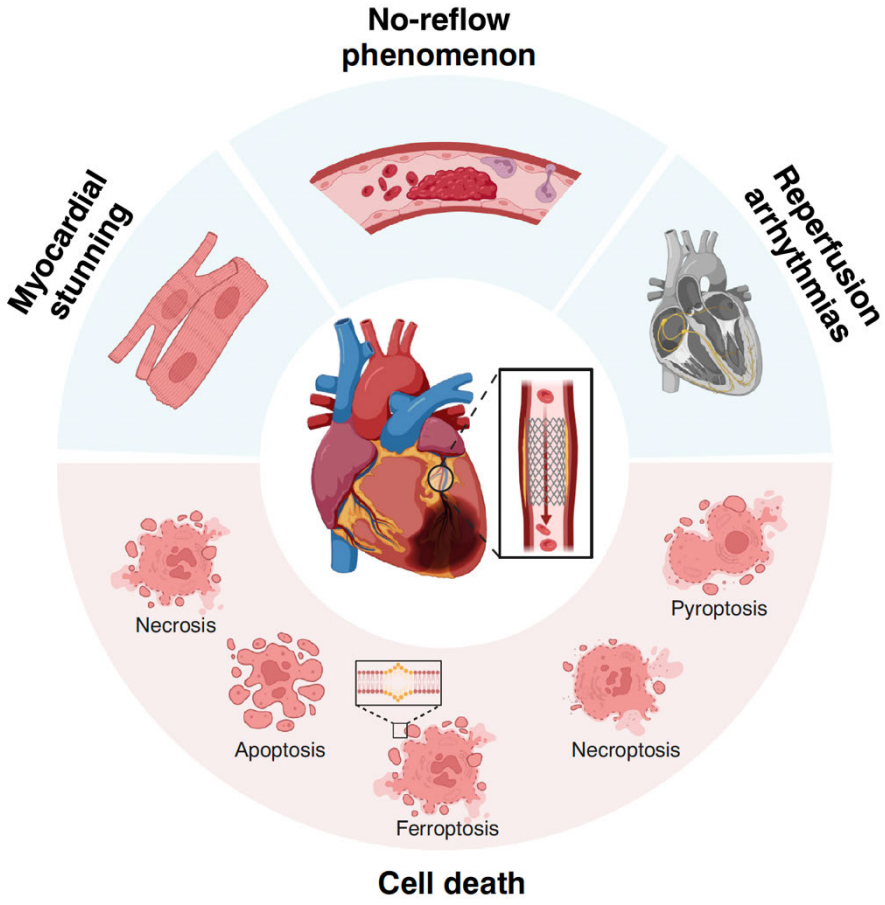

(Adapted from Qi Xiang, et al., Trends in Endocrinology & Metabolism. March 2024, Vol. 35, No. 3)

Figure 1.1. Schematic overview of myocardial ischemia–reperfusion (I/R) injury.

Myocardial I/R injury can lead to four types of cardiac dysfunction: myocardial stunning, no-reflow phenomenon, reperfusion arrhythmias, and cardiomyocyte death.

1.1.2.2 Inflammatory responses and immune cell recruitment

The innate immune system recognizes DAMPs and altered extracellular matrix signals, triggering robust cytokine production, upregulation of adhesion molecules (73), and complement cascade activation (74). Early infiltration of neutrophils and pro-inflammatory Ly6C^{high} monocytes clears dead cell debris while amplifying local inflammation through release of proteases and cytokines (75). This early inflammatory phase is followed by recruitment of reparative Ly6C^{low} macrophages

that secrete anti-inflammatory mediators, promote angiogenesis, and stimulate fibroblasts for scar formation (75). Excessive or prolonged inflammation exacerbates initial injury and drives adverse left ventricular remodeling, fibrosis, and progressive contractile dysfunction (76). Temporal regulation of immune cell phenotype switching is critical; disruption of this transition perpetuates injury and prevents myocardial recovery (76).

1.1.2.3 Autophagy and mitophagy dysregulation

Autophagy is an intracellular bulk degradation process whereby cytoplasmic proteins and damaged organelles are sequestered into double-membrane vesicles called autophagosomes and delivered to lysosomes for recycling (77). In the heart, basal autophagy serves as a homeostatic quality-control mechanism; inducible deletion of the autophagy-related gene Atg5 in the adult heart causes cardiac hypertrophy, chamber dilation, and contractile dysfunction, confirming that constitutive autophagy is essential for structural integrity (77, 78).

During myocardial ischemia, autophagy is markedly upregulated primarily through the AMPK-mTORC1-ULK1 signaling axis. Energy depletion activates AMPK, which inhibits mTORC1 and thereby disinhibits ULK1, triggering autophagosome formation(79). This ischemia-phase autophagy is broadly protective: it provides an alternative energy source through the release of free fatty acids and amino acids, removes toxic polyubiquitinated protein aggregates that accumulate when the ubiquitin-proteasome system is suppressed, and clears fragmented, ROS-producing mitochondria via the HIF-1α/BNIP3 pathway (80). Inhibition of autophagy during glucose deprivation accelerates ATP depletion and cardiomyocyte death, confirming its cytoprotective role in the ischemic phase (81). Upon reperfusion, however, the autophagic response undergoes a qualitative shift from protective to detrimental. The primary stimulus is no longer energy deficit but rather a massive surge in reactive oxygen species (ROS) generated by mitochondria during resumption of oxidative phosphorylation. ROS strongly induces upregulation of Beclin-1, a key pro-autophagic protein, initiating excessive autophagosome formation. Simultaneously, reduced Bcl-2 expression during reperfusion disrupts the Bcl-2-Beclin-1 inhibitory complex, further amplifying autophagic activity (82).

Mitophagy, the selective autophagic degradation of damaged or depolarized mitochondria. is a specialized branch of autophagy critical for mitochondrial quality control (83). The PINK1/Parkin signaling pathway is the predominant ubiquitin-dependent route for mitophagy in cardiomyocytes

(84). In healthy mitochondria, PINK1 undergoes constitutive import into the inner mitochondrial membrane where it is cleaved and degraded. When mitochondria become damaged or depolarized, PINK1 accumulates on the outer mitochondrial membrane, phosphorylates and recruits Parkin, which then ubiquitinates mitochondrial surface proteins and engages autophagy adaptor proteins (e.g., NDP52) that anchor the mitochondrion within autophagosomes via LC3 binding, culminating in lysosomal degradation (85). MIRI dysregulates this pathway in multiple ways. Moderate PINK1/Parkin-mediated mitophagy during the ischemic phase is generally cardioprotective, eliminating damaged mitochondria and limiting downstream ROS release (86). However, excessive PINK1/Parkin activation, which is driven by factors such as inhibition of the SIRT3/SOD2 antioxidant axis, upregulation of PARP, or elevated ALDH2 suppression, resulting in indiscriminate elimination of both damaged and functional mitochondria, compounding cellular injury (87). Conversely, MIR can also inhibit PINK1/Parkin-mediated mitophagy (e.g., through ZIP7 upregulation), preventing clearance of dysfunctional mitochondria and allowing ROS accumulation, which contributes to oxidative stress, ferroptosis, pyroptosis, and inflammatory damage (88).

SIRT1, an NAD^+-dependent histone deacetylase, integrates metabolic signals with autophagy regulation through deacetylation of multiple substrates, including the FOXO family transcription factors, autophagy-related proteins (ATG5, ATG7, ATG12), and LC3 (89). During the ischemic phase, SIRT1-mediated deacetylation of FOXO1 promotes Rab7 expression and enhances autophagic flux, while deacetylation of ATG proteins facilitates autophagosome elongation, collectively sustaining the protective autophagic response (90) (Figure 1.2).

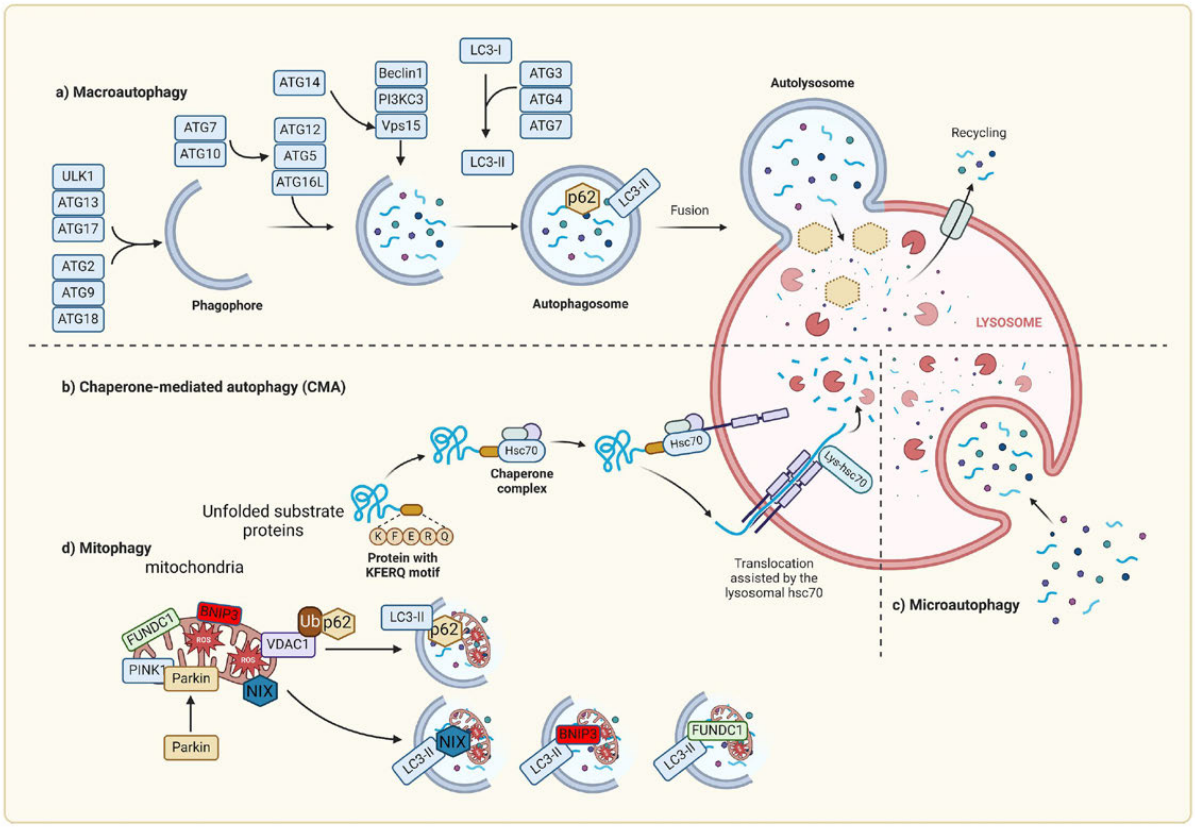

(Adapted from Tang J, et al., Autophagy Reports 2024; 3:2320605)

Figure 1.2 Molecular mechanisms of autophagy in macroautophagy

1.1.2.4 Metabolic inflexibility and impaired substrate utilization

Metabolic inflexibility, the inability to dynamically switch between metabolic substrates according to energy demand and substrate availability is profoundly exacerbates IR injury (91). Healthy hearts primarily oxidize fatty acids but retain capacity to rapidly shift to glucose or ketone utilization in response to workload changes (92). In obesity and diabetes, insulin resistance increases myocardial fatty acid uptake while reducing glucose transporter 4 (GLUT4) translocation (93). This substrate mismatch leads to incomplete fatty acid oxidation, toxic lipid intermediate accumulation (ceramides, diacylglycerols), excessive ROS generation, and dysregulation of calcium homeostasis. AMPK (adenosine monophosphate-activated protein kinase) dysfunction, commonly observed in metabolic disease, blunts adaptive energy responses, producing energy-

starved hearts that exhibit reduced efficiency despite abundant fuel availability (32) (94). This metabolic inflexibility is particularly pathological during ischemia-reperfusion, when rapid metabolic adaptation is essential for cellular survival. Restoring metabolic flexibility through AMPK activation, mitochondrial biogenesis enhancement, and substrate preference modification emerges as a critical therapeutic opportunity to mitigate MIRI in metabolically compromised hearts (95, 96).

1.1.3 Cardiac remodeling in pressure overload

1.1.3.1 Cardiac pressure overload

Cardiac pressure overload (PO) from hypertension or aortic stenosis triggers a stereotyped remodeling response characterized by concentric hypertrophy, progressive fibrosis, and eventual systolic and diastolic dysfunction (97). In the early compensated phase, increased wall thickness normalizes wall stress and preserves ejection fraction, but chronic PO drives maladaptive changes in cardiomyocytes, fibroblasts, immune cells, and the extracellular matrix (ECM) (7). Experimental PO is modeled mainly by transverse aortic constriction (TAC), which reduces aortic diameter by up to 70% and reliably produces left ventricular hypertrophy followed by heart failure (98).

1.1.3.2 Fibroblast activation and extracellular matrix expansion

A central feature of PO remodeling is fibroblast activation and ECM expansion. Within about five days of TAC, resident fibroblasts proliferate and transdifferentiate into myofibroblasts, expressing α-smooth muscle actin and depositing fibrillar collagens I and III in interstitial and perivascular regions (99). Collagen III tends to rise earlier, while sustained upregulation of collagen I dominates later, reducing myocardial distensibility and promoting diastolic stiffness (99). Matricellular proteins such as periostin, osteopontin, secreted protein acidic and rich in cysteine (SPARC), tenascin-C (100) (101-103), and thrombospondins are also induced and modulate fibroblast phenotype, collagen cross-linking, and matrix organization. Matrix metalloproteinases (especially MMP-2 and MMP-9) and their tissue inhibitors (TIMP-2, TIMP-4) are differentially regulated, so that net ECM accumulation reflects both increased synthesis and altered degradation (104) (105).

1.1.3.3 Central role of TGF-β1 in fibrotic remodeling

Transforming growth factor-β1 (TGF-β1) is a master profibrotic signal in PO hearts. Mechanical stress and local angiotensin II activate TGF-β1 in the ECM, which then signals via Smad2/3 and Rho/ROCK pathways to drive myofibroblast differentiation, collagen I/III production, and suppression of collagenase expression (106) (107). Circulating and myocardial TGF-β1 levels correlate with collagen content and myocyte hypertrophy in aortic stenosis patients (108). Pharmacologic inhibition of TGF-β/Smad signaling (e.g., with pirfenidone, nintedanib, ROCK2 inhibitor belumosudil, targeting TGF-β1-Smad/TAK1-p38) reduces TAC-induced fibrosis and improves function (109). Thus, TGF-β1 lies at the intersection of mechanical load, neurohormonal activation, and ECM remodeling in PO.

1.1.3.4 Inflammatory remodeling

Innate immune cells orchestrate much of the structural response to pressure overload (110). TAC and related models show rapid influx of neutrophils (peaking ~3 days), followed by expansion of monocyte-derived macrophages (~days 6-7), dendritic cells, and later mast cells and other subsets (110). These cells release cytokines such as TNF-α, IL-1, and IL-6, which induce cardiomyocyte hypertrophy, and secrete TGF-β, PDGF, MMPs, and osteopontin that activate fibroblasts and remodel ECM. Mast cell proteases (tryptase, chymase) convert latent TGF-β to its active form and generate angiotensin II locally, enhancing fibrosis and hypertrophy (111). Genetic or pharmacologic depletion or stabilization of mast cells, neutrophils, $CCR2^{+}$ monocytes, or selected macrophage subsets in TAC variably reduces fibrosis, wall thickening, or decompensation, highlighting both detrimental and reparative immune roles that depend on timing and cell phenotype (112) (113).

1.1.3.5 Metabolic reprogramming

Metabolic remodeling is another hallmark of PO hypertrophy. Early PO (HFpEF-like stage) shows increased glucose uptake (GLUT1 upregulation, relative GLUT4 downregulation) and enhanced glycolysis, often without a parallel rise in glucose oxidation, leading to accumulation of glycolytic intermediates (114). As PO progresses toward HFrEF, mitochondrial pyruvate uptake activity fall, glucose oxidation declines, and glycolytic reliance becomes energetically inefficient (115). In parallel, fatty acid oxidation capacity falls because of reduced CD36, CPT1b, PPAR/PGC-1 signaling, and accumulation of toxic lipid intermediates (116), while ketone and branched-chain amino acid catabolism are increasingly recruited but often dysregulated (117). These metabolic

shifts affect redox balance, ROS generation, and signaling (e.g., mTOR, AMPK, O-GlcNAc, NFAT), linking energy supply to hypertrophic growth, fibrosis, and eventual contractile failure (117).

1.1.4 Diabetic cardiomyopathy

Diabetic cardiomyopathy is myocardial dysfunction in diabetes without coronary artery disease, hypertension, or valvular disease. It often begins as diastolic dysfunction with preserved ejection fraction and can progress to HFpEF or HFrEF (118, 119).

1.1.4.1 Insulin resistance and impaired glucose metabolism

Insulin resistance impairs cardiomyocyte glucose uptake, glycolysis, and survival signaling. Stress kinase-mediated IRS-1 phosphorylation disrupts PI3K-Akt signaling, reducing GLUT4 translocation, eNOS activation, and anti-apoptotic pathways, while MAPK pathways remain active, causing selective insulin resistance, endothelial dysfunction, and microvascular impairment (120). Beyond glucose handling, impaired cardiac insulin signaling compromises mitochondrial function and energy homeostasis (121). The resulting metabolic inflexibility forces cardiomyocytes to rely excessively on fatty acid oxidation despite elevated circulating free fatty acids, creating a substrate mismatch that impairs ATP generation and promotes oxidative stress. This shift from glucose to fatty acid metabolism occurs despite glucose abundance, fundamentally altering myocardial energetics and initiating a cascade of cellular dysfunction that precedes overt systolic impairment (115).

1.1.4.2 Adipose tissue dysfunction and adipokine imbalance

Obesity and diabetes alter adipokine profiles profoundly: adiponectin decreases, worsening oxidative stress and apoptosis, while elevated leptin promotes hypertrophy, RAAS activation, and inflammation (122) (123). Decreased adiponectin impairs cardiac AMPK signaling and reduces ceramide catabolism, promoting lipid accumulation and mitochondrial dysfunction (122). Other adipokines (resistin, visfatin, omentin-1) contribute to a pro-inflammatory milieu promoting remodeling (124). The dysfunctional adipose tissue itself becomes a source of inflammatory cytokines and lipid metabolites, particularly ceramides and diacylglycerols, that circulate systemically and accumulate in cardiomyocytes(125). Importantly, adiponectin resistance develops in advanced heart failure despite paradoxically elevated circulating adiponectin levels,

reflecting impaired myocardial adiponectin receptor signaling and blunted cardioprotective responses (122).

1.1.4.3 Lipotoxicity and glucotoxicity

Excess fatty acid uptake generates ceramides and diacylglycerols, impairing Akt signaling, increasing ROS, and promoting apoptosis. Accumulated ceramides directly activate atypical PKCs and inhibit insulin receptor signaling, further exacerbating substrate utilization defects (126). Chronic hyperglycemia triggers advanced glycation endproducts (AGE) formation, PKC activation, and polyol pathway flux, further enhancing oxidative stress and cellular injury (127, 128). AGE-induced collagen cross-linking increases myocardial stiffness, while simultaneously promoting mitochondrial ROS generation through RAGE receptor signaling. The combination of ceramide accumulation and AGE formation creates a pro-apoptotic milieu in which cardiomyocytes undergo programmed cell death through multiple mechanisms including ferroptosis (127, 129).

1.1.4.4 Mitochondrial dysfunction and impaired energy metabolism

Diabetic hearts show reduced oxidative capacity, ATP production, and impaired dynamics due to defective PPARα/PGC-1α signaling, enhanced fission, reduced fusion, and impaired mitophagy (130). Reliance on fatty acid oxidation increases ROS and lipotoxicity, further impairing energetics. Mitochondrial quality control becomes dysregulated, with excessive fission-promoting Drp1 phosphorylation at Ser616 and O-GlcNAcylation, while fusion-promoting OPA1 and Mfn1/2 expression decline (131) (132). This mitochondrial fragmentation impairs calcium handling and promotes opening of the mitochondrial permeability transition pore, releasing pro-apoptotic factors (133). Emerging evidence indicates that decreased MFN2 activates the cGAS-STING pathway through mitochondrial DNA release, triggering sterile inflammation that exacerbates myocardial injury (130, 134-136).

1.1.5 Integrated Pathophysiological Mechanisms Across Cardiometabolic Diseases

Cardiometabolic disorders share overlapping mechanisms and systemic inflammation, oxidative stress, and disrupted inter-organ communication driving cardiovascular complications. These interconnected pathways create self-reinforcing cycles that amplify disease progression, with metabolic dysfunction in one tissue triggering compensatory changes in others that ultimately lead to cardiac injury.

1.1.5.1 Systemic inflammation and immune activation

In obesity, adipose-derived M1 macrophages and Th1 and Th17 cells secrete pro-inflammatory cytokines including TNF-α, IL-6, and MCP-1 (137), which drive endothelial activation, cardiomyocyte hypertrophy, fibrosis, and NLRP3 inflammasome-dependent IL-1β and IL-18 signaling (138). This process, termed meta inflammation, is a chronic low-grade inflammatory state distinct from classical acute inflammation and is characterized by immune cell infiltration into metabolic tissues such as visceral adipose tissue, liver, and skeletal muscle (139). As adipose tissue expands, macrophages undergo a phenotypic shift from anti-inflammatory M2 to pro-inflammatory M1 states, establishing a sustained inflammatory environment (140). In response to circulating inflammatory mediators, endothelial cells upregulate adhesion molecules including VCAM-1, ICAM-1, and E-selectin, thereby facilitating leukocyte adhesion, transmigration, and vascular inflammation (141, 142). The NLRP3 inflammasome functions as a metabolic danger sensor and is activated by saturated fatty acids, cholesterol crystals, and hyperglycemia, providing a mechanistic link between nutrient excess and innate immune activation (143). In parallel, regulatory T cells that normally suppress inflammation are depleted in obese adipose tissue, further skewing immune balance toward pro-inflammatory responses (144). Collectively, this dysregulated immune landscape drives insulin resistance in peripheral tissues and promotes atherosclerotic plaque formation, myocardial fibrosis, and electrical remodeling, increasing susceptibility to arrhythmias.

1.1.5.2 Oxidative stress and mitochondrial injury

ROS generated by mitochondria, NADPH oxidases, and xanthine oxidase reduce nitric oxide bioavailability, activate NF-κB and matrix metalloproteinases, disrupt calcium homeostasis, and exacerbate insulin resistance, thereby initiating a self-reinforcing cycle of mitochondrial injury (145, 146). Mitochondrial dysfunction is characterized by impaired ATP production, increased proton leak, and enhanced superoxide generation, particularly in the setting of nutrient overload or ischemia reperfusion injury (147). Reduced nitric oxide availability compromises endothelium dependent vasodilation, increases vascular stiffness, and promotes platelet aggregation. In parallel, oxidative modification of proteins, lipids, and DNA activates stress responsive transcription factors such as NF-κB, which amplifies inflammatory gene expression (148). Oxidative stress also activates matrix metalloproteinases that degrade extracellular matrix components, leading to

atherosclerotic plaque destabilization and adverse ventricular remodeling (148). In cardiomyocytes, disruption of sarcoplasmic reticulum calcium cycling impairs contractility and increases vulnerability to arrhythmias (149). Moreover, advanced glycation end products formed during hyperglycemia perpetuate oxidative stress through receptor mediated pathways, providing a mechanistic link between glucose toxicity and sustained vascular injury (150, 151).

1.1.6 Current therapeutic strategies

The management of cardiometabolic diseases has evolved significantly over the past decade, incorporating both established and emerging therapeutic approaches. Moreover, Current evidence-based therapeutic strategies include (Table 1):

Table 1.1 Current therapeutic approaches for cardiometabolic diseases

Category	Intervention	Key Agents	Effects
Pharmacological Interventions	PCSK9 Inhibitors	Evolocumab, Alirocumab	Reduce LDL-C; reduce cardiovascular events; prevent PCSK9-mediated LDLR degradation (152, 153)
	SGLT2 Inhibitors	Empagliflozin, Dapagliflozin, Canagliflozin	Reduce CV death, HF hospitalizations, and renal disease progression; mechanisms: diuresis, improved energetics, anti-inflammatory (154-156)
	GLP-1 Receptor Agonists	Liraglutide, Semaglutide	Reduce major adverse CV events (MACE), especially in established CVD; provide glycemic and CV protection (157, 158)
	Dual Antiplatelet Therapy	Aspirin + P2Y12 inhibitor	Standard for 12 months post-ACS (159, 160)

		(clopidogrel, ticagrelor, prasugrel)	
	High-Intensity Statins	Atorvastatin 80mg, Rosuvastatin 40mg	Target LDL <70 mg/dL (<1.8 mmol/L); essential for very high-risk patients (161)
	ACEi/ARBs + Beta-blockers	Lisinopril, Ramipril, Metoprolol, Carvedilol	Improve survival in post-MI patients with reduced EF (162, 163)
Interventional Therapies	Primary PCI	Door-to-balloon ≤90 min	Gold standard for STEMI (164-166)
	Complete Revascularization	Multivessel PCI	Superior to culprit-only PCI in STEMI patients (167, 168)
	Drug-Eluting Stents	3rd-gen DES with biodegradable polymers	↓ very late stent thrombosis; improved long-term outcomes
Emerging Therapies	Gene Therapy	CRISPR-Cas9 targeting PCSK9/lipid genes	Promising preclinical lipid management (169, 170)
	RNA-Based Therapies	Inclisiran (siRNA), mRNA cardiac regeneration	Durable lipid lowering, myocardial repair (171, 172)
	Stem Cell Therapy	Mesenchymal stem cells, cardiac progenitors	Myocardial repair, regeneration potential (173, 174)

1.2 Adiponectin

Adiponectin is an adipocyte-specific factor, first described in 1995 (175). It is a 244-amino acid protein hormone predominantly secreted by adipocytes, representing one of the most abundant

adipokines in circulation (176). Unlike most adipokines, adiponectin levels are inversely correlated with adiposity, with reduced concentrations observed in obesity, type 2 diabetes, and cardiovascular diseases. This unique profile suggests adiponectin serves as a protective factor against cardiometabolic dysfunction (177, 178).

1.2.1 Regulation and signaling mechanisms

Adiponectin exerts its biological effects through binding to specific receptors, primarily adiponectin receptor 1 (AdipoR1) and adiponectin receptor 2 (AdipoR2) (179). Upon receptor binding, adiponectin activates several keys signaling pathways that mediate its metabolic and cardioprotective effects. The two principal pathways activated by adiponectin are the AMP-activated protein kinase (AMPK) and p38 mitogen-activated protein kinase (p38MAPK) pathways (179). AMPK activation by adiponectin occurs through multiple mechanisms and represents a central mediator of adiponectin's metabolic effects. AMPK serves as a cellular energy sensor that promotes catabolic pathways while inhibiting anabolic processes when cellular energy is depleted (180). Adiponectin-mediated AMPK activation leads to increased fatty acid oxidation, glucose uptake, and mitochondrial biogenesis (Figure 1.3). The AMPK pathway also regulates autophagy through inhibition of mechanistic target of rapamycin (mTOR) signaling, promoting cellular quality control and stress resistance (180). The p38MAPK pathway represents another important signaling cascade activated by adiponectin. Research has demonstrated that the adaptor protein APPL1 mediates adiponectin-stimulated p38MAPK activation through scaffolding of the transforming growth factor-β-activated kinase 1 (TAK1) and mitogen-activated protein kinase kinase 3 (MKK3) cascade. This pathway is essential for adiponectin-induced glucose uptake and fatty acid oxidation in muscle cells, independent of AMPK activation (180). The interaction between AMPK and mTOR signaling is particularly important for adiponectin's effects on autophagy and cellular homeostasis. AMPK activation by adiponectin leads to mTOR inhibition through multiple mechanisms, including direct phosphorylation of raptor and activation of tuberous sclerosis complex 1/2 (TSC1/2). This results in release of mTOR-mediated inhibition of autophagy initiation, promoting cellular quality control mechanisms (181).

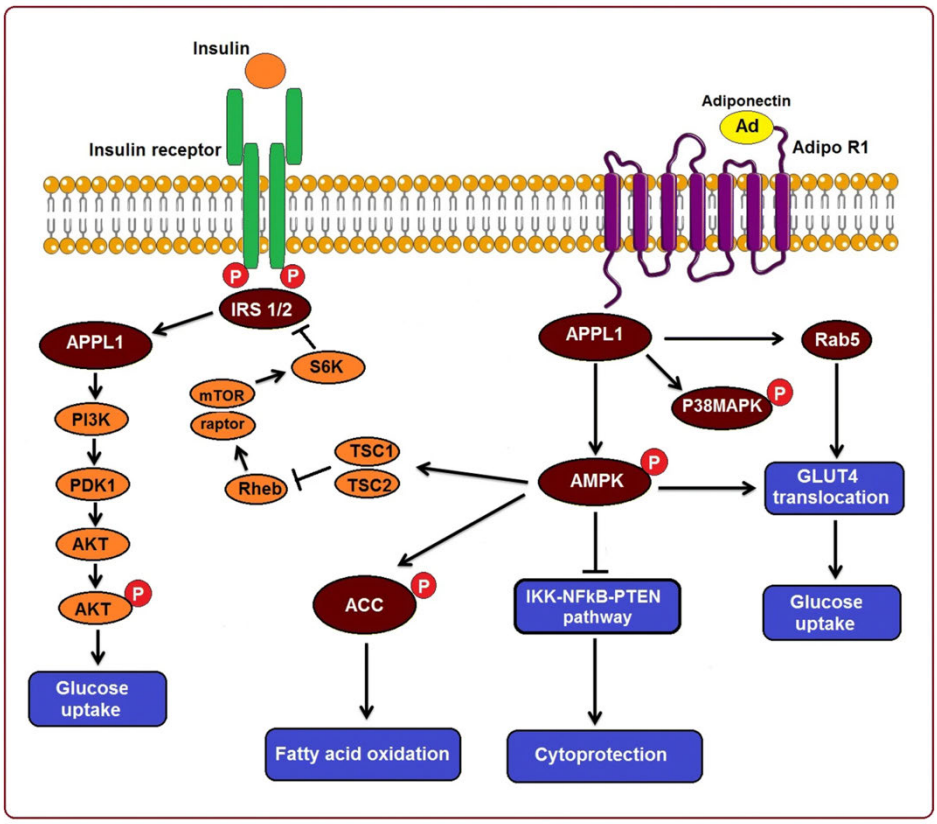

(Adapted from Karamian M, et al., Journal of Physiology and Biochemistry. 77, 205–214 (2021)

Figure 1.3 Adiponectin signaling

Figure 1. 3 Binding of adiponectin to adiponectin receptor can activate AMPK through adaptor protein APPL1. APPL1 binds to AMPK and PI3K, thereby activating fatty acid oxidation and glucose uptake.

1.2.2 Metabolic and cardioprotective effects

1.2.2.1 Anti-inflammatory actions

Adiponectin functions as a potent anti-inflammatory adipokine by orchestrating a multipronged suppression of inflammatory signaling across several cell types (182). In macrophages and monocytes, adiponectin mediates phenotypic polarization from the pro-inflammatory M1 state (characterized by TNF-α and IL-6 production) toward the anti-inflammatory M2 phenotype, which secretes protective IL-10 and tissue inhibitor of metalloproteinase-1 (183) (184). This macrophage repolarization occurs through sustained inhibition of NF-κB signaling and suppression of pro-

inflammatory cytokine production (184). Adiponectin directly blocks the NLRP3 inflammasome activation in microglia and macrophages, preventing assembly of the NLRP3-ASC-pro-caspase-1 complex and thereby reducing maturation of IL-1β and IL-18 (185). In endothelial cells, adiponectin suppresses TNF-α and resistin-induced expression of adhesion molecules including E-selectin, VCAM-1, and ICAM-1, thereby reducing monocyte recruitment to vessel walls (186). Additionally, adiponectin enhances constitutive production of NO through AMPK-dependent phosphorylation and activation of endothelial NO synthase (eNOS), creating a potent anti-inflammatory microenvironment through cAMP-PKA-dependent mechanisms. In vivo studies demonstrate that adiponectin-deficient mice develop exaggerated inflammatory responses, while adiponectin overexpression via adenoviral delivery dramatically reduces circulating pro-inflammatory markers and atherosclerotic lesion burden (186).

1.2.2.2 Anti-oxidative stress

Adiponectin exerts strong antioxidant effects by suppressing multiple sources of reactive oxygen species (ROS) production while simultaneously upregulating endogenous antioxidant enzyme systems (177). At the level of NADPH oxidase, adiponectin inhibits superoxide anion production induced by high glucose, oxidized LDL, and palmitate in vascular endothelial cells (187). This inhibition operates through both cAMP-dependent PKA-mediated and AMPK-dependent pathways, reducing basal and agonist-induced ROS generation. (187) Adiponectin activates the Nrf2 transcription factor pathway, leading to upregulation of cytoprotective antioxidant enzymes including superoxide dismutase (SOD), catalase, and glutathione peroxidase (GPx) (188). Adiponectin treatment restores eNOS coupling in vessels exposed to oxidative stress, shifting the balance from uncoupled eNOS to coupled eNOS (189). Within mitochondria, adiponectin promotes selective removal of damaged mitochondria through mitophagy, which is critical for preventing accumulation of mitochondrial ROS (mtROS) that would otherwise propagate oxidative damage and inflammasome activation (190).

1.2.2.3 Metabolic regulation

Adiponectin's metabolic effects center on enhancing insulin sensitivity and glucose homeostasis through coordinated actions across multiple tissues (179). In skeletal muscle, adiponectin stimulates AdipoR1-dependent AMPK activation, which phosphorylates and inactivates acetyl-CoA carboxylase (ACC), thereby promoting fatty acid oxidation and reducing ceramide

accumulation, a lipid intermediate that impairs insulin signaling (191) (192). Adiponectin directly enhances GLUT4 translocation to the cell membrane via AMPK-mediated signaling, increasing basal and insulin-stimulated glucose uptake capacity (193). In the liver, AdipoR2-mediated PPARα activation enhances fatty acid oxidation and ketogenesis while suppressing hepatic gluconeogenesis, contributing to fasting glucose normalization (194). In the heart, adiponectin preserves metabolic flexibility, the capacity to switch between glucose and fatty acid oxidation based on physiological demand. Critically, adiponectin activates PGC-1α-dependent mitochondrial biogenesis through AMPK and SIRT1 signaling, increasing mitochondrial copy number and oxidative capacity, which underlies sustained improvements in whole-body glucose disposal (195, 196). These coordinated metabolic effects explain the strong epidemiological associations between low adiponectin levels and development of insulin resistance, type 2 diabetes, and metabolic syndrome.

1.2.2.4 Autophagy regulation

Adiponectin modulates autophagy with exquisite tissue-specific precision, promoting protective autophagy and mitophagy in cardiac and skeletal muscle while suppressing excessive autophagy that would be maladaptive in ischemia-reperfusion injury contexts. The canonical adiponectin-autophagy pathway operates through AMPK activation: phosphorylated AMPK inhibits mTORC1 while simultaneously phosphorylating and activating ULK1, the master initiator of autophagy (197 {Sung, 2024 #175)}. ULK1 phosphorylates and recruits Beclin-1, facilitating formation of the Beclin-1-VPS34 complex essential for autophagosome biogenesis (198). Adiponectin-stimulated autophagy selectively targets removal of damaged or dysfunctional mitochondria via mitophagy, a critical process in cardiomyocytes where PINK1-Parkin-mediated mitophagy coordinates recognition of depolarized mitochondria and their engulfment by autophagosomes (199, 200). In cardiac tissue subjected to IR stress, adiponectin suppresses excessive and potentially detrimental autophagy, preventing accumulation of autophagosomes (201). Adiponectin-mediated autophagy enhancement contributes to clearance of protein aggregates, misfolded proteins, thereby ameliorating lipotoxicity and maintaining contractile function during metabolic stress (202). The context-dependent nature of adiponectin's autophagy regulation, promoting mitophagy in chronic metabolic conditions while limiting excessive autophagy during acute ischemic injury, exemplifies the sophisticated tissue-protective mechanisms that distinguish adiponectin as a therapeutic target.

1.2.3 Adiponectin therapeutics

Given the therapeutic potential of adiponectin, significant research efforts have focused on developing adiponectin mimetics and receptor agonists. These compounds aim to replicate the beneficial effects of adiponectin while overcoming limitations associated with protein-based therapeutics, such as short half-life and poor tissue penetration.

Osmotin-derived adiponectin-mimetic peptides represent one promising approach. These small peptides can cross the blood-brain barrier and activate adiponectin signaling pathways, showing neuroprotective effects in Alzheimer's disease models through AdipoR1/AMPK activation. Similar approaches are being investigated for cardiovascular applications (203). Small molecule adiponectin receptor agonists have emerged as another therapeutic strategy (204). AdipoRon is a key example, functioning as an agonist for both AdipoR1 and AdipoR2 receptors. This small molecule successfully ameliorates diabetes in genetically obese rodent models (db/db mice) and prolongs their lifespan during high-fat diet feeding (205) (206). AdipoRon has also demonstrated significant cardioprotective effects, attenuating cardiac remodeling induced by pressure overload (207). The compound activates the same beneficial signaling pathways as native adiponectin, including AMPK activation and ceramidase signaling, while offering advantages in terms of bioavailability and pharmacokinetics (208) (209).

Current therapeutic strategies also focus on restoring physiological adiponectin levels rather than supraphysiological enhancement. This approach addresses the adiponectin paradox (210), where extremely high adiponectin levels may sometimes correlate with poor cardiovascular outcomes, likely reflecting compensatory responses to underlying pathology rather than beneficial effects. Research increasingly supports targeting the adiponectin-to-leptin ratio as a more effective therapeutic strategy, combining adiponectin enhancement with leptin reduction approaches (211).

1.3 Extracellular Vesicles

1.3.1 EV biology and classification

Extracellular vesicles (EVs) are membrane-bound particles released by virtually all cells that mediate intercellular communication via proteins, lipids, and nucleic acids. EVs include exosomes (30-150 nm, from endosomal multivesicular bodies), microvesicles (100-1000 nm, from plasma membrane budding), and apoptotic bodies (1000-5000 nm, from cell fragmentation) (Figure 1.4) (212). EV cargo comprises cytosolic, membrane, and nuclear proteins, including tetraspanins

(CD9, CD63, CD81), HSPs, and ESCRT components; lipids enriched in cholesterol, sphingomyelin, and phosphatidylserine; and nucleic acids such as mRNAs, miRNAs, lncRNAs, circular RNAs, and DNA fragments, with miRNAs as key regulators of recipient cell gene expression (212).

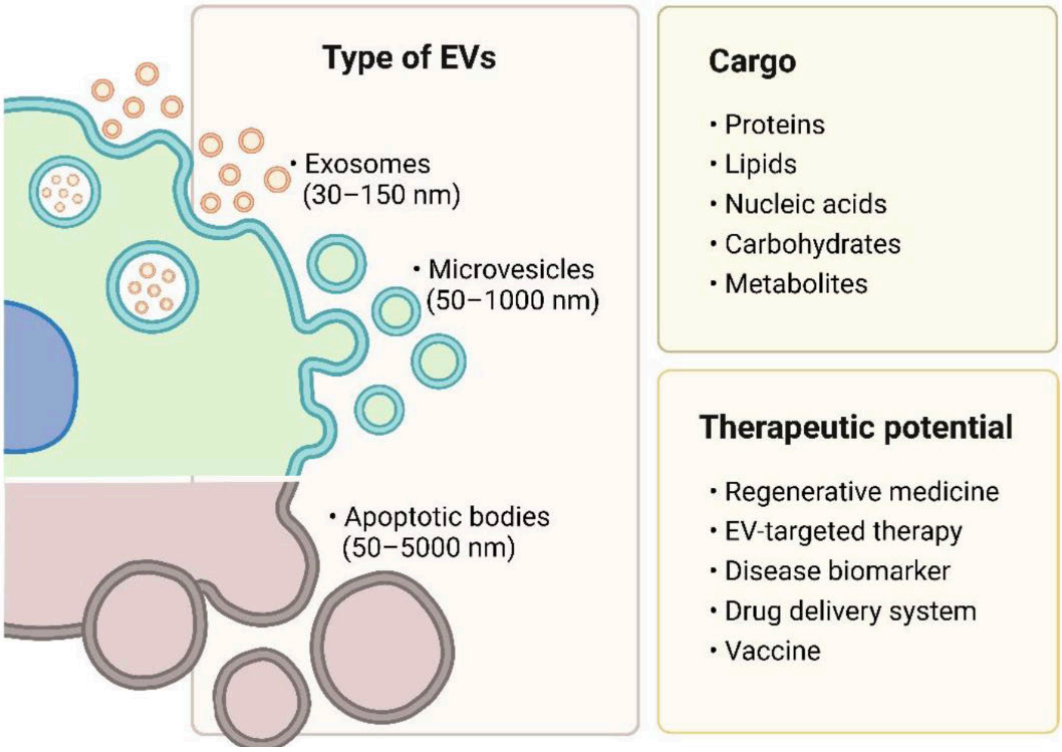

(Adapted from Ng C, Int. J. Mol. Sci. 2022, 23(14), 7986)

Figure 1.4 Type, cargo and therapeutic potential of EVs

1.3.2 EVs in heart

In healthy cardiovascular conditions, EVs facilitate essential communication between different cardiac cell types and contribute to the maintenance of cardiac function (213). Cardiomyocyte-derived EVs transfer protective factors to neighboring cells, including heat shock proteins (HSP20) with angiogenic, antiapoptotic, and antifibrotic properties (214). Endothelial cell-derived EVs promote angiogenesis and maintain vascular function through the delivery of specific miRNAs and proteins (215). The cardiac EV network involves multiple cell types working in concert. Mesenchymal stem cells (MSCs) secrete EVs that enhance cardiac repair through the delivery of miR-21, which activates the PI3K pathway and improves contractile function (216). Cardiac telocytes release EVs containing various miRNAs that promote endothelial cell migration,

proliferation, and tube formation (217). The composition and function of EVs are significantly altered in cardiovascular disease states. During pathological conditions, EVs may carry detrimental cargo that promotes inflammation, thrombosis, and tissue damage. In myocardial infarction, cardiac fibroblast-derived EVs can initiate cardiomyocyte hypertrophy through miR-21-3p, while cardiomyocyte EVs may inhibit autophagy and promote apoptosis via miR-30a (213, 218). The transition from cardioprotective to pathological EV signaling represents a critical shift in disease progression. Macrophage-derived EVs in injured tissue can inhibit fibroblast proliferation and promote inflammation, increasing the risk of cardiac rupture through miR-155 (219). This dysregulation of EV-mediated communication contributes to the progression from acute injury to chronic heart failure (219).

Adipose tissue has emerged as a significant source of EVs that mediate inter-organ communication and metabolic regulation (220). Adipose tissue-derived EVs carry metabolic regulators, including microRNAs and proteins, to distant organs including the heart (220). These vesicles demonstrate obesity-associated changes in their secretion patterns and cargo composition, with implications for metabolic health (221). Brown adipose tissue-derived EVs provide cardioprotection through the delivery of beneficial cargo molecules (222). (Table 1.2).

Table 1.2 Source of EVs and their actions on cardiometabolic diseases

EV Source	Key Features	Therapeutic Effects in Cardiac Disease	Disease Context
Mesenchymal Stem Cell (MSC) EVs	Transfer of anti-apoptotic factors, pro-angiogenic miRNAs (miR-126, miR-210, miR-132), antioxidant enzymes	Reduced infarct size, improved cardiomyocyte survival, enhanced angiogenesis, reduced fibrosis, improved mitochondrial function	Myocardial infarction (MI), heart failure, diabetic cardiomyopathy (223-227)

Cardiac Progenitor Cell (CPC) EVs	Delivery of cardiac transcription factors (GATA4, Nkx2.5), pro-survival and pro-proliferative signals	Promotes cardiac regeneration, enhances cardiomyocyte differentiation	Acute MI, heart failure with preserved ejection fraction, pressure overload-induced cardiomyopathy (228-231)
Induced Pluripotent Stem Cell (iPSC) EVs	Cardiac differentiation factors, low immunogenicity, scalable	Superior regenerative capacity compared to adult stem cell EVs	Broad cardiac regeneration applications (232-236)
Cardiosphere-Derived Cell (CDC) EVs	miR-181b-mediated macrophage repolarization, anti-inflammatory cytokines, matrix metalloproteinase activation	Anti-inflammatory, antifibrotic, improved cardiac function	Ischemic cardiomyopathy, dilated cardiomyopathy, diabetic cardiomyopathy (237-239)
Brown Adipose Tissue (BAT) EVs	Cardioprotective miRNAs (miR-125b-5p, miR-128-3p, miR-30d-5p), enhanced mitochondrial function, improved fatty acid oxidation	Reduced apoptosis, improved post-MI remodeling, enhanced energetics, reduced fibrosis	Myocardial infarction, heart failure, diabetic cardiomyopathy (222, 240, 241)
Endothelial Cell EVs	Delivery of VEGF, FGF, PDGF, angiogenic miRNAs (miR-126, miR-17-92 cluster)	Promotes angiogenesis, improved coronary perfusion, reduced vascular inflammation	MI, heart failure, diabetic cardiomyopathy (242-245)

White Adipose Tissue (WAT) EVs	Healthy WAT: adiponectin, anti-inflammatory cytokines; Obese WAT: pro-inflammatory cytokines	Improved insulin sensitivity, anti-inflammatory effects; Obese WAT may worsen fibrosis and dysfunction	Healthy vs. obesity-related cardiac conditions; interventions improve WAT-EV composition (246-248)
Macrophage EVs	M1: pro-inflammatory cytokines; M2: anti-inflammatory cytokines, pro-repair signals	M1: detrimental; M2: promotes tissue repair, angiogenesis, progenitor cell activation	Therapeutic targeting via macrophage polarization or EV engineering (249-251)
Platelet EVs	Hemostatic function; pro-thrombotic and inflammatory in disease	Context-dependent; may contribute to thrombosis or be modulated for cardioprotection	Cardiovascular disease: antiplatelet therapy modulates EV effects (252-256)

1.3.3 Adiponectin-EV interactions

Adiponectin, a major adipokine, plays a dual role in EV biology as both a modulator of EV biogenesis and as cargo within EVs. This unique glycosylphosphatidylinositol (GPI)-anchored cadherin, T-cadherin, serves as the primary receptor for high-molecular-weight forms of adiponectin (257). The interaction between adiponectin and T-cadherin enhances EV biogenesis and secretion, providing a mechanism for the systemic effects of this important metabolic hormone (257). The EV released by the stimulation of adiponectin conferred cardioprotective effect in heart failure mice model (258). Additionally, it was found that adipocyte-release EV carried adiponectin, and this EV-carried adiponectin exert adiponectin-mimetic insulin-sensitizing, and anti-inflammatory effect (259).

1.3.4 Raba8 and EV

Recently, Rab8a has emerged as a context-dependent regulator of EV biogenesis and release. Rab8a is a small GTPase linked to post-Golgi trafficking, polarized sorting, and exocytosis (260).

In prostate cancer, it acts as a positive regulator of EV secretion and is suppressed by the co-receptor Klotho-β (261). In carcinoma cells on stiff extracellular matrix (ECM), stiffness activates FAK-PI3K-Akt signalling, which enhances Rabin8 activity and increases GTP-Rab8 levels. This elevates EV secretion independently of Rab27 (262). In nucleus pulposus cell, abolish of Rab8a retained the secretion of EV (263). However, the action of Rab8a EV modulation effect remained unclear under the context of heart diseases.

1.4 Knowledge gaps and research objectives

Despite significant advances in understanding adiponectin's role in cardiometabolic disease, several important knowledge gaps remain. The molecular mechanisms underlying adiponectin's context-dependent effects, particularly the apparent paradox of elevated levels in some cardiovascular diseases, require further investigation. Additionally, the optimal strategies for therapeutic targeting of adiponectin signaling pathways need to be defined. The relationship between adiponectin and autophagy in cardiac disease represents an area requiring additional research. While the general framework of adiponectin-AMPK-autophagy signaling is established, the specific conditions under which this pathway provides protection versus potential harm need clarification. Furthermore, the development of autophagy-targeting therapeutics requires better understanding of the temporal and spatial regulation of this process. The role of extracellular vesicles in mediating adiponectin's effects represents an emerging research frontier. Understanding how adiponectin influences EV biogenesis, cargo selection, and intercellular communication could provide new insights into its mechanisms of action and suggest novel therapeutic approaches.

Future research should focus on developing more effective adiponectin mimetics and delivery systems. Additionally, combination approaches that target multiple aspects of cardiometabolic dysfunction, including inflammation, oxidative stress, and metabolic inflexibility, may provide superior therapeutic outcomes. The integration of systems biology approaches and personalized medicine strategies will be essential for translating these findings into effective clinical interventions.

The therapeutic potential of targeting adiponectin signaling pathways in cardiometabolic disease is substantial, but realizing this potential will require continued research to address the current knowledge gaps and develop safe, effective interventions. The complex interplay between

adiponectin, autophagy, and extracellular vesicle-mediated communication represents a particularly promising area for future investigation and therapeutic development.

1.4.1 General Hypothesis

Adiponectin receptor agonist ALY688 protects against myocardial ischemia-reperfusion injury through a multifaceted mechanism involving direct cardioprotective effects and Rab8a-dependent extracellular vesicle-mediated intercellular communication, with enhanced cardioprotection achieved through restoration of autophagy flux and preservation of lipid droplet-mitochondria metabolic coupling.

1.4.2 Specific Hypothesis

- ALY688 provides cardioprotection against myocardial ischemia-reperfusion injury through both direct cellular effects and Rab8a-dependent extracellular vesicle mechanisms, with enhanced EV biogenesis contributing to intercellular protective signaling.
- ALY688 modulates extracellular vesicle cargo composition to deliver cardioprotective signals, reprogramming EV proteomes to enhance metabolic resilience and reduce oxidative stress in target cardiomyocytes under ischemia injury.
- Loss of Rab8a-dependent tethering between lipid droplets and mitochondria drives hypoxia-reoxygenation injury, with ALY688 preserving this metabolic coupling to maintain fatty acid oxidation capacity during ischemic stress.
- Adiponectin deficiency exacerbates ischemia-induced cardiac dysfunction through impaired autophagy flux, leading to enhanced cardiomyocyte apoptosis and compromised myocardial recovery.

1.4.3 Research Objectives

Throughout my doctoral training at York University, I aimed to investigate the molecular mechanisms underlying adiponectin-mediated cardioprotective effects, focusing on their relationship to extracellular vesicle signaling, and metabolic coupling in ischemic heart disease.

Study 1: ALY688 and Extracellular Vesicle-Mediated Cardioprotection

This study aimed to determine the cardioprotective mechanisms of ALY688, a synthetic adiponectin receptor agonist, in the context of myocardial ischemia-reperfusion injury. Specifically,

I sought to evaluate both direct cellular effects and EV-mediated signaling pathways, and to investigate the role of Rab8a in regulating EV biogenesis and function.

Study 2: Modulation of Extracellular Vesicles by an Adiponectin Receptor Agonist

The objective of this study was to characterize how ALY688 influences EV biogenesis and cargo composition, and to assess the functional role of these EVs in mediating cardioprotective effects. This included evaluating EV-dependent signaling in cardiomyocytes and determining the therapeutic potential of EV-based interventions in myocardial ischemic injury.

Study 3: Rab8a-Dependent Metabolic Coupling in Ischemic Stress

This study aimed to investigate the role of Rab8a in mediating lipid droplet-mitochondria interactions and regulating metabolic coupling during hypoxia-reoxygenation injury. Additionally, I sought to determine how disruption of this pathway contributes to metabolic dysfunction in the ischemic heart, and whether adiponectin receptor activation modulates these processes.

Study 4: Role of Adiponectin in Autophagy Regulation During Ischemia

The objective of this study was to define the role of adiponectin in regulating cardiac autophagy during ischemic injury. This included characterizing autophagy dynamics *in vivo*, developing imaging approaches to monitor autophagic activity, and determining the contribution of adiponectin cardiomyocyte survival under hypoxic stress via autophagy modulation.

2. Chapter 2: ALY688 Protects Against Myocardial Ischemia-Reperfusion Injury via Direct Effects and Rab8a-dependent Extracellular Vesicles

2.1 Abstract

Despite advances in percutaneous coronary intervention, ischemia-reperfusion (IR) injury remains a major cause of morbidity and mortality. This study evaluated ALY688, a synthetic adiponectin receptor agonist, for cardioprotective potential in IR injury. We confirmed ALY688's receptor specificity and characterized pharmacokinetics and toxicology in rodent, mini-pig, and dog models. In a rat myocardial IR model, ALY688 administered intravenously during ischemia and subcutaneously thereafter for 28 days reduced troponin-I release, cardiomyocyte death, infarct size, and preserved cardiac function. ALY688 directly restored autophagic flux, reduced reactive oxygen species accumulation, and attenuated cardiomyocyte apoptosis after IR and hypoxia-reoxygenation injury. Proteomic analysis identified Rab8a as downregulated by IR but maintained with ALY688. ALY688 increased extracellular vesicle (EV) content in myocardium and plasma, with EVs exhibiting cargo enriched in glycolytic and stress-related proteins. These EVs protected cardiomyocytes from injury. CRISPR-mediated Rab8a knockout impaired ALY688-induced EV biogenesis and abrogated beneficial effects. These findings support ALY688 as promising therapy attenuating IR injury through direct protection and Rab8a-dependent signaling. Translational Perspective: Myocardial ischemia-reperfusion injury affects millions of patients undergoing percutaneous coronary intervention, yet no effective pharmacological therapy exists. ALY688 represents a breakthrough therapeutic approach addressing both direct cardioprotection and novel extracellular vesicle-mediated signaling. The drug's demonstrated safety profile across species, combined with its unique ability to enhance cardioprotective EV biogenesis through Rab8a-dependent pathways, positions it for rapid clinical translation. Given that EVs are emerging as both therapeutic agents and early biomarkers in cardiovascular disease, ALY688's dual mechanism offers unprecedented clinical potential. With reperfusion injury contributing up to 50% of final infarct size, this EV-enhanced cardioprotection could significantly improve patient outcomes and reduce heart failure development.

2.2 Introduction

Myocardial ischemia-reperfusion (IR) injury remains a leading cause of morbidity and mortality worldwide, despite significant advances in reperfusion therapies for acute myocardial infarction (49). While the prompt restoration of coronary blood flow is essential for salvaging viable myocardium, the process of reperfusion paradoxically initiates a cascade of deleterious events, including oxidative stress, inflammation, calcium overload, and mitochondrial dysfunction, which together contribute to substantial cardiomyocyte death and adverse ventricular remodeling (264). It is estimated that up to 50% of the final infarct size may be attributed to reperfusion injury rather than the initial ischemic insult (265). This phenomenon not only limits the efficacy of current therapeutic interventions but also highlights the complexity of myocardial IR injury as a multifactorial pathophysiological process (266).

Recent mechanistic insights have identified several regulated cell death pathways, including necroptosis, pyroptosis, and ferroptosis, as key contributors to myocardial damage following IR injury (267). The opening of the mitochondrial permeability transition pore during early reperfusion is recognized as a pivotal determinant of cardiomyocyte survival or death, linking mitochondrial dysfunction to the propagation of cell injury. Nevertheless, despite decades of investigation and numerous promising experimental strategies, the successful translation of cardioprotective interventions from bench to bedside has remained elusive, underscoring the urgent need for novel, multifaceted therapeutic approaches that target the diverse mechanisms underlying IR injury (264).

Among endogenous protective factors, adiponectin, an adipocyte-derived cytokine, has emerged as a central regulator of cardiovascular homeostasis. Multiple preclinical studies have demonstrated that adiponectin exerts potent cardioprotective effects, including the reduction of infarct size, inhibition of apoptosis, and attenuation of oxidative and inflammatory stress, primarily through the activation of AMP-activated protein kinase (AMPK) and cyclooxygenase-2 (COX-2) signaling pathways (268-270). In addition to its direct effects on cardiomyocytes, adiponectin modulates endothelial function, inhibits vascular inflammation, and improves metabolic homeostasis, further supporting its role in cardiovascular protection (271). In individuals with obesity, diabetes, or established cardiovascular disease, adiponectin levels are often pathologically reduced (177). This state of relative adiponectin deficiency has spurred interest in the development of strategies to activate adiponectin signaling (177). However, clinical application of native

adiponectin is hampered by its complex multimeric structure, limited tissue bioavailability, and rapid clearance from circulation (204).

To overcome these limitations, considerable efforts have been directed toward the development of small-molecule or peptide-based adiponectin receptor agonists. Among these, ALY688, a synthetic peptide adiponectin receptor agonist, has demonstrated robust cardioprotective efficacy in preclinical models of cardiac injury. ALY688 has been shown to improve cardiac function, reduce fibrosis, and attenuate adverse remodeling following pressure overload induced heart failure (272), effects that are potentially mediated at least in part through the activation of AMPK, phosphorylation of acetyl-CoA carboxylase (ACC), and stimulation of p38MAPK signaling pathway (273, 274). Importantly, as we describe in this manuscript, ALY688 exhibits favorable pharmacokinetic properties and metabolic stability compared to native adiponectin, making it a promising candidate for clinical evaluation. Yet, the precise molecular mechanisms by which ALY688 confers cardioprotection, especially in the setting of IR injury, remain incompletely defined.

In parallel, there has been growing recognition of the role of extracellular vesicles (EV), as critical mediators of intercellular communication in cardiovascular diseases (275). EV are membrane-bound particles released by virtually all cell types and are capable of transferring a diverse array of bioactive molecules, such as proteins, lipids, and nucleic acids, to recipient cells (276). In the context of myocardial IR injury, EV derived from cardioprotective cell types, such as cardiac progenitor cells or stem cells, have been shown to attenuate injury by delivering anti-apoptotic, anti-inflammatory, and pro-regenerative signals. Conversely, EV released from ischemic or injured myocardium may exacerbate cardiac damage through the transfer of pro-inflammatory or pro-apoptotic cargo (277-279). The biogenesis, cargo composition, and release of EV are tightly regulated processes that reflect the physiological or pathological state of the parent cell.

Notably, recent studies have revealed that adiponectin itself can be packaged into EV, and that adiponectin signaling actively promotes EV biogenesis and secretion. Mechanistically, adiponectin enhances exosome release through interactions with T-cadherin on the cell surface, a process linked to improved tissue protection and systemic metabolic regulation (280). Adiponectin-enriched EV have been demonstrated to exert protective effects on various target tissues, including the heart, by modulating oxidative stress, inflammatory responses, and cell survival pathways (259,

277). These findings suggest a complex interplay between adiponectin signaling and EV-mediated mechanisms in cardiovascular protection.

Despite recent advances, a detailed description of how adiponectin receptor agonists such as ALY688 influence EV biogenesis, cargo composition, and function in the context of myocardial IR injury is lacking. In this study, we investigate the effects of ALY688 on cardiac function and remodeling following IR, with a particular focus on its regulation of EV biogenesis and the cardioprotective properties of ALY688-modified EV. By elucidating these mechanisms, our work aims to advance the understanding of adiponectin receptor signaling and EV-based communication in the injured heart, and to identify novel therapeutic strategies for mitigating IR injury and improving cardiac outcomes.

2.3 Materials and Methods

Experimental studies in animal models

All study protocols were approved by the Animal Care Committee of Toronto General Hospital. Female Sprague Dawley rats (the Charles River, Canada) were maintained with *ad libitum* access to water and regular chow diet until 12 weeks of age when they were randomly separated into surgical groups (n=8 per group). All animals were housed in temperature and humidity-controlled rooms (21 ± 2°C, 35-40%) with a daily 12 h light/dark cycle in the animal care facility of Toronto General Hospital in accordance with the guidelines of the Canadian Council on Animal Care. Myocardial ischemia reperfusion injury was induced by 45 minutes of ligation of the left coronary (LAD) artery followed by reperfusion. Sham animals were treated identically except that the suture was passed through the myocardium beneath the LAD artery without ligation. ALY688ER at a dose of 10 mg/kg or vehicle was given via subcutaneous injection during ischemia or during reperfusion, and daily injection for 2 days in acute study and 28 days in chronic study. In the 28-day study, echocardiography was performed to measure cardiac function at baseline (prior to IR injury), 14 and 28 days after ligation. M-mode ultrasound imaging was conducted using LV parasternal short-axis view.

Histology analysis

Paraffin embedded heart sections were subjected to H&E (Sigma, HT1079, HT110216), Masson Trichrome (Sigma, HT15), TUNEL (Promega, G3250) according to manufacturer's protocol and visualized using a bright field slid scanning microscopy (Leica, Aperio AT2) or confocal microscopy (Nikon, Ti2).

Biochemistry analysis

Commercially available kits were used to measure LDH (Abcam, ab102526 for animal samples), LDH (Biosciences, 786210 for cellular samples), Troponin I (Abcam, ab246529), according to manufactural instructions.

Proteomics analysis

Infract zone of heart were frozen and used for proteomic analyses. The frozen sample was ground into powder in a liquid nitrogen-cooled mortar and pestle and kept on dry ice until mass-spec analysis. Proteins were extracted from cryopulverized tumors in a buffer containing 5% sodium

dodecyl sulfate (SDS) and 100 mM TRIS pH 7.8 supplemented with phosphatase and protease inhibitor cocktail The protein concentration of the lysate was determined using bicinchoninic acid assay (BCA) (Thermo Fisher Scientific, Waltham, MA, USA, part# 23225), and protein disulfide bonds were reduced and free Cysteines alkylated with 20 mM tris (2-carboxyethyl) phosphine (TCEP) and 30 mM iodoacetamide, respectively (Millipore-Sigma, part# 646547, and I1149 respectively). In brief, proteins were acidified by adding phosphoric acid to a final concentration of 1.3% v/v. The sample was then diluted in 165 µL of S-TRAP loading buffer (9:1 methanol:water in 100 mM TRIS, pH 7.8) and loaded onto an S-TRAP Micro cartridge (Protifi LLC, Huntington NY) and spun at 4,000 x g for 2 minutes. Samples were washed with 150 µL of STRAP loading buffer three times. Proteins were then digested using trypsin (Promega) at a 1:10 enzyme to substrate ratio for 2 hours at 47°C. Peptides were eluted with 40 µL of 50 mM ammonium bicarbonate, 0.1% formic acid in water, and 50% acetonitrile. Peptides were then desalted using self-made R3-STAGE tips. Desalted peptides were vacuum concentrated and reconstituted in 0.1% trifluoroacetic acid (TFA) prior to analysis by LC-MS/MS.

Nanoparticle tracking analysis (NTA)

To determine EV sizes, 300 µL of EV were analysed by the NanoSight LM10 system (NanoSight Ltd, Salisbury, UK). 60-second videos (number of experiments n = 3, number of videos n = 8) of EV were collected, averaged, and analyzed using LM10 NTA equipped with a 65 mWatt 405 nm violet laser (NanoSight Ltd, Salisbury, UK). 100 nm polystyrene beads (Malvern Instruments, Saint-Laurent, Canada) were used for size calibration, and data captured with sCMOS camera on NTA 3.1 (machine) with Build 3.1.46 (software) at the temperature of 22 °C.

Size-exclusion chromatography isolation of Serum-EV

Size-exclusion chromatography (SEC) using the qEV single columns 70 nm (IZON, Cambridge, MA) was the primary method to isolate EV from serum samples. In all experiments, serum was diluted in filtered PBS at a 1:3 ratio. Fractions 3 to 6 were collected and used for subsequent EV characterization and downstream applications as per manufacturer's recommendations.

Genetic modification of H9c2 cells

CRISPR knock-out lines were generated using guide RNAs cloned into the pX459 plasmid, as previously described (281).To generate Rab8a KO H9c2 cells, guide RNA targeting Rab8a gene

(TGATTGTCCGAAACCGCTCC) are cloned in pLentiCRISPRv2. We then generated viral particles using this vector as well as a control vector that does not target mammalian genomes and used these particles to transduce H9C2 cells. Following selection with puromycin (1 μg/mL), polyclonal populations were assessed for guide efficiency using a T7 endonuclease I assay as reported before (282). Autophagy LC3 HiBiT reporter vector (Promega, GA2550) has a HiBiT tag and contains a sequence encoding the MAP1LC3B gene. H9c2 cells were transfected with the autophagy LC3 HiBiT reporter vector according to the manufacturer manual (283).Nano-Glo HiBiT lytic reagent (Promega, N3040) was added to the cells after each treatment and luminescence was measured on a Thermo Varioskan LUX microplate reader. To generate H9c2 lines stably expressing Venus-based Caspase-3 like protease activity indicator (VC3AI; a gift from Dr Binghui Li, Addgene plasmid 78907), lentiviral particles were produced using pCDH-puro-CMV-VC3AI and transduced cells were selected using 1 μg/mL puromycin. This genetically encoded biosensor consists of cyclized chimeras containing a caspase-3 cleavage site as a switch. Upon cleavage by caspase-3-like proteases, the non-fluorescent indicator rapidly becomes fluorescent and thus detects activation in real-time.

H9c2 cell culture

H9c2 rat embryonic cardiac myoblasts (ATCC® CRL-1446TM) were grown in Dulbecco's Modified Eagle's Medium (DMEM) (Gibco, 11885-084) supplemented with 10% fetal bovine serum (FBS, Thermo, 11885084) and 1% (vol/vol) streptomycin/penicillin (Gibco, 15070063) at 37°C and 5% CO2. Hypoxia was achieved by placing cells in a hypoxic chamber (Onstage Incubator, ThermoFisher, NX7LIVE001) filled with a pre-analyzed gas mixture of 1% O_2 5% CO_2. Normoxia and reoxygenation were achieved by placing cells in the Onstage Incubator filled with 20% O_2 and 5% CO_2. 300 nM ALY688 was treated 30 mins before hypoxia reoxygenation or normoxia as indicated in each experiment.

iPSC culture and cardiomyocyte differentiation

iPSCs, PGPC14 line validated previously (284), were cultured on Matrigel (Corning, 354277) coated plates in mTeSR plus media (Stemcell Technologies, 100-0276) and passaged with ReLeSR (Stemcell Technologies, 100-0483) using a 1:6 – 1:12 dilution every 3-4 days, or upon reaching 80-90% confluence. For cardiomyocyte differentiation, iPSCs were dissociated into single cells using gentle cell dissociation reagent (Stemcell Technologies, 100-0485), and seeded on Matrigel

coated plates containing mTeSR plus media supplemented with 10μM of Y-27623 (Stemcell Technologies, 72304) for 24h. Media was changed daily with mTeSR plus media without Y-27623 until cells reached >95% confluence (3-4 days post-seeding), at which point differentiation was initiated using STEMdiff™ Ventricular Cardiomyocyte Differentiation Kit (Stemcell Technologies, 05010), following manufacturer protocol. Additionally, selection was performed on cardiomyocytes from day 12 – day 18 of differentiation with glucose-free RPMI supplemented with 4mM lactate and B27 containing insulin. Cells were allowed to recover for a minimum of 2 days, then dissociated using TrypLE™ Select (ThermoFisher, A1217701) for 30-45 minutes, pelleted by centrifugation, then seeded in Matrigel coated plates in STEMdiff™ Cardiomyocyte Support Medium (Stemcell Technologies, 05027) for 24h. Cardiomyocytes were seeded at a density of 250,000 – 300,000 cells/cm2 for western blot, and 50,000 – 60,000 cells/cm^2 for all other assays. Media change was performed every 2 days thereafter using RPMI media (Sigma, R8758) supplemented with B27 containing insulin (ThermoFisher, 17504044) for a minimum of 4 days. All cell treatments were carried out using RPMI media supplemented with B27 containing insulin.

Conditioned medium EV isolation

When the cell confluency reached approximately 80%, the culture medium was replaced with DMEM supplemented with 1% streptomycin/penicillin. Cells were then treated as specified for each experiment. To remove residual cells and debris, the conditioned medium was subjected to differential centrifugation at 300 × g for 10 minutes, followed by 2000 × g for 10 minutes, both at room temperature. The resulting supernatant was passed through a 0.22 μm filter. EVs were subsequently isolated from the filtered supernatant via ultracentrifugation at 100,000 × g for 2 hours at 4°C (Type 70.1 Ti Fixed-Angle Titanium Rotor, Beckman Coulter Optima MAX-XP Ultracentrifuge). Final EV pallet was resuspended in filtered PBS for downstream application.

Western blot

Heart tissues and H9c2 cells were used for western blot and cells were suspended in RIPA lysis buffer. BCA (ThermoFisher, A55864) was performed to normalize protein concentration. Proteins were separated by reducing SDS-PAGE and transferred to PVDF membrane. The following antibodies were used for western blot: GAPDH (1:2000, ThermoFisher, #MA5-15738), β-Tubulin (1:2000, Cell Signaling, 2128, Rab8a (1:1000, BD Science, 610844), CD63 (1:1000,

ThermoFisher, PA5-92370), Alix (1:1000, Cell Signaling, 92880), Flotillin 1 (1:1000, Abcam, 133497), Calnexin (1:1000, Abcam, 22595), p-p38 MAPK (1:1000, Cell Signaling, 4511), Total p38 (1:1000, Cell Signaling, 9212), p-AMPKα T172 (1:1000, Cell Signaling, 50081), Total AMPK (1:1000, Cell Signaling, 2532) anti-rabbit (1:5000, Cell Signaling, 7074), and anti-mouse (1:5000, Cell Signaling, 7076). The quantification of signals was performed by densitometry of scanned autoradiographs with the aid of ImageJ (version 1.4v).

Microscopic Imaging

H9c2 cells were seeded on glass coverslips, which were isolated as described previously (285). Staining using different dyes including, CellEvent Caspase 3/7 Detection Reagent (ThermoFisher, C10423), ReadyProbe (ThermoFisher, R37609), CellRox Green (ThermoFisher, C10444), DapRed (Dojindo, D677), DalGreen (Dojindo, D675), MagicRed (Immunochemistry Technologies, 938), and Phalloidin (ThermoFisher, R415) was performed according to manufacturer's protocols and DAPI (HCS NuclearMask Blue Stain, ThermoFisher, H10325) was added simultaneously. Cells were fixed in 4% formaldehyde (Sigma, HT501128) after treatment and mounted with ProLong Gold Antifade Mountant (ThermoFisher, P36930). Slides were visualized under Nikon Eclipse Ti2 and for continuous measurements Cellnsight CX7 Platform (ThermoFisher, CX7A1110) was used. Co-localization analysis was performed with ImageJ JACOP plug-in.

Immunofluorescent analysis

Cells were grown to 70% confluence in 24 well glass bottom plate, then subjected to HR or normoxia with treatment in absence or presence of 500nM N-acetylcysteine (Sigma, A720). After treatment, cells were fixed in ice-cold methanol for 5 min at -20°C. Cells were then blocked and permeabilized by incubation with 5% BSA + 0.1% Triton X-100 in PBS for 30 min at room temperature. Following blocking, cells were incubated overnight at 4°C with conjugated primary antibody (8-OHdG-Alexa 488, Santa Cruz, sc-393871, 1:250; LC3, MBL, M152-3, 1:200; p62, R&D, MAB8028, 1:200) diluted in 1% BSA + 0.05% Saponin in PBS. After primary incubation, cells were washed once for 5 min using 1% BSA + 0.05% Saponin in PBS, followed with secondary antibody incubation (Goat Alexa 488 Anti-Rabbit, A11008, 1:500, Donkey Alexa 594 Anti-Mouse, R37115, 1:500) for one hour at room temperature. Next, cells were incubated with Hoechst (1:2000 in 1% BSA + 0.05% Saponin in PBS) for 15 min at room temperature. Cells were

then washed three times for 5 min each using 1% BSA + 0.05% Saponin in PBS before being immersed in PBS for imaging. Imaging was performed using a Nikon A1 confocal microscope, and mean fluorescence intensity was quantified using ImageJ.

Cell-stained images analysis

Following staining with specific probes, images were acquired using confocal microscopy. All biological replicates were performed with a minimum of three technical replicates. For each technical replicate, at least five randomly selected fields of view were imaged, and a minimum of 50 cells were quantified.

Flow Cytometry

After treatment, adherent cells were incubated with appropriate staining dye then harvested with trypsin-EDTA-0.25% (Gibco, #25200056) after incubation. CellRox DeepRed (ThermFisher, C10422) was used in 0.5% FBS-DMEM at 37°C for 30 minutes. Upon harvest, cells were re-suspended in FACS buffer (2% FBS in PBS) and assessed by flow cytometry (Cytek™ Aurora). Analysis was performed in FlowJO software V10.

EV uptake assay

To confirm EV uptake, EV were stained with DiR (Thermo, D12731) at 37 degree for 1 h, and then subjected to ultracentrifugation at 120,000 x g for 2h for removal of unbound DiR dye by OptiPrep™ density gradient (Sigma, D1556). Recipient cells treated with DiR-labelled EV were countered with PlasMem Bright Green (Dojindo, P504). Visualization was performed using a Nikon A1 confocal microscope with an incubator (37 °C, 5% CO_2). The uptake efficiency of DiR-labelled EV at varied timepoints was collected on all samples using a Cytek® Aurora spectral flow cytometer and analyzed in FlowJo.

Seahorse flux assay

Oxygen consumption rates (OCRs) were determined by a Seahorse XFe24 extracellular flux analyzer (Agilent) as previously described (286). Briefly, WT H9c2 cells, RKO and AKO were seeded in each well of a pre-coated XFe24 cell culture plate and treated with Lalistat1, Paraoxon, ATGL, Rapaymycin, Bafilomycin, and ALY688 prior HR. After HR, cells were washed with XF media twice and incubated in a CO_2-free incubator at 37°C for 1 hour. The following reagents were used: Oligomycin (1 μM, Sigma, 75351), FCCP (carbonyl cyanide p-trifluoromethoxy

phenylhydrazone, 3 μM, Sigma, C2920), and Antimycin A (1 μM, Sigma, A8674) plus Rotenone (1 μM, Sigma, R8875).

Statistics

Data was presented as mean ± SEM. Statistical analysis was performed using GraphPad Prism 9. Student's t-test was used for comparison of two groups and one-way ANOVA or two-way ANOVA were used for comparison of more than two groups. $P<0.05$ was considered statistically significant.

2.4 Results

ALY688 intervention attenuated IR-induced cardiac dysfunction

To evaluate the effects of ALY688, as structure illustrated (Figure 2.1 A) on cardiac function and ventricular remodeling following IR injury, we subjected rats to 45 minutes of coronary artery ligation followed by reperfusion. Two cohorts were analyzed at 48 hours and 28 days post-IR. Groups of rats were administered ALY688ER during ischemia (IR-AI) or administered during reperfusion (IR-AR) or Vehicle (IR) systemically (10 mg/kg) by intravenous infusion starting 5 minutes after ischemia onset or upon reperfusion, followed by daily subcutaneous injections (10 mg/kg) for up to 28 days (Figure 2.1 B). Cardiac function and structure were assessed by transthoracic echocardiography at baseline (day 0), day 14, and day 28 (Figure 2.2 A, Table 2.1). IR injury resulted in a significant reduction in both ejection fraction (EF) and fractional shortening (FS) in the IR group compared to sham controls (Figure 2.1 C-H). Treatment with ALY688 significantly attenuated the decline in EF and FS, indicating preserved systolic function. Notably, the magnitude of functional improvement was similar whether ALY688 was administered during ischemia or initiated at reperfusion (Figure 2.1 E and H). Giving these findings, subsequent mechanistic investigations focused on the groups receiving ALY688 or vehicle at reperfusion. In addition to functional benefits, ALY688 treatment led to a significant reduction in infarct length and an increase in overall myocardial thickness in the region of the infarct (Figure 2.1 I and J), indicating attenuation of adverse ventricular remodeling.

ALY688 effects on cell death, oxidative stress and autophagy following IR

Next, we examined IR-induced cell death by measuring circulating levels of cardiac troponin-I and both circulating and tissue levels of lactate dehydrogenase (LDH), which are commonly used biomarkers of acute cardiac damage. IR led to increased levels of troponin-I and LDH, which were significantly attenuated by ALY688 intervention (Figure 2.3 A, B and C). Furthermore, using TUNEL (terminal deoxynucleotidyl transferase–mediated deoxyuridine triphosphate nick end labeling) to detect cell death, we observed a significant reduction in IR-induced apoptotic cells in myocardial tissue sections from animals treated with ALY688 (Figure 2.3 D and E). In line with the reduced infarct size, qualitative analysis of H&E-stained myocardial tissue sections indicated a decrease in necrotic area (Figure 2.2 B).

Next, we used a cellular model of hypoxia-reoxygenation (HR) in H9c2 cells derived from rat ventricle, subjected to hypoxia (H: 1% O_2) for 6 h followed by up to 24 h reoxygenation (R: 20% O_2). The small but significant increase in LDH release induced by HR was significantly reduced when cells were pretreated with ALY688 (Figure 2.3 F). A more detailed temporal analysis of caspase 3/7 activation, assessed using an activatable fluorescent probe and real-time confocal microscopy, indicated a sustained elevation upon reoxygenation that peaked after 30 hours (Figure 2.3 G) that was reduced in the presence of ALY688 (Figure 2.3 H). Additional studies in cells engineered to express the VC3Ai biosensor confirmed the ability of ALY688 to reduce HR-induced caspase activation (Figure 2.3 I and J).

To further validate the findings in the H9c2 cell line, we applied human induced pluripotent stem cell-derived cardiomyocytes (iPSC-CM), which are well-established for supplementing *in vitro* studies of cardiac IR models (287). Cell viability staining (ReadyProbe) was used to identify cell death induced by HR and the effect of ALY688 in both H9c2 and iPSC-CM. As shown, HR triggered a significant increase in dead cells, indicated by green fluorescence, but the number of dead cells was reduced upon ALY688 treatment (Figure 2.3 I, and K-M).

Reactive oxygen species (ROS) production is a crucial early driver of IR injury-induced cell death (288). To elucidate the role of ALY688 in ROS-associated IR-induced cell death, ROS was measured in cellular models. HR-induced ROS generation, measured by CellRox Green probe in both H9c2 and iPSC-CM (Figure 2.4 A, B and C) and CellRox DeepRed analyzed by flow cytometry in H9c2 (Figure 2.5 A and B), was attenuated by ALY688 pretreatment. To determine whether ALY688 diminished HR-triggered cell death via reducing ROS accumulation, we applied immunofluorescence staining of 8-OHdG to measure DNA oxidative stress. 8-OHdG expression was significantly enhanced upon HR incubation and reduced when treated with ALY688 in H9c2 cells as well as iPSC-CM (Figure 2.4 D and E, Figure 2.5 C and D).

In myocardial ischemia, induction of autophagy via the AMPK pathway is protective, whereas reperfusion stimulates autophagy with BECLIN-1 upregulation, and is implicated in causing myocyte death. An appropriate balance of autophagy is an important determinant of outcomes in ischemia (289). The processes through which adiponectin signaling induces autophagy activation to elicit cardioprotective or detrimental effects in IR injury have not been elucidated (77). We have previously shown that adiponectin mediates similar effects via stimulation of autophagy (201).

With this in mind, autophagy analysis in infarcted heart was performed. Increased heart tissue LC3-II and p62 levels were observed in rats subjected to IR compared to the sham group, whereas ALY688 intervention significantly attenuated p62 accumulation (Figure 2.4 F, G and H). Autophagy flux impairment during HR was further validated in the iPSC-CM model, demonstrated by increased LC3 lipidation and decreased p62 degradation (Figure 2.4 I, J and K). With the administration of ALY688, the disrupted flux was partially restored (Figure 2.4 I, J and K).

We next performed quantitative analysis of autophagy flux using a genetically engineered H9c2 cell line expressing the LC3 HiBiT reporter (285). A significant increase of red fluorescent signal, indicating accumulation of LC3-II, was detected in cells subjected to HR, while pretreatment with ALY688 effectively mitigated this (Figure 1.3 L and M). To clarify whether lysosome activity was altered in response to HR ± ALY688, we used MagicRed (MR), a cathepsin B probe, to measure lysosomal enzyme activity. We observed that in response to ALY688, lysosomal activity was increased, and that no change occurred in response to HR in H9c2 and iPSC-CM (Figure 1.3 L, M and O). As reported previously, DapRed labels both autophagosomes and autolysosomes, while DalGreen labels autophagosomes but fluoresces strongly only in autolysosomes, allowing their distinction (285). ALY688 partially restored the HR-disrupted autophagic flux, as further supported by DapRed (DR) and DalGreen (DG) staining, which showed an increase in DR but a decrease in DG during HR compared to normoxia. The decreased DG induced by HR was enhanced in ALY688-treated cells, suggesting an increased number of autolysosomes compared to the HR control (Figure 2.4 L, P and Q).

Lastly, to further interrogate the effect of HR and ALY688 on autophagic flux, we used H9c2 cells stably expressing the tandem GFP-RFP-LC3 plasmid (TF-LC3 cell). Using this construct, autophagosomes contain both red and green fluorescence; after fusing with lysosomes, GFP is quenched and only the RFP signal remains, allowing tracking of autophagic flux (285). Data indicated that the total number of autophagosomes and autolysosomes was decreased when cells were exposed to HR, and ALY688 restored autophagic flux with more autolysosome content evident (Figure 2.4 L and R). The ability of ALY688 to elicit adiponectin-like signaling was demonstrated by a significant increase in phosphorylation of p38 MAPK and AMPKα in H9c2 cells (Figure 2.4 E and F).

Proteome profiling of tissue from myocardial infarct region to discover new mechanisms of ALY688 action

To further elucidate the mechanisms underlying the cardioprotective effects of ALY688 against IR, we conducted proteomic profiling of the infarct and border regions of heart tissue collected at 28 days. Proteomic data were analyzed using partial least squares-discriminant analysis (PLS-DA) and hierarchical clustering, which revealed distinct protein expression profiles among the sham, IR, and IR-AI groups (Figure 2.6 A and D). Differential expression analysis ($FC \geq 1.5$, $FDR \leq 0.05$) identified 58 upregulated and 52 downregulated proteins in IR compared to sham (Figure 2.6 B), and 71 upregulated and 47 downregulated proteins in IR-AI compared to IR (Figure 2.6 C). Pathway enrichment analysis of these differentially expressed proteins showed that IR was associated with activation of pathways implicated in cardiac remodeling, including extracellular matrix, collagen deposition, metabolic dysregulation and inflammatory activation (Figure 2.7 A). On the other hand, the most prominent pathway altered by ALY688 treatment (IR-AI vs. IR) was adiponectin-like (autophagy) signaling, with additional changes observed in metabolism (including sphingolipid signalling pathway and metabolic pathways) inflammatory pathways (such as Innate immune system, Toll-like receptor cascades) (Figure 2.6 E). Of note, volcano plot analysis highlighted a marked downregulation of the small GTPase Rab8a in IR versus sham, with ALY688 treatment restoring Rab8a expression to baseline levels (Figure 2.6 B and C). This result was further confirmed by Western blot analysis of tissue homogenates from the infarct region (Figure 2.6 F and G).

Characterization of EV derived from IR rat serum

Given that Rab8a regulates vesicle transport and EV secretion (263) and was upregulated by ALY688 in the heart, we examined EV dynamics post-IR with ALY688 treatment. SEM of infarcted myocardium revealed EV accumulation (white arrows) (Figure 2.6 H). Upon ALY688 administration, the abundance of particles in the infarct area was greater compared to IR controls (Figure 2.6 H). with greater abundance in ALY688-treated rats than IR controls. Serum EVs (Pls-EV) from IR and ALY688-treated rats were isolated via size exclusion chromatography. NTA showed a trend toward reduced EV levels in IR rats compared to sham, partially restored by ALY688 (Figure 2.6 I and J). Particle size did not differ between sham and IR but was significantly increased in the IR-AI group (Figure 2.6 K). SEM results aligned with NTA findings (Figure 2.6

J). Cryo-EM confirmed lipid bilayers and electron-dense cargo in EVs (Figure 2.6 L). EVs were positive for Alix, CD63, and Flotillin 1, and negative for Calnexin (Figure 2.6 M, Figure 2.7 B-E). Notably, Rab8a was present in serum EVs, mirroring its pattern in infarcted heart tissue post-IR and ALY688 treatment (Figure 2.6 M, N). All EV samples showed expected size ranges by NTA, expressed canonical EV markers, and demonstrated acceptable purity via electron microscopy.

ALY688 regulates cardiomyocyte EV-mediated pro-survival effect via Rab8a activation during HR

Given the established role of superoxide anions and ROS in cardiovascular pathologies, particularly IR injury (290), we investigated whether serum EV from IR-AI rats exert protective effects by enhancing ROS clearance post-IR. Using HR-exposed H9c2 cells and iPSC-CM as in vitro models of IR, we assessed the impact of serum EV from IR-AI rats on cell death and antioxidant responses. First, we assessed the uptake efficiency by H9c2 cells of serum EV isolated from sham (EV^{sham}), IR (EV^{IR}), and IR-AI ($EV^{IR\text{-}AI}$) rat serum. H9c2 cells were incubated with DiR-labeled EV, and uptake was evaluated using confocal microscopy and flow cytometry. Confocal and flow cytometry data confirmed efficient internalization of all EV types (EV^{sham}, EV^{IR}, and $EV^{IR\text{-}AI}$), with no significant difference in uptake efficiency (Figure 2.8 A-C). Functionally, $EV^{IR\text{-}AI}$ significantly reduced HR-induced cell death in both cell types, as shown by ReadyProbe staining (Figure 2.9 A-C) and LDH release (Figure 2.9 G, H). EVIR-AI also attenuated ROS accumulation (Figure 2.9 D-F), indicating that ALY688-modified serum EV exert cytoprotective and antioxidant effects *in vitro.*

To explore the underlying mechanism, we considered the predominance of cardiomyocytes in the adult human left ventricle (291), Rab8a's role in EV biogenesis (263), and our proteomics data (Figure 2.9 A). We hypothesized that ALY688 enhances cardiomyocyte EV secretion via Rab8a activation, contributing to protection. Rab8a knockout (RKO) H9c2 cells were generated and validated by western blot (Figure 2.8 D, E). Conditioned medium (CM) from WT and RKO cells was used for EV isolation by ultracentrifugation. Immunoblotting revealed reduced Alix and CD63 expression in EV from RKO cells treated with ALY688 compared to WT (Figure 2.9 I-K). NTA confirmed EV presence in both cell types, but particle secretion was significantly lower in RKO cells (Figure 2.9 L). Although ALY688 increased EV output in both groups, the effect was

markedly greater in WT cells (Figure 2.9 M), supporting that Rab8a mediates ALY688-enhanced EV biogenesis and release, linking this pathway to ALY688's cardioprotective effects.

We also confirmed that CM EV from all sources were efficiently taken up by WT H9c2 cells (2.8 F), with no difference in uptake efficiency as measured by flow cytometry (Figure 2.8 G and H). Finally, we evaluated whether EV derived from WT and RKO cells treated with or without ALY688 could ameliorate HR injury. Equal concentrations of CM EV were added to H9c2 cells prior to HR challenge, and cell death and oxidative stress were assessed. Consistent with the protective effect of IR-AI serum EV, EV from WT cells treated with ALY688 reduced HR-induced cell death and ROS in H9c2 cells (Figure 2.8 N-Q). In contrast, the beneficial effects of ALY688-stimulated CM EV were abolished in the absence of Rab8a (Figure 2.8 N-Q). These results demonstrate that Rab8a is an essential mediator of the pro-survival function of ALY688-derived EV in the HR model.

Serum-derived EV from rats with ALY688 intervention exert cardioprotective metabolic effects

To investigate the EV-mediated mechanisms underlying the beneficial effects of ALY688 at the proteomic level, we performed quantitative proteomic analysis from serum EV isolated from sham, PBS-, and ALY688-injected IR rats and. A total of 247 proteins were identified in serum EV. Of these, 27 matched entries in the Vesiclepedia database, 182 corresponded to the ExoCarta database, and 38 were not listed in either database (Figure 2.10 A). Principal component analysis (PCA) and hierarchical clustering of the serum EV proteome revealed clear separation among the experimental groups (Figure 2.10 B and C). Differential protein expression analysis demonstrated that most proteins were significantly upregulated (greater than two-fold change; adjusted P-value < 0.05) in EV from IR serum compared to sham. In contrast, when comparing the serum EV proteome of IR-AI versus IR, downregulated proteins outnumbered upregulated ones (Figure 2.11 A and B). The top 22 significantly regulated proteins and their functions are listed (Table 2.2). Notably, Grp78, a key regulator of protein refolding and ER stress, was downregulated in IR-AI versus IR. Gene ontology biological pathway analysis of differentially expressed proteins revealed enrichment in pathways related to protein refolding, glucose metabolic processes, and superoxide anion generation (Figure 2.11 C). Predicted protein targets included GAPDH, PKM and PGK1 (Figure 2.10 E-G) in the glucose metabolism pathway. Functional metabolic assessment in H9c2

challenged by HR and treated with EVs mentioned above using Seahorse analysis further the beneficial effect of $EV^{IR\text{-}I}$ protected HR induced impaired energy metabolism (Figure 2.10 H and I). Concurrently, cytoskeletal proteins (Actb, Actg1, Thln1, Tuba4a) were dysregulated in IR EVs but normalized by ALY688 (Figure 2.11 5 D-G), aligning with phalloidin staining showing $EV^{IR\text{-}AI}$ preserved filament structure post-HR (Figure 2.10 J-L, Figure 2.11 H).These findings demonstrate that ALY688 reprograms EV proteomes to attenuate metabolic stress, ER dysfunction, and cytoskeletal disruption, collectively mitigating IR injury.

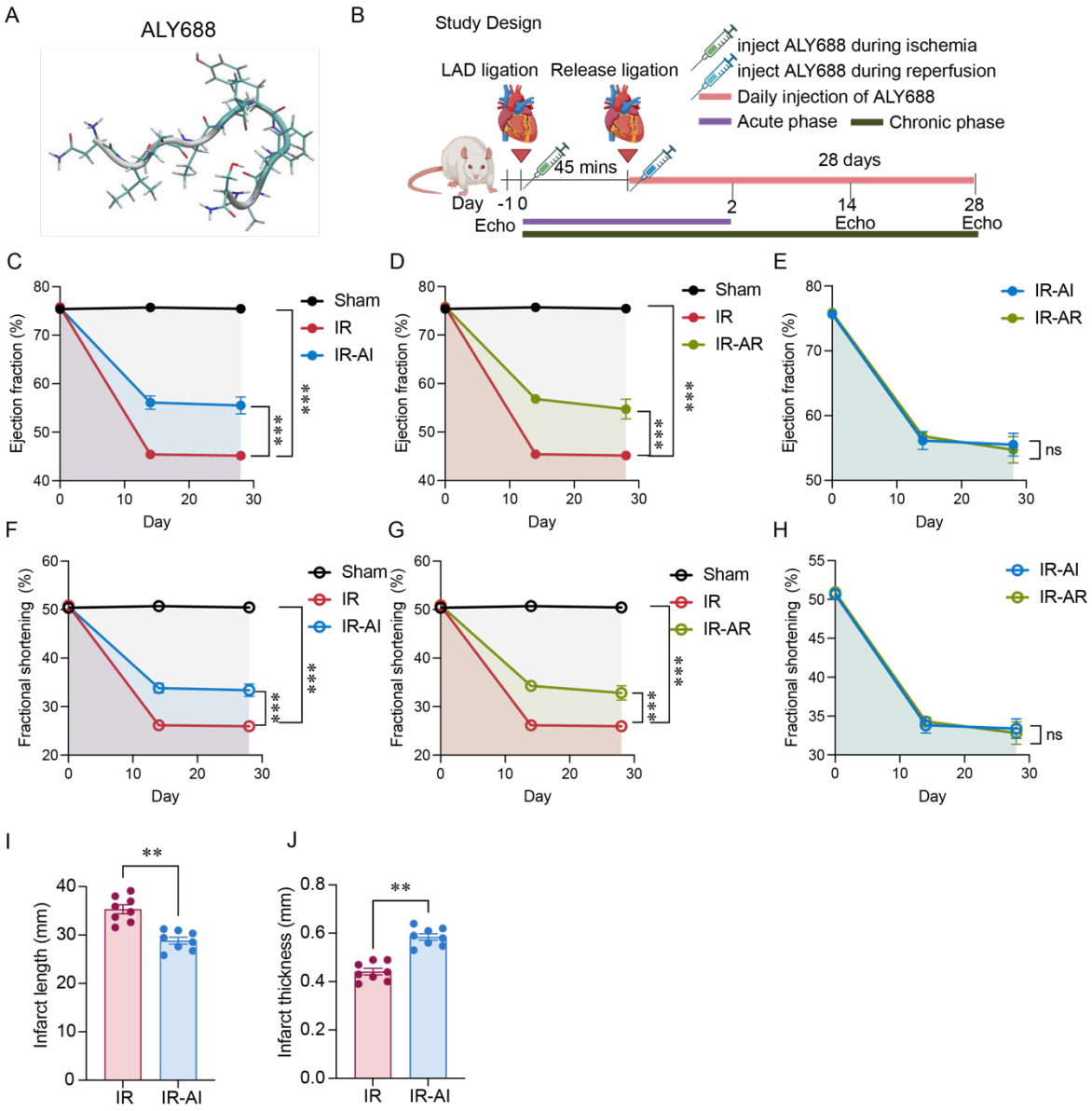

Figure 2.1 ALY688 improves cardiac function and reduces myocardial dysfunction following IR injury

A. Structure of ALY688. B. Schematic diagram of animal study design. C-E. Ejection fraction measured at day 0, 14, and 28 after LAD. F-H. Fractional shortening measured at day 0, 14, and 28 after LAD. I-J. Infract length and infarct thickness measured by echocardiography at day 28

after LAD. Results are presented as mean ± SEM (n=4 in sham and IR group, n=8 in IR-AI and IR-AR group). *P<0.05, **P<0.01, ***P<0.001 versus IR control. One-way ANOVA with Tukey post hoc test was run for statistical analysis

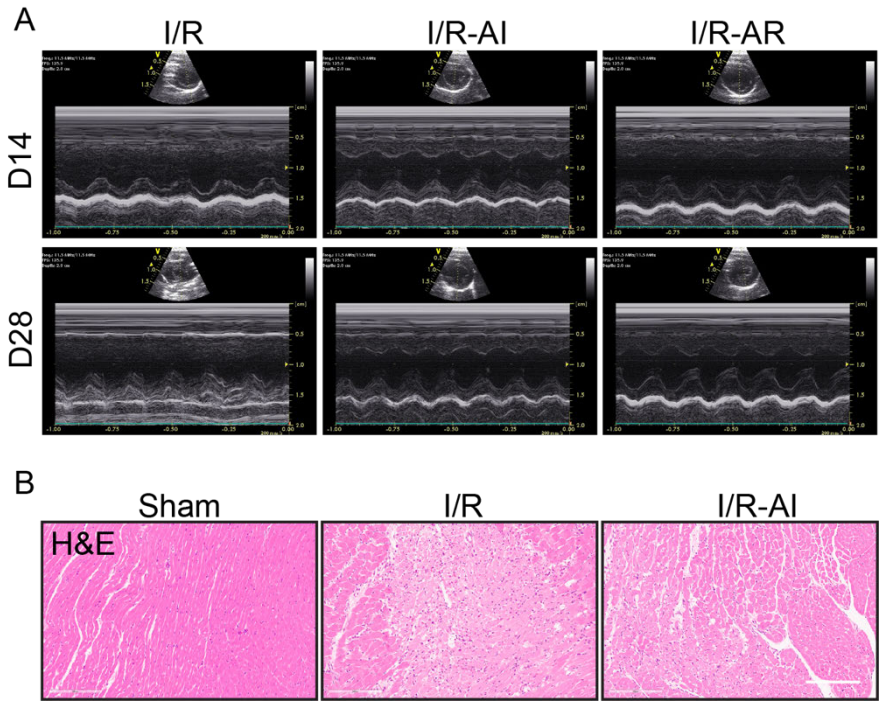

Figure 2.2 Echocardiographic and histological assessment of myocardial injury following IR.

A. Representative of echocardiography M-mode analysis at day 14, and 28 after LAD in rat. B. Representative image of H&E staining in infarct zone after 28 days of LAD in rat. (scale bar: 200 μm).

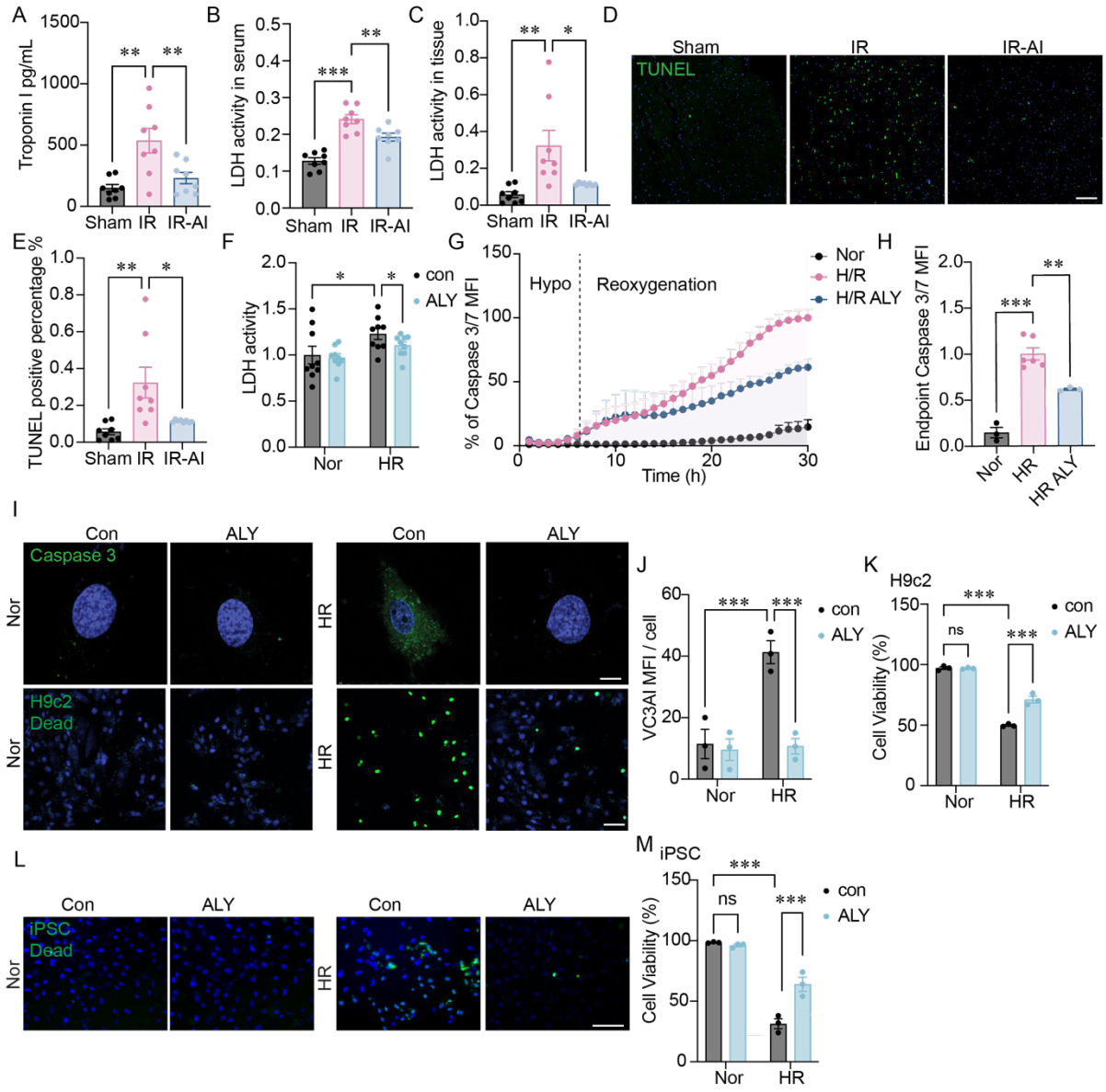

Figure 2.3 IR and HR induced apoptosis and cell death was ameliorated by ALY688

A. Troponin I level in serum of rat subjected to 2-day sham, IR, or IR-AI. B. LDH level in serum as indicated in panel A. C. LDH level in infarct heart as indicated in panel A. D. Representative image of TUNEL staining in infarct zone collected from rat sujected to 2-day sham, IR or IR-AI. E. Quantification of positive TUNEL staining. F. LDH level in H9c2 cell culture medium at endpoint. G. Progression of cell death in H9c2 cells measured by caspase 3/7 activity on an hourly basis. Data were normalized to HR. H. Endpoint caspase 3/7 activity in H9c2 subjected to HR. Data was normalized to HR. I. Representative image of VC3Ai biosensor H9c2 cells (scale bar:

10 μm), ReadyProbe staining in H9c2 cells treated with or without 300 nM ALY688 and subjected to normoxia or HR (scale bar: 30 μm). J. Quantification of Caspase 3 activation in VC3Ai biosensor H9c2 cells. K. Quantification of ReadyProbe staining in H9c2 cells. Data was normalized by fold change over normoxia control L. Representative image of ReadyProbe staining in iPSC-CM (scale bar: 250 μm). M. Quantification of ReadyProbe staining in iPSC-CM. Results are presented as mean ± SEM (n=3-5 per group). *P<0.05, **P<0.01, ***P<0.001 versus control. One-way ANOVA with Tukey post hoc test was run for statistical analysis of panel A-C, E and H. Two-way ANOVA with Tukey multiple comparisons post hoc test was run for statistical analysis of panel F, J, k and M.

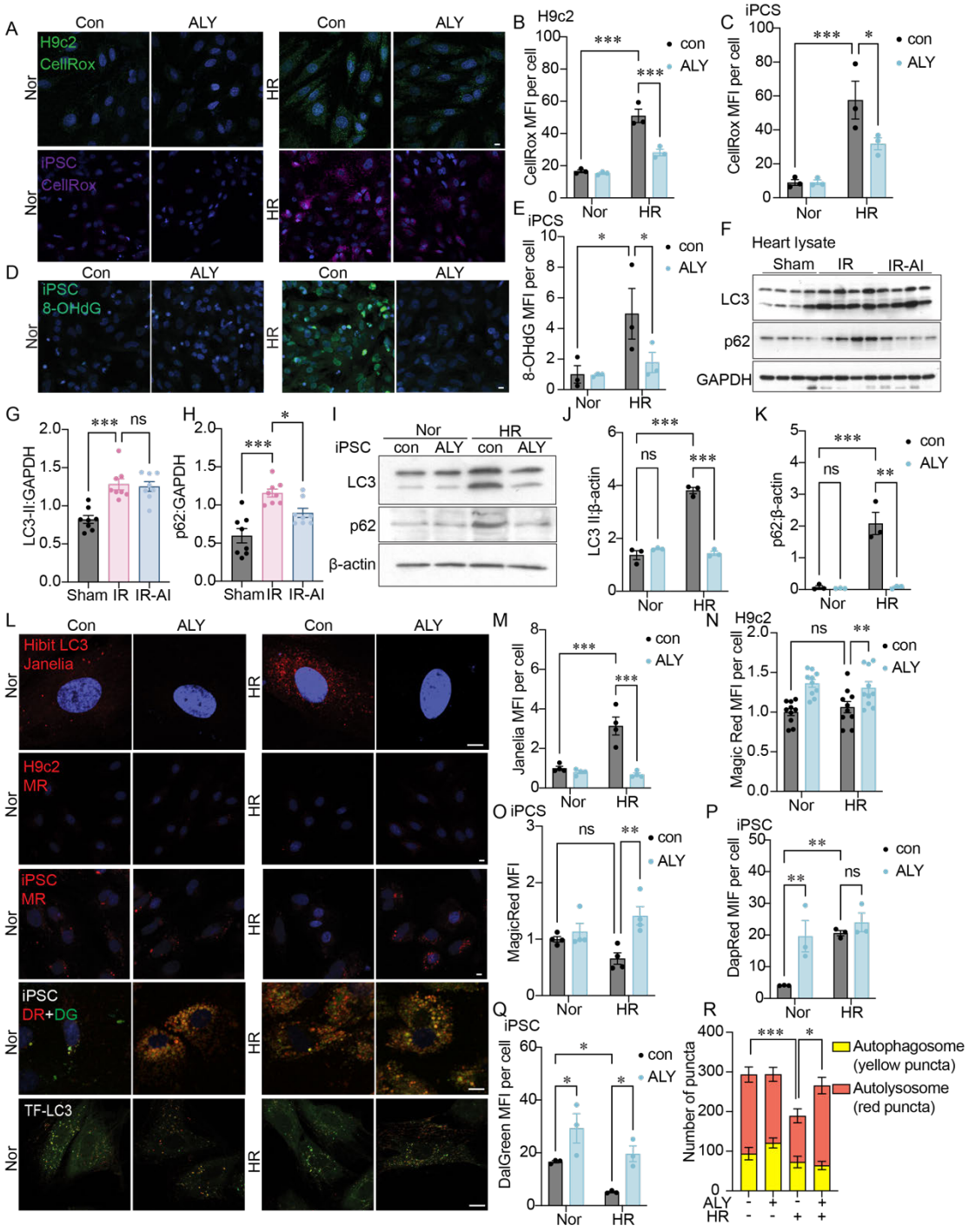

Figure 2.4 Disrupted autophagy flux induced by IR was restored by ALY688 administration

A. Representative image of CellRox staining in H9c2 cells and iPSC-CM treated with or without 300 nM ALY688 and subjected to normoxia or HR. B. Quantification of CellRox staining in H9c2 cells. C. Quantification of CellRox staining in iPSC-CM. D. Representative image of immunofluorescence staining of 8-OHdG was normalized to normoxia control. E. Quantification of immunofluorescence staining of 8-OHdG. Data was normalized by fold change to normoxia control F. SDS-PAGE and immunoblot analysis of rat infarct heart lysate using LC3, p62, and GAPDH was used as a loading control. G-H. Quantification of LC3 and p62. I. SDS-PAGE and immunoblot analysis of iPSC-CM using LC3, p62, and β-actin was used as a loading control. J-K. Quantification of LC3 and p62. M. Representative image of Hibit LC3 autophagy reporter cells, and MagicRed (MR) staining in H9c2 cells, MR staining in iPSC-CM, DapRed (DR) and DalGreen (DG) staining in iPSC-CM, TF-LC3 H9c2 cells subjected to HR treated with or without ALY688. M. Quantification of Janelia positive signals in Hibit LC3 reporter cells. N. Quantification of MR staining in H9c2 cells. Data was normalized by fold change to normoxia control. O. Quantification of MR staining in iPSC-CM. P. Quantification of DR in iPSC-CM. R. Quantification of DG in iPSC-CM. R. Quantification of autophagosome and autolysosome in TF-LC3 cell line. (scale bar: 10 μm) Results are presented as mean ± SEM. (n= 3-8 per group). *P<0.05, **P<0.01, ***P<0.001 versus control. Two-way ANOVA with Tukey multiple comparisons post-hoc test was run for statistical analysis of panel B-E, J-K, M-Q. One-way ANOVA with Tukey post-hoc test was run for statistical analysis of panel G-H, and R.

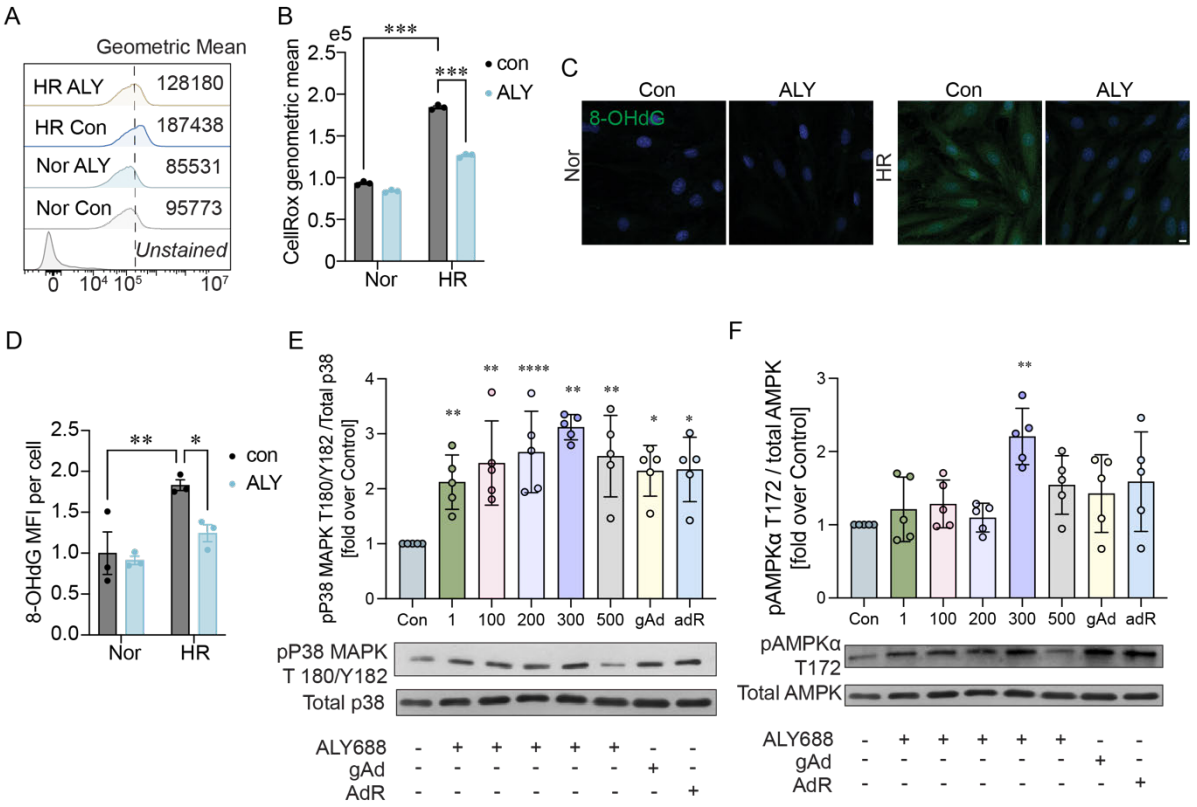

Figure 2.5 ALY688 attenuates oxidative stress and activates AMPK signaling in H9c2 cardiomyocytes subjected to HR

A. Total reactive oxygen species (ROS) level measured by CellRox DeepRed using flow cytometry in H9c2 treated with or without 300 nM ALY688 and subjected to normoxia or HR. B. Quantification of mean fluorescence intensity of CellRox DeepRed measured using flow cytometry. C. Representative image of immunofluorescence staining of 8-OHdG of H9c2 (scale bar: 10 μm) subjected to HR its quantification in D. Data was normalized to normoxia control. E-F. SDS-PAGE and immunoblot analysis H9c2 treated with different doses of ALY688 and globular adiponectin recombinant protein (gAd), full-length adiponectin recombinant protein (fAd), and adiponectin receptor (AdR) using pP38 MAPK, and pAMPKα T172. Total p38 and total AMPK were used as control. Results are presented as mean ± SEM. (n= 3-8 per group). *P<0.05, **P<0.01, ***P<0.001 versus control. Two-way ANOVA with Tukey multiple comparison post-poc test was run for statistical analysis.

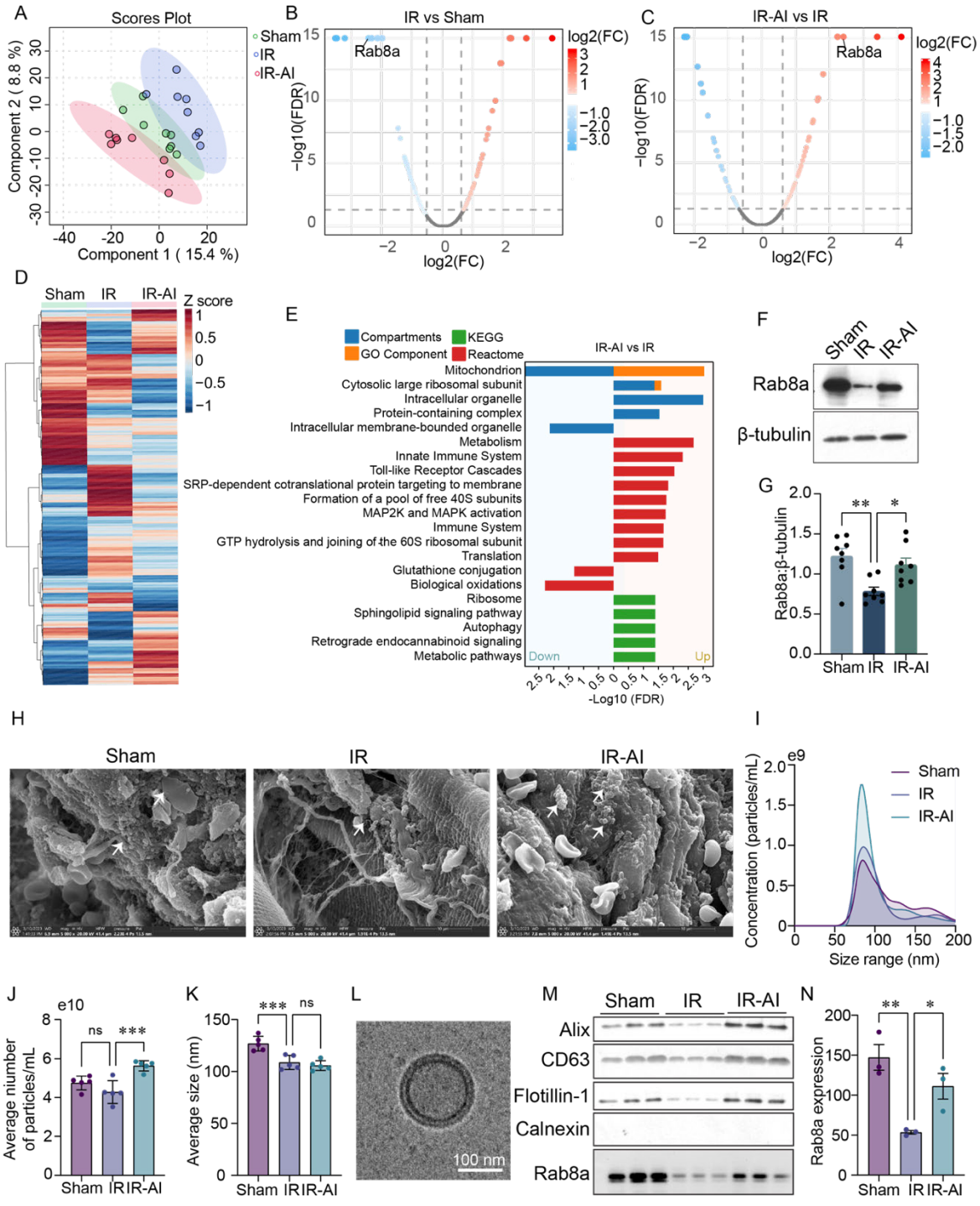

Figure 2.6 Proteomic analysis revealed altered protein expression in infarcted rat hearts following IR injury

A. PCA analysis of infract heart proteomics. B. Volcano plot of the comparison of IR versus sham. C. Volcano plot of the comparison of IR-AI versus IR. D. Hierarchical clustering heatmap. E. Pathway enrichment analysis in the comparison of IR-AI versus IR. F. SDS-PAGE and immunoblot analysis of infarct heart lysate using Rab8a. β-tubulin was used as a loading control. G. Quantification of panel F. H. Representative image of SEM of infarct area. I. NTA analysis of EV isolated as indicated, and quantification of particle number in J, size quantification in K. L. Representative image of Cryo EM of serum derived EV. M. SDS-PAGE and immunoblot analysis of EV isolated from serum of rats subjected to sham, IR, and IR-AI using Alix, CD63, Flotillin-1, Calnexin, and Rab8a. N. Quantification of Rab8a expression in EV. Results are presented as mean ± SEM. (n=3-8/group). *P<0.05, **P<0.01, ***P<0.001 versus control. One-way ANOVA with Tukey post-hoc test was run for statistical analysis.

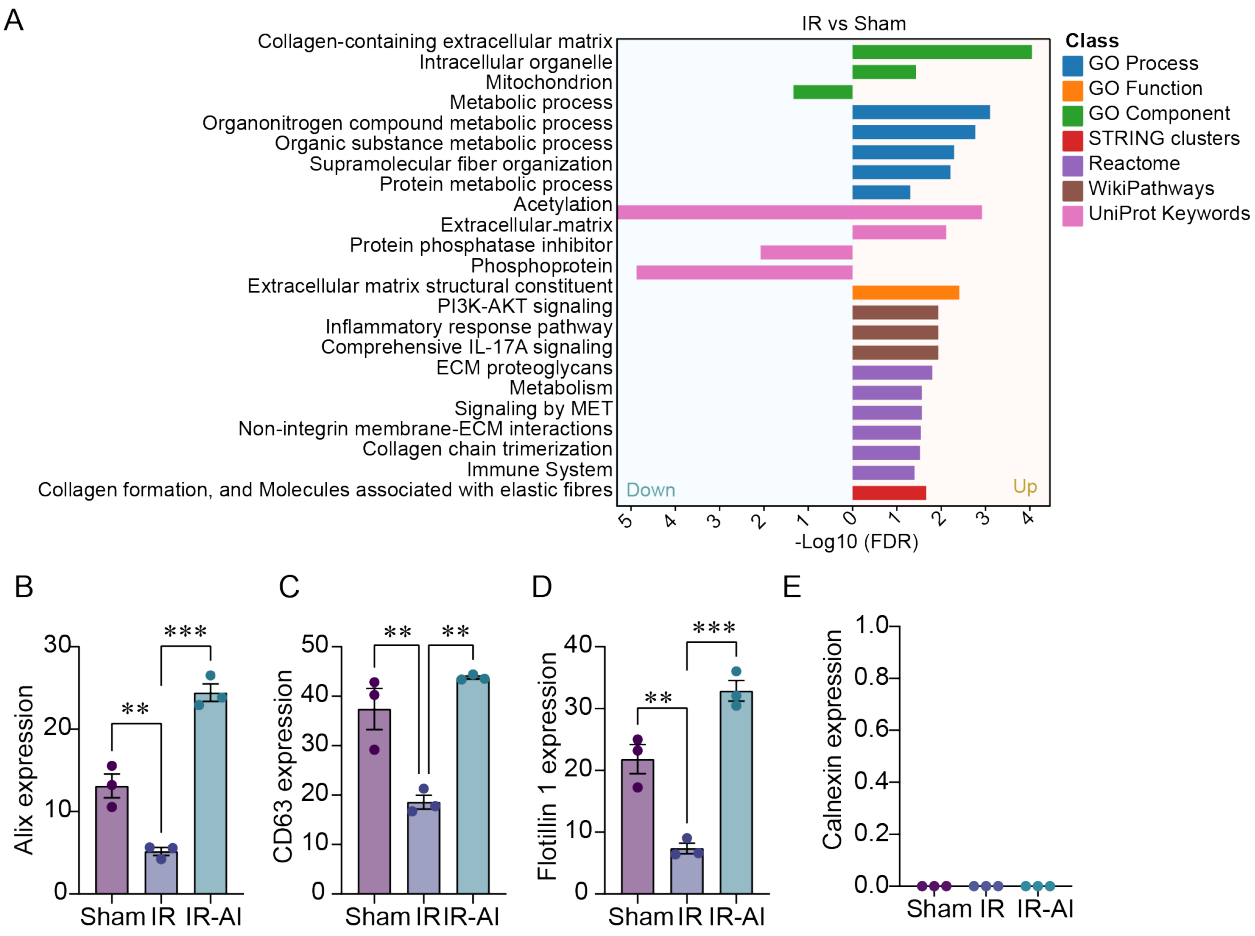

Figure 2.7 Pathway enrichment and EV marker validation in IR myocardium

A. Pathway enrichment analysis in the comparison of IR versus sham B-D. Quantification of Alix, CD63, Flotillin 1 and Calnexin. Results are presented as mean ± SEM. (n=3-8 per group). EV. P<0.05, **P<0.01, ***P<0.001 versus control. One-way ANOVA with Tukey post-hoc test was run for statistical analysis

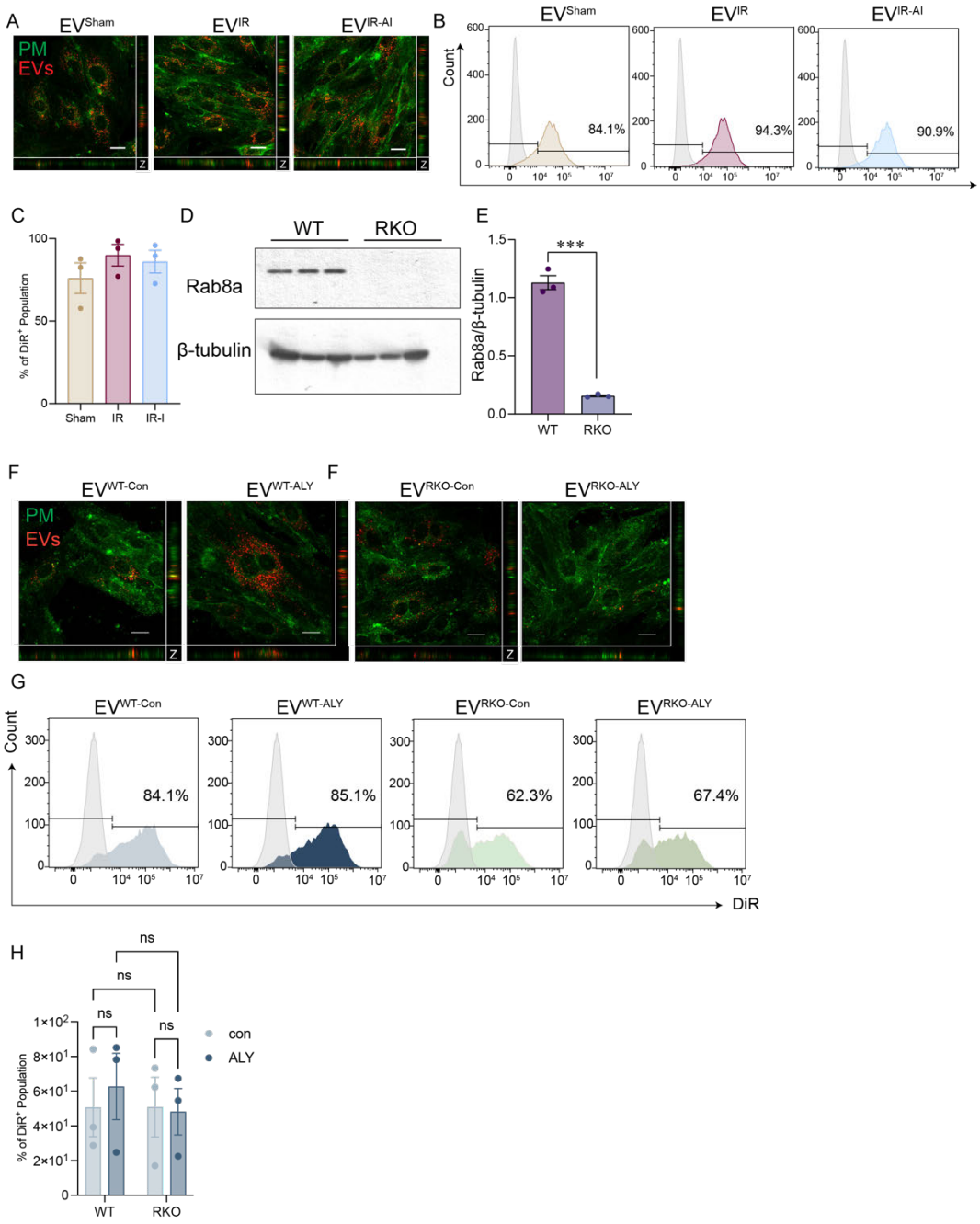

Figure 2.8 Uptake of circulating and cell-derived EVs in H9c2 cardiomyocytes and the role of Rab8a

A. Representative image of DiR-labeled EV isolated from serum of rats subjected to sham, IR, and IR-AI. B. Representative histogram of positive cell count presented positive DiR signal in H9c2 cells incubated with EV as indicated in panel A, and quantification in B. D. D. SDS-PAGE and

immunoblot analysis of WT and RKO H9c2 cells using Rab8a. GAPDH was used as a loading control. E. Quantifications of panel D. F. Representative image of DiR-labeled EV isolated from WT and RKO H9c2. G. Representative histogram of positive cell count presented positive DiR signal in H9c2 cells incubated with EV as indicated in panel F, and quantification in H. Results are presented as mean ± SEM. (scale bar: 125 μm) (n=3 per group). *P<0.05, **P<0.01, ***P<0.001 versus control. One way ANOVA with Tukey post-hoc test was run for statistical analysis for panel C. T-test was used for statistical analysis for panel D. Two-way ANOVA with Tukey multiple comparisons post-hoc test was run for statistical analysis for panel H.

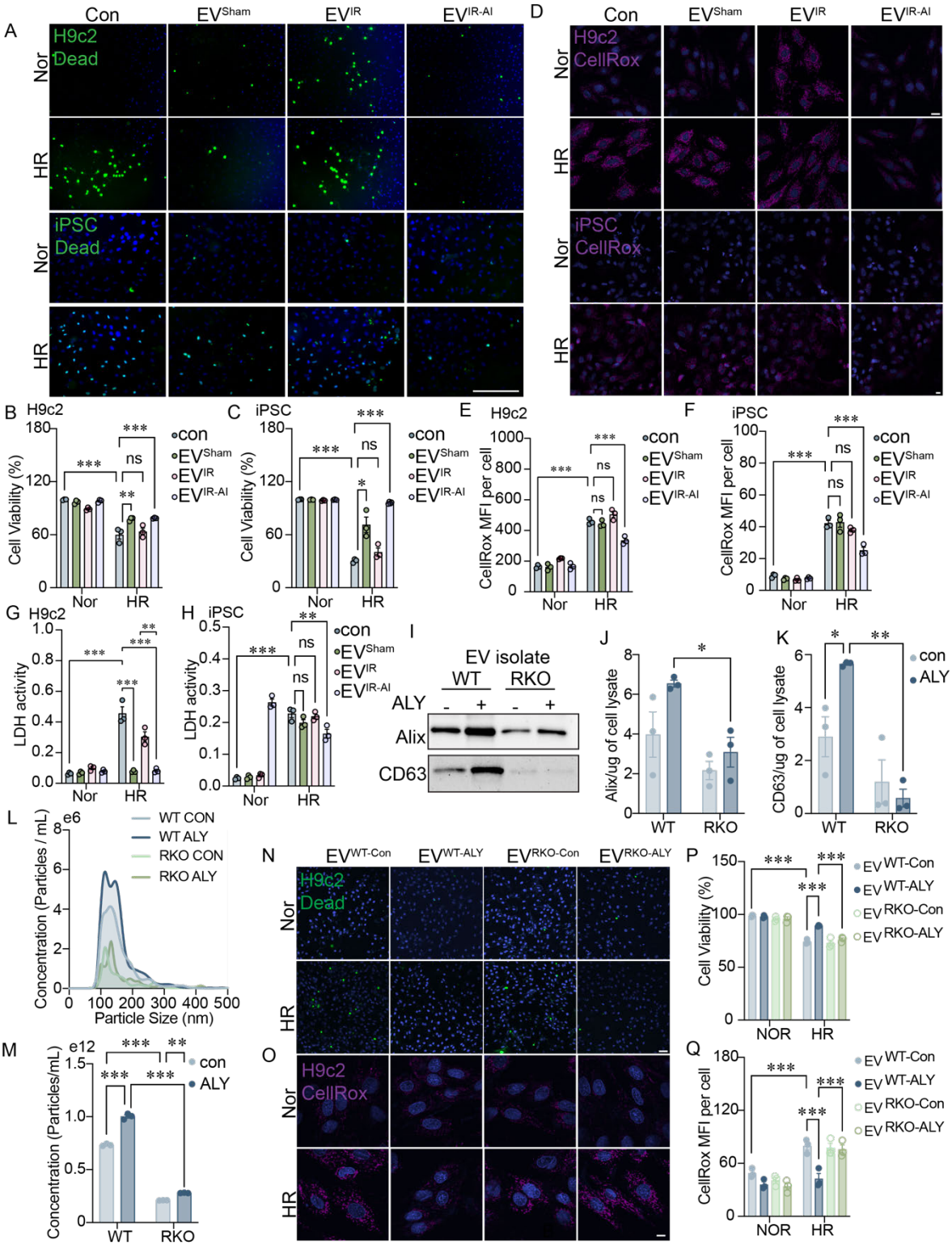

Figure 2.9 ALY688 enhances cardiomyocyte EV-mediated pro-survival effects through Rab8a activation under hypoxia/reoxygenation

A. Representative image of ReadyProbe signal in H9c2 cell, and iPSC-CM subjected to HR and treated with EV isolated from serum of rats subjected to sham, IR, and IR-AI (scale bar: 125 μm). B. Quantification of ReadyProbe staining in H9c2 cells (scale bar: 10 μm). C. Quantification of ReadyProbe staining in iPSC-CM. D. Representative image of CellRox staining in H9c2 cells and iPSC-CM subjected to HR and treated with EV as indicated in panel A. E. Quantification of CellRox in H9c2 cells. F. Quantification of CellRox in iPSC-CM. G. LDH activity in H9c2 cells subjected to HR and treated with EV as indicated in panel A. H. LDH level measured in iPSC-CM. I. SDS-PAGE and immunoblot analysis of EV isolated from WT and RKO H9C2 cells treated with or without 300 nM ALY688 for 24 hours using Alix and CD63, and quantification in J and K. L. NTA analysis of EV isolated from WT and RKO H9c2 as indicated in panel A, and quantification of particle number in M. N. Representative image of ReadyProbe staining (scale bar: 10 μm) in H9c2 cells subjected to HR and treated with EV isolated conditioned medium from WT or RKO cells treated with or without 300 nM ALY688, and quantification in O. P. Representative image of CellRox signal in H9c2 cells subjected to HR and treated with EV as indicated in previously, and quantification in Q. Results are presented as mean ± SEM. (n=3 per group), *P<0.05, **P<0.01, ***P<0.001 versus control. Two-way ANOVA with Tukey multiple comparisons post-hoc test was run for statistical analysis.

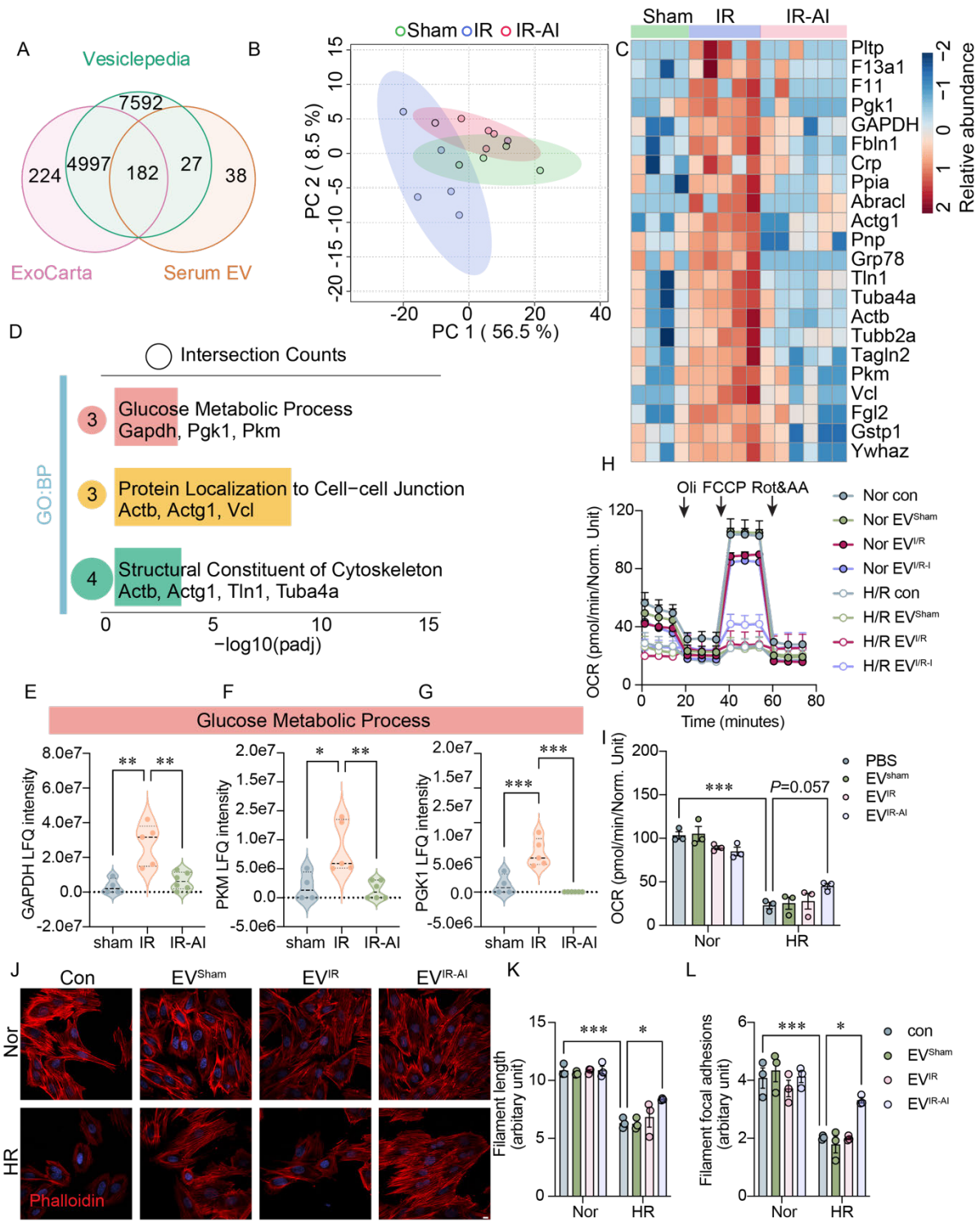

Figure 2.10 Proteomics analysis of serum derived EV and functional effect in HR cellular model

A Venn diagram of serum-derived EV proteomics overlapping with ExoCarta and Vesiclepedia. B. PCA analysis of serum-derived EV proteomics. C. Hierarchical clustering heatmap. D. Pathway analysis of significant expressed proteins. E-G. Expression of GAPDH, PGK1and PKM in serum EV. H. Seahorse analysis of H9c2 treated with or without EV isolated from serum of rats subjected to sham, IR, and IR-AI, and subjected to normoxia or HR. I. Measurement of maximal respiration capacity during Seahorse experiment. J. Representative image of Phalloidin staining in H9c2 treated with or without EV isolated from serum of rats subjected to sham, IR, and IR-AI, and subjected to normoxia or HR. K. Filament length quantification of Phalloidin staining. L. Filament focal adhesions quantification of Phalloidin staining. Results are presented as mean ± SEM. (n=3-5/group) *P<0.05, **P<0.01, ***P<0.001 versus control. Two-way ANOVA with Tukey multiple comparisons post-hoc test was run for statistical analysis of panel I, K and L. One-way ANOVA with Tukey post-hoc test was run for statistical analysis of panel E-G.

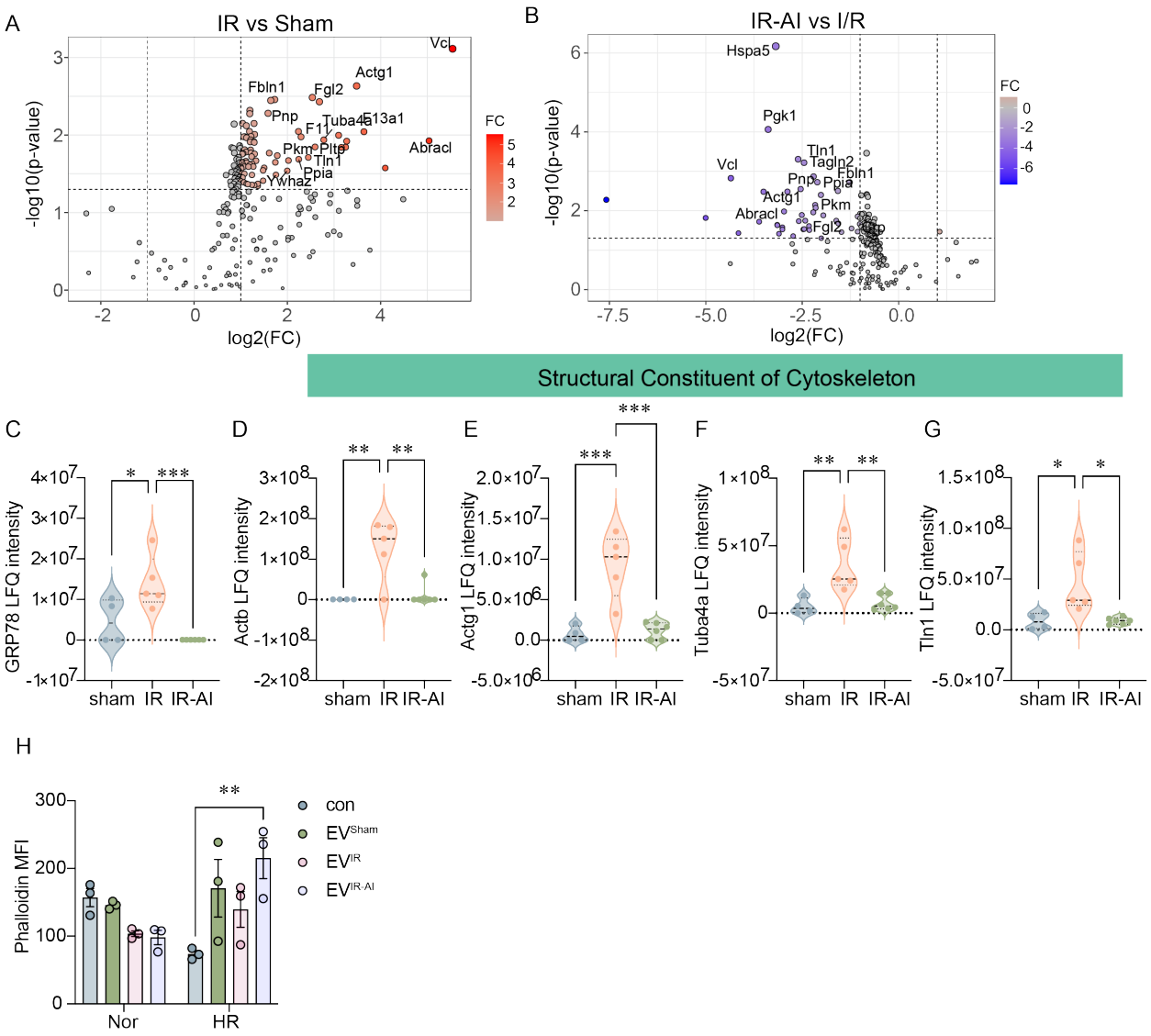

Figure 2.11Proteomic and cytoskeletal alterations in serum EVs following ALY688 treatment in IR rats

A. Volcano plot of the comparison of IR versus sham. B. Volcano plot of the comparison of IR-AI versus IR. C-G. Expression of GRP78, Actb, Actg1, Tuba4a, and Tln1 in serum EV. H. MFI quantification of Phalloidin staining. Results are presented as mean ± SEM. (n=3-5 per group). *P<0.05, **P<0.01, ***P<0.001 versus control. One-way ANOVA with Tukey post-hoc test was run for statistical analysis for panel C-G. Two-way ANOVA with Tukey multiple comparisons post-hoc test was run for statistical analysis for panel H.

Table 2.1 Summary of Echocardiography parameters of rat undergone sham and I/R surgery

Summary of Echocardiography parameters of rat undergone sham and I/R surgery					
day 0 after I/R	**Unit**	**Sham**	**IR**	**IR-AI**	**IR-AR**
heart rate	bmp	365.38 ± 25.76	359.20 ± 21.60	368.16 ± 25.01	353.35 ± 23.92
LVDD	mm	6.62 ± 0.12	6.52 ± 0.10	6.63 ± 0.16	6.53 ± 0.07
LVSD	mm	3.29 ± 0.69	3.21 ± 0.07	3.27 ± 0.07	3.21 ± 0.05
ejection fraction	%	75.54 ± 0.69	75.82 ± 0.56	75.64 ± 0.74	75.88 ± 0.74
fractional shortening	%	75.38 ± 0.69	50.83 ± 0.57	50.65 ± 0.75	50.90 ± 0.76
day 14 after I/R	**Unit**	**Sham**	**IR**	**IR-AI**	**IR-AR**
heart rate	bmp	352.98 ± 24.34	338.13 ± 15.73	357.40 ± 37.23	339.5- ± 29.93
LVDD	mm	6.72 ± 0.13	7.94 ± 0.22	7.46 ± 0.11	7.45 ± 0.12
LVSD	mm	3.31 ± 0.09	5.84 ± 0.27	4.94 ± 0.26	4.89 ± 0.09
ejection fraction	%	75.71 ± 0.76	45.92 ± 2.20	56.13 ± 3.91	56.81 ± 1.59
fractional shortening	%	50.72 ± 0.77	26.48 ± 1.50	33.82 ± 2.84	34.29 ± 1.22
day 28 after I/R	**Unit**	**Sham**	**IR**	**IR-AI**	**IR-AR**
heart rate	bmp	349.08 ± 30.27	337.20 ± 15.03	369.78 ± 26.18	337.20 ± 15.03
LVDD	mm	6.79 ± 0.12	7.54 ± 0.08	7.74 ± 0.20	7.54 ± 0.08
LVSD	mm	3.37 ± 0.07	5.10 ± 0.28	5.16 ± 0.39	5.10 ± 0.28

ejection fraction	%	75.43 ± 0.62	54.13 ± 5.95	55.50 ± 4.97	54.13 ± 5.95
fractional shortening	%	50.44 ± 0.63	32.39 ± 4.25	33.38 ± 3.56	32.39 ± 4.25

Table 2.2 Top 22 significantly expressed proteins and functions in serum EV proteomics analysis

		I/R vs Sham		I/R-I vs I/R		
Protein	Protein Function	Log2(FC)	p-value	Log2(FC)	p-value	Reference
Grp78	Endoplasmic reticulum chaperone that plays a key role in protein folding and quality control in the endoplasmic reticulum lumen. Acts as a key repressor of the ERN1/IRE1-mediated unfolded protein response (UPR). Accumulation of misfolded protein in the endoplasmic reticulum causes release of Grp78/BiP from ERN1/IRE1, allowing homodimerization and subsequent activation of ERN1/IRE1.	1.3673	0.045255	-3.1861	6.7306E-07	(292, 293)
Pgk1	Catalyzes one of the two ATP producing reactions in the glycolytic pathway via	2.237	0.008992	-3.3831	8.66E-05	(294-296)

	the reversible conversion of 1,3-diphosphoglycerate to 3-phosphoglycerate. In addition to its role as a glycolytic enzyme, it seems that PGK-1 acts as a polymerase alpha cofactor protein (primer recognition protein).					
Tuba4a	Tubulin is the major constituent of microtubules, a cylinder consisting of laterally associated linear protofilaments composed of alpha- and beta-tubulin heterodimers. Microtubules grow by the addition of GTP-tubulin dimers to the microtubule end, where a stabilizing cap forms. Below the cap, tubulin dimers are in GDP-bound state, owing to	2.7805	0.011536	-2.6067	0.00049336	(297)

	GTPase activity of alpha-tubulin. TUBA4A is the only tubulin isotype translated in its detyrosinated form and interestingly is one of the most highly expressed isotypes in the heart.					
Tln1	Probably involved in connections of major cytoskeletal structures to the plasma membrane. High molecular weight cytoskeletal protein concentrated at regions of cell-substratum contact and, in lymphocytes, at cell-cell contacts. TLN1 has been found to be up-regulated in the costameres, both in a HCM mouse model and in the myocardium of adult humans with heart failure	2.4483	0.019434	-2.4525	0.0006 0417	(298)

Tagln2	The protein encoded by this gene is similar to the protein transgelin, which is one of the earliest markers of differentiated smooth muscle. miR-133a mediates the hypoxia-induced apoptosis by inhibiting TAGLN2 expB7:B8	1.7827	0.018405	-2.2054	0.0013549	(299, 300)
Vcl	Actin filament (F-actin)-binding protein involved in cell-matrix adhesion and cell-cell adhesion. Regulates cell-surface E-cadherin expression and potentiates mechanosensing by the E-cadherin complex. May also play important roles in cell morphology and locomotion.	5.5428	0.00077065	-4.3506	0.0014935	(301)
Tubb2a/Tubb2b/Tubb3	The protein encoded by this gene is a beta isoform of tubulin,	2.5922	0.01424	-2.1084	0.0018877	(302)

	which binds GTP and is a major component of microtubules. This gene is highly similar to TUBB2A and TUBB2C.					
Fbln1	Fibulin 1 is a secreted glycoprotein that becomes incorporated into a fibrillar extracellular matrix. Calcium-binding is apparently required to mediate its binding to laminin and nidogen. It mediates platelet adhesion via binding fibrinogen. Fibulin-1 level was elevated in heart failure patients with impaired glucose metabolism.	1.6439	0.0035774	-1.2701	0.0019021	(303)
Pnp	Catalyzes the phosphorolytic breakdown of the N-glycosidic bond in the beta-(deoxy)ribonucleoside molecules, with the formation of the	1.585	0.0052429	-2.5409	0.002818	

	corresponding free purine bases and pentose-1-phosphate					
Actb	This gene encodes one of six different actin proteins. Actins are highly conserved proteins that are involved in cell motility, structure, integrity, and intercellular signaling. The encoded protein is a major constituent of the contractile apparatus and one of the two nonmuscle cytoskeletal actins that are ubiquitously expressed.	1.6098	0.017075	-1.5748	0.0031402	
Actg1	Actins are highly conserved proteins that are involved in various types of cell motility and in maintenance of the cytoskeleton. The beta and gamma actins co-exist in most cell types as components	3.4839	0.0023255	-2.8831	0.0032823	(304)

	of the cytoskeleton and as mediators of internal cell motility. The expression of ACTG1 in the scar was significantly higher in comparison with that in unwounded tissue.					
Ppia	Catalyzes the cis-trans isomerization of proline imidic peptide bonds in oligopeptides. Activates endothelial cells (ECs) in a pro-inflammatory manner by stimulating activation of NF-kappa-B and ERK, JNK and p38 MAP-kinases and by inducing expression of adhesion molecules including SELE and VCAM1. Induces apoptosis in ECs by promoting the FOXO1-dependent expression of CCL2	2.2432	0.02054	-2.0149	0.003976	(305)

	and BCL2L11 which are involved in EC chemotaxis and apoptosis. Extracellular CyPA encoded by ppia is one of the key factors linking oxidative stress and cardiac hypertrophy.					
Pkm	Pkm is a pyruvate kinase that catalyzes the transfer of a phosphoryl group from phosphoenolpyruvate to ADP, generating ATP and pyruvate. This protein has been shown to interact with thyroid hormone and may mediate cellular metabolic effects induced by thyroid hormones. PKM2/PKM1 or PKM2 levels were found to be higher in conditions such as MI,	2.0224	0.021301	-2.1513	0.0084202	(306-308)

	MI/R injury, and DM-STEM.					
Ywhaz	Adapter protein implicated in the regulation of a large spectrum of both general and specialized signaling pathways . Binds to a large number of partners, usually by recognition of a phosphoserine or phosphothreonine motif. This protein interacts with IRS1 protein, suggesting a role in regulating insulin sensitivity. XST alleviates AMI injury by attenuating the expression of Ywhaz and Ywhab.	1.9968	0.02896	-2.213	0.010984	(309)
F13a1	Factor XIII is activated by thrombin and calcium ion to a transglutaminase that catalyzes the formation of gamma-glutamyl-epsilon-	3.6415	0.0090522	-2.5105	0.012826	(310)

	lysine cross-links between fibrin chains, thus stabilizing the fibrin clot. The role of F13A1 gene variants in AMI onset, recurrence, and in post-AMI outcomes is still controversial, including gender disparities					
Gstp1	Conjugation of reduced glutathione to a wide number of exogenous and endogenous hydrophobic electrophiles. Involved in the formation of glutathione conjugates of both prostaglandin A2 (PGA2) and prostaglandin J2 (PGJ2).	1.1983	0.02416	-1.9529	0.013069	(311)
Gapdh	Has both glyceraldehyde-3-phosphate dehydrogenase and nitrosylase activities,	2.6867	0.0037183	-1.6167	0.017852	

	thereby playing a role in glycolysis and nuclear functions, respectively					
Pltp	The protein encoded by this gene is one of at least two lipid transfer proteins found in human plasma. The encoded protein transfers phospholipids from triglyceride-rich lipoproteins to high density lipoprotein (HDL). In addition to regulating the size of HDL particles, this protein may be involved in cholesterol metabolism.	3.1579	0.014434	-2.4209	0.017862	(312, 313)
Abracl	Predicted to be involved in regulation of actin filament-based process.	5.0379	0.011857	-3.6171	0.018951	(314)
Fgl2	The protein encoded by this gene is a secreted protein that is similar to the beta-	2.5351	0.0032756	-1.5626	0.021038	(315)

	and gamma-chains of fibrinogen. In heart failure patients, higher levels of plasma FGL2 were associated with a greater degree of functional impairment as measured by peak VO2.					
Crp	Displays several functions associated with host defense: it promotes agglutination, bacterial capsular swelling, phagocytosis and complement fixation through its calcium-dependent binding to phosphorylcholine. Can interact with DNA and histones and may scavenge nuclear material released from damaged circulating cells. High C-reactive protein (CRP) levels have been associated with higher mortality	1.4799	0.038829	-1.0622	0.033879	(316)

	rate in patients with acute myocardial infarction (AMI).					
F11	Factor XI triggers the middle phase of the intrinsic pathway of blood coagulation by activating factor IX. In humans, plasma FXI levels are associated with risk for venous thromboembolism and ischemic stroke. Factor XI deficiency is associated with reduced risk of cardiovascular events.	2.2921	0.010548	-1.4819	0.03477	(317)

2.5 Discussion

Myocardial IR injury remains a major complication post-infarction, as reperfusion, though essential, can exacerbate damage via oxidative stress, inflammation, and mitochondrial dysfunction (49). Despite progress in reperfusion strategies, no therapies directly target IR-induced injury, highlighting the need for new interventions (318). We found that the adiponectin receptor agonist ALY688 provided robust cardioprotection, improving left ventricular function, reducing infarct size, and limiting remodeling, consistent with adiponectin's known effects (272). Decreased circulating troponin-I and LDH levels further support its role in mitigating myocardial damage. Proteomic analysis confirmed activation of cardioprotective pathways, underscoring ALY688's therapeutic potential in IR injury.

ALY688 confers cardioprotection by restoring autophagic flux in HR-challenged cardiomyocytes. Autophagy, a lysosome-mediated degradation pathway, maintains cellular homeostasis under stress. While moderate autophagy during ischemia is cytoprotective, reperfusion induces excessive, dysregulated autophagy via ROS and aberrant signaling, promoting cell death through degradation of vital cellular components. ALY688 mitigates this maladaptive response, preserving cardiomyocyte viability (290). In our model, ALY688 normalized autophagic flux, as evidenced by reduced LC3-II accumulation and increased lysosomal activity, preventing both the buildup of dysfunctional organelles and excessive self-digestion. Mechanistically, ALY688 appears to fine-tune autophagy via AMPK signaling, consistent with the action of adiponectin in suppressing excessive autophagy and promoting cellular homeostasis (198, 201). By restoring autophagic flux, ALY688 enhances the clearance of damaged organelles, reduces oxidative stress, and prevents autophagic cell death, which collectively contribute to its cardioprotective effects.

Emerging evidence suggests that autophagy and EV biogenesis share regulatory pathways, prompting our hypothesis that ALY688 may also modulate EV dynamics. Cardiac proteomics revealed that ALY688 significantly restored Rab8a expression, a small GTPase essential for vesicle trafficking and increasingly recognized as a regulator of secretory autophagy and EV biogenesis (319). Rab8a loss impairs degradation of autophagic cargo and inhibits secretion of autophagic and lysosomal proteins via Golgi-derived vesicles, whereas Rab8a activation enhances secretory autophagy and cargo export (320). Functionally, Rab8a facilitates docking and fusion of vesicles with the plasma membrane by interacting with the exocyst complex, allowing precise vesicular release through transient membrane fusion events (321). In secretory autophagy, Rab8a

specifically mediates the fusion of amphisomes with the plasma membrane, enabling EV-mediated release of autophagic cargo, such as annexin A2 (321). Its role in EV biogenesis is further supported by evidence that Rab8a knockdown reduces EV release and disrupts cargo trafficking (261, 263). Thus, ALY688-induced Rab8a upregulation may enhance both secretory autophagy and EV biogenesis, linking improved autophagic flux with augmented intercellular communication.

Proteomic profiling of serum EVs from ALY688-treated rats revealed downregulation of glycolytic enzymes such as PKM and PGK1, key contributors to proton accumulation and calcium overload during reperfusion. Emerging evidence shows that PGK1 and PKM contribute to ischemic heart disease beyond glycolysis. PGK1 supports ATP generation while modulating the Na^+/H^+ exchanger and macrophage polarization, thereby influencing cardiac remodeling and inflammation. Altered PGK1 activity affects mitochondrial function, calcium handling, and cell death pathways in cardiomyocytes and immune cells (322, 323). Similarly, PKM, particularly the PKM2 isoform acts as a metabolic and signaling hub. Its upregulation during ischemia-reperfusion (IR) promotes metabolic reprogramming, inflammation, and dysregulation of mitochondrial dynamics and autophagy (306, 307, 324). Dysregulated PKM/PGK1 exacerbates acidosis and ionic imbalance, aggravating myocardial injury. In infarcted hearts, EV-mediated downregulation of these enzymes supports metabolic restoration and mitigates calcium overload. Targeting PKM/PGK1 may thus offer new therapeutic strategies for modulating metabolism and inflammation in ischemic heart disease. Simultaneously, ALY688-EV restored cytoskeletal protein expression (e.g., Actb, Tuba4a) and filament organization in cardiomyocytes, preserving structural integrity alongside enhanced autophagic clearance of damaged organelles. These adaptations, combined with ER stress reduction via Grp78 downregulation, extend ALY688's cardioprotective effects beyond cell-autonomous mechanisms to intercellular coordination of repair. This aligns with reports that EV-mediated metabolic reprogramming mitigates IR injury by orchestrating tissue-level responses (277, 325). Moreover, EVs from regenerative or stem cells carry anti-apoptotic, anti-fibrotic, and angiogenic miRNAs and proteins to injured myocardium, amplifying repair (326). Functionally, ALY688-EV reduced HR-induced cell death and ROS accumulation in vitro, recapitulating the cardioprotective actions of stem cell-derived EVs (327-329). Downregulation of GRP78 further suggests a role in relieving ER stress, consistent with

effects observed in MSC-EV treatment(330). These findings underscore the therapeutic promise of modulating EV biogenesis and cargo in IR injury.

The translational potential of ALY688 is underscored by its favorable pharmacokinetics and its dual action of direct cardiomyocyte protection coupled with systemic EV-mediated effects. The ability to modulate both intracellular and intercellular signaling pathways positions ALY688 as a promising candidate for clinical translation in acute myocardial infarction and other cardiovascular diseases characterized by IR injury.

Challenges for clinical translation of ALY688 include optimizing its timing, dosage, and delivery route. The therapeutic window remains undefined, especially in comorbidities like diabetes, where adiponectin resistance may impair efficacy. Additionally, the heterogeneity of EV populations and cargo complicates standardization and quality control in therapeutic EV production (331). Pathological conditions can markedly alter EV composition and function, affecting the enrichment of cardioprotective miRNAs and proteins (277). For example, cytokine stimulation may shift EV cargo profiles, enhancing or diminishing cardioprotective potential (332). Whether adiponectin signaling selectively enriches EVs with cardioprotective factors remains unknown. Future studies should determine if adiponectin-induced EVs possess a unique molecular signature and whether Rab8a upregulation can enhance EV uptake and therapeutic efficacy in ischemic myocardium. The timing of EV release and administration post-IR also warrants investigation, as delayed delivery might better address chronic remodeling. Lastly, EV-immune system interactions must be considered. Although ALY688-EV exhibited anti-inflammatory effects, the risks of immunogenicity or unintended immune modulation require thorough evaluation in preclinical and clinical settings.

This study has several limitations. While Rab8a's role in EV biogenesis is established in vitro, its *in vivo* contribution requires validation using cardiomyocyte-specific knockout models. The proteomic analysis of EV cargo did not distinguish between exosome and microvesicle subsets, which may have distinct functional roles. The long-term effects of ALY688-EV on cardiac remodeling and function were not assessed beyond the acute and subacute phases. Finally, the relevance of our findings to human myocardial IR injury remains to be established, and further studies in large animal models and human tissues are warranted.

In summary, our findings highlight ALY688 as a potent adiponectin receptor agonist capable of mitigating IR injury through multiple mechanisms. We demonstrated that ALY688 protects against myocardial damage *in vivo*, reduces oxidative stress and apoptosis *in vitro*, and modulates EV biogenesis and cargo composition. Importantly, we identified Rab8a-mediated EV regulation as a key contributor to ALY688's cardioprotective effects, pinpointing EV as crucial mediators in its therapeutic potential. These insights provide a foundation for the development of novel EV-targeted therapies for myocardial IR injury and support further investigation of ALY688 in clinical settings.

2.6 Statement of contribution

Animal experiments were performed by Jun Li. Echocardiographic images acquisition wad done by Jun Li. Histological section preparation and staining were carried out by the Histology Facility at Sunnybrook Research Institute. Image acquisition was conducted at the Advanced Optical Microscopy Facility, University Health Network. Image analysis and all the biochemical experiments were performed by Jialing Tang. Proteomics analysis was conducted by Yubin Lei and Vincent Richard at McGill University. Nanoparticle tracking analysis (NTA) was performed by Hye Kyoung Sung and Yubin Lei. Extracellular vesicle (EV) isolation was carried out by Khang Nguyen. Genetic modification of H9c2 cells was performed by the Genome Editing and Molecular Biology Facility at University of Ottawa. H9c2 cell culture and associated experiments were conducted by Jialing Tang and Yubin Lei. Induced pluripotent stem cell (iPSC) culture and cardiomyocyte differentiation were carried out by Jialing Tang, Yubin Lei, Khang Nguyen, Eddie Tam, and Hye Kyoung Sung. Conditioned medium-derived EV isolation was performed by Yubin Lei, Eddie Tam, and Jialing Tang. Western blotting and microscopic imaging were conducted by Jialing Tang, Yubin Lei, and Khang Nguyen. Immunofluorescence analysis was performed by Jialing Tang. Flow cytometry and associated analyses were carried out by Yubin Lei. EV uptake assays were performed by Yubin Lei and Jialing Tang. Seahorse extracellular flux assays were conducted by Jialing Tang and Eddie Tam. Statistical analysis was performed by Jialing Tang. The original manuscript draft was written by Jialing Tang. Funding was acquired by Gary Sweeney.

3. Chapter 3: Extracellular Vesicle Modulation by ALY688 Provides a Novel Cardioprotective Therapy for Myocardial Infarction

3.1 Abstract

Ischemic heart disease remains the leading cause of global morbidity and mortality, with no effective clinical therapies to mitigate cardiac ischemic injury. Extracellular vesicles (EVs) mediate intercellular communication in cardiac pathophysiology, while adiponectin demonstrates cardioprotective effects. ALY688, an adiponectin receptor agonist, shows cardiovascular promise, but its relationship with EV biology remains unexplored. We investigated whether ALY688 modulates EV biogenesis and cargo composition to mediate cardioprotection in myocardial infarction (MI). We used a mouse MI model with left anterior descending ligation in standard chow and high-fat diet conditions, treating with ALY688 (15 mg/kg for 28 days). Plasma EVs were characterized using nanoparticle tracking analysis, proteomics, and functional assays. Cardioprotective mechanisms were evaluated in hypoxic H9c2 cells and iPSC-cardiomyocytes, followed by in vivo EV intervention studies. ALY688 significantly improved MI-induced cardiac dysfunction, reduced infarct size, and decreased fibrosis in both lean and obese mice. While MI reduced circulating EV numbers, ALY688 restored EV production and enhanced loading with bioactive adiponectin. Proteomic analysis revealed ALY688-shaped EVs were enriched in metabolic pathways. In hypoxic cardiomyocytes, ALY688-derived EVs (EV^{ALY}) reduced apoptosis, cell death, and ROS accumulation while restoring mitochondrial function and enhancing autophagy flux. Systemic EV^{ALY} administration in acute MI mice reduced plasma troponin I and LDH levels, decreased cardiac apoptosis, and improved mitochondrial dynamics. ALY688 enhances EV-mediated cardioprotection through multiple mechanisms including adiponectin delivery, oxidative stress reduction, autophagy restoration, and mitochondrial recovery. The robust cardioprotective effects across metabolic states highlight ALY688-shaped EVs' translational potential for myocardial infarction treatment, particularly in patients with metabolic comorbidities. These findings provide compelling evidence for harnessing endogenous repair mechanisms through EV modulation to improve cardiovascular outcomes.

3.2 Introduction

Ischemic heart disease has emerged as the leading cause of global morbidity and mortality. Myocardial ischemia results from coronary blood flow obstruction following rupture or erosion of coronary artery plaques. (333). Currently, no effective clinical therapies exist to mitigate cardiac ischemic or ischemia injury, highlighting an urgent need for novel therapeutic interventions (334). The mechanisms underlying post-ischemic cardiac remodeling are complex and multifaceted (335). involving intricate molecular pathways including inflammatory cascades, oxidative stress, metabolic reprogramming, and neurohormonal activation that collectively orchestrate the transition from compensatory adaptation to pathological dysfunction. These pathophysiological processes encompass myocyte loss, cardiac hypertrophy, extracellular matrix disruption, fibrosis, defective autophagy, and mitochondrial dysfunction, prompting intensive research efforts to identify new therapeutic targets (336).

Extracellular vesicles represent a heterogeneous population of membrane-enclosed nanoparticles delimited by a lipid bilayer and generated through inward budding of the limiting membrane during endosome maturation into multivesicular bodies (MVBs) within the endocytic pathway. These vesicles functionally mediate intercellular communication under both physiological and pathological conditions by transferring bioactive cargo including proteins, lipids, mRNAs, and small non-coding RNAs through various biological fluids (337). EVs play pivotal roles in metabolic regulation pathways (338, 339). and serve as critical mediators of organ-organ crosstalk. EVs biogenesis is tightly regulated by multiple cellular signaling pathways, including ESCRT complexes, ceramide metabolism, and metabolic stress responses such as AMPK activation, which can influence both EV production and cargo selection (340, 341). Recent advances in EV research have revealed their extraordinary therapeutic potential, with engineered EVs emerging as promising candidates for targeted cardiovascular therapeutics due to their inherent biocompatibility, low immunogenicity, and ability to cross biological barriers. Accumulating evidence demonstrates that EV-mediated communication is intimately involved in ischemic injury, exerting both beneficial and detrimental effects on cardiac outcomes (342, 343) . On the beneficial side, extracellular vesicles from multiple sources demonstrate cardioprotective properties. Stem cell-derived EVs reduce infarct size, preserve ventricular function, and enhance angiogenesis (223). Similarly, cardiosphere-derived cell EVs reprogram macrophages toward anti-inflammatory phenotypes via miR-181b transfer, which targets PKCδ to suppress inflammatory gene expression

(239). Beyond stem cell sources, brown adipose tissue EVs deliver cardioprotective miRNA cargo that attenuates MAPK-mediated apoptosis during exercise preconditioning (222). In parallel, healthy cardiomyocyte-derived EVs transfer mitochondrial components such as ATP5a1, maintaining mitochondrial homeostasis and preventing ferroptosis following ischemia-reperfusion (343). Additionally, endothelial progenitor cell-derived EVs enhance angiogenesis through pro-angiogenic factors that promote endothelial proliferation and tube formation (344). Furthermore, M2 macrophage EVs support cardiac recovery through anti-inflammatory and tissue remodeling mechanisms (250). Conversely, EVs can exacerbate myocardial injury through pro-inflammatory pathways. Specifically, post-infarction cardiac EVs expressing cardiomyocyte and endothelial markers enhance monocyte secretion of IL-6, CCL2, and CCL7 within the infarct zone (345). Moreover, inflammatory EVs carrying IL-1α, IL-1β, and RANTES trigger cardiomyocyte cytotoxicity through TLR4-dependent NF-κB activation (346). Complementing this inflammatory response, M1 macrophage-derived EVs activate pro-inflammatory signaling cascades (347), while EVs from ischemic cardiomyocytes further impair macrophage cardioprotective functions, reducing phagocytic capacity during ischemia-reperfusion (348). The complex interplay between beneficial and detrimental EVs functions underscores their central importance in MI pathophysiology, positioning them as critical mediators that determine cardiac repair versus maladaptive remodeling outcomes.

Adiponectin, a circulating anti-inflammatory cytokine secreted from the adipose tissue, has been previously reported to have multiple cardioprotective effects, including in ischemic injury (268, 349-352). Induction of myocardial infarction in adiponectin knockout mice results in exacerbated left-ventricular dilation and hypertrophy with increased apoptosis and fibrosis (268, 353, 354), which holds the promise for adiponectin as a translational application in cardiovascular medicine. Robust evidence indicates that adiponectin regulates EV biogenesis and in mesenchymal stem cells (258). The administration of adiponectin driven EVs derived from mesenchymal stem cells notably enhanced cardiac function in mice subjected to pressure overload (258). Recent findings suggest that adipose tissue-derived EVs play an important role in the onset of insulin resistance and glucose intolerance, and further study suggests that EVs are carriers of adiponectin with insulin-sensitizing and anti-inflammatory properties (259, 355). ALY688 is a 10 amino acid peptide that has been shown to bind AdipoR1 and AdipoR2 and induce adiponectin-like effects and cardiac protection in several cellular and animal models (356-358). Mechanistically, ALY688 activates key signaling

pathways including AMPK phosphorylation (T172) and p38MAPK activation, which are known regulators of cellular metabolism, stress responses, and endosomal trafficking, processes integral to EV biogenesis and cargo loading (357) (359). Furthermore, AMPK activation has been implicated in the regulation of autophagy and multivesicular body formation, suggesting potential crosstalk between adiponectin receptor signaling and EV production pathways (360).

Despite the promising therapeutic potential of both adiponectin signaling and EVs in cardiovascular disease, the mechanistic intersection between adiponectin receptor activation and EV biology remains unexplored. Given that metabolic reprogramming and cellular stress responses are central to both adiponectin signaling and EV biogenesis regulation and considering that ALY688-induced AMPK activation could potentially influence endosomal trafficking and MVB formation, we hypothesized that ALY688 treatment might enhance EV production, modify EV cargo composition toward cardioprotective profiles, and improve EV-mediated intercellular communication in the ischemic heart. Understanding this potential ALY688-EV axis could reveal novel therapeutic mechanisms and provide a foundation for developing EV-based cardiovascular therapeutics.

Given the critical role of EVs in cardiac pathophysiology and the promising cardioprotective effects of adiponectin signaling, investigating the intersection between adiponectin receptor activation and EV biology represents a novel therapeutic avenue. EVs critically contribute to organ-organ communication. However, whether and how ALY688 affects EV biogenesis, cargo loading, and therapeutic delivery, as well as how ALY688-modulated EVs mediate post-myocardial infarction cardiac protection and cardiomyocyte communication remains unknown. Here, we aimed to fully delineate the mechanistic role of ALY688 as a regulator of EV biogenesis and secretion and elucidate ALY688-EV-mediated cardiac protection in a myocardial ischemia mouse model.

3.3 Materials and Methods

Myocardial infarction model

Myocardial infarction was induced using a surgical model of heart failure involving the permanent ligation of the left anterior descending coronary artery (LAD). Standard chow (Research diet, D12450J) or high fat diet (Research diet, D12492) were fed to mice for 3 weeks prior to surgery intervention. Mice were treated pre-operatively with 1.2mg/kg buprenorphine (1.2mg/kg; subcutaneous) and meloxicam (5mg/kg) and treated with meloxicam (5mg/kg) 24hr and 48hr post-surgery. Mice were anesthetized with isoflurane (2%) and intubated by intra-tracheal insertion of a 20G flexible catheter. The mice were maintained on a ventilator set to 130 breaths per minute throughout the procedure. The mouse was positioned supine on a heating pad on the surgical platform. The chest cavity was opened and maintained open with a chest retractor to expose the heart. The LAD was visualized underneath a surgical microscope and ligated 1-2mm below the tip of the left atrium using a 7-0 silk. Infarction was confirmed by the loss of color on the anterior wall of the left ventricle. The chest retractor was moved, and the muscles and skin were closed with 6-0 absorbable nylon sutures. Sham mice underwent the same procedure without ligation of the LAD. Mice were moved to a 30°C recovery chamber and returned to housing rooms after recovery. After surgery, mice were administered daily injection of 15 mg/kg ALY688 (Alllysta Pharmaceutical) or equivalent sterile PBS for 4 weeks.

Echocardiography

Echocardiographic images were acquired using Vevo 3100 high-frequency small animal ultrasound system (FUJIFILM VisualSonics, Toronto, Canada), using the MX550D (Vevo 3100) linear array transducers. Images of the LV were taken at baseline, before thoracotomy and left coronary artery ligation, and at 2-week post-surgery using PLAX, SAX in 2D B-mode. At 4-week post-surgery, images of the LV were acquired by using both PLAX, SAX in both 2D and 4D B-mode. To acquire 4D mode images, a step motor was used to collect serial, ECG- and respiratory-gated images along the SAX, with a step size of 80-130 μm and a frame rate of 300–400 Hz.

EV intervened myocardial infarction model

Myocardial infarction was induced as mentioned previously. After LAD, 10 µg plasma EV dissolved in 100 µL sterile PBS isolated from mice injected with or without 15 mg/kg ALY688 for 3 days, or 100 µL sterile PBS was injected to mice via tail vein.

Histology analysis

Paraffin embedded heart sections were subjected to H&E (Sigma, HT1079, HT110216), Masson Trichrome (Sigma, HT15) according to manufacturer's protocol and visualized using a bright field slid scanning microscopy (Leica, Aperio AT2).

Biochemistry analysis

Commercially available kits were used to measure LDH (Abcam, ab102526 for animal samples), LDH (Biosciences, 786210 for cellular samples), Troponin I (novus, NBP3-00456), and mouse Adiponectin ELISA (Antibody and Immunoassay Service, HongKong University, 32010) according to manufactural instructions.

Size-exclusion chromatography isolation of plasma EV

Size-exclusion chromatography (SEC) using the qEVsingle columns 70 nm (IZON, Cambridge, MA) was the primary method to isolate EV from serum samples. In all experiments, serum was diluted in filtered PBS at a 1:3 ratio. Fractions 3 to 6 were collected and used for subsequent EV characterization and downstream applications as per manufacturer’s recommendations.

Nanoparticle tracking analysis (NTA)

To determine EV sizes, 300 µL of EV were analysed by the NanoSight LM10 system (NanoSight Ltd, Salisbury, UK). 60-second videos (number of experiments n = 3, number of videos n = 8) of EV were collected, averaged, and analyzed using LM10 NTA equipped with a 65 mWatt 405 nm violet laser (NanoSight Ltd, Salisbury, UK). 100 nm polystyrene beads (Malvern Instruments, Saint-Laurent, Canada) were used for size calibration, and data captured with sCMOS camera on NTA 3.1 (machine) with Build 3.1.46 (software) at the temperature of 22 °C.

Proteomics analysis

Isolated EVs were lysed in 5% SDS (Fisher Chemical), 200 mM TRIS (Fisher BioReagnets) pH 8.5 with 10 mM TCEP (60C x 25 minutes). Free disulfides were alkylated with 40 mM IAA (RT, dark, 30 minutes) prior to proteolytic digestion by S-TRAP micro (see attached for the SOP from

the vendor that we use). Peptide containing eluates were lyophilized and rehydrated at 10 ng/uL prior to loading on EvoTips and analysis by library free DIA using an Evosep One system coupled to a Bruker timsTOF HT MS operated in DIA-PASEF mode. Samples were separated on an EV1137 column at 30SPD. For recipient cell proteomics, wild-type L6 cells were seeded on 6-well plate until reaching 80-90% confluency. Confluent cells were treated with EVs isolated from mice plasma, at the concentration of 10 µg/ mL. After 24 h of EVs treatment, cells were trypsinized and centrifuged for 5 minutes at 2000 rpm. Cell pellets were collected and lysed in NP40 lysis buffer for 30 min on ice. Cell lysate was then subjected to in-solution digestion following protocol by Promega (V5280). Gene ontology (GO) enrichment analysis was performed following the guidelines from the protocol using cytoscape software (version 3.10.2).39 KEGG pathway enrichment analysis was performed using the ClueGO plugin (version 2.5.10) in Cytoscape software. ClueGO was used to identify significantly enriched KEGG pathways, applying two-sided hypergeometric test for pathway analysis. The p-values were adjusted for multiple testing using either the Bonferroni or Benjamini-Hochberg correction, with an adjusted p-value threshold of 0.05.

Genetic modification of H9c2 cells

CRISPR knock-out lines were generated using guide RNAs cloned into the pX459 plasmid, as previously described (281). Autophagy LC3 HiBiT reporter vector (Promega, GA2550) has a HiBiT tag and contains a sequence encoding the MAP1LC3B gene. H9c2 cells were transfected with the autophagy LC3 HiBiT reporter vector according to the manufacturer manual (283). Nano-Glo HiBiT lytic reagent (Promega, N3040) was added to the cells after each treatment and luminescence was measured on a Thermo Varioskan LUX microplate reader. To generate H9c2 lines stably expressing Venus-based Caspase-3 like protease activity indicator (VC3AI; a gift from Dr Binghui Li, Addgene plasmid 78907), lentiviral particles were produced using pCDH-puro-CMV-VC3AI and transduced cells were selected using 1 µg/mL puromycin. This genetically encoded biosensor consists of cyclized chimeras containing a caspase-3 cleavage site as a switch. Upon cleavage by caspase-3-like proteases, the non-fluorescent indicator rapidly becomes fluorescent and thus detects activation in real-time.

H9c2 cell culture

H9c2 rat embryonic cardiac myoblasts (ATCC® CRL-1446TM) were grown in Dulbecco's Modified Eagle's Medium (DMEM) (Gibco, 11885-084) supplemented with 10% fetal bovine serum (FBS, Thermo, 11885084) and 1% (vol/vol) streptomycin/penicillin (Gibco, 15070063) at 37°C and 5% CO2. Hypoxia was achieved by placing cells in a hypoxic chamber (Onstage Incubator, ThermoFisher, NX7LIVE001) filled with a pre-analyzed gas mixture of 1% O_2 5% CO2. Normoxia and reoxygenation were achieved by placing cells in the Onstage Incubator filled with 20% O_2 and 5% CO_2.

iPSC culture and cardiomyocyte differentiation

iPSCs, PGPC14 line validated previously (284), were cultured on Matrigel (Corning, 354277) coated plates in mTeSR plus media (Stemcell Technologies, 100-0276) and passaged with ReLeSR (Stemcell Technologies, 100-0483) using a 1:6 – 1:12 dilution every 3-4 days, or upon reaching 80-90% confluence. For cardiomyocyte differentiation, iPSCs were dissociated into single cells using gentle cell dissociation reagent (Stemcell Technologies, 100-0485), and seeded on Matrigel coated plates containing mTeSR plus media supplemented with 10μM of Y-27623 (Stemcell Technologies, 72304) for 24h. Media was changed daily with mTeSR plus media without Y-27623 until cells reached >95% confluence (3-4 days post-seeding), at which point differentiation was initiated using STEMdiff™ Ventricular Cardiomyocyte Differentiation Kit (Stemcell Technologies, 05010), following manufacturer protocol. Additionally, selection was performed on cardiomyocytes from day 12 – day 18 of differentiation with glucose-free RPMI supplemented with 4mM lactate and B27 containing insulin. Cells were allowed to recover for a minimum of 2 days, then dissociated using TrypLE™ Select (ThermoFisher, A1217701) for 30-45 minutes, pelleted by centrifugation, then seeded in Matrigel coated plates in STEMdiff™ Cardiomyocyte Support Medium (Stemcell Technologies, 05027) for 24h. Cardiomyocytes were seeded at a density of 250,000 – 300,000 cells/cm^2 for western blot, and 50,000 – 60,000 cells/cm2 for all other assays. Media change was performed every 2 days thereafter using RPMI media (Sigma, R8758) supplemented with B27 containing insulin (ThermoFisher, 17504044) for a minimum of 4 days. All cell treatments were carried out using RPMI media supplemented with B27 containing insulin.

RAW-Dual™ cells culture and assay

RAW-Dual™ (InvivoGen, rawd-ismip) were grown in high-glucose DMEM supplemented with antibiotics and heat-deactivated FBS as required. Cells were routinely cultured in FBS- and antibiotics-supplemented media in the humidified incubator at 37 °C with 5% CO2. RAW-Dual™ cells were harvested and seeded in 96-well plates for 24 h before treatment. 1 mL of complete media was added to each well without any selection antibiotic. Time and concentration were indicated in the corresponding figure legends. 40 µL of supernatants from treated reporter cells were mixed with 160 µL Quanti-Blue reagent (InvivoGen, rep-qbs) and incubated at 37 °C for 6 h. The absorbance was measured at λ=620 nm after 10 s shaking by a microplate reader. The readouts were blanked with negative control (i.e., sterile dH2O). 20 µL of supernatants from treated reporter cells were mixed with 50 µL of Quanti-Luc 4 reagent (InvivoGen, rep-qlc4lg1) and luminescence was detected immediately. Auto gate and default luminescence filter were set for recording.

RAW-Dual™ cells culture and assay

RAW-Dual™ cells (InvivoGen, rawd-ismip) were harvested and seeded in 96 well plate 24 hour before EV treatment and hypoxia incubation. 40 µL of supernatants from treated reporter cells were mixed with 160 µL Quanti-Blue reagent (InvivoGen, rep-qbs) and incubated at 37 °C for 6 h. The absorbance was measured at λ=620 nm after 10 s shaking by a microplate reader. 20 µL of supernatants from treated reporter cells were mixed with 50 µL Quanti-Luc reagent (InvivoGen, rep-qlc4lg1). The luminescence was measured with a 4 second start time and 0.1 second reading time by a microplate reader. The readouts were blanked with negative control (i.e., sterile dH2O) and also subtracted.

Western blot

Heart tissues and H9c2 cells were used for western blot and cells were suspended in RIPA lysis buffer. BCA (ThermoFisher, A55864) was performed to normalize protein concentration. Proteins were separated by reducing SDS-PAGE and transferred to PVDF membrane. The following antibodies were used for western blot: GAPDH (1:2000, ThermoFisher, #MA5-15738), β-Tubulin (1:2000, Cell Signaling, 2128, Rab8a (1:1000, BD Science, 610844), CD63 (1:1000, ThermoFisher, PA5-92370), Alix (1:1000, Cell Signaling, 92880), Flotillin 1 (1:1000, Abcam, 133497), Calnexin (1:1000, Abcam, 22595), cleaved caspase 3 (1:1000, Cell Signaling, 9662), ANP (1:1000, St John Laboratory, STJ72680), MFF (1:1000, Cell Signaling, 84580), p-Drp1 s637 (1:1000, Cell Signaling, 4867), p-Drp1 s616 (1:1000, Cell Signaling, 3455), OPA1 (1:1000, Cell

Signaling, 80471), LC3 (1:1000, Cell Signaling, 2775), p62 (1:1000, Cell Signaling, 5114), ATG3 (1:1000, Cell Signaling, 3415), anti-rabbit (1:5000, Cell Signaling, 7074), and anti-mouse (1:5000, Cell Signaling, 7076). The quantification of signals was performed by densitometry of scanned autoradiographs with the aid of ImageJ (version 1.4v).

Microscopic Imaging

H9c2 cells were seeded on glass coverslips, which were isolated as described previously (285). Staining using different dyes including, CellEvent Caspase 3/7 Detection Reagent (ThermoFisher, C10423), ReadyProbe (ThermoFisher, R37609), CellRox DeepRed (ThermoFisher, C10422), MitoTracker Green (ThermoFisher, M7514), MagicRed (Immuno Chemistry, 938) was performed according to manufacturer's protocols and DAPI (HCS NuclearMask Blue Stain, ThermoFisher, H10325) was added simultaneously. Cells were fixed in 4% formaldehyde (Sigma, HT501128) after treatment and mounted with ProLong Gold Antifade Mountant (ThermoFisher, P36930). Slides were visualized under Nikon Eclipse Ti2 and for continuous measurements Cellnsight CX7 Platform (ThermoFisher, CX7A1110) was used. Co-localization analysis was performed with ImageJ JACOP plug-in.

Cell-stained images analysis

Following staining with specific probes, images were acquired using confocal microscopy. All biological replicates were performed with a minimum of three technical replicates. For each technical replicate, at least five randomly selected fields of view were imaged, and a minimum of 50 cells were quantified.

EV uptake assay

To confirm EV uptake, EV were stained with DiR (Thermo, D12731) at 37 degree for 1 h, and then subjected to ultracentrifugation at 120,000 x g for 2h for removal of unbound DiR dye by OptiPrep™ density gradient (Sigma, D1556). Recipient cells treated with DiR-labelled EV were countered with PlasMem Bright Green (Dojindo, P504). Visualization was performed using a Nikon A1 confocal microscope with an incubator (37 °C, 5% CO2). The uptake efficiency of DiR-labelled EV at varied timepoints was collected on all samples using a Cytek® Aurora spectral flow cytometer and analyzed in FlowJo.

Quantitative real-time PCR

PureLink™ RNA Mini Kit (Thermo, 12183018A) and cDNA Synthesis Kit (Thermo, K1691) to extract total RNA and synthesize first strand cDNA According to the manufacturer's instructions. qPCR was performed in SYBR Green Supermix (Bio-Rad, 1725274) method. The primers used were listed in Table 1. The data were normalized to 18s RNA, and the fold change was calculated via the $2^{-\Delta\Delta Ct}$ method Based on the untreated group, the relative concentration of mRNA was expressed in arbitrary units, and its assigned value was 1.

Seahorse flux assay

Oxygen consumption rates (OCRs) were determined by a Seahorse XFe24 extracellular flux analyzer (Agilent) as previously described (71). Briefly, WT H9c2 cells, RKO and AKO were seeded in each well of a pre-coated XFe24 cell culture plate (Agilent, 103015) and treated with Lalistat1, Paraoxon, ATGL, Rapamycin, Bafilomycin, and ALY688 prior HR. After HR, cells were washed with XF media twice and incubated in a CO2-free incubator at 37°C for 1 hour. The following reagents were used: Oligomycin (1 μM, Sigma, 75351), FCCP (carbonyl cyanide p-trifluoromethoxy phenylhydrazone, 3 μM, Sigma, C2920), and Antimycin A (1 μM, Sigma, A8674) plus Rotenone (1 μM, Sigma, R8875).

Statistical analysis

Data was presented as mean ± SEM. Statistical analysis was performed using GraphPad Prism 9. Student's t-test was used for comparison of two groups and one-way ANOVA, or two-way ANOVA were used for comparison of more than two groups. $P<0.05$ was considered statistically significant.

Primer sequences

See supplementary Table 3.4

3.4 Results

Result 1: ALY688 improved MI induced cardiac dysfunction and reduced fibrosis in both SC and HFD mice

To induce MI *in vivo*, we performed LAD ligation in mice, a classic model for myocardial ischemia. Considering the obesity is the predominant risk factor of coronary heart disease (361), mice were fed a 3-week HFD before being subjected to surgery (Figure 3.1 A, Figure 3.2 A). ALY688 was administered to mice consecutively for 28 days at a dose of 15 mg/kg (Figure 2.1 A). At terminal time point, heart weight (HW) was measured, and the ratio of HW and tibial length (TL) was used as an index of cardiac hypertrophy. Results showed that MI induced hypertrophy was decreased by ALY688, though there was no difference between SC and HFD groups (Figure 3.2 B). To assess functional recovery following ALY688 treatment and examine cardiac fibrosis, mice were evaluated by serial echocardiography over 4 weeks to assess functional recovery by ALY688 and terminal histologic analysis of hearts was performed to examine fibrosis. To determine the effects of ALY688 on cardiac function after MI and to demonstrate the clinical relevance of our findings, we measured ejection fraction and fractional shortening by echocardiography at 2 and 4 weeks after MI. Notably, the dysregulation of ejection fraction and fractional shortening induced by MI was ameliorated following ALY688 intervention in both SC and HFD groups (Figure 3.1 B-C, E-F, Figure 3.2 C). Interestingly, while ALY688 provided cardiac function protection in both SC and HFD groups, there was no further exacerbation of ejection fraction, fractional shortening, end diastolic volume, and end systolic volume by HFD feeding in MI mice (Figure 3.1 D and F, Figure 3.2 D and E). MI size was evaluated using 2D akinetic length from the parasternal long-axis view, and 4D volumetric measurement as described previously (362) at 4 weeks post-MI (Figure 3.1 G). ALY688 administered mice displaying a decreased akinetic length (Figure 3.2 F), infarct size (Figure 3.1 H) and infarct volume (Figure 3.2 G). Correspondingly, histological analysis of hearts by Masson trichrome and H&E staining demonstrating the increased collagen deposition induced by MI was decreased by ALY688, no further changes was observed in the HFD groups compared to SC (Figure 3.2 H and I). Similarly, α-SMA, Timp1, and Col1a1 mRNA expression in infarct heart tissue presenting the same trend with the previous parameters, confirming that ALY688 reduced the fibrosis at 4 weeks post MI regardless of dietary intervention (Figure 3.1 I-K). However, there is no consistent mRNA expression changes of Col3a1, Col4a1, MMP3, or MMP9 in infarcted hearts (Figure 3.2 J-M).

Results 2: Characterization of dysregulated EV derived from MI mice plasma

Alterations in EVs has been reported to contribute to coronary heart disease (363, 364), and adiponectin is well-documented to increase extracellular vesicle biogenesis (257, 258). To investigate the impact of MI on circulating EVs and determine whether the adiponectin receptor agonist ALY688 affects EVs biogenesis, plasma EVs from mice described above was isolated by size exclusive chromatography. Nanoparticle tracking assay (NTA) revealed that ALY688 increased circulating number of EVs in both SC and HFD MI groups. Surprisingly, MI surgery significantly decreased EV number, while this reduction was slightly improved by ALY688 treatment (Figure 3.3 A, C and Figure 3.4 A). Cryo-EM confirmed lipid bilayers and electron-dense cargo in EVs (Figure 3.3 B). Regarding EVs size, MI increased EV diameter in the SC group, and this enlargement was prevented by ALY688. However, this effect was not observed in the HFD group, although EVs from HFD MI were larger than those from SC MI mice (Figure 3.4 B). All isolated vesicles were positive for the canonical EV markers CD63, CD81 and Alix (Figure 3.3 D and E). To elucidate the EV-mediated mechanisms underlying the MI pathology, HFD effects, and the beneficial actions of ALY688 at the proteomic level, we performed quantitative proteomic analysis in the isolated plasma EVs. Principal component analysis (PCA) and hierarchical clustering demonstrated more distinct separation between treatment groups in the HFD condition compared to the SC condition (Figure 3.3 F-I, Figure 3.4 C-J). Analysis of the EV proteomes revealed a strong diet-dependent effect: HFD produced substantially larger and more distinct changes in EVs protein composition than standard chow, either under sham or MI (Figure 3.3 F-I), whereas the gross cardioprotective effect of ALY688 indicated by echocardiography was observed under both diet conditions (Figure 3.1). Nevertheless, pathway enrichment analysis with the significant expressed proteins from the comparison of MI treated with ALY versus PBS demonstrated fructose metabolism was enriched in SC context, while cholesterol metabolism and metabolic pathway were enriched in HFD context (Figure 3.4 K and L). Comparative proteomic profiling showed that ALY688 or MI induced only a few significant changes under SC, while extensive remodeling occurred in the HFD background. Notably, there was almost no overlap in differentially expressed proteins between SC and HFD groups, with only two proteins shared (Figure 3.3 J and L, Table 3.2 and Table 3.3). This divergence indicated that HFD imposes a distinct EV proteomic landscape. Pathway enrichment analysis (GO: Molecular Function) further highlighted the diet-dependent divergence in EV proteomes. In the comparison of SC sham ALY

versus HFD sham ALY, significantly altered proteins were enriched for functions related to immune binding and regulation of protease activity, including antigen binding, peptidase inhibitor/regulator activity, enzyme inhibitor activity (Figure 3.3 K). By contrast, in the comparison of SC MI ALY versus HFD MI ALY, enriched terms were predominantly associated with lipid metabolism and enzymatic activity, such as lipid binding, cholesterol and sterol transfer activity, lipoprotein particle receptor binding, and phosphatidylcholine-sterol O-acyltransferase activity, along with antioxidant and peptidase-related activities (Figure 3.3 M). These distinct functional enrichments emphasize that HFD imposes a unique EVs proteomic landscape, particularly by engaging pathways linked to protease regulation and lipid handling, which were not prominent under SC conditions.

Results 3: ALY688 enhanced EV-loading adiponectin

Next, we tested adiponectin content in the isolated plasma EV. Interestingly, EV adiponectin levels were elevated following ALY688 injection in sham condition, with a trend toward further enhancement when comparing MI and sham groups, regardless of dietary intervention (Figure 3.5 A-C). Upon MI injury, ALY688 intervention further increased the abundance of EV-carried adiponectin was further increased in the SC group (Figure 3.5 A-C). To determine whether the alterations of EV-adiponectin reflect cardiac adiponectin status, we also examined the adiponectin level in infarcted heart tissue. Consistently, MI injury significantly enhanced cardiac adiponectin levels, with further increase observed following ALY688 treatment in both SC and HFD groups (Figure 3.5 D-F). Under nonreducing conditions, low-molecular-weight forms of adiponectin, recognized as metabolically active forms, were particularly enriched in the SC MI mice injected with ALY688, though this difference was not statistically significant (Figure 3.6 A-C). In parallel, these active forms also showed an increasing trend when comparing MI ALY versus MI PBS groups, but only in the SC condition (Figure 3.6 D-F). Correlation analysis revealed a weak but significant association between adiponectin levels in EVs and infarcted heart tissue following MI injury and ALY688 administration (Figure 3.5 G and H). To further investigate ALY688's capacity to enhance EV-adiponectin loading, we administered ALY688 to mice 15 mg/kg for 3 days, then collected plasma for EV isolation. NTA data demonstrated that ALY688 significantly increased the EVs biogenesis while particle size remained unchanged (Figure 3.5 I-K), which is consistent with our previous observations. EV characterization confirmed positivity for the markers (Figure 3.5 L-P). Following ALY688 injection, EV-loaded adiponectin was significantly enhanced as anticipated

(Figure 3.5 L and Q). To validate the functional potency of EV-carried adiponectin in cardiomyocytes, we treated rat cardiomyoblast H9c2 cell lines with EVs isolated from mice injected with either PBS (EV^{PBS}) or ALY (EV^{ALY}) and examined adiponectin signaling activation. As presented, phospho-AMPK and phosphor-p38 was activated upon EV^{ALY} treatment, whereas no activation was observed with of EV^{PBS} treatment (Figure 3.5 R-T). Together, these findings suggest that ALY688 enhances EV-carried adiponectin content, which maintains similar functional properties to native adiponectin. Because the subsequent mechanistic experiments including EVs functional assays and targeted validation required a consistent metabolic background, all follow-up studies were conducted in the SC cohort to minimize diet-driven confounding and allow clearer interpretation of ALY688- and MI-related EV changes.

Results 4: ALY688 driven plasma EV protective effect in hypoxia cellular model

Before examining how the ALY688-shaped EVs elicit cardioprotective effects, we assessed the internalization efficacy of EVs in recipient cardiomyocytes. Based on our demonstration that HFD feeding did not exacerbate MI-induced cardiac dysfunction and that ALY688 therapeutic effects were equivalent across dietary conditions (Figure 3.1), we focused our mechanistic studies on EVs derived from SC mice. This approach provides representative characterization of ALY688-shaped EV therapeutic potential, as both the pathological target (MI) and therapeutic response (ALY688 protection) appear independent of donor metabolic status. H9c2 cells were incubated with DiR-labeled EVs isolated from SC mice as described in Figure 1, and cellular uptake was evaluated using confocal microscopy and flow cytometry. Both confocal and flow cytometry data confirmed efficient internalization of all EV types, and EVs from MI ALY treated mice showed higher uptake efficiency compared to MI PBS (Figure 3.6 A and B). To better understand the functional effects of EV^{ALY} in ischemic injury, we employed a hypoxia system in H9c2 and iPSC cardiomyocytes (iPSC-CM) to simulate *in vivo* ischemia. We first measured apoptosis and cell death in the hypoxia model, as these represent the major event during ischemic remodeling (365). Caspase 3/7 activity was used to evaluate apoptosis and Propidium Iodide (PI) staining and LDH release were used to measure cell death as described before (285). In H9c2 cells, hypoxia induced apoptosis and cell death was significantly reduced by the EV^{ALY} treatment compared to control (Figure 3.7 A, Figure 3.6 C-E). Similar protective effects against cell death were observed in iPSC-CM (Figure 3.7 B). Mitochondrial dysfunction is the major cause of cellular ROS accumulation and subsequent cell death under ischemia conditions (366). Next, we tested whether EV^{ALY} reduced mitochondrial

damage and the consequent ROS production in cardiomyocytes. Mitochondrial morphology was evaluated by the index of networking, demonstrating that hypoxia impaired mitochondrial networking and the impairment was improve by EV^{ALY} in both H9c2 cells and iPSC-CM (Figure 3.7 C-E). Furthermore, IMARIS sphericity analysis, used as an index of mitochondrial fission, revealed increased mitochondrial fragmentation during hypoxia, which was reduced by EV^{ALY} in H9c2 cell (Figure 3.7 F and G). ROS accumulation assessed by CellRox staining demonstrated that EV^{ALY} significantly decreased hypoxia-induced ROS level in H9c2 cells and iPSC-CM, whereas this protective effect was not observed with EV^{PBS} treatment (Figure 3.7 H-J). Autophagy, a well-characterized function of adiponectin, and an important regulatory mechanism for ischemic cardiac protection (367, 368) (201) (285). We then investigated how the EV^{ALY} modulates autophagy under hypoxic conditions by performing quantitative analysis of autophagy flux using a genetically engineered H9c2 cell line expressing the LC3 HiBiT reporter (285). A significant increase of red fluorescent signal, indicating accumulation of LC3-II, was detected in cells subjected to hypoxia, while pretreatment with EV^{ALY} effectively mitigated this response (Figure 3.7 K and L). To determine whether lysosome activity was altered in response to hypoxia ± EV^{ALY}, we used MagicRed (MR), a cathepsin B probe, to measure lysosomal enzyme activity. We observed that in response to EV^{ALY} treatment increased lysosomal activity, whereas hypoxia alone produced no change in H9c2 cells (Figure 3.7 M and Figure 3.6 F). Autophagic flux was further investigated by western blot analysis, showing that p62 degradation was disrupted during hypoxia, but returned to normal levels the presence of EV^{ALY}, while LC3 II remained unchanged in H9c2 cells (Figure 3.6 G-I). Furthermore, inflammation was also measured with RAW-Dual™ cells system. As shown, raw cell primed with LPS followed with hypoxia challenge demonstrated activated interferon (IFN) and NKκB, while suppressed when treated with EV^{ALY} (Figure 3.6 J and K).

To validate the observed effects of EV^{ALY} in hypoxic cell, we performed recipient cell proteomics analysis in cell subjected to hypoxia and treated with EV^{PBS} or EV^{ALY}. PCA and hierarchical clustering plotted among hypoxia EV^{PBS} and hypoxia EV^{ALY} groups revealed distinct separation between treatment conditions (Figure 3.9 A and B). Volcano plot analysis revealed EV^{ALY} predominantly upregulated rather than downregulated protein expression (Figure 3.9 C). Differentially expressed proteins (Padj. < 0.05, fold change ≥ 1.5) identified from the volcano plot were used for subsequent pathway enrichment analysis. Among GO molecular function, biology

process, cellular component, and KEGG pathway, mitochondrial related pathway (eg. ATP-dependent activity, mitochondrion membrane organization, metabolic pathways, reactive oxygen species, and oxidative phosphorylation), energy homeostasis (eg. Fatty acid degradation, thermogenesis, carbon metabolism) and autophagy were significantly enriched (Figure 3.9 D-G). Notably, ATG3, a key component of the autophagosome formation complex, complex I and complex V proteins of the of electron transport chain proteins, and proteins governing fatty acid breakdown showed significant increase when comparing hypoxia EV^{ALY} versus hypoxia EV^{PBS} (Figure 3.9 H). This observation is further validated by Seahorse assay, showing that hypoxia challenge in H9c2 suppressed mitochondrial respiration capacity, but rescued by the presence of EV^{ALY} (Figure 3.9I and J).

Results 5: ALY688 driven plasma EV improved myocardium remodeling in MI mice

Circulating EVs have diagnostic, prognostic, and therapeutic potential in CVD (369). Therefore, we sought to determine whether ALY688 shaped-EVs mediate pro-autophagy and mitochondrial protective actions in cardiomyocytes under physiological conditions of acute myocardial infarction. Mice were injected with injected EV^{ALY} or EV^{PBS}, both previously characterized for standard EV markers and confirmed to be enriched with adiponectin in the EV^{ALY} preparation (Figure 3.10 A). One hour following myocardial ischemia induced by LAD occlusion, EV^{ALY} or EV^{PBS} were administered to mice via tail vein injection, and mice were sacrificed 2 days post-MI (Figure 3.10 A). Plasma Troponin I and LDH levels were measured to determine cell death. Following MI, both troponin I and LDH were significantly elevated, while only EV^{ALY} treatment suppressed the increase in these cardiac injury markers (Figure 3.10 B and C). Apoptosis in infarcted hearts was then evaluated by caspase-3 cleavage, demonstrating more abundant cleaved caspase-3 in MI compared to sham conditions, which was reduced following EV^{ALY} treatment (Figure 3.10 D and E). Collectively, these data evidenced that EV^{ALY} reduced apoptosis and cell death induced by acute MI. Mitochondrial function was next assessed through analysis of fission and fusion proteins, EV^{ALY} treated mice showed slight decrease in MFF (mitochondrial fission factor), p-Drp1 s616, and increase in p-Drp1 s637 and OPA1 (Optic Atrophy 1), suggesting reduced in MI-induced mitochondrial dynamic disruption (Figure 3.10 F-J). Mice treated with EV^{ALY} also displayed significant restoration of antioxidant gene expression, including *Sod*1, *Sod2*, and *Sod3*, though no significant difference were observed in *Nox1* and *Nox2* expression (Figure 3.10 K, and Figure 3.11 A). To further correspond with the previous recipient cell proteomics findings, autophagy flux was

also measured in infarcted heart. EV^{ALY} treatment resulted in increased LC3-II and ATG3 levels, along with enhanced p62 degradation (Figure 3.10 L-O). As such, autophagic flux impaired by MI was relieved by EV^{ALY}. Additionally, *IL-6*, *MCP1* and *iNOS* mRNA expression presented reduction in EV^{ALY} treatment compared to sham (Figure 3.11 B), while no changes were observed in *IL-1β, IL-18, IL-12a, IL-12b, IL-10, TNFα,* and *CD206* in infarcted heart. Taken together, these data indicate that under the tested conditions, the ALY688-shaped EVs enhance cardiac resilience in acute MI.

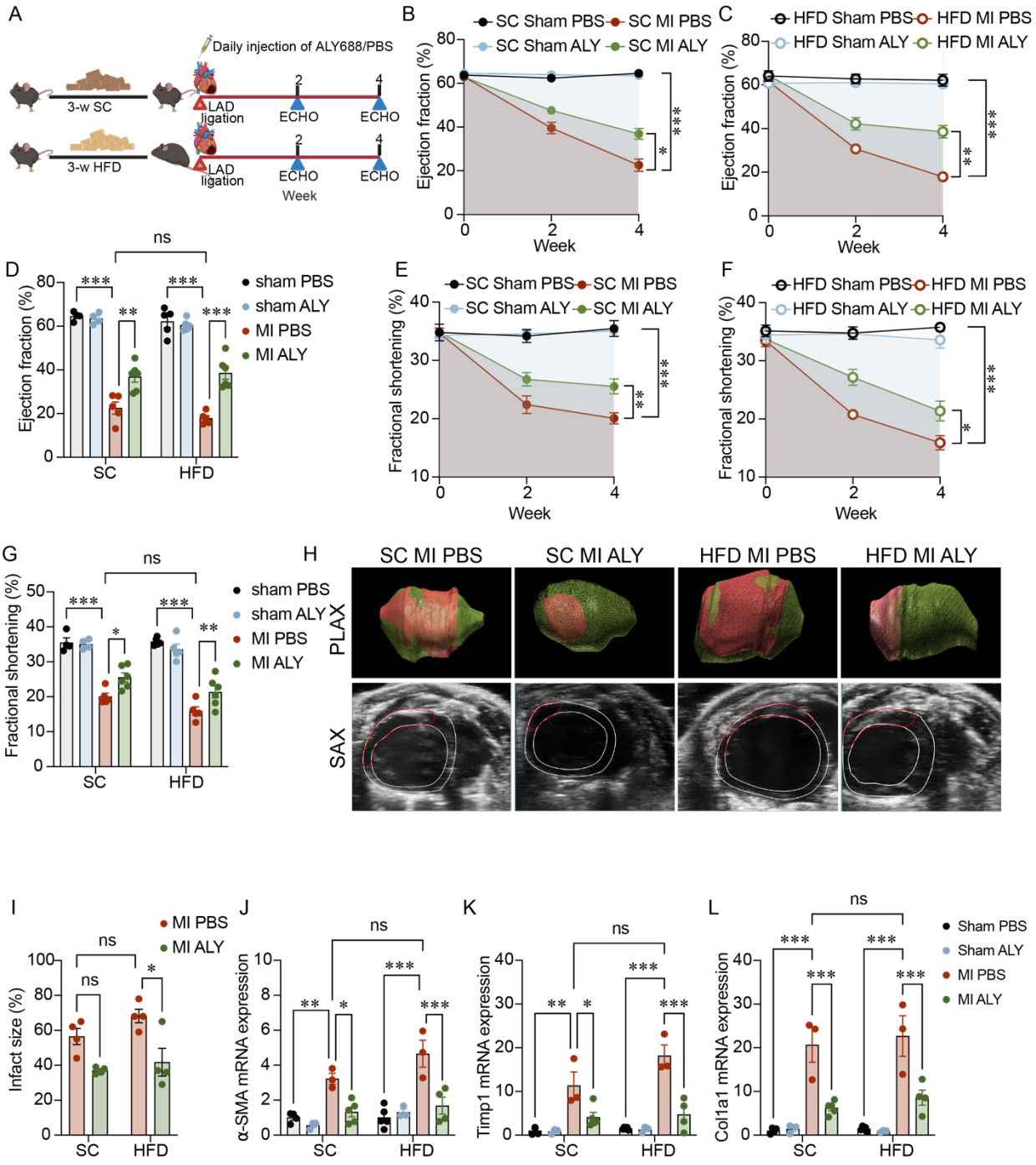

Figure 3.1 ALY688 improves post-MI cardiac function and limits fibrosis across metabolic states

(A) Animal study schematic diagram. (B-C) Ejection fraction measurement of SC or HFD mice subjected to sham or MI, and injected with PBS or ALY at 0-, 2- and 4-week post LAD ligation.

(D) Ejection fraction measurement at 4-week post LAD ligation. (E-F) Fractional shortening measurement of SC or HFD mice subjected to sham or MI, and injected with PBS or ALY at 0-, 2- and 4-week post LAD ligation. (F) Ejection fraction measurement at 4-week post LAD ligation. (H) Representative image 3-D mesh of infarct and LV using Vevo LAB 4-D visualization, at end diastole, infraction indicated in red, and SAX view of infarct, indicated in red, using Vevo LAB 4-D visualization, at end diastole. Images obtained at 4-week post MI. (I) Infarct size measurement at 4-week post MI. (J-L) αSMA, Timp1, and Col1a1 mRNA expression of in infarcted heart tissue. Results are presented as mean ± SEM. (n=4-6/group). *P<0.05, **P<0.01, ***P<0.001 versus control. Two-way ANOVA followed by Tukey's multiple comparisons *post hoc* test. 4-D, four-dimensional; PLAX, parasternal long-axis view; SAX, several short-axis; 3-D, three-dimensional.

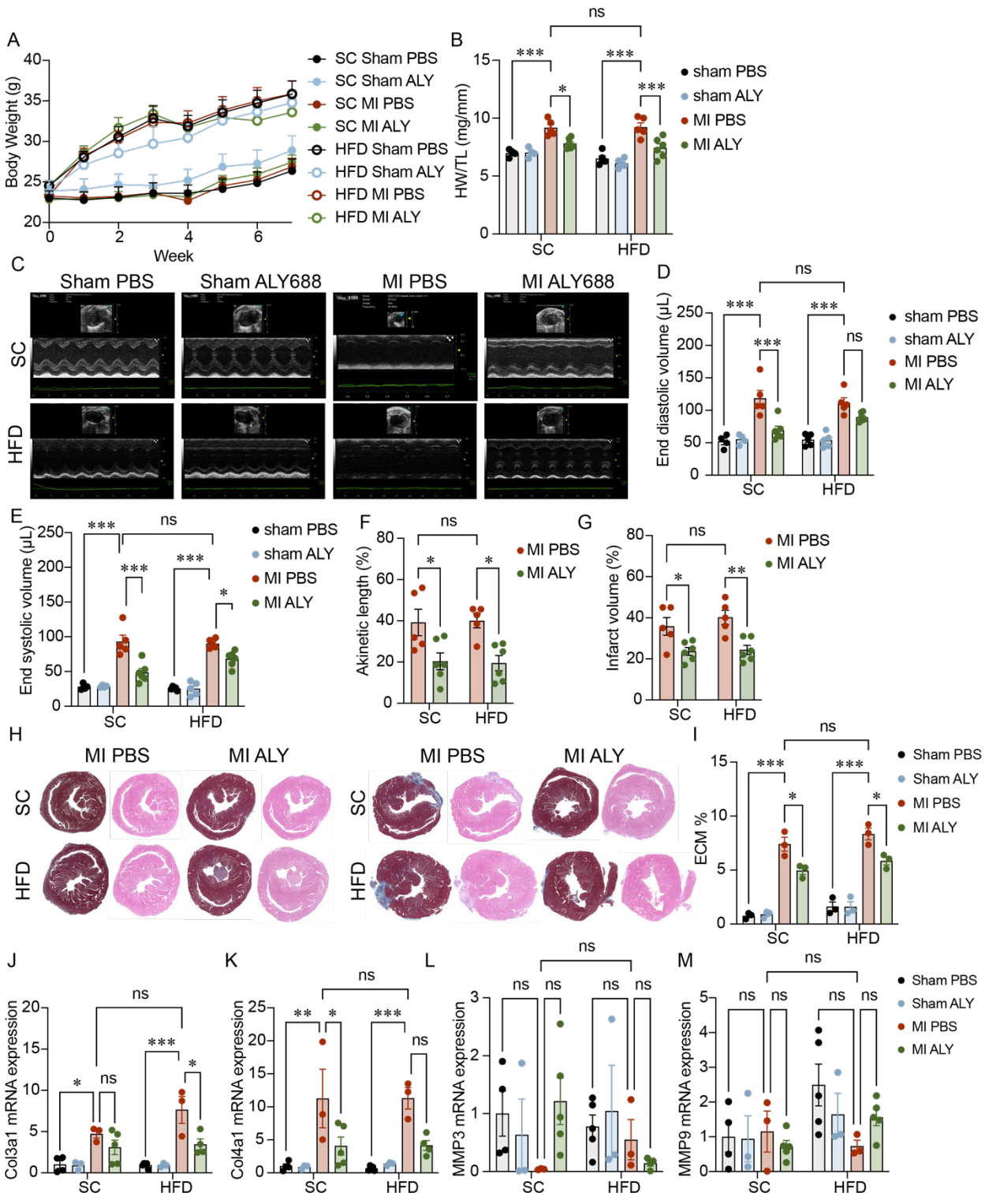

Figure 3.2 Echocardiography and histology confirm functional rescue and reduced fibrosis post-MI

(A) Body weight measurement over the first seven weeks following the start of HFD feeding in SC mice. (B) Ratio of heart weight to tibial length. (C) Representative of echocardiography M-mode analysis at 4-week after LAD ligation. (D-E) End diastolic and end systolic volume measurement at 4-week post LAD ligation. (F-G) Akinetic length and infract volume measurement. at 4-week post LAD ligation. (H) Representative image of Masson trichrome and H&E staining in heart. (I) Quantification of ECM percentage in Masson trichrome stained images. (J-M) Col3a1, Col4a1, MMP3 and MMP9 mRNA expression of in infarcted heart tissue. Results are presented as mean ± SEM. (n=4-6/group). *P<0.05, **P<0.01, ***P<0.001 versus control. Two-way ANOVA followed with multiple comparisons post-hoc test was run for statistical analysis.

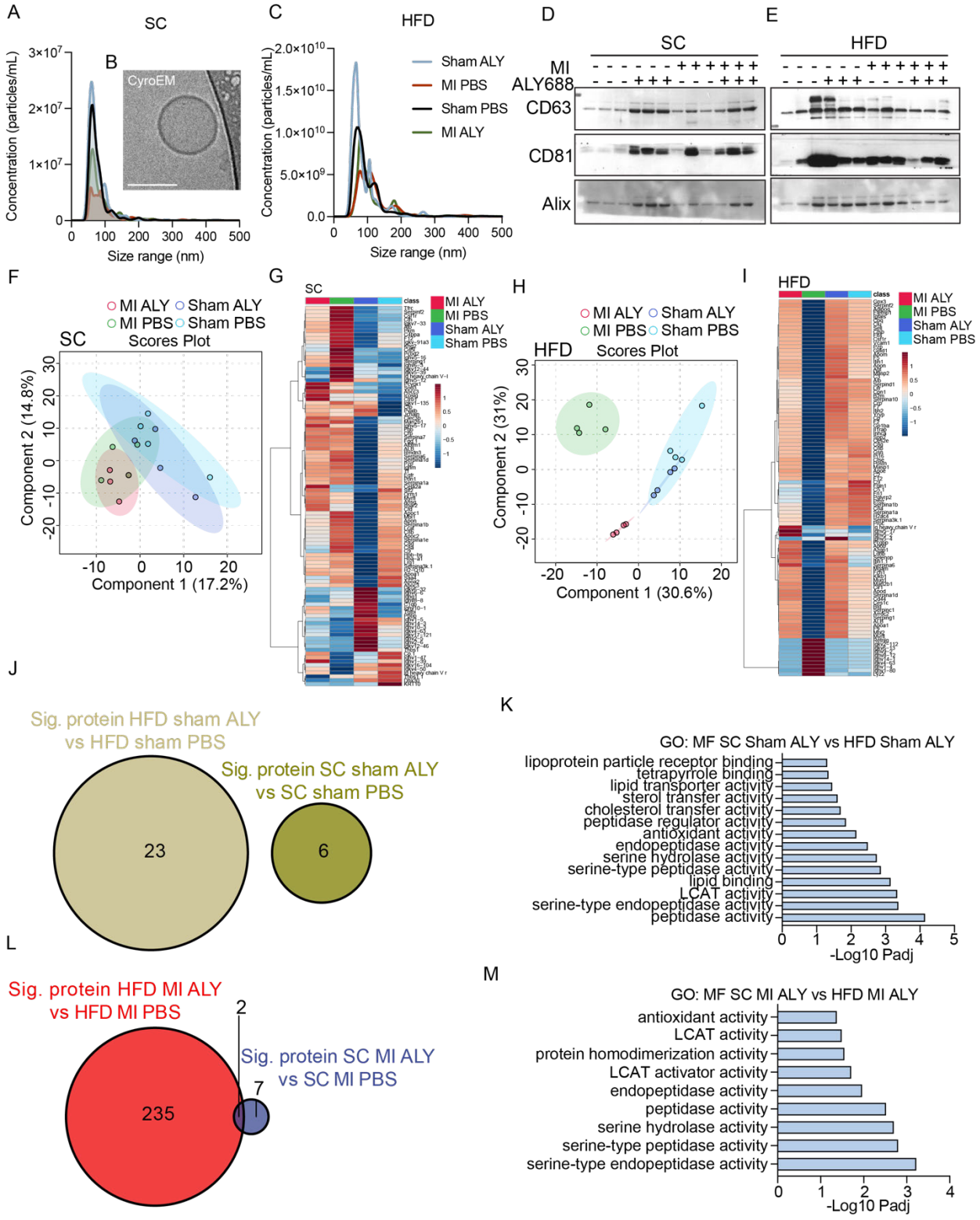

Figure 3.3 MI and ALY688 reshape plasma EV abundance and proteomes in a diet-dependent manner

(A and C) NTA analysis of EV isolated from SC and HFD mice plasma described above. (B) Representative image of Cryo EM of plasma derived EVs. (D-E) SDS-PAGE and immunoblot analysis of SC and HFD plasma EVs using CD63, CD81 and Alix. (F) PLSDA plot of SC groups plasma EVs proteomics. (G) Hierarchical clustering heatmap of SC groups plasma EVs proteomics. (H) PLSDA plot of HFD groups plasma EVs proteomics. (I) Hierarchical clustering heatmap of HFD groups plasma EVs proteomics. (J) Venn diagram presenting the overlapping proteins between significant expressed protein in the comparison of HFD sham ALY versus HFD sham PBS, and SC sham ALY versus SC sham PBS. (K) GO molecular function pathway enrichment analysis with significant expressed protein in the comparison of HFD sham ALY versus SC sham ALY. (L) Venn diagram presenting the overlapping proteins between significant expressed protein in the comparison of HFD MI ALY versus HFD MI PBS, and SC MI ALY versus SC MI PBS. (M) GO molecular function pathway enrichment analysis with significant expressed protein in the comparison of HFD MI ALY versus SC MI ALY. (n=3-4/group).

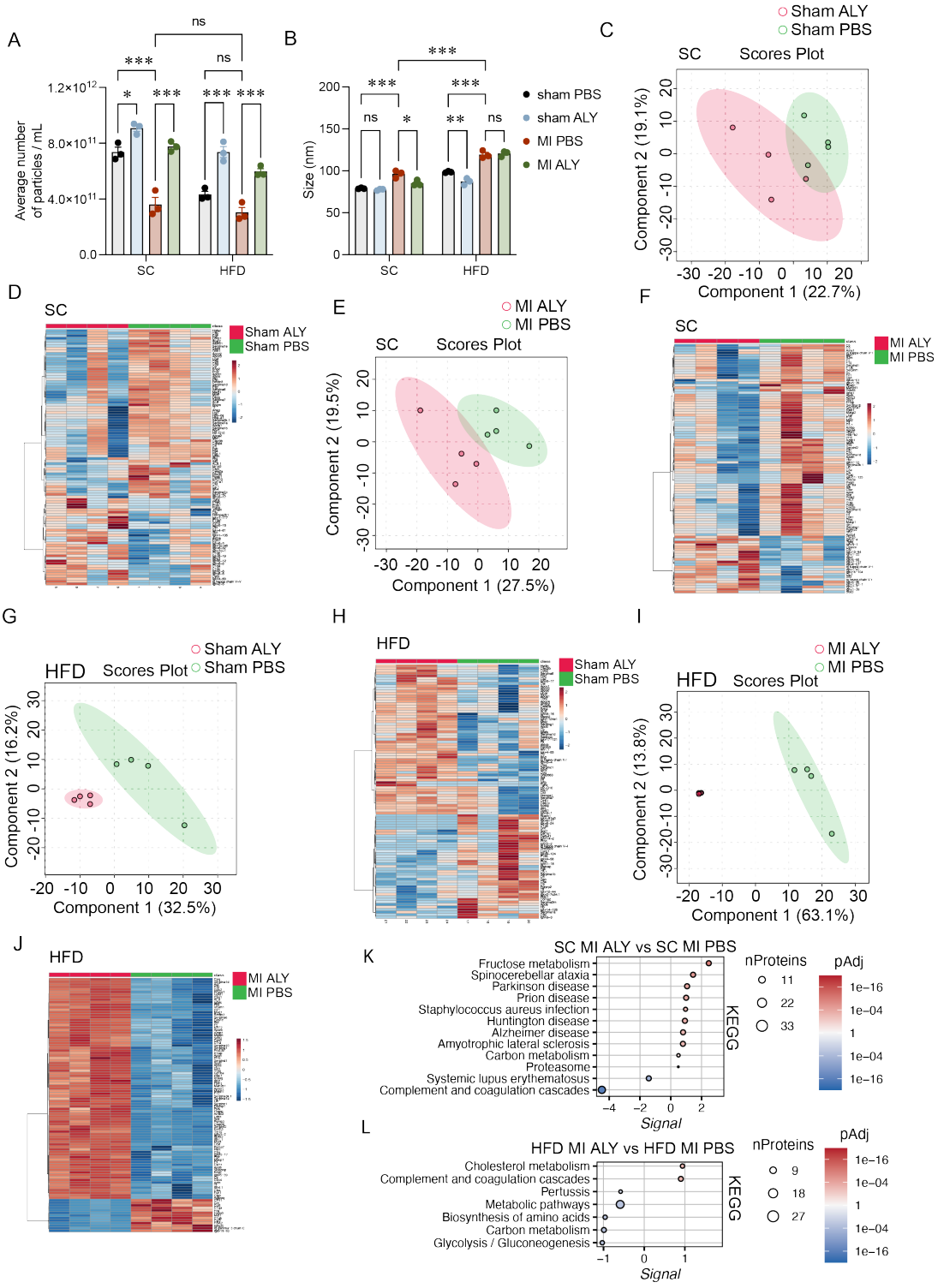

Figure 3.4 Plasma EV quantity, size, and pathway signatures shift with MI, diet, and ALY688

(A) Average number of mice plasma EVs analyzed by NTA. (B) Size of mice plasma EVs analyzed by NTA. (C) PLSDA plot of SC sham ALY and SC sham PBS plasma EVs proteomics, and (E) Hierarchical clustering heatmap. (E) PLSDA plot of SC MI ALY and SC MI PBS plasma EVs proteomics, and (F) Hierarchical clustering heatmap. (G) PLSDA plot of HFD sham ALY and HFD sham PBS plasma EVs proteomics, and (H) Hierarchical clustering heatmap. (I) PLSDA plot of HFD MI ALY and HFD MI PBS plasma EVs proteomics, and (J) Hierarchical clustering heatmap. (K) KEGG pathway enrichment of significant expressed protein in the comparison of SC MI ALY vs SC MI PBS. (L) KEGG pathway enrichment of significant expressed protein in the comparison of HFD MI ALY vs HFD MI PBS. (n=4/group)

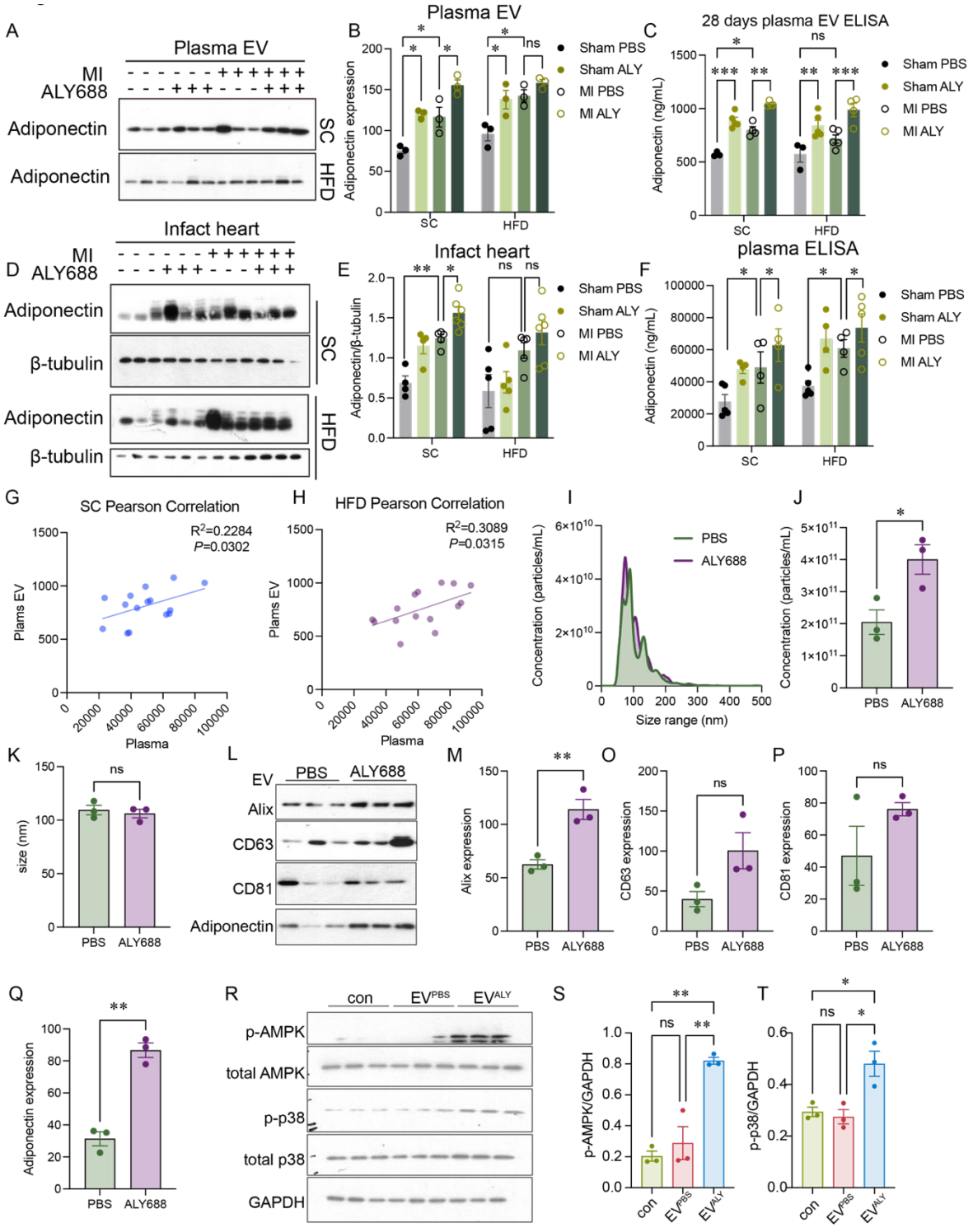

Figure 3.5 ALY688 increases EV biogenesis and enriches EV cargo with bioactive adiponectin

(A) SDS-PAGE and immunoblot analysis of plasma EVs isolates from SC and HFD mice subjected to sham or MI, and injected with PBS or ALY, using adiponectin. (B) Quantification of adiponectin expression in EVs. Data is normalized by particle number. (C) ELISA analysis of adiponectin abundance in EVs isolates. (D) SDS-PAGE and immunoblot analysis of infarcted heart tissue from SC and HFD mice subjected to sham or MI, and injected with PBS or ALY, using adiponectin. β-tubulin was used as loading control. (F) Quantification of adiponectin expression in infarcted heart. (E) ELISA analysis of adiponectin abundance in infarcted heart tissue lysate. (G-H) Pearson correlation of adiponectin abundance in plasma EVs and infarcted heart tissue in SC and HFD. (I) NTA analysis of EVs isolated from plasma from mice subjected to 3 days PBS or ALY injection. (J) Particle number analysis from NTA. (K) Size analysis from NTA. (L) SDS-PAGE and immunoblot analysis of EVs isolated from conditioned culture medium of plasma as described above, using Alix, CD63, CD81 and adiponectin. (M-Q) Quantification of Alix, CD63, CD81 and adiponectin abundance in EVs isolates. Data is normalized by particle number. (R) SDS-PAGE and immunoblot analysis of H9c2 cells treated with EV^{PBS} or EV^{ALY}, using p-AMPK, total AMPK, p-p38, and total p38. GAPDH was used as loading control. (S-T) Quantification of p-AMPK and p-p38 expression. Results are presented as mean ± SEM. (n=3-6/group). *P<0.05, **P<0.01, ***P<0.001 versus control. Two-way ANOVA with Tukey multiple comparison post-hoc test was run for statistical analysis in panel B, C, E and F. One-way ANOVA was run for statistical analysis for panel S and T. T-test was run for statistical analysis for panel J-K, and M-Q.

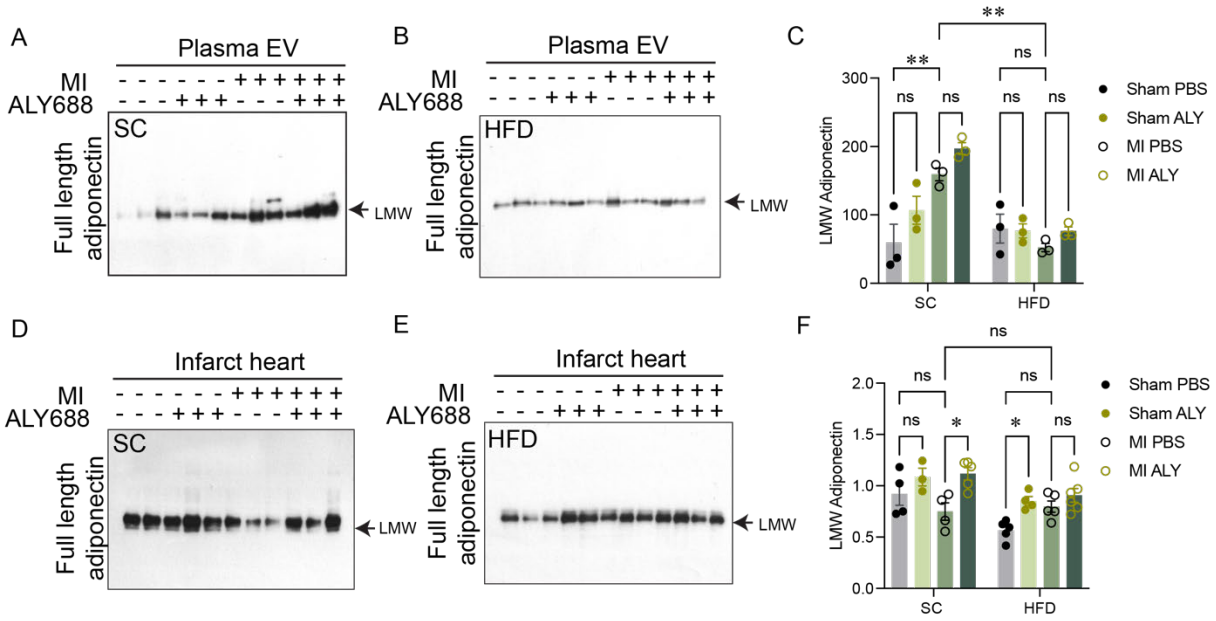

Figure 3.6 Analysis of LMW adiponectin in EVs and infarcted myocardium

(A-B) Unreducing SDS-PAGE and immunoblot analysis of plasma EVs isolated from SC and HFD mice, using full length adiponectin. (C) Quantification of low molecular weight (LWM) adiponectin in plasma EVs. (D-E) Unreducing SDS-PAGE and immunoblot analysis of infarcted heart tissue from SC and HFD mice, using full length adiponectin. (C) Quantification of low molecular weight (LWM) adiponectin in infarcted heart tissue. Results are presented as mean ± SEM. (n=3/group). **P*<0.05, ***P*<0.01, ****P*<0.001 versus control. Two-way ANOVA with Tukey multiple comparisons post-hoc test was run for statistical analysis.

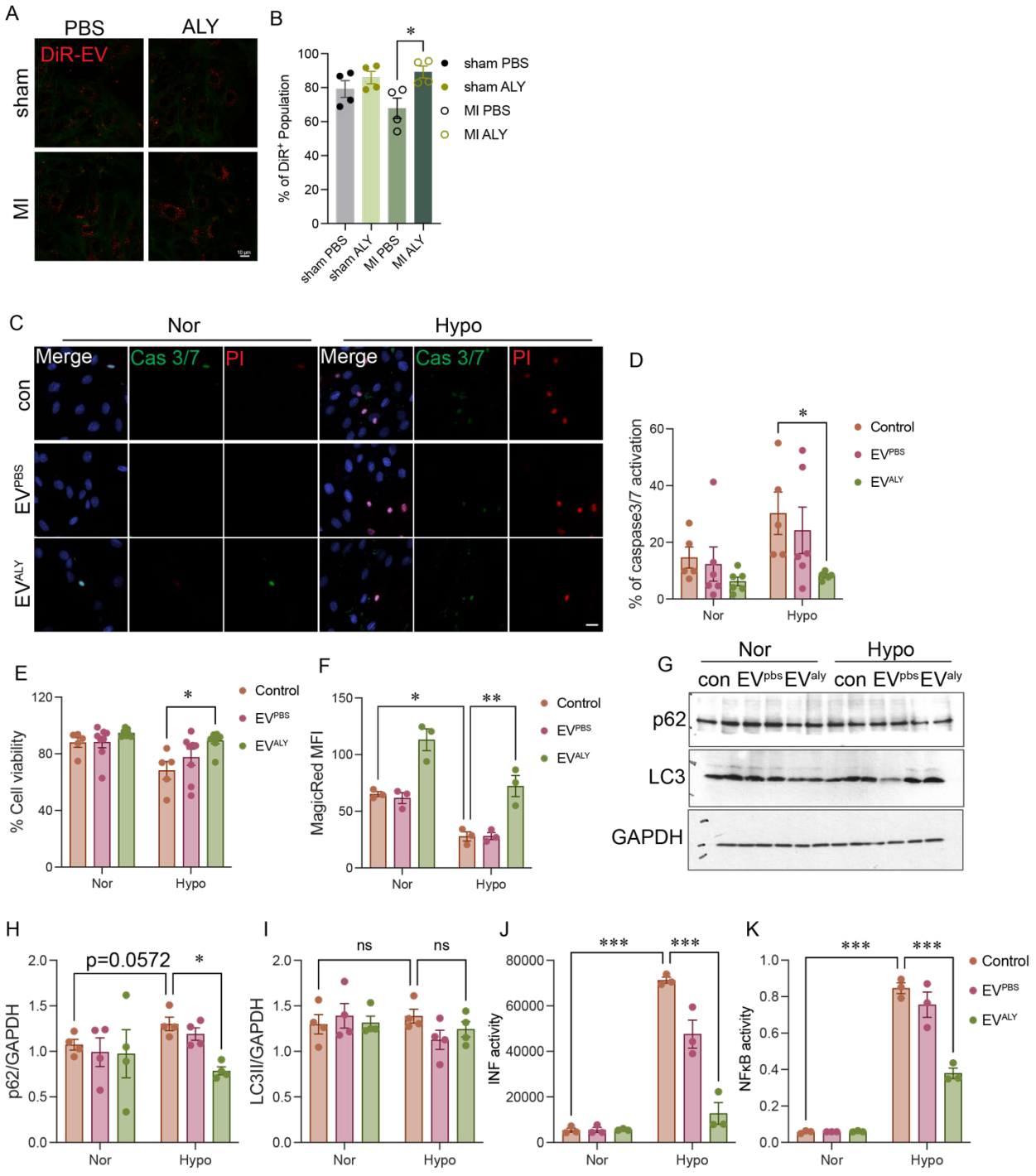

Figure 3.7 EV^{ALY} reduces apoptosis and ROS while restoring autophagy and dampening inflammation

(A) Representative image of EVs uptake assay in H9c2. (B) Quantification of positive percentage of DiR population in H9c2 by flow cytometry. (C) Representative image of Caspase 3/7 green and

PI red staining in H9c2 subjected to 24 hours hypoxia treated with 10 μg/mL EV^{PBS} and EV^{ALY}. (D) Quantification of % of Caspase 3/7 positive staining in H9c2 cells. (E) Quantification of % cell viability in PI staining in H9c2 cells. (F) Quantification of MFI of MagicRed staining in H9c2 cells. (G) SDS-PAGE and immunoblot analysis of H9c2 subjected to 24 hours hypoxia treated with 10 μg/mL EV^{PBS} and EV^{ALY}, using p62 and LC3. GAPDH was used as loading control. (H-I) Quantification of p62 and LC3 expression in H9c2 cell. (J) INF activity in macrophage. Arbitrary unit was used in this data. (K) NFκB activity in macrophage. Arbitrary unit was used in this data. Results are presented as mean ± SEM. (n=3-7/group). *P<0.05, **P<0.01, ***P<0.001 versus control. One-way ANOVA with Tukey post-hoc test was run for statistical analysis for the rest of panel B. Two-way ANOVA with Tukey post-hoc multiple comparisons post-hoc test was run for statistical analysis for the rest of panels. Scale bar: 10 μm.

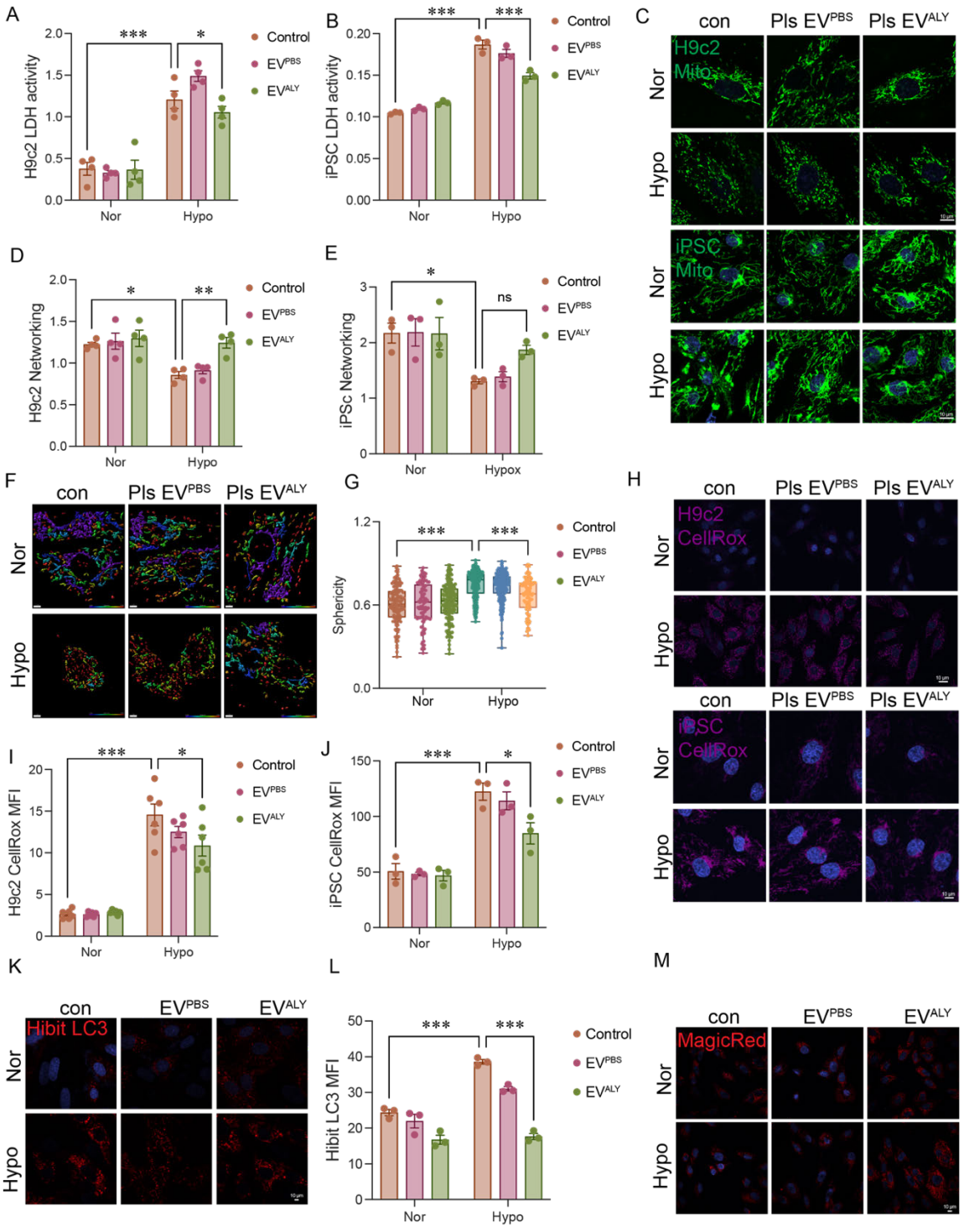

Figure 3.8 ALY688-shaped EVs protect hypoxic cardiomyocytes via mitochondrial preservation and autophagy

(A-B) LDH analysis in H9c2 or iPSC-CM subjected to 24 hours hypoxia treated with 10 µg/mL EV^{PBS} and EV^{ALY}. (C) Representative image of MitoTracker green staining in H9c2 and iPSC-CM subjected to 24 hours hypoxia treated with 10 µg/mL EV^{PBS} and EV^{ALY}. (D-E) Quantification of mitochondrial networking in H9c2 or iPSC-CM based on MitoTracker staining. (F) IMARIS analysis of mitochondrial sphericity in H9c2, and quantification in (G). (H) Representative image of CellRox deep red staining in H9c2 and iPSC-CM subjected to 3 hours hypoxia treated with 10 µg/mL EV^{PBS} and EV^{ALY}. (I-J) Quantification of MFI (mean fluorescence intensity) in H9c2 or iPSC-CM based on CellRox deep red staining. (K) Representative image of Hibit-LC3 H9c2 cells subjected to 24 hours hypoxia treated with 10 µg/mL EV^{PBS} and EV^{ALY}. (L) Quantification of Hibit-LC3 positive MFI. (M) Representative image of MagicRed staining in H9c2 cells subjected to 24 hours hypoxia treated with 10 µg/mL EV^{PBS} and EV^{ALY}. Results are presented as mean ± SEM. (n=3-6/group). *P<0.05, **P<0.01, ***P<0.001 versus control. Two-way ANOVA with Tukey multiple comparisons post-hoc test was run for statistical analysis. Scale bar: 10 µm.

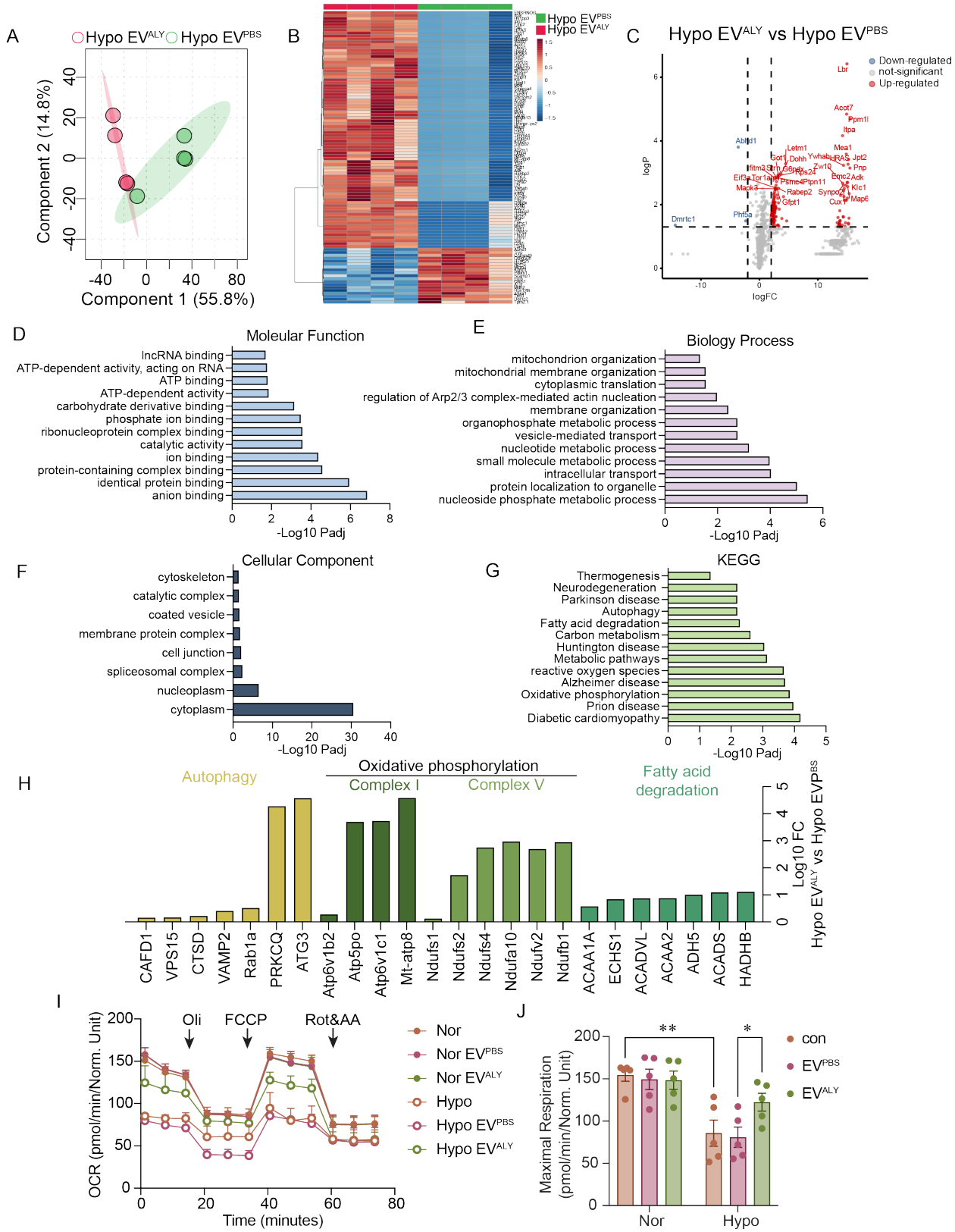
A
Hypo EVALY
Hypo EVPBS
Component 2 (14.8%)
Component 1 (55.8%)
B
Hypo EVPBS
Hypo EVALY
C
Hypo EVALY vs Hypo EVPBS
Down-regulated
not-significant
Up-regulated
logP
logFC
D
Moleular Function
lncRNA binding
ATP-dependent activity, acting on RNA
ATP binding
ATP-dependent activity
carbohydrate derivative binding
phosphate ion binding
ribonucleoprotein complex binding
catalytic activity
ion binding
protein-containing complex binding
identical protein binding
anion binding
-Log10 Padj
E
Biology Process
mitochondrion organization
mitochondrial membrane organization
cytoplasmic translation
regulation of Arp2/3 complex-mediated actin nucleation
membrane organization
organophosphate metabolic process
vesicle-mediated transport
nucleotide metabolic process
small molecule metabolic process
intracellular transport
protein localization to organelle
nucleoside phosphate metabolic process
-Log10 Padj
F
Cellular Component
cytoskeleton
catalytic complex
coated vesicle
membrane protein complex
cell junction
spliceosomal complex
nucleoplasm
cytoplasm
-Log10 Padj
G
KEGG
Thermogenesis
Neurodegeneration
Parkinson disease
Autophagy
Fatty acid degradation
Carbon metabolism
Huntington disease
Metabolic pathways
reactive oxygen species
Alzheimer disease
Oxidative phosphorylation
Prion disease
Diabetic cardiomyopathy
-Log10 Padj
H
Autophagy
Oxidative phosphorylation
Complex I
Complex V
Fatty acid degradation
Log10 FC
Hypo EVALY vs Hypo EVPBS
CAFD1
VPS15
CTSD
VAMP2
Rab1a
PRKCQ
ATG3
Atp6v1b2
Atp5po
Atp6v1c1
Mt-atp8
Ndufs1
Ndufs2
Ndufs4
Ndufa10
Ndufv2
Ndufb1
ACAA1A
ECHS1
ACADVL
ACAA2
ADH5
ACADS
HADHB
I
Oli
FCCP
Rot&AA
OCR (pmol/min/Norm. Unit)
Time (minutes)
Nor
Nor EVPBS
Nor EVALY
Hypo
Hypo EVPBS
Hypo EVALY
J
Maximal Respiration (pmol/min/Norm. Unit)
con
EVPBS
EVALY
Nor
Hypo

Figure 3.7 EV^{ALY} reprograms hypoxic cardiomyocyte proteome toward oxidative metabolism and autophagy

(A) PLSDA plot proteomics analysis of H9c2 cell subjected to hypoxia and treated with EV^{ALY} or EV^{PBS}, and (B) Hierarchical clustering heatmap. (C) Volcano plot of the comparison of hypo EV^{ALY} or hypo EV^{PBS}. (D-G) Pathway enrichment analysis (GO: molecular function, biology process, cellular component, and KEGG pathway) with significant expressed protein in the comparison of hypo EV^{ALY} or hypo EV^{PBS}. (H) Log_{10} fold change of the significant expressed protein enriched in autophagy, oxidative phosphorylation and fatty acid degradation pathway. (I) Seahorse analysis of H9c2 treated with EV^{ALY} or EV^{PBS}, then subjected with normoxia or hypoxia. (J) Measurement of maximal respiration capacity during Seahorse experiment. Results are presented as mean ± SEM. (n=4-5/group). *P<0.05, **P<0.01, ***P<0.001 versus control. Two-way ANOVA with Tukey multiple comparison post-hoc test was run for statistical analysis.

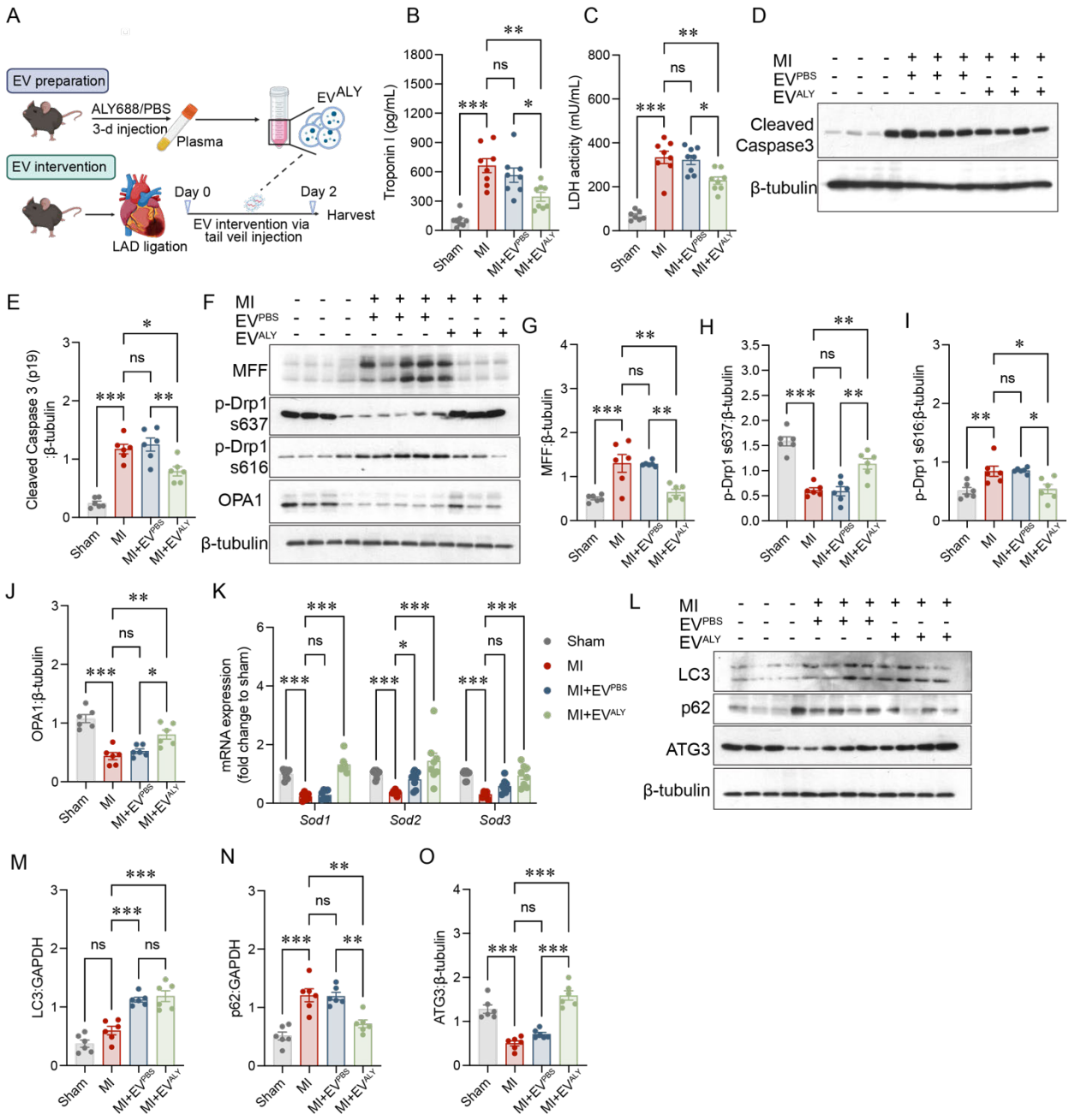

Figure 3.8 Therapeutic EV^{ALY} reduces acute myocardial injury and restores mitochondrial dynamics in vivo

(A) Animal study schematic diagram. (B) Troponin I level measured in plasma from mice subjected to sham or acute MI and injected with EV^{PBS} or EV^{ALY}, 6 hours post MI. (C) Terminal LDH level measured in mice plasma as described above. (D) SDS-PAGE and immunoblot analysis of infarcted heart, using cleaved caspase 3. β-tubulin was used as loading control. (E)

Quantification of cleaved caspase 3 in infarcted heart. (F) SDS-PAGE and immunoblot analysis of infarcted heart, using MFF, p-Drp1 s637, p-Drp1 s616, and OPA1. β-Tubulin was used as loading control. (G-J) Quantification of MFF, p-Drp1 s637, p-Drp1 s616, and OPA1. (K) Sod1, Sod2 and Sod3 mRNA expression in infarcted heart. (L) SDS-PAGE and immunoblot analysis of infarcted heart, using LC3, p62, and ATG3. β-tubulin was used as loading control. (M-O) Quantification of LC3, p62, and ATG3. Results are presented as mean ± SEM. (n=6-8/group). **P*<0.05, ***P*<0.01, ****P*<0.001 versus control. Two-way ANOVA with Tukey multiple comparisons post-hoc test was run for statistical analysis for panel K. One-way ANOVA with Tukey post-hoc test was run for statistical analysis for the rest of panels.

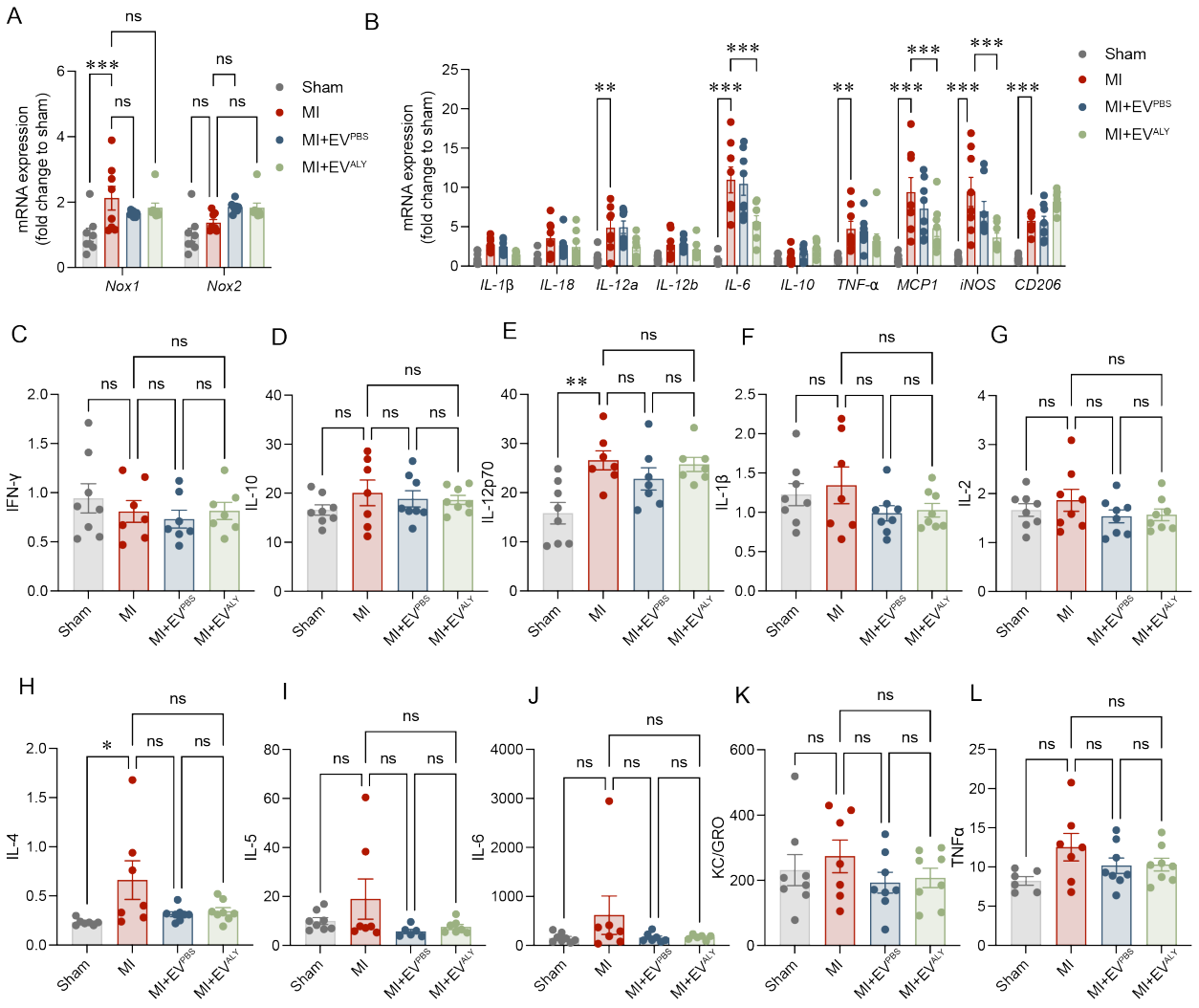

Figure 3.9 EV^{ALY} modulates cardiac oxidative stress and inflammatory cytokine profiles after MI

(A) Nox1 and Nox2 mRNA expression of infarcted heart from mice subjected to sham or acute MI and injected with EV^{PBS} or EV^{ALY}. (B) IL-1β, IL-18, IL-12a, IL-12b, Il-10, TNF-α, MCP1, iNOS, and CD206 mRNA expression of infarcted heart. (C) Circulating level of IFN-γ, IL-10, IL-12p70, IL-1β, IL-2, IL-4, IL-5, IL-6, KC/GRO and TNFα at terminal stage of mice. Results are presented as mean ± SEM. (n=6-8/group). *P<0.05, **P<0.01, ***P<0.001 versus control. Two-way ANOVA with Tukey multiple comparisons post-hoc test was run for statistical analysis for panel A-B. One-way ANOVA with Tukey post-hoc test was run for statistical analysis for the rest of panels.

Table 3.1 Summary of Echocardiography parameters of mice undergone sham and MI

Summary of Echocardiography parameters of mice undergone sham and MI									
day 0 after MI	**Unit**	**SC sham PBS**	**SC sham ALY**	**SC MI PBS**	**SC MI ALY**	**HFD sham PBS**	**HFD sham ALY**	**HFD MI PBS**	**HFD MI ALY**
Heart rate	bmp	532 ± 23.01	541 ± 21.85	528 ± 35.32	561 ± 31.32	549 ± 21.32	543 ± 30.44	523 ± 15.32	545 ±32.32
Ejection fraction	%	63.75 ± 2.56	64.63 ± 3.49	63.02 ±13.11	62.92 ± 1.67	64.13 ± 5.47	60.80 ± 2.19	61.62 ± 2.46	64.45 ± 2.96
Fractional shortening	%	34.78 ± 2.89	34.29 ± 1.93	34.74 ± 6.99	34.90 ± 1.52	35.13 ± 2.27	34.44 ± 2.98	33.43 ± 2.26	33.73 ± 2.08
day 14 after MI	**Unit**								
Heart rate	bmp	522 ± 30.66	536 ± 21.12	529 ± 53.11	582 ± 12.32	544 ± 31.33	573 ± 27.32	543 ± 43.23	523 ± 29.32
Ejection fraction	%	62.36 ± 2.51	63.92 ± 3.34	39.53 ± 10.60	47.64 ± 3.06	62.75 ± 4.90	61.09 ± 3.65	30.73 ± 1.91	42.21 ± 7.04
Fractional shortening	%	34.17 ± 2.15	34.56 ± 1.70	22.41 ± 2.94	26.75 ± 2.87	34.75 ± 2.41	34.63 ± 1.72	20.76 ± 1.23	27.16 ± 3.38
day 28 after MI	**Unit**								
Heart rate	bmp	542 ± 32.21	533 ± 25.32	583 ± 42.23	573 ± 35.93	541 ± 39.23	530 ± 31.03	537 ± 31.83	527 ± 19.92
Ejection fraction	%	64.54 ± 2.09	63.48 ± 2.53	22.58 ± 6.26	36.87 ± 6.14	62.14 ± 6.14	60.49 ± 2.66	17. 92 ± 2.71	38.58 ± 6.99

Fractional shortening	%	35.47 ± 2.73	35.05 ± 1.38	20.05 ± 2.17	25.55 ± 3.14	35.75 ± 1.08	33.58 ± 3.23	15.91 ± 2.70	21.36 ± 4.17
End diastolic volume	µL	51.92 ± 10.08	55.04 ± 7.59	118.36 ± 27.41	69.15 ± 15.83	54.50 ± 8.90	53.57 ± 10.94	111.43 ± 17.57	89.34 ± 6.81
End systolic volume	µL	27.92 ± 4.20	28.54 ± 1.59	93.12 ± 20.67	48.35 ± 14.07	25.56 ± 2.49	25.10 ± 9.71	90.16 ± 6.47	68.16 ± 11.09

Table 3.2 Overlapping proteins in the between HFD sham ALY vs HFD sham PBS and SC sham ALY vs SC sham PBS

Supplementary Table 1. Overlapping proteins in the between HFD sham ALY vs HFD sham PBS and SC sham ALY vs SC sham PBS		
Sig. protein HFD sham ALY vs HFD sham PBS	Sig. protein SC sham ALY vs SC sham PBS	Overlapping n=0
Ctss	Jchain	
Igkv-91a3	C8b	
Iglc2	Cpn2	
C9	Hgfac	
Apoe	Serpina3k	
Agt		
Ig heavy chain V region 6.96		
Serpinc1		
Col1a2		
Serpina3m		
Serpina6		
Myrfl		
Proz		
Ctrb1		
Cpb2		
Ighv5-4		
Ighv5-16		
Ighv9-1		

Ighv1-18		
Gm2663		
Itih1		
Gpld1		
C6		

Table 3.3 Overlapping proteins in the between HFD MI ALY vs HFD MI PBS and SC MI ALY vs SC MI PBS

Supplementary Table 2. Overlapping proteins in the between HFD MI ALY vs HFD MI PBS and SC MI ALY vs SC MI PBS		
Sig. protein HFD MI ALY vs HFD MI PBS	Sig. protein SC MI ALY vs SC MI PBS	Overlapping n=2
Abcc3	Cfd	F9, full name: Coagulation factor IX
Fga	Cela2a	cp, full name: Ceruloplasmin
Apob	F9	
Prdx6	Tgfbi	
Man2b1	Masp1	
Sod3	Itih3	
Ifnar2	Il1rap	
Fcn1	Igkv5-39	
Hnrnpa2b1	Cp	
F10		
Amy1		
Igkv2-112		
Igkv2-7s34.1		
Igkv2-26-10		
Igkv12-41		
Gm10881		

Igkv-123e6		
Ig kappa chain V-III region PC 2880/PC 1229		
Ig kappa chain V-III region ABPC 22/PC 9245		
Ig kappa chain V-III region PC 7043		
Ig kappa chain V-III region PC 7175		
Ig kappa chain V-VI region XRPC 44		
Ig lambda-1 chain V region S178		
Ig lambda-2 chain V region		
Ig heavy chain V region 93G7		
Ighv1-61		
Ig heavy chain V region 102		
Ig heavy chain V-III region E109		
Ig heavy chain V region MOPC 141		
Iglc2		
Ig kappa chain V-II region 17S29.1		
Ig kappa chain V-III region 50S10.1		

Ig gamma-3 chain C region		
Mup3		
Igf1		
Aldoa		
Ldha		
Ig heavy chain V region AC38 205.12		
C9		
C5		
Apoa4		
Bpifa2		
Apoe		
Sod1		
C4bpa		
Lyz2		
Ubb		
Col1a1		
Cfp		
C1qb		
H2-Q8		
Ldhb		
F9		
Lcat		
Sell		

Ig heavy chain V region 6.96		
Cfl1		
Hspa5		
Plg		
Cst3		
Gc		
Pnp		
Lta4h		
Mst1		
Mug1		
Grn		
Ahsg		
Ppic		
Mif		
KRT2		
Flt4		
Mbl1		
Gpx3		
Igfbp2		
Serpind1		
Sftpb		
Pkm		
Cdh5		

PPIA		
Hspa8		
HBA2		
Selenop		
F7		
Serping1		
Serpinf1		
C1qa		
Tubb5		
Apoa1		
Serpina1d		
Egfr		
Apoh		
Vcp		
C1qc		
Bche		
Serpina3m		
Scgb1a1		
Serpina6		
Ambp		
F13b		
Fbln1		
Cfap96		

Rmdn3		
Myrfl		
Ddx46		
Adipoq		
Cfi		
Serpinf2		
Apoc4		
Ecm1		
Pzp		
Postn		
Azgp1		
Sh3d21		
F13a1		
Qsox1		
Efemp1		
H6pd		
Habp2		
Fgb		
Retnlg		
Blmh		
C8g		
Pglyrp2		
Hpx		

Kcnh5		
Tf		
Taldo1		
Park7		
Pcyox1		
Arrdc2		
Cir1		
Cpn2		
Inhca		
Hrg		
Pi16		
Hgfac		
Gda		
Psmb3		
Psma1		
Fbln5		
Ccl8		
Pf4		
Psma7		
Igkv9-124		
Igkv17-121		
Igkv10-94		
Igkv4-80		

Igkv6-29		
Igkv6-13		
Igkv3-1		
Ighg2b		
Ighv5-2		
Ighv2-2		
Ighv5-4		
Ighv5-9		
Ighv2-5		
Ighv5-12		
Ighv2-9		
Ighv5-9-1		
Ighv5-16		
Ighv5-17		
Ighv7-3		
Ighv4-1		
Ighv14-3		
Ighv9-1		
Ighv7-1		
Ighv9-4		
Ighv3-8		
Ighv6-3		
Ighv6-6		

Ighv1-4		
Ighv10-3		
Ighv1-9		
Ighv1-19		
Ighv1-22		
Ighv1-42		
Ighv1-47		
Ighv1-50		
Ighv1-55		
Ighv1-58		
Ighv8-9		
Ighv1-80		
Igkv4-53		
Ighv1-62-2		
Ighv1-62-1		
Ighv2-6		
Igkv19-93		
Fn1		
Ighv1-15		
Ighv1-18		
Ighg2c		
Igkv4-57		
Igkv1-135		

Igkv16-104		
Igkv4-70		
Igkv4-68		
Igkv4-50		
Igkv5-43		
Ighv9-2		
Ighv9-3		
Ighv10-1		
Ighv1-82		
Ighv1-76		
Ighv8-12		
Kng1		
Igkv1-117		
Igkv12-44		
Igkv8-30		
Igkv8-19		
Igkv6-15		
Igkv13-84		
Igkv6-23		
Igkv9-123		
Igkv6-14		
Igkv15-103		
Igkv8-24		

Igkv12-46		
Igkv6-17		
Mgam		
Marchf1		
C7		
Fcgbp		
Cfhr4		
Serpina3g		
Itih1		
Cp		
Serpina3n		
Apon		
F2		
Fgg		
Cfhr1		
Kng2		
Try10		
Gpld1		
C6		
Prss3b		
Ppbp		

Table 3.4 Sequence of primers

Sequence of primers			
Target	Species	Forward 5'-3'	Reverse 5'-3'
α-SMA	mouse	CCCAGACATCAGGGAGTAATGG	TCTATCGGATACTTCAGCGTCA
Col1a1	mouse	GCTCCTCTTAGGGGCCACT	ATTGGGGACCCTTAGGCCAT
Col1a3	mouse	CTGTAACATGGAAACTGGGGAAA	CCATAGCTGAACTGAAAACCACC
Col1a4	mouse	CCTGGCACAAAAGGGACGA	ACGTGGCCGAGAATTTCACC
Timp1	mouse	CGAGACCACCTTATACCAGCG	ATGACTGGGGTGTAGGCGTA
MMP2	mouse	TGTCTTGCGTCTGACACTGC	CTCCTTTGGGCTAGGTATCTCT
MMP9	mouse	GCAGAGGCATACTTGTACCG	TGATGTTATGATGGTCCCACTTG
TGF-β	mouse	CCACCTGCAAGACCATCGAC	CTGGCGAGCCTTAGTTTGGAC
IL-6	mouse	CTGCAAGAGACTTCCATCCAG	AGTGGTATAGACAGGTCTGTTGG
IL-1b	mouse	GAAATGCCACCTTTTGACAGTG	TGGATGCTCTCATCAGGACAG
IL-18	mouse	GTGAACCCCAGACCAGACTG	CCTGGAACACGTTTCTGAAAGA
IL-10	mouse	CTTACTGACTGGCATGAGGATCA	GCAGCTCTAGGAGCATGTGG
IL-12a	mouse	CAATCACGCTACCTCCTCTTTT	CAGCAGTGCAGGAATAATGTTTC
IL-12b	mouse	GTCCTCAGAAGCTAACCATCTCC	CCAGAGCCTATGACTCCATGTC
TNF	mouse	CAGGCGGTGCCTATGTCTC	CGATCACCCCGAAGTTCAGTAG
MCP1	mouse	TAAAAACCTGGATCGGAACCAAA	GCATTAGCTTCAGATTTACGGGT
CD68	mouse	TGTCTGATCTTGCTAGGACCG	GAGAGTAACGGCCTTTTTGTGA
CD206	mouse	CTCTGTTCAGCTATTGGACGC	TGGCACTCCCAAACATAATTTGA
SOD1	mouse	AACCAGTTGTGTTGTCAGGAC	CCACCATGTTTCTTAGAGTGAGG
SOD2	mouse	CAGACCTGCCTTACGACTATGG	CTCGGTGGCGTTGAGATTGTT

NOX1	mouse	CCTGATTCCTGTGTGTCGAAA	TTGGCTTCTTCTGTAGCGTTC
NOX2	mouse	AGTGCGTGTTGCTCGACAA	GCGGTGTGCAGTGCTATCAT

3.5 Discussion

The present study shows that ALY688 significantly attenuates MI-induced cardiac dysfunction, ventricular remodelling, and fibrosis in both SC and HFD-fed mice, without worsening MI pathology by HFD. Circulating EVs are markedly downregulated in both lean and obese experimental MI models. Conversely, administration of ALY688 markedly increased EV production, suggesting that EVs are an ALY688-modulated protective factor in MI. Interestingly, EVs proteome was changes upon MI injury and ALY688 intervention was more significant under HFD condition compared SC. These findings indicate that ALY688-shaped EVs are a robust therapeutic approach with maintained efficacy across metabolic backgrounds, supporting their translational potential for diverse populations with varying metabolic states. Mechanistically, ALY688-shaped EVs carry active form of adiponectin and transported to injury heart in MI. In addition to adiponectin, ALY688-shaped EVs also reduce ROS accumulation, cell death, and mitochondrial bioenergetic impairment in cardiomyocytes during hypoxic challenge. Importantly, cardiac cell death, disrupted autophagy, and impaired mitochondrial function in mice with acute MI were improved by intervention with ALY688-shaped EVs. Consequently, our study broadens the understanding of EV-dependent MI protection and may provide new therapeutic options for MI treatment by restoring EVs function.

Given the established cardioprotective role of adiponectin and the emerging importance of EVs in cardiac repair, we investigated whether EVs serve as mediators of ALY688's therapeutic effects. Previous results have indicated that decreased circulating adiponectin levels are seen in several cardiovascular disorders, including atherosclerosis, diabetic cardiomyopathy, myocardial infarction, suggesting that restoring adiponectin levels is a potential strategy for protecting against cardiovascular disorders (370-372). Various studies in mice has showed that MI injury was further exacerbated in adiponectin KO mice (353) (201). ALY688, an adiponectin receptor agonist, has demonstrated adiponectin-mimetic effects, including insulin sensitization, anti-inflammatory activity, and autophagy activation, with protective effects shown in pressure overload mouse models (272). In this study, our study showed that ALY688 significantly reduced MI induced cardiac dysfunction, infraction and fibrosis. Adiponectin receptors are predominately expressed in adipose, liver and skeletal muscle (373, 374), adiponectin levels were significantly elevated in the infarcted heart following ALY688 administration. This suggests that tissues with abundant adiponectin receptor expression, such as adipose tissue, may serve as primary sites for adiponectin

production in response to MI and ALY688 injection, and that ALY688 exerts its beneficial effects against MI via the fine-tuning of multiorgan crosstalk. Supporting this notion, we sought to determine whether EVs mediate the transport of adiponectin to the heart.

Emerging studies has showed that demonstrate dual pathophysiological roles in myocardial infarction, functioning as both pathogenic mediators and reparative messengers through complex intercellular communication networks (363). Among all the sources, adipose-derived EVs exhibit contrasting roles in myocardial infarction depending on their tissue source and metabolic state, functioning as either protective or detrimental mediators of cardiac outcomes. Therapeutic adipose-derived stem cell (ADSC) extracellular vesicles have been shown to reduce infarct size, improve left ventricular function, promote angiogenesis, and inhibit cardiomyocyte apoptosis by delivering beneficial microRNAs such as miR-205, miR-31, and miR-221/222 that enhance endothelial cell proliferation, suppress pro-apoptotic pathways, and stimulate neovascularization in the injured myocardium (293, 375, 376). Brown adipose tissue-derived extracellular vesicles provide exercise-mediated cardioprotection by delivering cardioprotective microRNAs (miR-125b-5p, miR-128-3p, miR-30d-5p) that suppress the pro-apoptotic MAPK pathway, reduce ischemia-reperfusion injury, and enhance cardiac survival mechanisms through targeted inhibition of apoptotic signaling cascades (222, 377). Adiponectin has been proved stimulating EVs production from healthy adipose-derived stem cells and mesenchymal stem cells, that significantly amplifies the cardioprotective effects of cell-based therapies in heart failure models (257, 258, 378). Mechanistically, adiponectin-enhanced EVs deliver protective cargo—including anti-apoptotic factors, anti-inflammatory mediators, and pro-angiogenic molecules—while also reducing harmful cellular ceramides via their efflux in EVs, thereby providing protection through AMPK-dependent anti-apoptotic pathways and COX-2-dependent anti-inflammatory mechanisms (258). Here, we found that MI significantly impaired the EVs production but reversed upon ALY688 intervention. We next showed that ALY688 injection not only improved the production of circulating EVs in mice but importantly, the increased EVs also contained higher abundant active form of adiponectin. Beyond adiponectin, proteomic analysis of ALY688-derived EVs in the MI context revealed enrichment in fructose metabolism, cholesterol metabolism, and metabolic pathways. The enrichment of fructose metabolism pathways in ALY688-derived EVs is particularly important, as fructose can serve as an alternative energy substrate that bypasses rate-

limiting glycolytic steps, providing crucial metabolic flexibility during ischemic conditions, when traditional energy pathways are compromised (379, 380).

Autophagy is an intracellular process responsible for the turnover of cellular constituents (381). The critical role of autophagy in MI has been established, showing that activation of autophagy reduces infarct size (382, 383). In our work, we demonstrated that acute MI impaired heart autophagic flux, while administration of ALY688-EVs partially relieved this disruption. Similar findings were observed in hypoxic cardiomyocytes *in vitro*. ATG3 plays a central role in autophagosome formation (384). Notably, proteomics analysis revealed that hypoxic cardiomyocytes treated with ALY688-shaped EVs had higher ATG3 levels compared to those treated with PBS-shaped EVs. A central contributor in the pathophysiology of myocardial ischemic injury is oxidative stress, which damages myocardial cellular structures and dysregulates coronary microvascular function (385). This mitochondrial ROS production elicits acute damage, as well as initiates subsequent pathology that develops over time. Oxidative damage to mitochondria can result in decreased ATP production, activation of the mitochondrial permeability transition pore, and release of mtDNA that triggers a sterile inflammatory response (385). While the detailed mechanisms by which autophagy induction protects against MI injury remain unclear, it is generally accepted that mitochondrial dysfunction and ROS production are central drivers of cardiomyocyte death in this context (386). Here, we present evidence that induction of cardiomyocyte autophagy by ALY688-shaped EVs in MI heart and hypoxia cardiomyocytes leads to a decrease in oxidative stress, and inflammation. This, in turn, may result in a decrease in cell death, thus limiting the infarct size.

Mitochondria are considered the powerhouses of eukaryotic cells, generating the majority of ATP required to sustain biological activities (387, 388). In the heart, the most energy-demanding organ, constant ATP production through mitochondrial oxidative phosphorylation (OXPHOS) is essential to maintain its function (389). Mitochondrial dysfunction, characterized by impaired bioenergetics, is widely recognized as a central pathological event in cardiac disorders such as MI (390). Our results indicate that ALY688-shaped EVs ameliorated hypoxia-induced impairment of mitochondrial bioenergetics in cardiomyocytes. Because mitochondrial energy generation depends on OXPHOS and the activity of electron transport chain (ETC) complexes (I–V), we further examined these components (391). Proteomic analysis showed that most ETC complexes were up-regulated in ALY688-shaped EVs cardiomyocytes under hypoxia condition, compared to PBS-

EVs. Mitochondrial respiratory capacity was measured, and the hypoxia-induced impairment was restored by ALY688-shaped EVs. Furthermore, mitochondrial bioenergetics-related morphological changes characterized by fusion and fission were also verified in this study by mitochondrial networking and sphericity analysis. Additionally, we observed that ALY688-shaped EVs influences mitochondrial function through its effect on fusion and fission dynamics in MI heart. These opposing processes are regulated by distinct mediators (Opa1, Mfn1, Mfn2, and p-DRP1 S637 for fusion; and p-DRP1 S616 for fission (392). Excessive fission and impaired fusion disrupt cardiac metabolism and jeopardize cardiomyocyte survival, thereby worsening disease outcomes (393, 394). ALY688-shaped EVs effectively restored mitochondrial dynamics by reversing MI-induced changes in fusion-fission balance. Specifically, ALY688-EV treatment upregulated mitochondrial fusion markers (Opa1, Mfn1, Mfn2) and downregulated fission markers (p-DRP1 S616), thereby promoting healthy mitochondrial networking necessary for cardiomyocyte survival

In conclusion, this study establishes ALY688 as a promising therapeutic intervention for myocardial infarction through its unique ability to modulate extracellular vesicle production and cargo composition. The demonstrated cardioprotective effects of ALY688 across both lean and obese metabolic states highlight the robustness and translational potential of this therapeutic approach for diverse patient populations. The mechanistic insights revealing that ALY688-shaped EVs deliver active adiponectin while simultaneously addressing multiple pathological processes, including oxidative stress reduction, autophagy restoration, and mitochondrial bioenergetic recovery, together underscoring the multifaceted protective effects of this intervention. Importantly, the restoration of mitochondrial fusion-fission dynamics and the enhancement of electron transport chain function demonstrate that ALY688-shaped EVs target fundamental cellular mechanisms essential for cardiomyocyte survival during ischemic injury. These findings not only advance our understanding of extracellular vesicle-mediated cardioprotection but also provide compelling evidence for the clinical development of ALY688 as a novel therapeutic strategy that harnesses the endogenous repair mechanisms to improve outcomes following myocardial infarction, particularly in the context of metabolic comorbidities that are increasingly prevalent in cardiovascular disease patients.

3.6 Statement of contribution

Animal experiments were performed by Jialing Tang and Megan Fortier at the Heart Institute, University of Ottawa. Echocardiographic image acquisition and analysis were conducted by Jialing Tang. Histological section preparation and staining were carried out by the Histology Facility at Sunnybrook Research Institute. Image acquisition, image analysis, biochemical experiments, immunofluorescence, and TUNEL staining were performed by Jialing Tang. Proteomics analysis was conducted by Jialing Tang and Khang Nguyen. Nanoparticle tracking analysis (NTA) was performed by Hye Kyoung Sung and Yubin Lei. Extracellular vesicle (EV) isolation was carried out by Khang Nguyen. Cryo-electron microscopy of EVs (cryo-EM) was performed by the Microscopy Imaging Lab at University of Toronto. Genetic modification of H9c2 cells was performed by the Genome Editing and Molecular Biology Facility at the University of Ottawa. H9c2 and RAW-Dual cell culture and associated experiments were conducted by Jialing Tang and Wing Yan Chung. Induced pluripotent stem cell (iPSC) culture and cardiomyocyte differentiation were carried out by Jialing Tang, Yubin Lei, Khang Nguyen, and Eddie Tam. Conditioned medium-derived EV isolation was performed by Yubin Lei, Eddie Tam, and Jialing Tang. Western blotting and microscopic imaging were conducted by Jialing Tang and Wing Yan Chung. qPCR analysis was performed by Jialing Tang. Inflammatory cytokines analysis was performed by Nadya Morrow from University of Ottawa. EV uptake assays were performed by Yubin Lei and Jialing Tang. Seahorse extracellular flux assays were conducted by Jialing Tang and Eddie Tam. Statistical analysis was performed by Jialing Tang. The original manuscript draft was written by Jialing Tang. Funding was acquired by Gary Sweeney.

4. Chapter 4: Loss of Rab8a-Dependent Tethering of Lipid Droplets to Mitochondria Contributes to Hypoxia-Reoxygenation Injury

4.1 Abstract

Tethering of lipid droplets (LDs) to mitochondria facilitates fatty acid oxidation and is a key adaptive response that helps cardiomyocytes cope with hypoxia-reoxygenation (HR) stress. However, the molecular mechanisms regulating these interactions during ischemia are not fully understood. We found that HR significantly decreased cardiomyocyte expression and phosphorylation of Rab8a, a small GTPase that interacts with the LD-associated protein perilipin 5 to mediate LD-mitochondria tethering. Using long-chain fatty acid (LCFA) tracking assays we confirmed that loss of Rab8a disrupted physical contact between these organelles to impair the transfer of LCFAs from LDs to mitochondria. Furthermore, HR led to the accumulation of intracellular lipids via a combination of both lipolysis and lipophagy, resulting in metabolic stress. To counteract this defect, we evaluated the therapeutic potential of ALY688, a peptide agonist of adiponectin receptors known to stimulate the AMPK-Rab8a signaling axis. Our data indicated that treatment with ALY688 preserved Rab8a expression during HR, thereby maintaining LD-mitochondria interactions and improving metabolic function. These findings uncover a novel Rab8a-dependent mechanism regulating lipid metabolism under ischemic/hypoxic stress and highlight the potential of adiponectin mimetics like ALY688 to mitigate metabolic dysfunction in ischemic heart disease.

4.2 Introduction

The heart has a substantial energy demand, requiring the production of large amounts of ATP to support its contractile function (134). ATP is primarily generated through mitochondrial oxidation of various substrates, including fatty acids, glucose, lactate, ketones, and amino acids (395). A healthy heart is metabolically flexible, capable of switching between fatty acids and other energy sources like glucose, depending on factors such as workload, neurohormonal signals, and fuel availability. In contrast, heart failure is associated with significant alterations in cardiac energy metabolism, resulting in a metabolically compromised heart, reduced cardiac efficiency, and progressive contractile dysfunction (115, 396, 397). Changes in cardiac metabolism during ischemia reperfusion (I/R) injury are well documented, which include fatty acid oxidation (398) and uncoupling of glycolysis from glucose oxidation (399). Adult mammalian cardiomyocytes have high energy demands. Under fasting conditions, they obtain about 70% of their energy from the oxidation of long-chain fatty acids (LCFA) (400).

Lipid droplets (LDs) are intracellular organelles that mainly store triacylglycerol (TAG) and sterol esters as energy reserves. During starvation, cells shift from glycolysis to fatty acid oxidation. This occurs by breaking down LDs and transporting free fatty acids (FFAs) to mitochondria for β-oxidation. The breakdown happens via enzymatic hydrolysis by neutral lipases (classical lipolysis) or through a selective form of autophagy called lipophagy (401). Both processes are tightly regulated by members of the perilipin (PLIN) family of LDs proteins (135). In addition to serving as a nutrient source, excessive cytoplasmic FFAs can be harmful by generating reactive oxygen species (ROS), which can damage mitochondria and other cellular components (402). Lipophagy may provide a cytoprotective role by breaking down lipids to sustain energy supply, which helps prevent necrosis, apoptosis, and ATP depletion facilitated by mitochondrial dysfunction. It also promotes the metabolism of potentially lipotoxic molecules (402). Disrupted lipid metabolism, especially imbalanced lipolysis and lipophagy, is a key factor in the development of many heart diseases. The heart mainly uses fatty acids to produce energy. When the balance between lipid uptake and oxidation is disrupted, lipids accumulate excessively. This buildup contributed to cardiac lipotoxicity and eventually leads to myocardial dysfunction (403). In healthy hearts, lipolysis and lipophagy function synergistically to regulate LD catabolism, where lipolysis breaks down large LDs into smaller ones that can be effectively degraded through lipophagy (400, 404). However, conditions such as obesity, diabetes, and heart failure disrupt these processes. This

disruption creates a harmful feedback loop. Lipolysis becomes dysregulated, and lipophagy is impaired. As a result, LDs accumulate excessively, and inflammation persists (403, 405). This metabolic imbalance leads to the buildup of toxic lipid intermediates, especially ceramides and diacylglycerol. Unlike neutral triacylglycerols, these molecules damage cells. They contribute to cardiac steatosis, impair mitochondrial function, and drive the progression of heart failure (406).

Cardiomyocyte LD turnover is tightly controlled by membrane contact sites (MCSs). These structures coordinate lipid trafficking between LDs, mitochondria, lysosomes, and the endoplasmic reticulum (ER). This coordination maintains metabolic balance and prevents lipotoxicity. Mitochondria–LD tethering is mediated by proteins such as perilipin 5 (PLIN5) and the Mfn2/Hsc70 complex. This tethering enables direct fatty acid transfer from LDs to mitochondria for β-oxidation. The process is essential for cardiac energy production. PLIN5 deficiency has been shown to impair this mechanism (407-410). Rab8a (Ras-related protein 8A), a small GTPase, further stabilizes ER-LD-mitochondria tripartite junctions, supporting phospholipid exchange, LDs expansion and mitochondrial membrane integrity (411-414). In parallel, lysosome-LD contacts, regulated by Annexin A4 and Rab7, mediate lipophagic degradation, while Rab8a also modulates lysosomal positioning to facilitate lipid hydrolysis (415) (416). In heart failure, disruption of these contact sites broadly impairs cardiac lipid metabolism. LD-mitochondria proximity is reduced, and fatty acid oxidation declines. While Rab8a deficiency worsens phospholipid imbalance and lipotoxicity by disrupting ER-LD-mitochondria junctions and altering lysosomal positioning (417, 418), This underscores the central role of organelle tethering networks in maintaining cardiac lipid homeostasis and driving the development of metabolic cardiomyopathies.

Adiponectin, an adipokine secreted predominantly by adipose tissue, exerts pleiotropic cardioprotective effects in cardiometabolic diseases. These effects occur through activation of its receptors, AdipoR1 and AdipoR2, and downstream signaling pathways, mainly the AMPK pathway (177). During ischemia reperfusion injury, adiponectin attenuates myocardial damage by suppressing oxidative stress through upregulation of antioxidant enzymes, inhibiting inflammatory cytokine production, and reducing cardiomyocyte apoptosis (181, 419). Synthetic adiponectin receptor agonists, such as the small molecule AdipoRon and the peptide mimetic ALY688, mimic these protective effects in preclinical models. Studies show they improve left ventricular function, reduce infarct size, and lessen pathological remodeling after myocardial infarction (272, 420). At

the subcellular level, adiponectin regulates LDs dynamics through AMPK activation, facilitating lipid mobilization during metabolic stress (421). In cardiomyocytes, adiponectin improves mitochondrial function. It promotes assembly of electron transport chain complexes, optimizes membrane potential, and increases ATP production. These actions protect the heart from lipotoxicity and energy loss during hypoxic stress (422). Recent evidence reveals a mechanistic link between adiponectin signaling and LD-mitochondria coupling via the AMPK-Rab8a axis. Adiponectin activates AMPK, which increases GTP-bound active Rab8a. Active Rab8a binds to PLIN5, promoting LD-mitochondria interactions which facilitating fatty acid transfer for mitochondrial oxidation (411). This mechanism is supported by studies showing that metformin, which activates AMPK similarly to adiponectin, modulates Rab8a expression in regulating LDs dynamics, and inhibition of AMPK signaling attenuates Rab8a expression (423). Together, these findings suggest that adiponectin serves as a critical regulator of cardiometabolic homeostasis by coordinating LD-mitochondria interactions through AMPK-dependent mechanisms.

Although the cardiac protective functions of adiponectin are widely characterized, little is known about adiponectin's roles in I/R, and the subcellular mechanism whereby it protects against I/R. Here, we used ALY688 as an adiponectin mimetic to elucidate these mechanisms We demonstrate that during H/R in cardiomyocytes, LDs content decreased, primarily via lipophagy-mediated lipolysis, producing excessive amounts of FFAs. Rab8a activity was decreased by H/R, resulting in reduced β-oxidation of produced FFAs and lipotoxicity. Our results reveal that upregulation of Rab8a expression by the adiponectin receptor agonist ALY688 during H/R protects against lipotoxicity contributed by the uncoupling of LDs breakdown from fatty acid utilization.

4.3 Materials and Methods

Cell Culture and cell line generation

H9c2 rat embryonic cardiac myoblasts (ATCC® CRL-1446™) were cultured in Dulbecco's Modified Eagle's Medium (Gibco, 11885-084) with 10% fetal bovine serum (Thermo, 11885084) and 1% streptomycin/penicillin (vol/vol, Gibco, 15070063) at 37°C under 5% CO2. Hypoxia was induced by placing cells in a hypoxic chamber (Onstage Incubator, Thermo Fisher, NX7LIVE001) containing a pre-mixed gas of 1% O_2 and 5% CO2. Normoxia and reoxygenation were achieved by incubating cells in the same chamber with 20% O_2 and 5% CO_2.

CRISPR knock-out cell lines were created using guide RNAs cloned into the pX459 plasmid, as previously described (282). 9c2 cells were transfected with vectors carrying guides targeting atg7 using Lipofectamine 3000. Transduced cells were selected with 1 μg/ml puromycin for 5 days and then expanded in media without selection. T7 endonuclease assays were performed using T7 endonuclease I on PCR products generated with the primers 5'-GCTGCTGCAGGTAGGTGTAA and 5'-GGTGTCCTGTCTGAGACTGC, following the manufacturer's instructions.

To generate Rab8a KO H9c2 cells, guide RNA targeting Rab8a gene (TGATTGTCCGAAACCGCTCC) are cloned in pLentiCRISPRv2. We then generated viral particles using this vector as well as a control vector that does not target mammalian genomes and used these particles to transduce H9c2 cells. Following selection with puromycin (1 μg/mL), polyclonal populations were assessed for guide efficiency using a T7 endonuclease I assay as reported before(282).

Lentiviruses for stable expression of Rosella-Plin2 (rat) or Rosella-Plin5 (rat) were produced at the University of Ottawa Genomic Editing and Molecular Biology (GEMb) core facility. H9c2 cells were transduced with these lentiviruses in the presence of 8 μg/mL polybrene (Sigma, H9268). Transduced cells were then selected by fluorescence-activated cell sorting using a BD FACS Aria IIIu (Beckton Dickinson).

Western blot

Cells were lysed in RIPA buffer containing protease and phosphatase inhibitors. Protein concentration was measured and normalized using a BCA assay (Thermo, A55864). Proteins were separated by reducing SDS-PAGE, transferred to PVDF membranes, and incubated with primary

antibodies overnight at 4°C. Secondary antibodies were applied for 1 hour at room temperature. Signal quantification was performed by densitometry of scanned autoradiographs using ImageJ (version 1.4v)

Immunoprecipitation

Lysates were prepared from H9c2 cells in ice-cold lysis buffer containing 20 mM Tris HCl pH 8, 137 mM NaCl, 10 % glycerol, 1 % NP-40, 2 mM EDTA, Complete Protease Inhibitor Cocktail. Cell lysates were then immunoprecipitated with Rab8a antibody conjugated with protein A/G agarose beads (ThermoFisher, 20421) and then resolved on 12 % SDS gel before being probed with indicated antibodies. IgG was used as isotype control (Proteintech, 98136-1-RR).

Inhibitors, chemicals and antibodies

The following chemicals, dyes and antibodies were used: 100 nM Rapamycin (Sigma, R8781), 50 μM Chloroquine (Sigma, C6628), 50 μM Bafilomycin (Sigma, 196000), 100 μM Paraoxon (Sigma, 36186), 10 μM Lalistat 1 (Med Chem Express, HY-116815), 60 μM Etomoxir (Sigma, 236020),1 μM MDIVI-1 (Med Chem Express, HY-15886), 20 μM Compound C (Sigma, 171260), and 100 nM ALY688 (Allysta Pharmaceutical). 1 mM BODIPY 558/568 C12 (Thermo, D3835), 10 mM BODIPY™ 493/503 (Thermo, D3922), 100 nM MitoTracker Red (Thermo, M22425), 100 nM MitoTracker Green (Thermo, M7514), 300 nM Hoechst (Thermo H10325). GAPDH (Thermo Fisher, MA5-15738), β-Tubulin (Cell Signaling, 2128), Rab8a (BD Science, 610844), perilipin 2 (Proteintech, 60340), perilipin 5 (Proteintech, 26951), LC3 (Cell Signaling, 2775), p62 (Cell Signaling, 5114), HIF1α (Cell Signaling, 79233), CPT1α (Proteintech, 15184-1-AP), Tom20 (Proteintech, 66777), VDAC (Cell Signaling, 4661), P-DRP1 Ser616 (Cell Signaling, 3455), P-DRP1 Ser637 (Cell Signaling, 4867), Parkin (Proteintech, 66674), MFF (Cell Signaling, 84580), Mitofusin 2 (Cell Signaling, 9482), anti-rabbit (Cell Signaling, 7074), and anti-mouse (Cell Signaling, 7076).

Immunofluorescence

Cells were washed three times with 1X PBS and fixed with 4% paraformaldehyde (Sigma, HT501128) for 10 minutes at room temperature. Cells were then blocked and permeabilized for 30 minutes in 5% BSA with 0.01% Triton X-100. Primary antibodies were applied overnight at 4°C in wash buffer containing 1% BSA and 0.025% saponin. Alexa Fluor or Alexa Fluor Plus-

conjugated secondary antibodies were incubated for 1 hour at 37°C in the same wash buffer. Cells were counterstained with DAPI for 5 minutes at room temperature. Slides were imaged using a Nikon Eclipse Ti2 microscope for visualization and continuous measurements.

Mitochondrial network visualization and analysis

After treatment, cells were washed three times, then incubated with 100 n M Mitotracker green (M7514, ThermoFisher Scientific) and nuclear stain (H10325, Thermo FisherScientific) for 30 min in serum-free DMEM at 37 °C protected from light. Following three more washes, cells were imaged using a Nikon A1 confocal microscope with an incubator (37 °C, 5% CO_2). Mitochondrial branch length and networking were quantified as described in the literature to assess fission in 2D (424). For 3D images, z-stacks were captured with a step size of 0.2 μm and rendered using surfaces tool on IMARIS (Oxford Instruments, Abingdon, London) along with sphericity (value approaches 1 as an object approaches the shape of a perfect sphere).

Cell-stained images analysis

Following staining with specific probes, images were acquired using confocal microscopy. All biological replicates were performed with a minimum of three technical replicates. For each technical replicate, at least five randomly selected fields of view were imaged, and a minimum of 50 cells were quantified.

Quantitative real-time PCR

Total RNA was extracted using the PureLink™ RNA Mini Kit (Thermo, 12183018A), and first-strand cDNA was synthesized with the cDNA Synthesis Kit (Thermo, K1691) following the manufacturer's instructions. qPCR was performed using SYBR Green Supermix (Bio-Rad, 1725274). Primers are listed in Table 1. Data were normalized to 18S RNA, and fold changes were calculated using the $2^{-\Delta\Delta Ct}$ method. Relative mRNA levels are expressed in arbitrary units, with the untreated group set to 1.

Mitochondrial isolation

Muscle samples were homogenized with a glass-Teflon Dounce Homogenizer in extraction buffer (70 mM sucrose, 1 mM EGTA, 10 mM mannitol, 5 mM HEPES, 10 mM $MgCl_2$, protease and phosphatase inhibitor cocktail). The homogenates were centrifuged twice at 1,000 g for 10 min to remove the tissue debris and nucleus. The post nuclear supernatants were then transferred into 1.5

mL Eppendorf tubes and adjusted to equal concentrations. Equal amounts of PNS were centrifuged at 10,000 g for 10 min to precipitate mitochondria. The pellets were washed in extraction buffer two times with centrifugation at 10,000 g for 10 min in between. The mitochondrial fractions were dissolved in SDS sample buffer for immunoblotting analysis.

Biochemistry analysis

Commercially available kits were used to measure LDH (Abcam, ab102526), free fatty acid (Abcam, ab65341), ATP (Abcam, GA5010), according to manufacturer's instructions.

Seahorse flux assay

Oxygen consumption rates (OCRs) were determined by a Seahorse XFe24 extracellular flux analyzer (Agilent) as previously described (286). Briefly, WT H9c2 cells, RKO and AKO were seeded in each well of a pre-coated XFe24 cell culture plate (Agilent, 103015) and treated with Lalistat1, Paraoxon, ATGL, Rapamycin, Bafilomycin, and ALY688 prior HR. After HR, cells were washed with XF media twice and incubated in a CO_2-free incubator at 37°C for 1 hour. The following reagents were used: Oligomycin (1 μM, Sigma, 75351), FCCP (carbonyl cyanide p-trifluoromethoxy phenylhydrazone, 3 μM, Sigma, C2920), and Antimycin A (1 μM, Sigma, A8674) plus Rotenone (1 μM, Sigma, R8875).

Lipidomics analysis

The lipids from H9c2 cells and whole heart tissues were extracted in (1:10 w:v mg:uL) extraction solvent Butanol:MeOH (1:1) containing 1 ug/mL Equisplash internal standard mix. The samples were homogenized, sonicated, and centrifuged 13000 x g for 10 minutes at room temperature (23°C). ~100μL of each sample supernatants were used for the LC-MS analysis. Leftover samples were transferred to -20°C storage. Pooled samples for each group were made by combining 5μL of each sample (Total). LC-MRM-MS analyses were performed using Agilent 1290 LC with 16 minutes gradient (A): 0.1% formate in 5:3:2 water: acetonitrile: 2-propanol. (B): 0.1% formate in 1:9:90 water: acetonitrile: 2-propanol at 400 μL/min flow rate on Zorbax eclipse plus C18 RRHD 100x2.1 mm 1.8u (RP-LC-MS). 1μL injection volumes were used for each run. MRMs were acquired using Agilent 6495A spectrometer in positive and negative modes in 2 separate runs. 519 and 768 lipid species were detected in H9c2 cells and heart tissues, respectively. Data for each

LC/acquisition type were analyzed using MassHunter (Agilent). Statistical analysis was performed using MetaboAnalyst.

Proteomic analysis

Isolated EVs were lysed in 5% SDS (Fisher Chemical), 200 mM TRIS (Fisher BioReagnets) pH 8.5 with 10 mM TCEP (60C x 25 minutes). Free disulfides were alkylated with 40 mM IAA (RT, dark, 30 minutes) prior to proteolytic digestion by S-TRAP micro (see attached for the SOP from the vendor that we use). Peptide containing eluates were lyophilized and rehydrated at 10 ng/uL prior to loading on EvoTips and analysis by library free DIA using an Evosep One system coupled to a Bruker timsTOF HT MS operated in DIA-PASEF mode. Samples were separated on an EV1137 column at 30SPD. For recipient cell proteomics, wild-type L6 cells were seeded on 6-well plate until reaching 80-90% confluency. Confluent cells were treated with EVs isolated from mice plasma, at the concentration of 10 µg/ mL. After 24 h of EVs treatment, cells were trypsinized and centrifuged for 5 minutes at 2000 rpm. Cell pellets were collected and lysed in NP40 lysis buffer for 30 min on ice. Cell lysate was then subjected to in-solution digestion following protocol by Promega (V5280). Gene ontology (GO) enrichment analysis was performed following the guidelines from the protocol using cytoscape software (version 3.10.2).39 KEGG pathway enrichment analysis was performed using the ClueGO plugin (version 2.5.10) in Cytoscape software. ClueGO was used to identify significantly enriched KEGG pathways, applying two-sided hypergeometric test for pathway analysis. The p-values were adjusted for multiple testing using either the Bonferroni or Benjamini-Hochberg correction, with an adjusted p-value threshold of 0.05.

Statistical analysis

Data was presented as mean ± SEM. Statistical analysis was performed using GraphPad Prism 9. Student's t-test was used for comparison of two groups and one-way ANOVA or two-way ANOVA were used for comparison of more than two groups. $P<0.05$ was considered statistically significant.

Primer sequences

See supplementary Table 1

4.4 Results

Hypoxia-reoxygenation altered the lipidome of H9c2 cells and decreased LD content

Hypoxia incubation was first validated by the activation of HIF1α (Figure 4.1 A-B). To better understand lipid composition changes induced by hypoxia/reoxygenation (H/R) in rat cardiomyocyte H9c2 cells, we performed a comprehensive lipidomic analysis. Principal component analysis (PCA) and hierarchical clustering heatmaps revealed distinct lipid species profiles between normoxia and H/R conditions in H9c2 cells (Figure 4.2 A and B). Further analysis identified diacylglycerol (DAG) as one of the most significantly increased glycolipid classes in H/R cells (Figure 4.2 C). Additionally, ceramide (Cer) Cer (d18:1/16:0) was significantly elevated under H/R conditions compared with normoxia and is often considered a primary mediator of insulin resistance and lipotoxicity. Cer (d18:1/18:0) and Cer (d18:1/24:1), which have been positively associated with cardiovascular mortality in clinical studies, were also significantly upregulated in response to H/R stress (Figure 4.1 C-E). Lipidomic pathway analysis using BioPan (36) demonstrated marked activation of enzymatic reactions involved in the hydrolysis of TAG into DAG (Figure 4.2 D). To further explore lipid pathways enriched under H/R conditions, we utilized the KEGG database, which identified autophagy, a crucial process for cellular adaptation to metabolic stress and clearance of damaged components, as being upregulated under H/R (Figure 4.2 E). Given the role of LDs as primary storage sites for TAG, we hypothesized that LD dynamics might be altered under H/R. To test this, we measured LD content in both normoxia and H/R conditions. H/R significantly reduced LD content, as indicated by decreased mean fluorescence intensity (MFI; Figure 3.1 F and G), reduced LD number (Supplemental Figure 1 F), though no change in LD size (Figure 4.1 G). Since DAG can be converted to TAG by diacylglycerol acyltransferases (DGATs) and stored in LDs, and LDs are coated by perilipin (PLIN) family proteins (PLIN1-PLIN5) that stabilize LDs and protect them from lipase activity, we next examined gene expression changes. During H/R, we observed significant decreases in Dgat2, Plin2, and Plin5 mRNA levels (Figure 4.2 H), while DGAT1, PLIN1, PLIN3, and PLIN4 remained unchanged (Figure 4.1 H-K). Finally, we assessed lipase gene expression and found that H/R reduced the expression of both neutral lipases, adipose triglyceride lipase (ATGL), monoacylglycerol lipase (MGL), and hormone sensitive lipase (HSL), as well as the acidic lipase lysosomal acid lipase (LAL) (Figure 3.1 H). Collectively, these results demonstrate that H/R

reduces cellular LD content in cardiomyocytes, indicating altered LDs dynamics and metabolism under these conditions.

Lipophagy contributes to LD degradation triggered by HR

In addition to the breakdown of TAG in LDs through cytosolic lipolysis, LDs can be engulfed by autophagosomes for lysosomal degradation, a process known as lipophagy (425, 426). Pathway analysis revealed autophagy activation following H/R exposure (Figure 4.1 E) prompting examination of lipophagy's role in H/R-mediated LD catabolism. We detected diminished expression of PLIN2 and PLIN5 proteins after H/R treatment (Figure 4.3 A-C), while autophagic flux simultaneously increased, as evidenced by elevated LC3-II levels and enhanced p62 degradation (Figure 3.2 A, D and E). Inhibition of lysosome acidification by chloroquine (CQ) or inhibition of autophagosome-lysosome fusion at preventing the acidification of the lysosomes by Bafilomycin (Baf) disrupted autophagic flux (Figure 4.4 A-C) and significantly mitigated the H/R-associated decline in PLIN2 and PLIN5 levels (Figure 4.3 A-E). Additionally, we observed increased colocalization of LC3 with LDs following H/R, evidenced by reduced BODIPY MFI and elevated LC3 expression, consistent with lipophagy activation (Figure 4.3 F and G, Figure 4.4 D). Blocking autophagic flux with CQ and Baf reversed these H/R-associated alterations in BODIPY and LC3 patterns (Figure 4.3 F and G, Figure 4.4 D).

To determine which PLIN proteins facilitated lipophagy during H/R stress, immunofluorescence analysis assessed spatial associations between PLIN2/LC3 and PLIN5/LC3 pairs. While both PLIN2/LC3 and PLIN5/LC3 associations intensified during H/R conditions, the PLIN5-LC3 interaction predominated (Figure 4.4 E-H). Normoxia and H/R conditions showed comparable PLIN2-PLIN5 colocalization (Figure 4.4 E and H). Autophagy suppression with Baf confirmed PLIN5's involvement in H/R-mediated lipophagy, as evidenced by increased LC3 and PLIN5 upon H/R following autophagy inhibition, although the colocalization of LC3 and PLIN5 sustained (Figure 4.4 I-L). We then employed Rosella-PLIN2 H9c2 cells and Rosella-PLIN5 H9c2 cells to assess specific autophagic targeting of PLIN2- and PLIN5-decorated LDs during H/R stress. This reporter system relies on pH-dependent fluorescence properties: both GFP and RFP emit signals at neutral pH, but GFP fluorescence is selectively quenched in the acidic environment after autophagosome-lysosome fusion (427). Tagging PLIN with this system enables precise tracking of cellular lipophagy flux as reported previously (428). During H/R, the ratio of red versus green

fluorescence was increased in Rosella-PLIN2 (Ros-PLIN2) and Rosella-PLIN5 (Ros-PLIN5), indicating that PLIN2-LDs and PLIN5-LDs are both degraded by autophagy (Figure 4.3 I-K). To examine the functional significance of the autophagy machinery in H/R-dependent LD metabolism, we generated an autophagy-deficient H9c2 cell line by deleting ATG7 (autophagy related 7) via CRISPR-Cas9 technology as previously reported (285). Unlike their wild-type counterparts, ATG7 KO cells (AKO) maintained their LD content during H/R exposure, as assessed with BODIPY staining (Figure 4.3 L and M) and the expression of PLIN2 and PLIN5 (Figure 3.2 N-P).

To delineate the relative contributions of lipophagy and lipolysis to LD breakdown during H/R, we employed specific inhibitors targeting key hydrolytic enzymes: Lalistat 1 (acidic lipase inhibitor, LALi), Paraoxon (neutral lipase inhibitor, Para), and Atglistatin (adipose triglyceride lipase inhibitor, ATGL). BODIPY staining revealed that LD degradation was effectively abolished under H/R regardless of whether lipophagy, lipolysis, or both pathways were inhibited individually or in combination, suggesting that both lipophagy and lipolysis contribute to LD catabolism during H/R injury in cardiomyocytes (Figure 4.3 Q and R). Interestingly, upon lipolysis and lipophagy inhibition during H/R, the restoration of PLIN5 reduction induced by H/R was only observed in the presence of LALi, suggesting that the H/R-induced PLIN5 degradation relied mostly on lipophagy (Figure 4.4 M and N). These findings collectively establish PLIN5-associated lipophagy as a central mechanism in H/R-induced LD catabolism.

LD-mitochondria tethering is disrupted during HR

LDs act as reservoirs of fatty acids, which are transported to mitochondria for β-oxidation and ATP production under stress conditions or nutrient limitations (429). PLIN5 is essential for LD-mitochondrial interactions and promoting fatty acid transport (409, 430-432). Building on our findings that H/R enhances PLIN5-LD lipophagy, we next investigated whether H/R affects PLIN5-mediated LD-mitochondria interactions. To assess this, we first examined the proximity of LDs and mitochondria during H/R. As expected, H/R disrupted the interaction of these two organelles, as evidenced by decreased proximity (Figure 4.5 A-B). To further characterize this disruption, we employed a LCFA (long chain fatty acid) tracking assay, as previously reported (433), to trace the fate of lipids stored in LDs under H/R. Under normoxia, a substantial portion of LFCA localized outside LDs, indicating normal mobilization (Figure 4.5 C and D). In contrast, under H/R conditions, LCFAs were predominantly co-localized with LDs (Figure 4.5 C and D),

while LCFA co-localization with mitochondria was markedly reduced (Figure 4.5 E and F), suggesting a failure of LCFA transport to mitochondria for subsequent β-oxidation. These findings were further validated using 3D IMARIS co-localization analysis (Figure 4.5 G-J).

We next examined expression patterns of genes involved in fatty acid transport. The expression of *Cd36* and *Fabp4* was increased under H/R (Figure 4.6 A and B), while the expression of mitochondrial fatty acid oxidation-related genes, including *Cpt1α, Pparα*, and *Rxrα*, was downregulated (Figure 4.6 C-D). *Fatp1*expression remained unchanged, whereas the lipophagy-related gene Rab7 expression increased under H/R (Figure 4.6 D and E). CPT1α protein expressed presented the same changes as the gene level upon H/R challenge (Figure 4.6 F-G). Additionally, extracellular free fatty acid levels were elevated upon H/R (Figure 4.6 H), collectively suggesting that H/R does not impair intracellular or extracellular fatty acid transport but specifically reduces LCFA transport to mitochondria.

Given that efficient LD-mitochondria tethering facilitates ATP production via β-oxidation, we assessed cellular bioenergetics using the Seahorse extracellular flux analysis. Seahorse extracellular flux analysis revealed that H/R drastically reduced maximal respiratory capacity in H9c2 cells compared to normoxia control (Figure 4.5 K and L). Basal respiration and ATP production were similarly diminished (Supplemental Figure 3 I), consistent with impaired fatty acid oxidation and mitochondrial dysfunction. Under normoxia, pharmacological autophagy inhibition by CQ, or genetic ablation of ATG7 (ATG7 KO) reduced maximal respiration versus WT, indicating basal autophagic activity supports mitochondrial function. However, during H/R, neither CQ nor ATG7 KO exacerbated respiratory suppression, suggesting that H/R itself or H/R-induced loss of LD-mitochondria contacts overwhelms autophagy-dependent metabolic regulation (Figure 4.6 J and K).

To investigate mitochondrial structural changes under H/R, we analyzed mitochondrial morphology. H/R decreased mitochondrial density, length, and networking (Figure 3 N-Q). IMARIS sphericity analysis, used as in index of fission, revealed increased mitochondrial fragmentation during H/R (Figure 4.5 R and S). This fragmentation was further corroborated by increased p-DRP1 (Ser 616), decreased p-DRP1 (Ser 637), and elevated MFF, and decreased MFN2 levels (Figure 4.6 4 A-F). Additionally, H/R significantly decreased *Pparα* and *Rxrα* mRNA expression in H9c2 (Figure 4.6 G and H). Concurrently, H/R stimulated mitophagy as evidenced

by increased Parkin, and LC3 expression and decreased p62 in mitochondrial fraction (Figure 4.6 I-L), together suggesting that decreased nuclear receptor activity contributes to enhanced mitochondrial degradation during H/R-induced stress in cardiomyocytes.

To examine whether H/R-induced mitochondrial fission contributed to impaired fatty acid utilization, we treated cells with the mitochondrial fission inhibitor Midivi-1. This intervention successfully alleviated fission by measuring mitochondrial morphology (Figure 4.6 M-P). Interestingly, despite preserving mitochondrial morphology induced by H/R, LCFA remained sequestered in LDs and failed to transfer to mitochondria for utilization (Figure 4.5 S and T). This observation suggests that mitochondrial fragmentation is not the primary factor responsible for disrupted LD-mitochondrial tethering and subsequent impairment of fatty acid metabolism during H/R.

Identification of Rab8a as a critical regulator of LD-mitochondria fatty acid transfer in H9c2 cells during HR

Rab small GTPases serve as key regulators of membrane dynamics, including trafficking, contact formation, and fusion (434). Among Rab family proteins, Rab8a has been identified as a mitochondrial receptor for LDs in skeletal muscle (411) and mediates LD fusion in adipocytes (413). However, its role in cardiomyocytes remains uncharacterized. Notably, we observed significant downregulation of Rab8a protein expression in H9c2 cells subjected to H/R (Figure 4.8 A and B). To investigate the functional significance of Rab8a during H/R, we generated Rab8a knockout H9c2 cells (RKO) using CRISPR-Cas9 technology. Knockout efficiency was confirmed by western blot analysis (Figure 4.9 A and B). Proteomic analysis was performed to measure the functional significance of Rab8a. Hierarchical clustering heatmaps and principal component analysis (PCA) revealed distinct proteome profiles between WT and RKO (Figure 4.9 C and D). Pathway enrichment analysis comparing RKO and WT indicated that fatty acid degradation and fatty acid metabolism were significantly dampened when Rab8a was deleted (Figure 4.8 C). We then evaluated LD-mitochondria interactions under various conditions. Under normoxic conditions, Rab8a deletion significantly increased the spatial separation between these organelles, an effect that was further amplified during H/R exposure (Figure 4.9 E and F). Next, we assessed LCFA trafficking in RKO versus WT cells under both normoxia and H/R conditions. Rab8a deficiency significantly impaired LCFA mobilization from LDs, as evidenced by an increased

overlap coefficient between LCFA and LDs under normoxia, which was further exacerbated during H/R (Figure 4.9 G and H, Figure 4.8 D and F). However, Rab8a deficiency did not further exacerbate the H/R-induced diminution of LCFA overlapping coefficient with mitochondria (Figure 4.9 G and I, Figure 4.8 and G). Intracellular and extracellular free fatty acid levels were unchanged between WT and RKO cells (Figure 4.8 H, Figure 4.9 J and K). Moreover, we validated the protein interaction of Rab8a with Tom20 and PLIN5 upon H/R by immunoprecipitation. We found that there under normoxic conditions, Tom20 and PLIn5 was both expressed in H9c2 cell lysate immunoprecipitated with Rab8a antibody conjugated with protein A/G agarose beads, however, decreased under H/R condition (Figure 4.9 L-M). Functionally, RKO cells exhibited a marked reduction in ATP production compared to WT cells during H/R (Figure 4.8 I). The mitochondrial respiratory impairment was further substantiated by Seahorse extracellular flux analyses, which revealed significantly impaired mitochondrial respiration in Rab8a-deficient cells (Figure 4.8 J and K). To determine whether Rab8a influences H/R-induced PLIN-mediated lipophagy, we expressed Rosella-PLIN2 and Rosella-PLIN5 in RKO cells. In contrast to WT cells (Figure 4.8 I-K), no significant increase in PLIN2- or PLIN5-associated lipophagy was observed upon H/R in RKO cells (Figure 4.8 L-N). Collectively, these data establish Rab8a as a critical mediator of LD-mitochondria LCFA transfer that becomes dysregulated during H/R, contributing to impaired bioenergetics and cellular stress in cardiomyocytes.

ALY688 restores LD-mitochondria communication by replenishing Rab8a activation upon HR and protects against cell death

Previous studies have demonstrated that AMPK activation enhances LD motility and promotes LD-mitochondria interactions to facilitate fatty acid oxidation (435). However, whether adiponectin, a well-established AMPK activator, regulates LD-mitochondria interaction in cardiomyocytes remains unclear. Here, we investigated this using the adiponectin receptor agonist ALY688. As reported previously 30 mins pretreatment with ALY688 activated adiponectin signaling pathway (358). In this study we pretreated ALY688 30 mins prior to H/R challenge. As showed, ALY688 significantly prevented the H/R-induced reduction of Rab8a protein expression (Figure 4.10 A and B), suggesting a potential regulatory relationship between adiponectin signaling and Rab8a-mediated organelle tethering. Besides, when AMPK inhibitor Compound C was used, the re-activation of Rab8a upon ALY688 treatment was diminished, indicated the effect derived from ALY688 was potentially dependent on AMPK pathway (Figure 4.11 A and B). To assess the

functional impact of ALY688 on fatty acid trafficking, we performed an LCFA tracking assay. Consistent with enhanced LD-mitochondria coupling, ALY688 treatment significantly stimulated LCFA mobilization from LDs to mitochondria during H/R (Figure 4.10 C and D). Additionally, the H/R induced decreased Rab8a-Tom20 and Rab8a-PLIN5 interaction was improved upon ALY688 treatment evaluated by immunoprecipitation (Figure 4.11 C). ALY688-mediated restoration of LD-mitochondria proximity significantly attenuated H/R-induced impairment of fatty acid oxidation, as evidenced by partial recovery of mitochondrial β-oxidation capacity (Figure 4.11 D and E). Importantly, this beneficial effect on LD-mitochondria proximity was completely abolished in Rab8a-deficient cells (Figure 4.10 C and D, Figure 4.11 F and G), demonstrating that Rab8a is essential for mediating adiponectin's effects on intracellular lipid trafficking. These findings were further validated using Seahorse extracellular flux analysis, which confirmed that ALY688-induced improvements in mitochondrial respiration during H/R required Rab8a expression (Figure 4.10 E and F). To further validate these findings, we used a proximity ligation assay (PLA), a sensitive *in situ* method for inferring protein-protein interactions with high specificity (436). In WT cells, H/R reduced the association of Rab8a with the mitochondrial marker Tom20, as well as PLIN5 and Tom20 (Figure 4.10 G-I). ALY688 treatment effectively restored these interactions during H/R. Notably, in Rab8a knockout cells, the ability of ALY688 to restore organelle contacts was completely abrogated (Figure 4.10 I), further confirming Rab8a's indispensable role in mediating adiponectin-induced organelle tethering. To evaluate the functional significance of ALY688-mediated Rab8a-dependent LD-mitochondria coupling during H/R, we measured the cell viability using an LDH release assay. ALY688 pretreatment significantly reduced H/R-induced cell death in WT cells (Figure 4.10 J). However, this cytoprotective effect was completely abolished in Rab8a-deficient cells (Figure 4.10 J), demonstrating that Rab8a is required for the protective effects of adiponectin receptor activation during H/R injury. Collectively, these findings establish that Rab8a-mediated interactions between LDs and mitochondria are critical for maintaining efficient fatty acid oxidation and cardiomyocyte viability during metabolic stress. Furthermore, they identify the adiponectin-Rab8a axis as a novel therapeutic target for protecting cardiomyocytes against H/R-induced metabolic dysfunction and cell death.

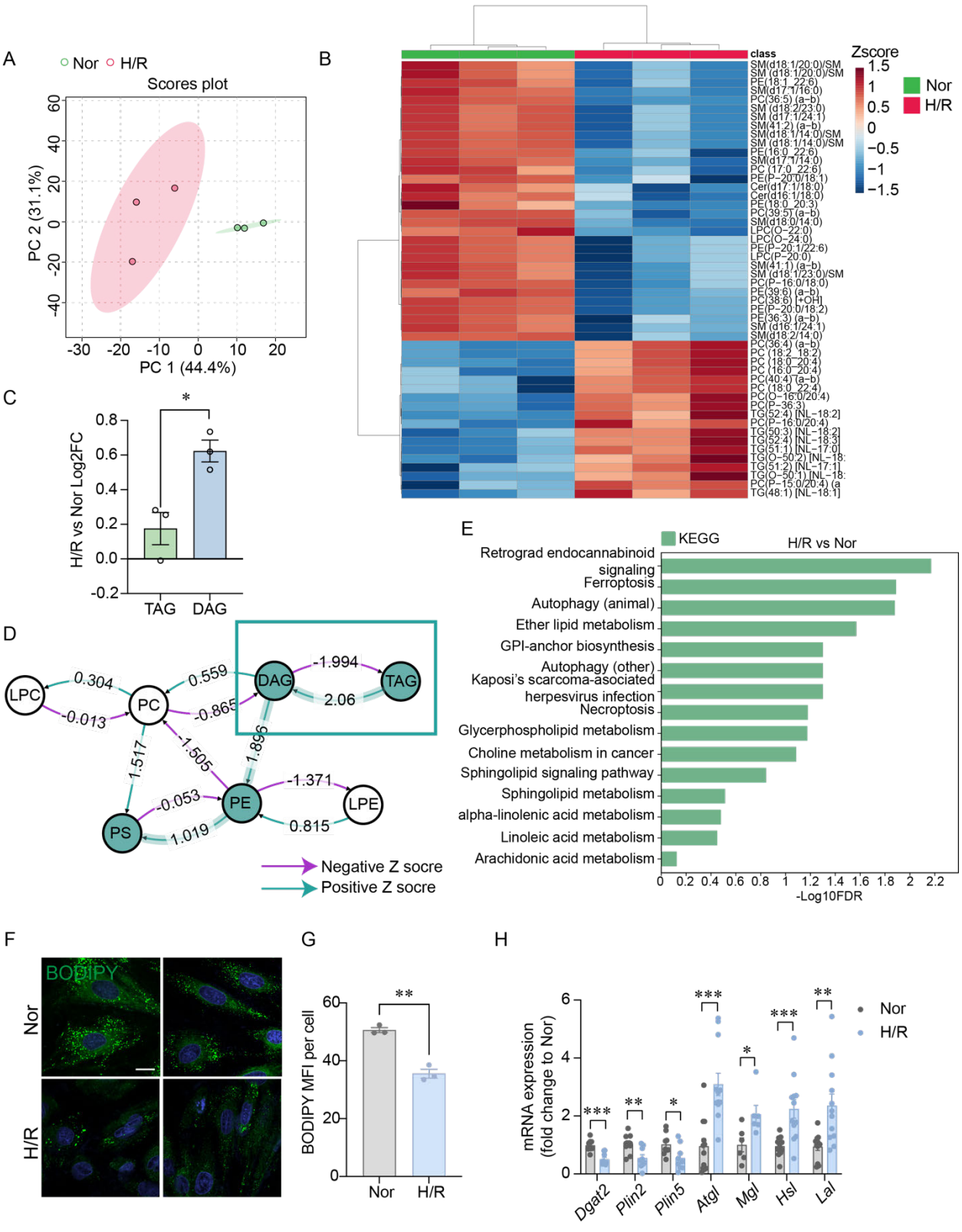

Figure 4.1 H/R reduced LD content in H9c2 cell

(A) PCA of lipidomics analysis in H9c2 cells subjected to normoxia or H/R. (B) Heat map hierarchical clustering of lipidomics analysis of H9c2 cells subjected to normoxia or H/R. (C) TAG and DAG level in H9c2 cells subjected to normoxia or H/R. (D) Lipidomic pathway analysis by BioPan. (E) KEGG pathway enrichment analysis of significant lipids revealed by lipidomics analysis. (F-G) Representative images of BODIPY staining and quantification comparing normoxia and H/R in H9c2 cells. (H) mRNA expression of DGAT2, PLIN2, PLIN5, ATGL, MGL, HSL, LAL in H9c2 cells subjected to normoxia or H/R. Scale bar: 10 μm. Results are presented as mean ± SEM (n=3-9 per group). *P<0.05, **P<0.01, ***P<0.001 versus normoxia control. T-test was run for statistical analysis.

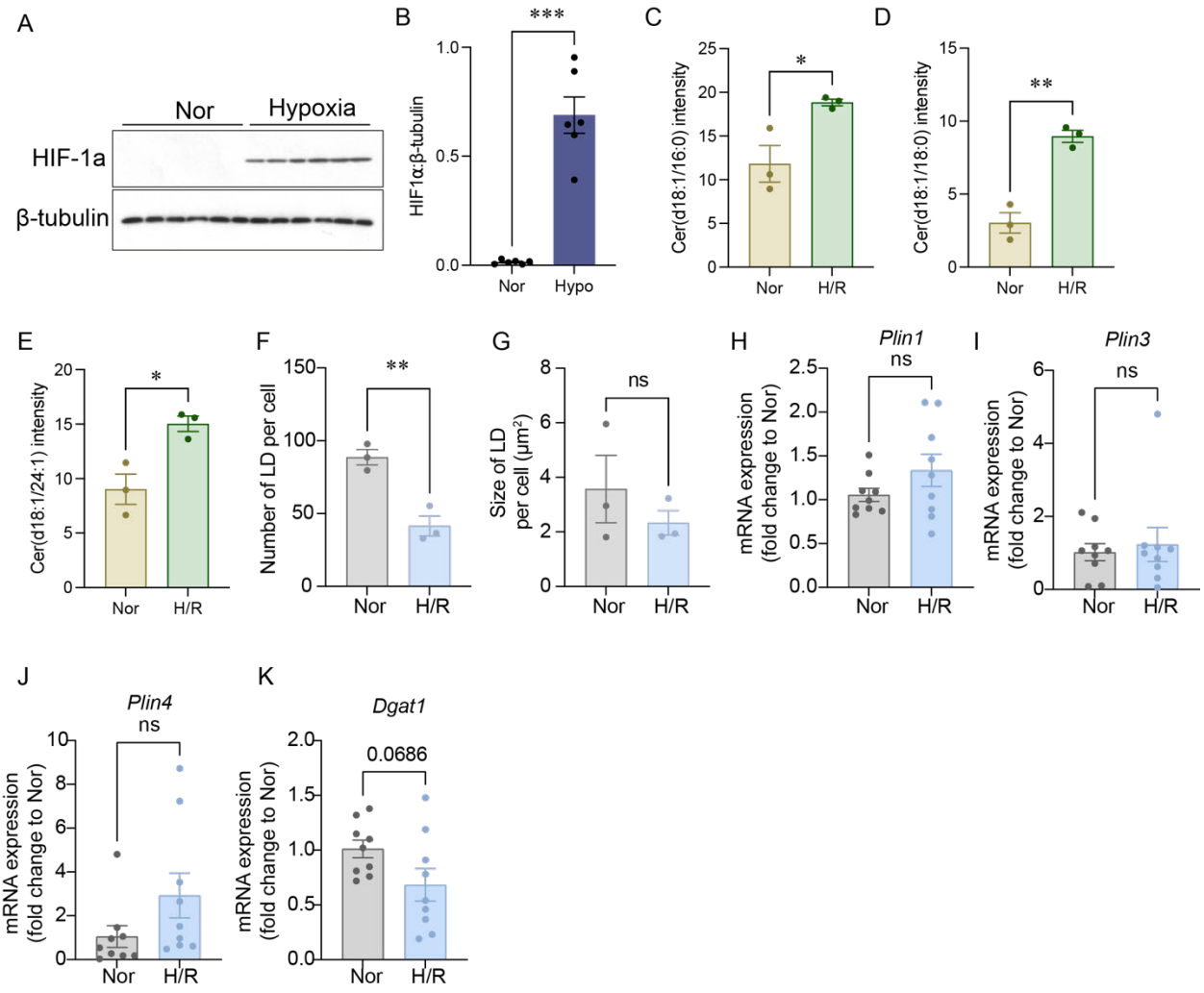

Figure 4.2 HR altered ceramide species, and remodels lipid droplet dynamics and lipid metabolism gene expression in H9c2 cells

(A) SDS-PAGE and immunoblot analysis of cell lysate of H9c2 cell subjected to nromoxia or HR using HIF1α, β-tubulin was used as a loading control. (B) Quantification of HIF1α. (C) Intensity of Cer(d18:1/16:0). (D) Intensity of Cer(d18:1/18:0). (E) Intensity of Cer(d18:1/24:1). (F) Quantification of number of LD of H9c2 cells subjected to normoxia or H/R. (G) Quantification of size of LD of H9c2 cells subjected to normoxia or H/R. (H-K) mRNA expression of PLIN1, PLIN3, PLIN4, DGAT1 in H9c2 cells subjected to normoxia or H/R. Results are presented as mean ± SEM (n=3-9 per group). *P<0.05, **P<0.01, ***P<0.001 versus normoxia control. T-test was run for statistical analysis.

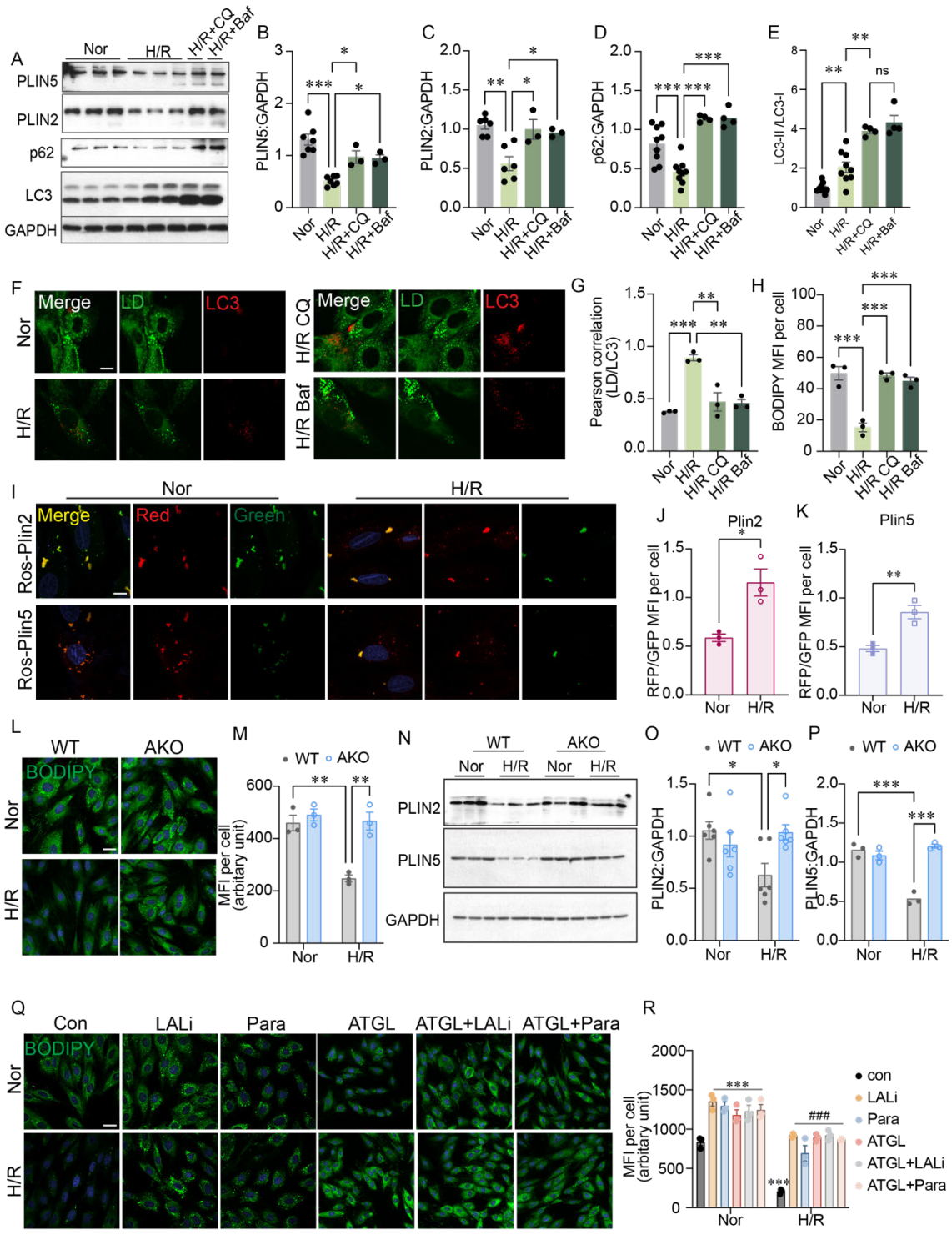

Figure 4.3 Lipophagy contributed to LD degradation during H/R in H9c2 cell

(A) SDS-PAGE and immunoblot analysis of H9c2 lysate using PLIN5, PLIN2, LC3, p62, and GAPDH was used as a loading control. H9c2 cells were treated with or without 50 μM Chloroquine, 50 μM Bafilomycin, and subjected to normoxia or H/R. (B-E) Quantification of PLIN5, PLIN2, LC3, and p62. (E) Representative image of immunofluorescence staining of LC3 and BODIPY in H9c2 treated with or without 50 μM Chloroquine, 50 μM Bafilomycin, and subjected to normoxia or H/R. (F-H) Pearson correlation of LC3 and BODIPY, and MFI quantification of BODIPY (F). (I) Representative image of Rosella PLIN2-H9c2 cell and of Rosella PLIN5-H9c2 cell subjected to normoxia or H/R, and quantification in (J) and (K). (L) Representative image of BODIPY staining in WT H9c2 cell and AKO cell subjected to normoxia or H/R, and quantification in (M). (N) SDS-PAGE and immunoblot analysis of WT H9c2 cell and ATG7KO-H9c2 cell lysate using PLIN5, PLIN2, and GAPDH was used as a loading control. (O-P) Quantification of PLIN2 and PLIN5. (R) Representative image of BODIPY staining in H9c2 cell treated with or without 10 μM Lalistat 1, 100 μM Paraoxon, 20 μM Atglistatin, combination of Atglistatin and Lalistat 1, and combination of Atglistatin and Paraoxon and subjected to normoxia or H/R, and quantification in (P). Scale bar: 10 μm. Results are presented as mean ± SEM (n=3-6 per group). *P<0.05, **P<0.01, ***P<0.001 versus normoxia control. $^{\#\#\#}P$<0.001 versus H/R control. One-way ANOVA with Tukey post-hoc test was run for statistical analysis for panel B-E, G-H. Two-way ANOVA with Tukey multiple comparisons post-hoc test was run for the rest of panels.

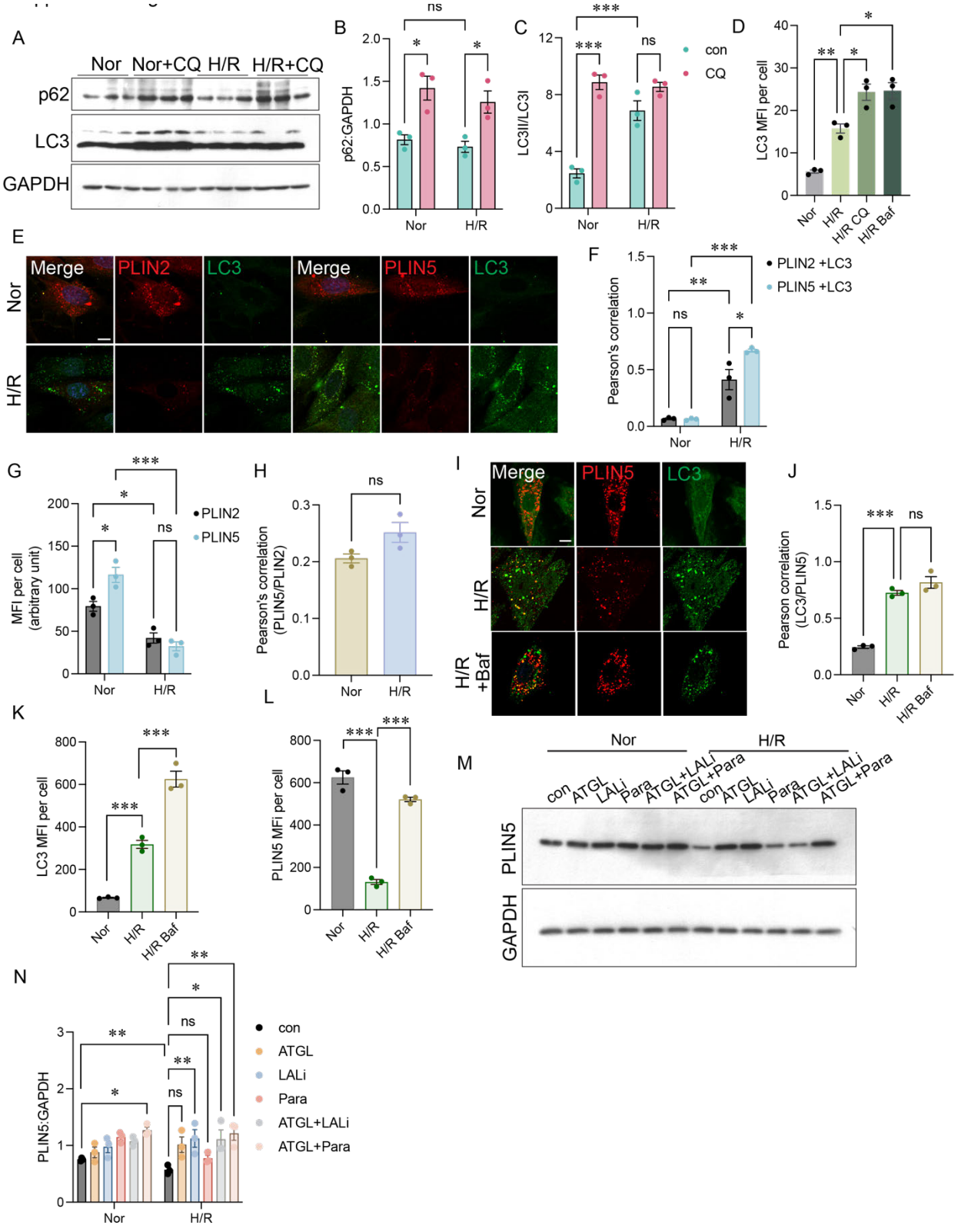

Figure 4.4 HR promoted lipid droplet-associated autophagy and PLIN-LC3 interactions in H9c2 cells, modulated by lysosomal and lipolytic pathways

(A) SDS-PAGE and immunoblot analysis of H9c2 lysate using p62 and LC3, GAPDH was used as a loading control. (B-C) Quantification of p62 and LC3. (D) MFI quantification of LC3. (E) Representative image of immunofluorescence staining of LC3 and PLIN2 and PLIN5 in H9c2 subjected to normoxia or H/R. (F) Pearson correlation of PLIN2 and LC3, PLIN5 and LC3. (G) MFI quantification of PLIN2 and PLIN5. (H) Pearson correlation of PLIN2 and PLIN5. (I) Representative image of immunofluorescence staining of PLIN5 and LC3 in H9c2 treated with or without50 μM Bafilomycin and subjected to normoxia or H/R. (J) Pearson correlation of LC3 and PLIN5. (K) MFI quantification of LC3. (L) MFI quantification of PLIN5. (M) SDS-PAGE and immunoblot analysis of H9c2 lysate treated with or without 10 μM Lalistat 1, 100 μM Paraoxon, 20 μM Atglistatin, combination of Atglistatin and Lalistat 1, and combination of Atglistatin and Paraoxon and subjected to normoxia or H/R, using PLIN5, PLIN2, LC3, p62, and GAPDH was used as a loading. (N) Quantification of PLIN5. Scale bar: 10 μm. Results are presented as mean ± SEM (n=3 per group). *P<0.05, **P<0.01, ***P<0.001 versus normoxia control. One-way ANOVA with Tukey post-hoc test was run for statistical analysis for panel D, J-L. T-test was run for statistical analysis for panel H. Two-way ANOVA with Tukey multiple comparisons post-hoc test was run for statistical analysis for the rest of panels.

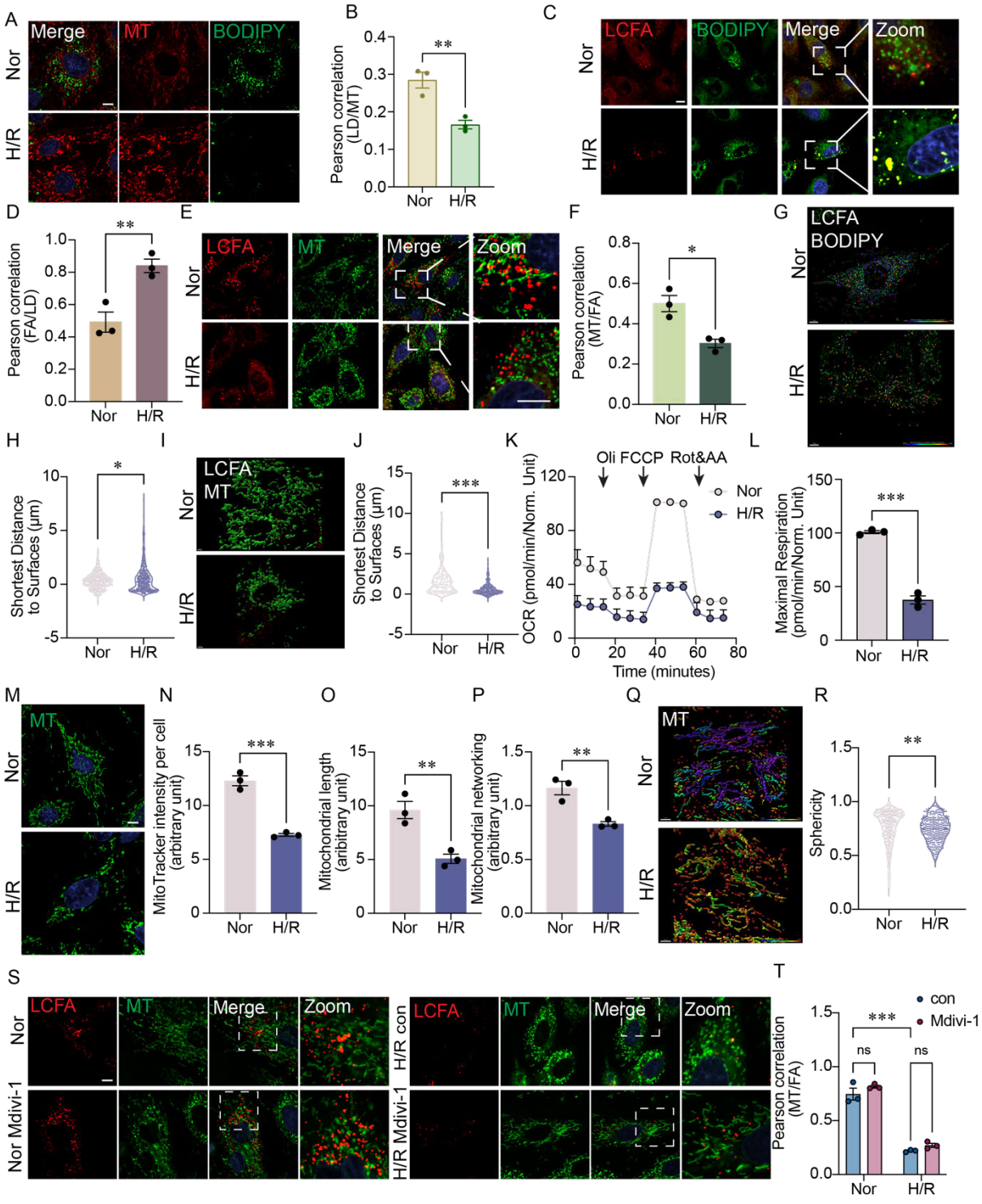

Figure 4.5 H/R disrupted LD and mitochondria tethering

(A) Representative image of Mitotrakcer (MT) and BODIPY (LD) staining in H9c2 cells subjected to normoxia or H/R. (B) Pearson correlation of MT and LD. (C) Representative image of long chain free fatty acid (LCFA) and BODIPY (LD) staining in H9c2 cells subjected to normoxia or

H/R. (D) Pearson correlation of LCFA and LD. (E) Representative image of long chain free fatty acid (LCFA) and Mitotrakcer (MT) staining in H9c2 cells subjected to normoxia or H/R. (F) Pearson correlation of LCFA and MT. (G) Representative image of IMARIS analyzed long chain free fatty acid (LCFA) and BODIPY (LD) staining in H9c2 cells subjected to normoxia or H/R. (H) Quantification of (G). (I) Representative image of IMARIS analyzed long chain free fatty acid (LCFA) and Mitotrakcer (MT) staining in H9c2 cells subjected to normoxia or H/R. (J) Quantification of (I). (K) Seahorse mitochondrial stress test and quantification for parameters of mitochondrial function in H9c2 cells subjected to normoxia or H/R. (L) Quantification of maximal respiration capacity in Seahorse experiment. (M) Representative image of Mitotrakcer (MT) staining of H9c2 cells subjected to normoxia or H/R. (N-P) Quantification of mitochondria density, branch length, and networking. (Q) Representative image of IMARIS analyzed Mitotrakcer (MT) staining of H9c2 cells subjected to normoxia or H/R. (R) Quantification of sphericity of mitochondria. (S) Representative image of long chain free fatty acid (LCFA) and Mitotrakcer (MT) staining in H9c2 cells treated with or without 10 μM Mdivi-1 and subjected to normoxia or H/R. (T) Pearson correlation of MT and LCFA. Scale bar: 10 μm. Results are presented as mean ± SEM (n=3 per group). **P*<0.05, ***P*<0.01, ****P*<0.001 versus normoxia control. Two-way ANOVA with Tukey multiple comparisons post-hoc test was run for statistical analysis for panel T. T-test was run for statistical analysis for the rest of panels.

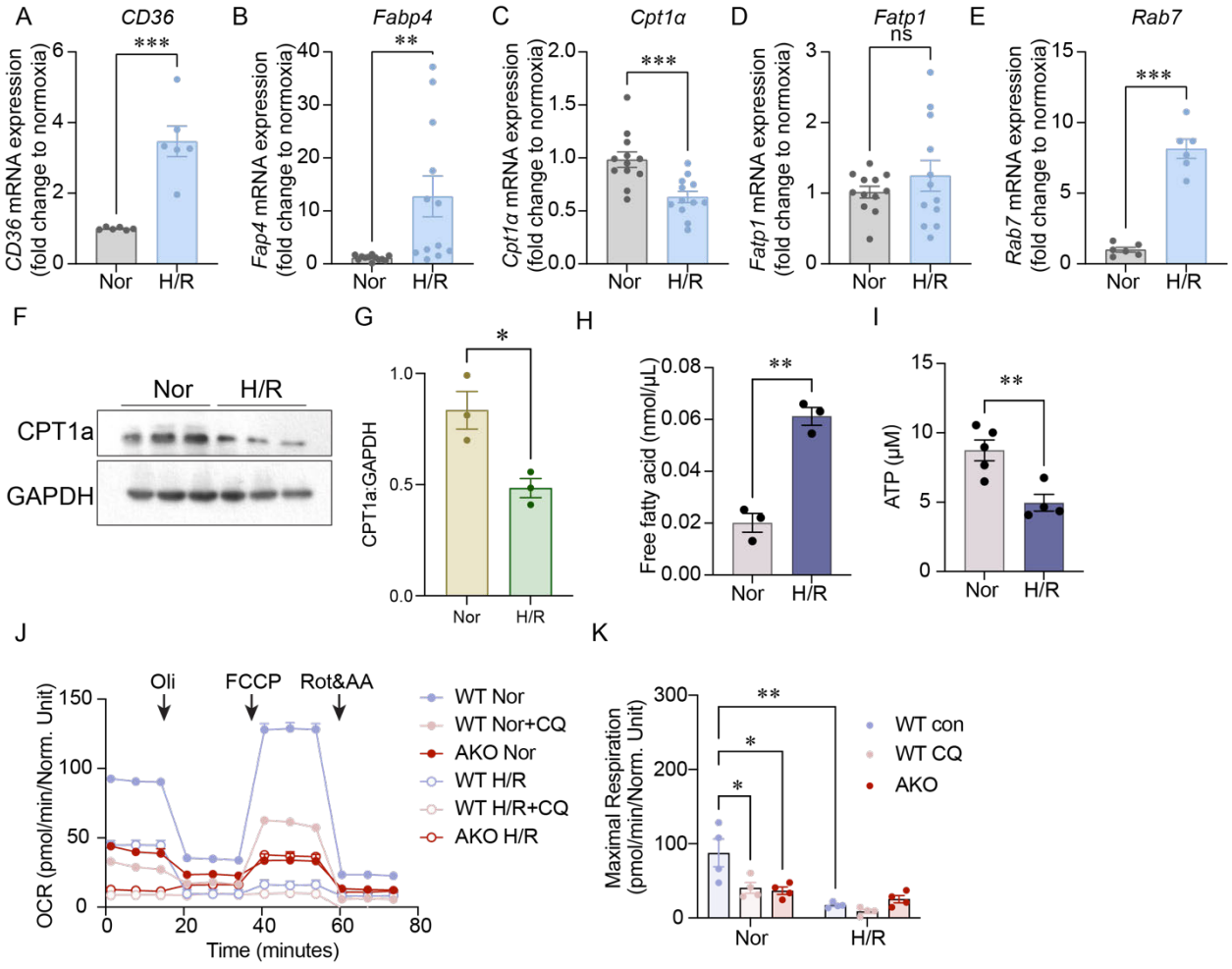

Figure 4.6 HR altered fatty acid transport, oxidation, and mitochondrial bioenergetics in an autophagy-dependent manner

(A-E) mRNA expression of CD36, FABP4, CPT1α, FATP1, and Rab7 in H9c2 cells subjected to normoxia or H/R. (F) SDS-PAGE and immunoblot analysis of H9c2 lysate CPT1α, GAPDH was used as loading control. (G) Quantification of CPT1α. (H) Extracellular free fatty acid measurement in culture medium of H9c2 cells subjected to normoxia or H/R. (I) ATP measurement in culture medium of H9c2 cells subjected to normoxia or H/R. (J) Seahorse mitochondrial stress test and quantification for parameters of mitochondrial function in WT treated with or without chloroquine, or ATG7 KO and subjected to normoxia or H/R. (K) Quantification of maximal respiration capacity in Seahorse experiment. Scale bar: 10 μm. Results are presented as mean ± SEM (n=3-12 per group). *P<0.05, **P<0.01, ***P<0.001 versus normoxia control. Two-way

ANOVA with Tukey multiple comparisons post-hoc test was run for statistical analysis of panel K. T-test was run for statistical analysis for the rest of the panels.

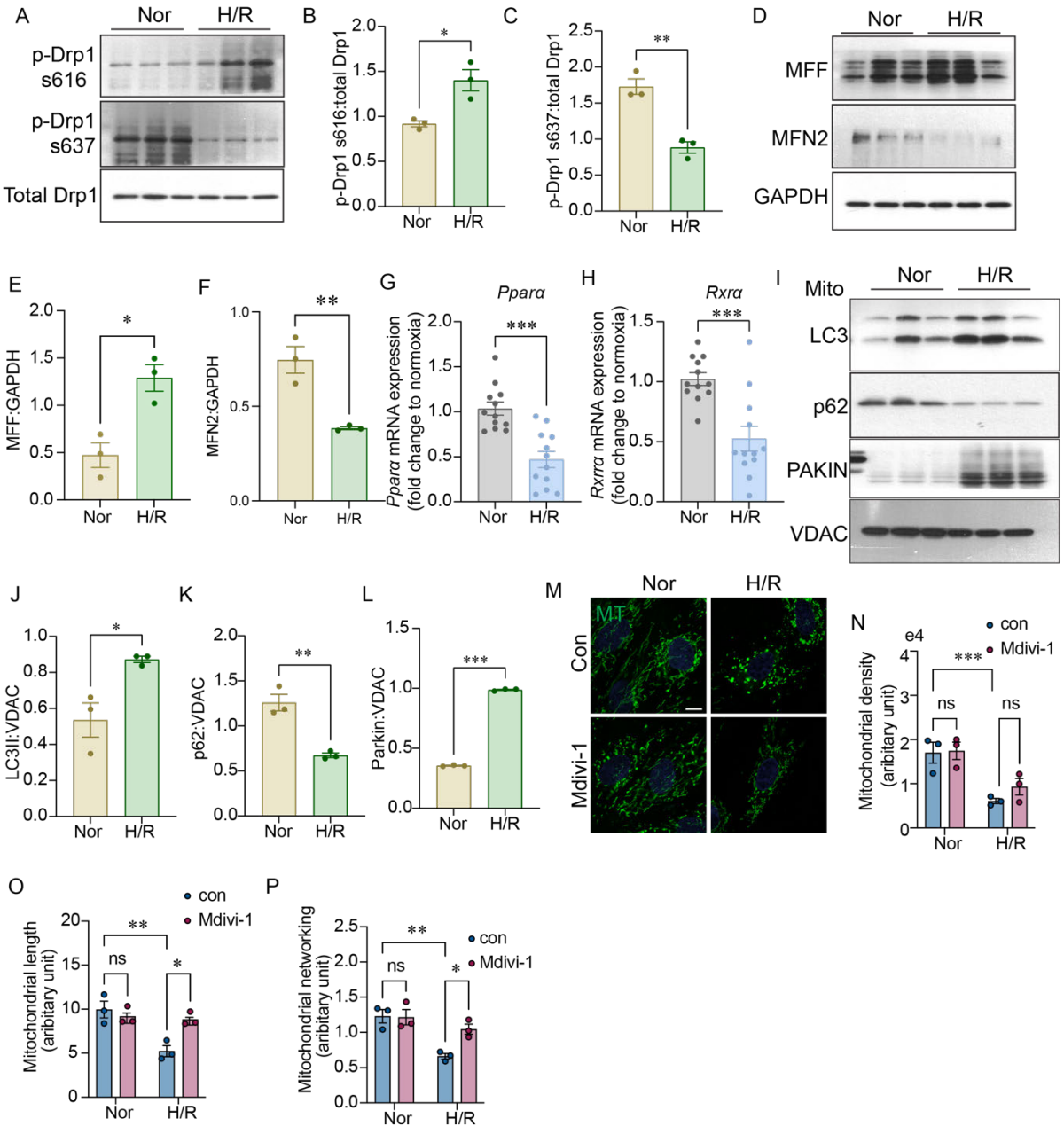

Figure 4.7 HR disrupted mitochondrial dynamics, mitophagy signaling, and transcriptional regulation of lipid metabolism in H9c2 cells

(A) SDS-PAGE and immunoblot analysis of H9c2 lysate using p-Drp1 s616, p-Drp1 s637 and total Drp1, GAPDH was used as a loading control. (B-C) Quantification of p-Drp1 s616, and p-Drp1 s637. (D) SDS-PAGE and immunoblot analysis of H9c2 lysate using MFF and MFN2, and β-

tubulin was used as loading control. (E-F) Quantification of MFF and MFN2. (G-H) mRNA expression of PPARα, and RXRα in H9c2 cells subjected to normoxia or H/R. (I) SDS-PAGE and immunoblot analysis of mitochondrial fraction lysate from H9c2 using LC3, p62, PAKIN, and VDAC was used as loading control. (J-K) Quantification of LC3, p62 and PARKIN. (M) Representative image of Mitotrakcer (MT) staining in H9c2 cells treated with or without 10 μM Mdivi-1 and subjected to normoxia or H/R. (N-P) Quantification of mitochondria density, branch length, and networking. Scale bar: 10 μm. Results are presented as mean ± SEM (n=3) per group. **P*<0.05, ***P*<0.01, ****P*<0.001 versus normoxia control. Two-way ANOVA with Tukey multiple comparisons post-hoc test was run for statistical analysis for panel N-P. T-test was run for statistical analysis for the rest of the panels.

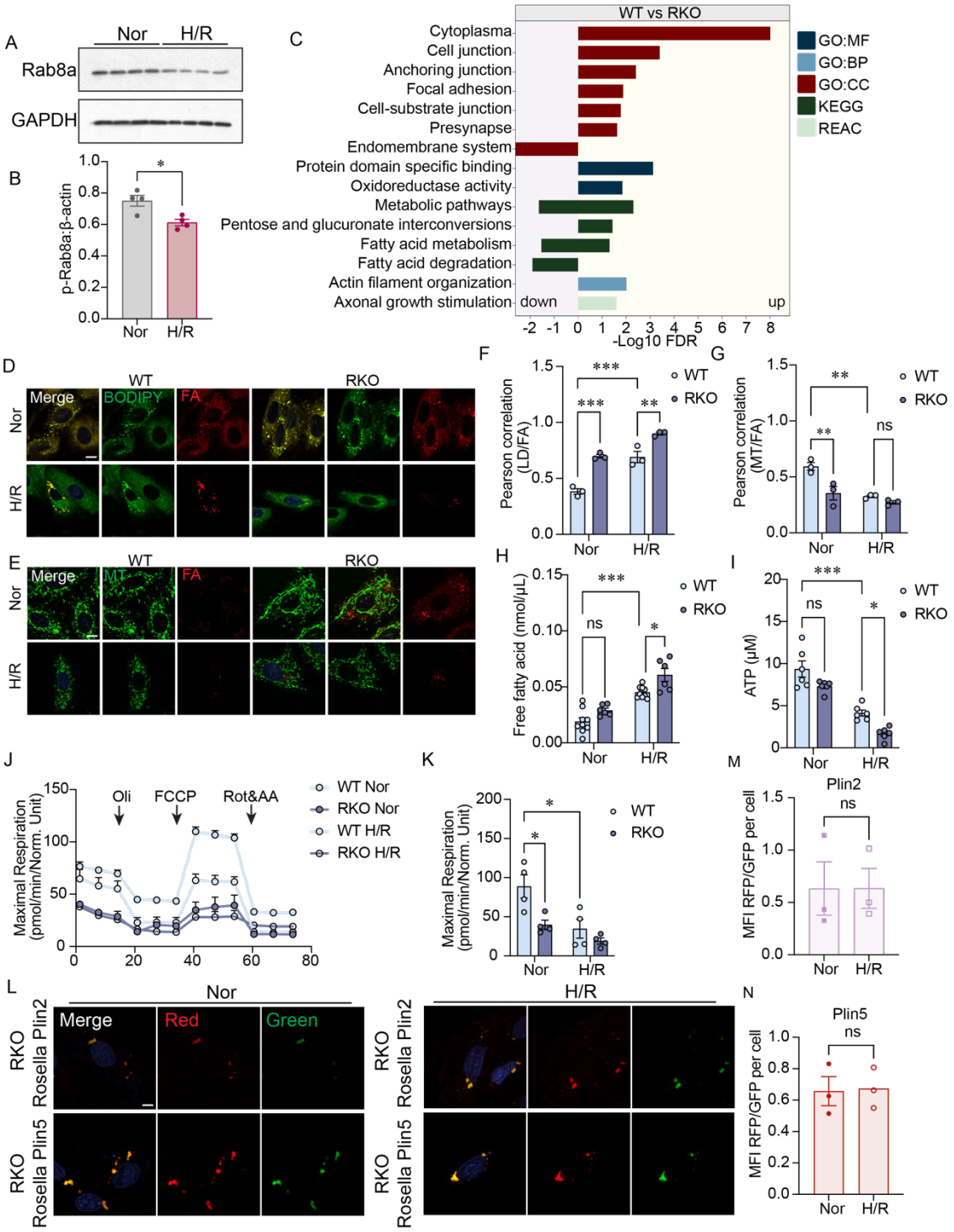

Figure 4.8 Rab8a role in the LD and mitochondrial tethering during H/R

(A) SDS-PAGE and immunoblot analysis of H9c2 lysate using Rab8a, and GAPDH was used as loading control. (B) Quantification of Rab8a. (C) Pathway enrichments of significant expressed proteins. (D) Representative image of long chain free fatty acid (LCFA) and BODIPY (LD) staining in WT and Rab8a KO H9c2 cell (RKO) subjected to normoxia or H/R. (E) Representative image of long chain free fatty acid (LCFA) and Mitotrakcer (MT) staining in WT and RKO subjected to normoxia or H/R. (F-G) Pearson correlation of FA and LD, FA and MT. (H) Extracellular free fatty acid measurement in culture medium of WT and RKO subjected to normoxia or H/R. (I) ATP measurement in culture medium of WT and RKO subjected to normoxia or H/R. (J) Seahorse mitochondrial stress test and quantification for parameters of mitochondrial function in WT and RKO subjected to normoxia or H/R. (K) Quantification of maximal respiration capacity in Seahorse experiment. (L) Representative image of Rosella PLIN2-RKO and of Rosella PLIN5-RKO subjected to normoxia or H/R and quantification in (M) and (N). Scale bar: 10 μm. Results are presented as mean ± SEM (n=3-4) per group. **P*<0.05, ***P*<0.01, ****P*<0.001 versus normoxia control. Two-way ANOVA with Tukey multiple comparisons post-hoc test was run for statistical analysis for panel F-G, H-I, and K. T-test was run for statistical analysis for the rest of the panels.

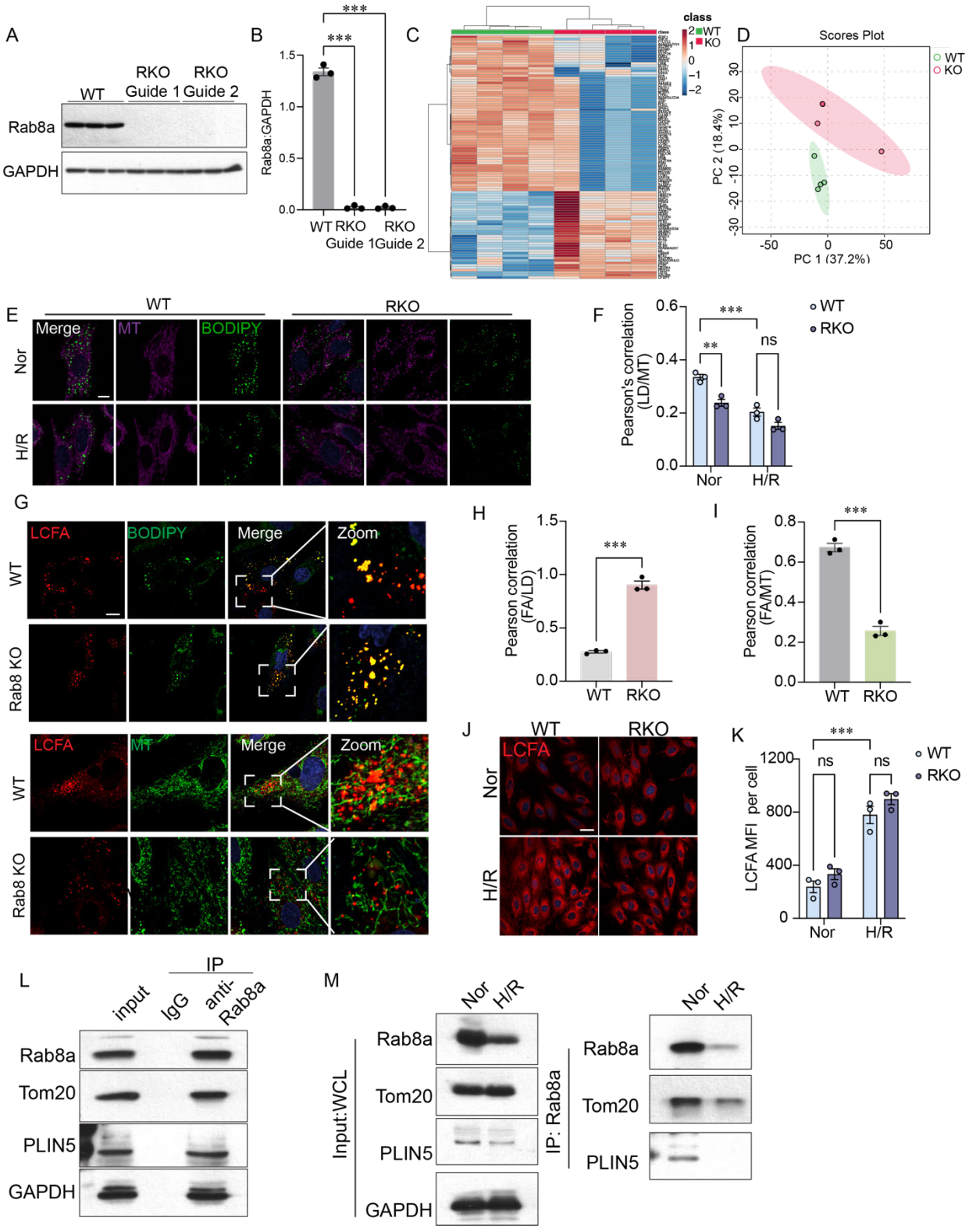
A
WT
RKO Guide 1
RKO Guide 2
Rab8a
GAPDH
B
Rab8a:GAPDH
WT
RKO Guide 1
RKO Guide 2
C
class
WT
KO
D
Scores Plot
WT
KO
PC 2 (18.4%)
PC 1 (37.2%)
E
WT
RKO
Merge
MT
BODIPY
Nor
H/R
F
Pearson's correlation (LD/MT)
WT
RKO
Nor
H/R
G
LCFA
BODIPY
Merge
Zoom
WT
Rab8 KO
LCFA
MT
Merge
Zoom
WT
Rab8 KO
H
Pearson correlation (FA/LD)
WT
RKO
I
Pearson correlation (FA/MT)
WT
RKO
J
WT
RKO
LCFA
Nor
H/R
K
LCFA MFI per cell
ns
ns
WT
RKO
Nor
H/R
L
IP
input
IgG
anti-Rab8a
Rab8a
Tom20
PLIN5
GAPDH
M
Nor
H/R
Input:WCL
Rab8a
Tom20
PLIN5
GAPDH
IP: Rab8a
Rab8a
Tom20
PLIN5

Figure 4.9 Rab8a regulated lipid droplet-mitochondria crosstalk, long-chain fatty acid trafficking, and proteomic remodeling under HR stress

(A) SDS-PAGE and immunoblot analysis of RKO lysate using Rab8a, and β-tubulin was used as loading control. (B) Quantification of Rab8a. (C) Heat map hierarchical clustering of proteomics analysis of WT and RKO cells. (D) PCA of proteomics analysis of WT and RKO cells (E) Representative image of MT and BODIPY staining in WT and RKO subjected to normoxia or H/R. (F) Pearson correlation of LD and MT. (G) Representative image of LCFA and BODIPY staining in WT and RKO. (H) Pearson correlation of LCFA and LD. (H) Representative image of LCFA and MT staining in WT and RKO. (I) Pearson correlation of LCFA and MT. (J) Representative image of LCFA staining in WT and RKO subjected to normoxia or H/R. (K) Quantification of LCFA MFI. (L) Immunoprecipitation (IP) of Rab8a or IgG from lysates of H9c2 cells or whole cell lysates (WCL) subjected to normoxia or H/R and then blotted for Tom20 and PLIN5. (M) IP of Rab8a from lysates of H9c2 cells or whole cell lysates (WCL) subjected to normoxia or H/R and then blotted for Tom20 and PLIN5. Scale bar: 10 μm. Results are presented as mean ± SEM (n=3 per group). **P*<0.05, ***P*<0.01, ****P*<0.001 versus normoxia control. One-way ANOVA with Tukey post-hoc test was run for statistical analysis for panel B. Two-way ANOVA with Tukey multiple comparisons post-hoc test was run for statistical analysis for panel F and K. T-test was run for statistical analysis for the rest of panels

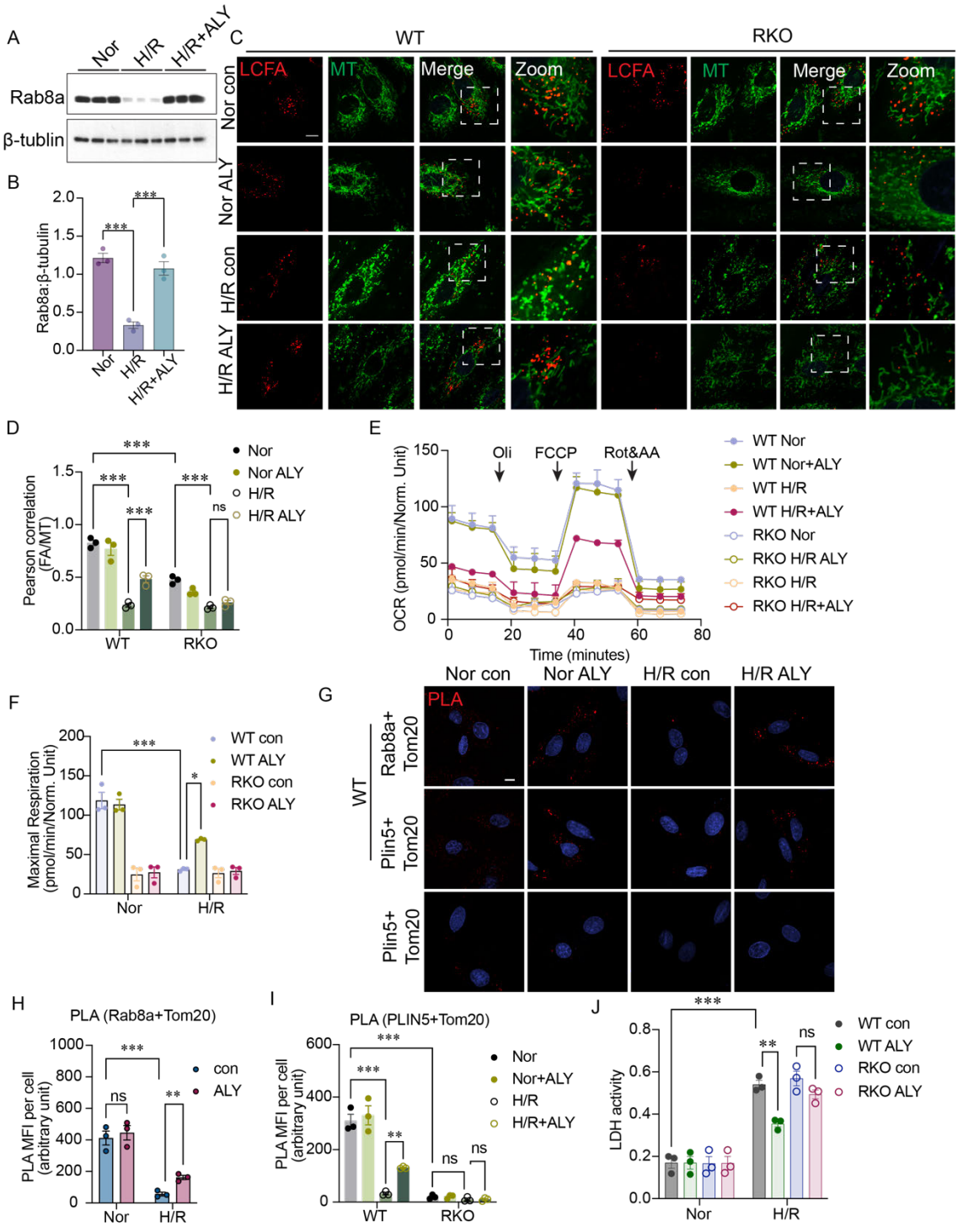

Figure 4.10 ALY688 improved LD and mitochondria communication during H/R

(A) SDS-PAGE and immunoblot analysis of H9c2 lysate using Rab8a, and β-tubulin was used as loading control. (B) Quantification of Rab8a. (C) Representative image of long chain free fatty acid (LCFA) and Mitotracker (MT) staining in H9c2 treated with or without 100 nM ALY688 and subjected to normoxia or H/R. (D) Pearson correlation of FA and MT. (E) Seahorse mitochondrial stress test and quantification for parameters of mitochondrial function in H9c2 treated with or without 100 nM ALY688 and subjected to normoxia or H/R. (F) Quantification of maximal respiration capacity in Seahorse experiment. (G) Representative image of PLA using combination of Rab8a and Tom20, PLIN5 and Tom20 in WT and RKO treated with or without 100 nM and subjected to normoxia or H/R. (H) Quantification of Rab8a and Tom20 PLA MFI. (I) Quantification of PLIN5 and Tom20 PLA MFI. (J) LDH measurement of WT, RKO, treated with or without ALY688, and subjected to normoxia or H/R. Scale bar: 10 μm. Results are presented as mean ± SEM (n=3) per group. **P*<0.05, ***P*<0.01, ****P*<0.001 versus normoxia control. One-way ANOVA with Tukey post-hoc test was run for statistical analysis for panel B. Two-way ANOVA with Tukey multiple comparisons post-hoc test was run for statistical analysis for the rest of panels.

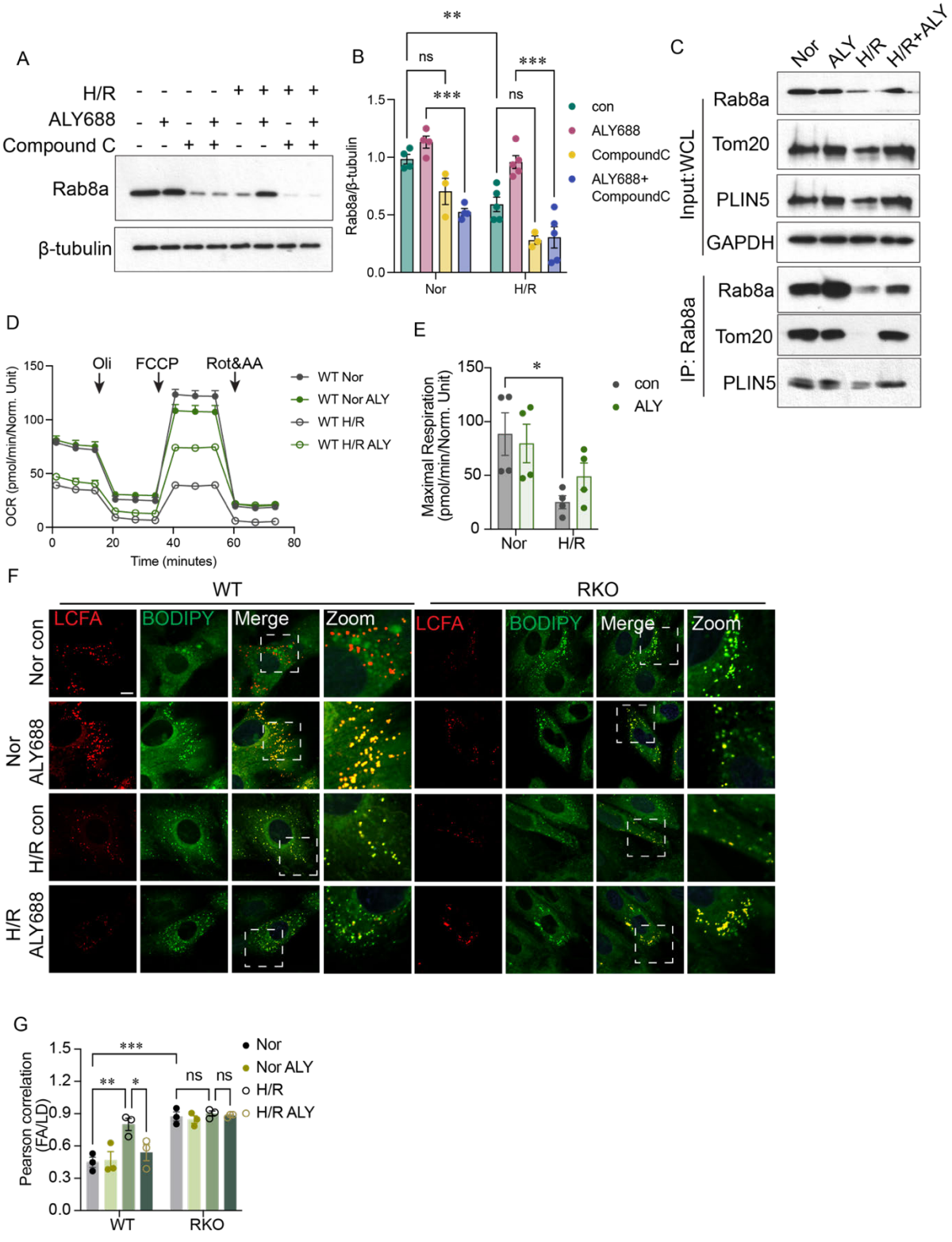
A
H/R
ALY688
Compound C
Rab8a
β-tubulin
B
Rab8a/β-tubulin
con
ALY688
CompoundC
ALY688+ CompoundC
Nor
H/R
C
Nor
ALY
H/R
H/R+ALY
Input:WCL
Rab8a
Tom20
PLIN5
GAPDH
IP: Rab8a
D
Oli
FCCP
Rot&AA
OCR (pmol/min/Norm. Unit)
Time (minutes)
WT Nor
WT Nor ALY
WT H/R
WT H/R ALY
E
Maximal Respiration (pmol/min/Norm. Unit)
F
WT
RKO
LCFA
BODIPY
Merge
Zoom
Nor con
Nor ALY688
H/R con
H/R ALY688
G
Pearson correlation (FA/LD)
Nor
Nor ALY
H/R
H/R ALY

Figure 4.11 ALY688 enhanced Rab8a-associated lipid handling and preserves mitochondrial function during HR injury

(A) SDS-PAGE and immunoblot analysis of H9c2 cells lysate using Rab8a, and β-tubulin was used as loading control. (B) Quantification of Rab8a. (C) IP of Rab8a from lysates of H9c2 cells or whole cell lysates (WCL) subjected to normoxia or H/R and treated with ALY688 and then blotted for Tom20 and PLIN5. (D) Seahorse mitochondrial stress test and quantification for parameters of mitochondrial function in H9c2 treated with or without 100 nM ALY688 and subjected to normoxia or H/R. (E) Quantification of maximal respiration capacity in Seahorse experiment. (F) Representative image of long LCFA and BODIPY staining in H9c2 treated with or without 100 nM ALY688 and subjected to normoxia or H/R. (G) Pearson correlation of FA and BODIPY. Scale bar: 10 μm. Results are presented as mean ± SEM (n=3-4 per group). **P*<0.05, ***P*<0.01, ****P*<0.001 versus normoxia control. Two-way ANOVA with Tukey multiple comparisons post-hoc test was run for statistical analysis.

A

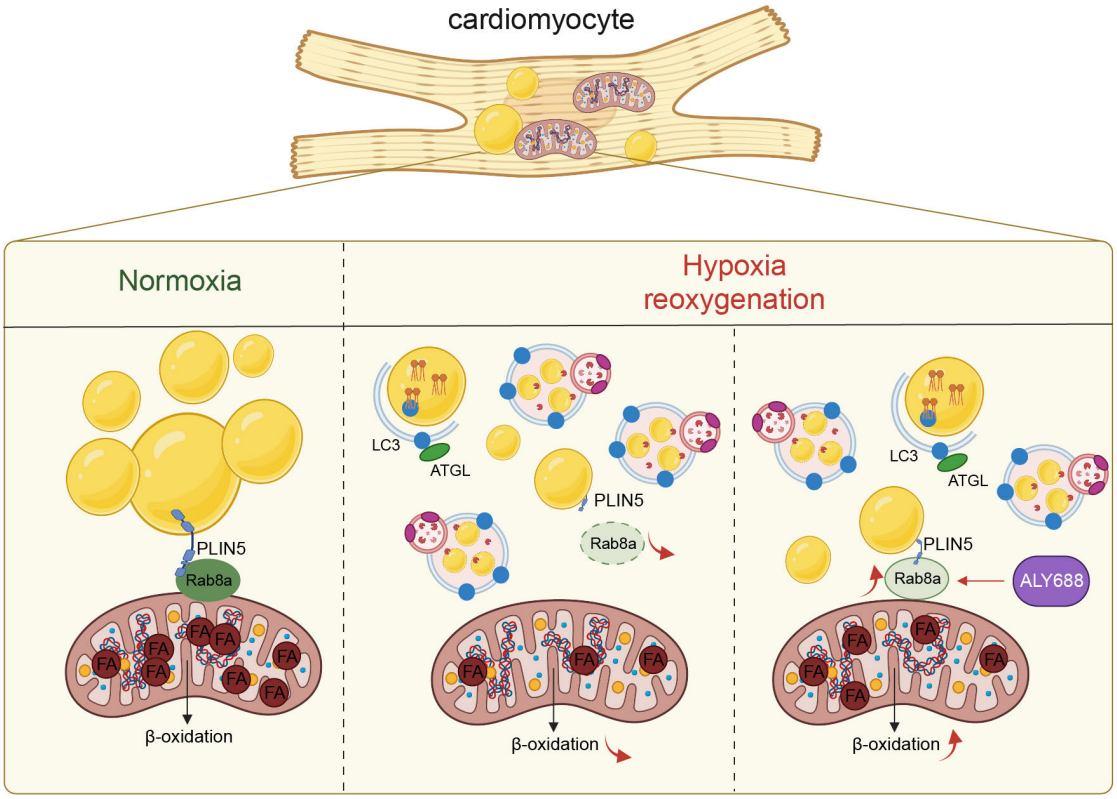

Figure 4.12 Graphic abstract

Table 4.1 Sequence of primers

Target	Species	Forward 5'-3'	Reverse 5'-3'
Dgat1	Rat	GAACTAGCTAGCCGTCCGTC	AAAGGATCTGCCCTGTCACG
Dgat2	Rat	ACCACGCACCAATTCAGGAT	TCCTTTTCACCAGGTGCCAT
Plin1	Rat	GTGCCATCGTCTGCAAGATTC	GCATCACCACACACCAATTCAG
Plin2	Rat	GCGCTACTTCCGAGACTACTT	GGGCCTTATGCCAGGAAACT
Plin3	Rat	GAGTCACAACCCCACGATGT	CGAGAGAGGAAAGAGTCGAC
Plin4	Rat	CAGTACTTGCCGCTCACTCA	TCAGATGGACAGTGGAGTGG
Pline5	Rat	CTCAGTGTCTGGTGCAAAGG	CTAGTTCTGTGTCTGTCAGG
Atgl	Rat	GGCTACCGAGATGGACTTCG	AGACTCCGTCTCCCATCCTC
Hsl	Rat	ATGCTGTGTGAGAATGCCGA	GGCCTGACAGAGCAAAGAGT
Mgl	Rat	ACTAATGGAAACAGGGCCCAA	TGTCCTGACTCGGGGATGAT
Lal	Rat	GGTACACTGGACCCAGGTTG	GATGTCACTGGTGTCTGCCA
Cpt1α	Rat	CCAGGCTACAGTGGGACATT	GAAGAGCCGAGTCATGGAAG
Cd36	Rat	ACAGATGCAGCCTCCTTTCC	ACACAGCATAGATGGACCTGC
Fatp1	Rat	TCTACCCTTCTGGCTCCCAT	TCTACCAGGTGTCAAGGCTCA
Fabp4	Rat	AGA AGT GGG AGT TGG CTT CG	ACT CTC TGA CCG GAT GAC GA
Rxrα	Rat	CAGGGGATGCACAACGCTGGC	CCGACTGTCCGCTTAGAG
Pparα	Rat	TAGCAACAATCCGCCTTTTGT	GCGATCAGCATCCCGTCTT

4.5 Discussion

Cardiac energy metabolism depends on the precise coordination of lipid storage, mobilization, and mitochondrial oxidation. These processes are severely disrupted during ischemic stress. IR injury affects cardiac energy metabolism through multiple mechanisms. Among them, impaired lipid handling is a key contributor to cardiomyocyte damage (437). Physical and functional coupling between LDs and mitochondria are essential for maintaining metabolic flexibility and preventing lipotoxicity in the heart (115, 410, 438, 439). This study uncovers a previously unrecognized mechanism of metabolic dysfunction during H/R. Rab8a-mediated LD-mitochondria tethering is downregulated, impairing fatty acid utilization and promoting lipotoxicity. We found that the adiponectin receptor agonist ALY688 provides cardioprotection partly by restoring this communication axis. These findings enhance our understanding of ischemic injury and suggest potential therapeutic strategies.

Membrane contact sites serve as crucial metabolic junctions for intracellular trafficking and signaling. We demonstrate that H/R significantly disrupted LD-mitochondria proximity, compromising fatty acid channeling despite concurrent activation of lipid mobilization pathways. This uncoupling represents a fundamental aspect of metabolic inflexibility during cardiac stress. Recent ultrastructural analyses have established that approximately 30-45% of LDs in healthy cardiomyocytes maintain close proximity (<100 nm) to mitochondria, facilitating efficient substrate delivery (438). The disruption of these contacts during H/R, coupled with downregulation of fatty acid oxidation genes (*CPT1α, PPARα, RXRα*), creates a severe mismatch between lipid mobilization and utilization that contributes to accumulation of lipotoxic intermediates, particularly DAG, as documented in various models of cardiac stress (395, 401). It is worth noting that the relationship between cardiac lipid metabolism and hypoxic signaling is likely bidirectional. Recent evidence suggests that defects in lipid handling can induce a state of 'pseudo-hypoxia,' where metabolic intermediates or oxidative stress stabilize HIF-1α even in the absence of severe environmental hypoxia (440-444). In our study, the HR-induced loss of Rab8a leads to an accumulation of untethered lipid droplets and free fatty acids. The subsequent lipotoxicity and generation of ROS from these accumulated lipids may inhibit prolyl hydroxylases (PHDs), thereby reinforcing HIF-1α stabilization. This lipid-driven pseudo-hypoxic state could potentially create a maladaptive feedback loop, further entrenching the metabolic inflexibility observed in ischemic cardiomyocytes.

Here, we show that lipid catabolism during H/R occurs through both lipolysis and lipophagy, the latter being particularly significant for predominant degradation of PLIN5-coated LDs. While lipophagy has been extensively studied in hepatocytes and adipocytes (404, 407, 415, 425, 445, 446), its role in cardiomyocyte metabolism during ischemic stress has remained less defined. The observation that inhibition of lysosomal acid lipase specifically prevents PLIN5 degradation during H/R highlights selective vulnerability of PLIN5-coated LDs to autophagy-mediated degradation. This selectivity likely reflects specific cargo receptor interactions that have been described in recent studies of selective autophagy (447-449). Lipophagy generally serves as an adaptive response to provide substrates for mitochondrial oxidation during nutrient deprivation (450, 451). However, when LD-mitochondria coupling is disrupted, as seen with reduced Rab8a activity during H/R, enhanced lipophagy appears to become metabolically uncoupled. While lipophagy typically supports energy production, in the absence of Rab8a-mediated tethering, the fatty acids mobilized by autophagy cannot be efficiently transferred to mitochondria. This mismatch between lipid mobilization and oxidation likely results in the accumulation of lipotoxic intermediates rather than ATP synthesis.

The identification of Rab8a as a key regulator of LD–mitochondria tethering in cardiomyocytes expands its known roles beyond vesicular trafficking to include metabolic coordination. Rab8a has also been previously linked to LD fusion in adipocytes (413) and identified as a mitochondrial receptor for LDs in skeletal muscle (411), its role in cardiac lipid metabolism remained unexplored until now. Rab8a deficiency mirrors key features of H/R-induced metabolic dysfunction. It increases LD-mitochondria proximity, impairs long-chain fatty acid mobilization, and reduces bioenergetic capacity. The fact that Rab8a does not influence PLIN5-associated lipophagy suggests it specifically mediates organelle tethering rather than lipid breakdown, highlighting its specialized role in metabolic coordination. Recent super-resolution microscopy studies show extensive contact networks between organelles, with about 90% of LDs maintaining stable contacts with at least one other organelle (452). H/R-induced Rab8a downregulation disrupts this intricate communication network, with profound consequences for metabolic homeostasis.

Preventing mitochondrial fragmentation using the inhibitor Mdivi-1 did not restore LCFA transfer to mitochondria during H/R in cardiomyocytes. This observation challenges the prevailing paradigm that mitochondrial structural integrity directly determines metabolic function. Our data suggests that LD-mitochondria tethering rather than mitochondrial morphology itself constitutes

the critical determinant of efficient fatty acid trafficking. This distinction carries implications for therapeutic strategies targeting mitochondrial dysfunction in cardiac disease. Recent investigations have demonstrated that mitochondrial fission and fusion proteins participate in tethering mitochondria to other organelles, suggesting that their distinct roles extend beyond morphology regulation to include inter-organelle communication (409, 410, 414, 430, 431, 453-456). These findings align with emerging research showing that mitochondrial dynamics and substrate preference can be mechanistically uncoupled under specific conditions, supporting the broader conclusion that organelle tethering represents a distinct regulatory layer in cardiac metabolism (457-459).

ALY688 restores Rab8a expression and LD-mitochondria tethering, offering both mechanistic insight and therapeutic potential. In Rab8a-KO cells, ALY688's beneficial effects are completely lost, confirming Rab8a as a key mediator of adiponectin's metabolic actions. Adiponectin itself has been widely studied for cardioprotection during IR, with benefits linked to AMPK activation, anti-inflammatory effects, and enhanced mitochondrial function. (460). These findings add a new dimension to adiponectin's protective effects by showing its role in preserving organelle communication via Rab8a. Mechanistically, this likely involves AMPK-dependent activation of Rab8a. Recent studies show that AMPK phosphorylation increases GTP-bound active Rab8a, which promotes LD-mitochondria tethering through binding to PLIN5 (411). These results establish a direct link between adiponectin signaling, organelle tethering, and cardiomyocyte survival during metabolic stress.

Targeting the adiponectin-Rab8a axis could help restore metabolic flexibility by improving fatty acid utilization. The fact that ALY688 reduces cell death during H/R indicates that preserving LD-mitochondria tethering may protect against lipotoxicity-induced apoptosis, a major contributor to ischemic injury and heart failure progression (399, 400, 409). This mechanism complements adiponectin's established effects on cardiac remodeling, inflammation, and oxidative stress. Together, these actions may provide a multi-faceted approach to cardioprotection.

In conclusion, this study identifies Rab8a-mediated LD-mitochondria tethering as a critical metabolic junction that becomes dysregulated during H/R in cardiomyocytes. The findings demonstrate that the adiponectin receptor agonist ALY688 restores this communication axis and attenuates metabolic dysfunction, providing mechanistic insight into adiponectin's

cardioprotective actions and identifying Rab8a as a promising therapeutic target for ischemic heart disease.

While our data show that Rab8a deletion exacerbates HR injury and ALY688 (which restores Rab8a) mitigates it, we did not perform direct Rab8a re-expression experiments in the knockout background. Therefore, we cannot rule out that ALY688 may exert protective effects through parallel, Rab8a-independent pathways. Future studies involving genetic rescue of Rab8a will be required to definitively establish its sufficiency in preventing HR-induced metabolic dysfunction. Additionally, while we infer that the increased lipophagic flux is detrimental based on the concurrent reduction in ATP and accumulation of lipid intermediates, we did not normalize autophagic flux directly to mitochondrial β-oxidation rates in real-time. Future studies using dual-pulse chase assays or flux-metabolism coupling models would be beneficial to quantitatively define the 'efficiency ratio' of lipophagy-derived fuel utilization under stress conditions.

4.6 Statement of contribution

Genetic modification of H9c2 cells was performed by the Genome Editing and Molecular Biology Facility and Nathan Joyce at the University of Ottawa. Lipidome and proteomics analysis service was provided by McGill University, and the analysis was performed by Jialing Tang. Cell culture and associated experiments were conducted by Jialing Tang. Western blotting and microscopic imaging were conducted by Jialing Tang. qPCR analysis was performed by Jialing Tang. Mitochondrial isolation and associated experiments were done by Jialing Tang and Eddie Tam. Seahorse extracellular flux assays were conducted by Jialing Tang, Nathan Joyce, Thomas Laval, and Eddie Tam. Statistical analysis was performed by Jialing Tang. The original manuscript draft was written by Jialing Tang. Funding was acquired by Gary Sweeney.

5. Chapter 5: Ischemia-induced Cardiac Dysfunction Is Exacerbated In Adiponectin-knockout Mice Due To Impaired Autophagy Flux

5.1 Abstract

Strategies to enhance autophagy flux have been suggested to improve outcomes in cardiac ischemic models. We explored the role of adiponectin in mediating cardiac autophagy under ischemic conditions induced by permanent coronary artery ligation. We studied the molecular mechanisms underlying adiponectin's cardio-protective effects in adiponectin knockout (Ad-KO) compared with wild type (WT) mice subjected to ischemia by coronary artery ligation and H9c2 cardiomyocyte cell line exposed to hypoxia. Systemic infusion of a cathepsin-B activatable near-infrared probe as a biomarker for autophagy and detection via non-invasive 3-dimensional fluorescence molecular tomography (FMT) combined with computerized tomography (CT) to quantitate temporal changes, indicated increased activity in the myocardium of wild-type mice after myocardial infarction which was attenuated in adiponectin knockout (Ad-KO). Seven days of ischemia increased myocardial adiponectin accumulation and elevated ULK1/AMPK phosphorylation and autophagy assessed by western blotting for LC3 and p62, an outcome not observed in Ad-KO mice. Cell death, assessed by TUNEL analysis and the ratio of Bcl-2:Bax, and cardiac dysfunction, measured using echocardiography with strain analysis, were exacerbated in Ad-KO mice. Using cellular models, we observed that adiponectin stimulated autophagy flux in isolated primary adult cardiomyocytes and increased basal and hypoxia-induced autophagy in H9c2 cells. Real-time temporal analysis of caspase-3/7 activation and caspase-3 western blot indicated that adiponectin suppressed activation by hypoxia. Hypoxia-induced mitochondrial ROS production and cell death were also attenuated by adiponectin. Importantly, the ability of adiponectin to reduce caspase-3/7 activation and cell death was not observed in autophagy-deficient cells generated by CRISPR-mediated deletion of Atg7. Collectively, our data indicate that adiponectin acts in an autophagy-dependent manner to attenuate cardiomyocyte caspase-3/7 activation and cell death in response to hypoxia in vitro and ischemia in mice

5.2 Introduction

Cardiovascular disease (CVD) stands as the primary cause of mortality in developed regions, with coronary heart disease (CHD) being responsible for the majority of fatalities within this classification (333). CHD triggers cardiac remodeling, encompassing changes in both the structure and function of the heart, commonly described as ischemic injury (334). Consequently, there is a significant focus on unraveling the multifaceted mechanisms that drive cardiac remodeling post-ischemia due to *heightened interest in this area* (461). In recent years, intense efforts have been made to determine the mechanisms underlying ischemia or IR injury and to explore therapeutic targets (336, 462).

Extensive research has been conducted on the process of autophagy, a mechanism that facilitates the bulk degradation of cellular components, particularly in the context of ischemia, both with and without reperfusion (336, 463). The role of cardiac autophagy is crucial for sustaining heart function and supporting the adaptive response under both basal and stress-induced condition (463, 464). Nevertheless, inhibiting autophagy during ischemia has been shown to exacerbate myocardial injury, highlighting the protective role of autophagy in such conditions (465). Overall, an appropriate balance of autophagy is an important determinant of heart failure outcomes in ischemia (289, 466). Further exploration is required to gain additional insights into the processes through which autophagy activation can exert either cardioprotective or detrimental effects in the heart (77).

Adiponectin, secreted predominantly from the adipose tissue, has been previously reported to have multiple cardioprotective effects, including in ischemic settings (268, 349, 350). A growing body of clinical and basic research has revealed associations between circulating adiponectin levels and the development or extent of cardiac disease, leading to adiponectin being proposed as a potential therapeutic target to improve outcomes in myocardial ischemia/reperfusion injury It has also been suggested that myocardial ischemia/reperfusion injury could alter adiponectin levels in the heart (202). Furthermore, myocardium can crosstalk with adipose tissue and treatment of adipocytes with plasma from mice having ischemia/reperfusion injury resulted in increased adiponectin expression (202).

The interaction between adiponectin and autophagy has been acknowledged in previous studies. Adiponectin triggers intracellular AMP kinase (AMPK) signaling, initiating various catabolic

processes, including autophagy, and mitigating remodeling induced by myocardial infarction.(268, 467). Concurrently, the mechanistic target of rapamycin (mTOR), a pivotal regulator of cell growth and metabolism, plays a crucial role, with adiponectin acting as an inhibitor of mTOR signaling, thereby instigating autophagy processes (202, 467). Further dissection of the molecular landscape involves Beclin-1, a pivotal regulator of autophagy initiation. Adiponectin's influence extends to the upregulation of Beclin-1 expression, facilitating autophagosome formation a pivotal step in the autophagic cascade. Adiponectin's capacity to enhance microtubule-associated protein 1A/1B-light chain 3 (LC3) lipidation underscores its induction of the initiation and progression of autophagy. The selective autophagy substrate p62/SQSTM1, degraded upon augmented autophagy flux and enhanced cellular waste clearance, is another marker regulated by adiponectin (336) (468). Collectively, we and others have demonstrated that adiponectin is associated with autophagy rates in multiple tissues (271, 469).

The objective of this study was to test the hypothesis that adiponectin-stimulated autophagy was of functional significance in mediating cardioprotection in mice with myocardial ischemia and in cellular cardiomyocyte models subjected to hypoxia. We investigated the role of adiponectin on autophagy and ischemic damage in vivo using an adiponectin knockout (Ad-KO) mouse model subjected to myocardial infarction. Whether adiponectin mitigates hypoxia-induced apoptosis through activation of autophagy was determined using autophagy deficient cells generated via deletion of Atg7.

5.3 Materials and Methods

Animals and Echocardiography

All animals were housed in temperature and humidity-controlled rooms (21 ± 2°C, 35-40%) with a daily 12h light/dark cycle in the animal care facility of York University in accordance with the guidelines of the Canadian Council on Animal Care. All study protocols were approved by the Animal Care Committee of York University. In-house adiponectin knockout (Ad-KO) mice(470) and age-matched C57BL/6J (wild type, WT) mice (the Jackson Laboratory, USA) were maintained with *ad libitum* access to water and regular chow diet until 12 weeks of age when they were randomly separated into surgical groups (n=5 per group). Myocardial infarction (MI) was induced with coronary artery ligation (CAL) surgery, as previously described(471). Mice were euthanized 7 days, or in some experiments 1 day, after MI without reperfusion. Echocardiography was performed as previously described(469) using the Vevo2100 system (Visual Sonics, Canada) equipped with an MS550D transducer. Mice were lightly anesthetized using 2-3.0% isoflurane mixed with 100% O_2 for the duration of the imaging. M-mode images of the parasternal short-axis views at the papillary level were used to calculate cardiac functions. B-mode movie files of the parasternal short-axis views were used to perform Speckle-tracking cardiac strain rate analysis. All parameters were averaged for at least three cardiac cycles for analysis. Primary cardiomyocytes from adult rats were prepared as described by us before.(472)

Tissue Immunofluorescence staining

Paraffin embedded heart tissue sections were de-paraffinized with serial rehydration, and antigen retrieval was performed in sodium citrate buffer (pH 6.0). Heart sections were permeabilized and blocked with blocking buffer (3% BSA, 5% goat serum, Vector Laboratories, S-1000, 0.3 % Triton X-100) for 120 minutes and stained with primary antibody solution (Rabbit anti-LC3B, MBL, #PM036 at a 1:200 dilution or Rabbit anti-Adiponectin, in-house polyclonal antibody at a 1:200 dilution or Wheat Germ Agglutinin (WGA), Invitrogen, #W11261 at a 1:1000 dilution) and incubated overnight at 4 degrees. The slides were kept in secondary antibody (Goat anti-Rabbit Alexa 488, Goat anti-Rabbit 546, ThermoFisher, #A-11008, #A-11035) at 1:1000 for 1 hour at room temperature after three washes. Slides were mounted in DAPI containing medium (Vectashiled®, #H-1200) after three washes, and slides were visualized under Zeiss LSM700 confocal microscope at 20X or 40X.

Histology analysis

Paraffin embedded heart sections were subjected to TUNEL (*In Situ* Cell Death Detection kit, Roche, #11684795910), WGA (Invitrogen, #W11261) or picrosirius red staining (Abcam, #ab150681) according to manufacturer's protocol and visualized using an Olympus IX71 inverted fluorescence microscope (Olympus Canada, Richmond Hill, ON, Canada) or EVOS2 FL Auto 2 Microscope.

Fluorescent Molecular Tomography (FMT) imaging in mice

Two nanomoles of pan-cathepsin protease sensor (ProSense® 680, Perkin Elmer, #NEV10003) were infused into mice via tail vein injection for the assessment of lysosomal activity. Probes were delivered 24 hours prior to imaging. The intensity of fluorescence was visualized at 680nm with FMT using VisEn FMT 2500 LX Quantitative Tomography System (Perkin Elmer, MA USA). Mice were anesthetized, placed in a supine position, and the scan region was established to capture the upper half of the mouse (i.e., nose to above the liver) using an in-plane resolution of 1×1 mm^2. After FMT signals were captured, mice were transferred to micro–computed tomography (CT) imaging (eXplore Ultra, GE Healthcare) while maintained under light anesthesia. FMT and CT images were reconstructed, merged, and a 3D image was constructed using Amide software (Amide's a Medical Imaging Data Examiner). Hearts were isolated from mice after FMT scanning and placed on an opaque resin block in the FMT plexiglass mouse holder and imaged at 680nm. Epifluorescence images were captured for each mouse heart, and analysis of the *ex vivo* images was performed using the FMT System software (TrueQuant 4.0).

Western blot

The ischemic zone of the left ventricle (LV) heart tissue was snap frozen and ground with mortar and pestle in liquid nitrogen. The powdered tissue was then suspended in RIPA lysis buffer.(473) H9c2 cells were used for western blot analysis and cells were suspended in lysis buffer. Proteins were separated by reducing SDS-PAGE and transferred to a PVDF membrane. The following antibodies were used for western blot: p-AMPK T172 (1:1000, Cell Signaling, #2535), p-ULK1 S555 (1:1000, Cell Signaling, #5869), GAPDH (1:2000, ThermoFisher, #MA5-15738), Adiponectin (1:1000, ImmunoDiagnostics, #12010), ATG5-12 (1:1000, Novus Biologicals, #NB110-53818), ATG7 (1:1000, Santa Cruz, #sc-376212), Beclin1 (1:1000, Cell Signaling, #3738), LC3B (1:1000, Cell Signaling, #2775), p62 (1:1000, Cell Signaling, #5114), BAX (1:1000,

Cell Signaling, #2772), cleaved Caspase 3 (1:1000, Cell Signaling, #9661), bcl-2 (1:1000, Cell Signaling, #3489), β-actin (1:2000, ThermoFisher, #PA1-46296) were used. The quantification of signals was performed by densitometry of scanned autoradiographs with the aid of ImageJ (version 1.4v).

Cell Culture

H9c2 rat embryonic cardiac myoblasts (ATCC® CRL-1446™) were grown in Dulbecco's Modified Eagle's Medium (DMEM) (Gibco, Invitrogen) supplemented with 10% fetal bovine serum (FBS) and 1% (vol/vol) streptomycin/penicillin (Gibco, Invitrogen) at 37°C and 5% CO_2. When cells reached confluence, they were incubated in 1% FBS-DMEM overnight. Then, medium was switched to FBS-free DMEM with or without globular adiponectin (Ad) (ImmunoDiagnostics, #42012) at indicated concentrations. Hypoxia was achieved by placing cells in a hypoxic chamber (Onstage Incubator, ThermoFisher, #NX7LIVE001) filled with a pre-analyzed gas mixture of 1%O_2 5% CO_2. Normoxia was achieved by placing cells in the Onstage Incubator filled with 20% O_2 and 5% CO_2.

Generation of ATG7-KO and VC3AI Transduced H9c2 Cells

CRISPR knock-out lines were generated as previously described using guide RNAs cloned into pX459.(281) Vectors carrying guides targeting Atg7 were transfected into H9C2 cells using Lipofectamine 3000. Transduced cells were selected using 1 ug/ml puromycin over 5 days, and then expanded in medium without selection. T7 endonuclease assays were carried out using T7 endonuclease I (NEB) according to the manufacturer's recommendations on PCR products generated using the following primer pair 5'-GCTGCTGCAGGTAGGTGTAA and 5'-GGTGTCCTGTCTGAGACTGC. To generate H9C2 lines stably expressing VC3AI, lentiviral particles were produced using pCDH-puro-CMV-VC3AI (474) and transduced cells were selected using 1 μg/ml puromycin.

Flow Cytometry

After treatment, cells were harvested with trypsin-EDTA-0.25% (Gibco, #25200056) and cell pellets were incubated with appropriate staining dye. mBBr (ThermFisher, #M1378), MitoSox (ThermoFisher, #M36008), Annexin V and Propidium Iodide (PI) (ThermoFisher, #V13245) were used in 1% FBS-DMEM at 37°C for 30 minutes. After incubation, cells were re-suspended in

FACS buffer (2% FBS in PBS) and assessed by flow cytometry (Attenute NxT BRV6, ThermoFisher). For oxidative stress stain, cells were stained with 2.5 µM MitoSox Red (Thermo Fisher) and 40 µM mBBr (Thermo Fisher) diluted in FACS buffer for 10 min at 37ºC. Cells were stained in 1:40 dilution of Annexin V (eBioscience) diluted in 1x binding buffer for 10 minutes at room temperature. Cells were then washed once in binding buffer and resuspended in 190 ml binding buffer. Finally, 10 ml of PI (1.5µM) was added to the cells and analysed immediately by flow cytometry. Compensation and analysis were performed in FlowJO software V10.

Microscopic Imaging

H9c2 cells and adult rat cardiomyocytes, which were isolated as described previously (Song et al., 2018) were seeded on glass coverslips. Staining using different dyes including Cyto-ID, (1:1000, Enzo life sciences, #51031), Magic Red (1:260, ImmunoChemistry Technologies, #942), DalGreen (1:1000, Dojindo, #D675) DapRed (1:1000, Dojindo, #D677), cleaved caspase 3/7 (1:500, ThermoFisher, #C10423), ReadyProbe (ThermoFisher, #R37609) was performed according to manufacturer's protocols and DAPI (HCS NuclearMask Blue Stain, ThermoFisher, #H10325) was added simultaneously. Cells were fixed in 10% formalin (Sigma, #HT501128) after treatment and mounted with ProLong Gold Antifade Mountant (ThermoFisher, #P36930). Slides were observed under Nikon Eclipse Ti2, Zeiss LSM700 confocal microscope at 60X, Evos FL Auto 2 and for continuous measurements Cellnsight CX7 Platform (ThermoFisher, #CX7A1110) was used. Co-localization analysis was performed with an ImageJ JACOP plug-in.

Cell-stained images analysis

Following staining with specific probes, images were acquired using confocal microscopy. All biological replicates were performed with a minimum of three technical replicates. For each technical replicate, at least five randomly selected fields of view were imaged, and a minimum of 50 cells were quantified.

Statistics

Data is presented as mean ± SEM. Statistical analysis was performed using GraphPad Prism 9. Student's t-test was used for comparison of two groups and one-way ANOVA or two-way ANOVA were used for comparison of more than two groups. $P<0.05$ was considered statistically significant.

5.4 Results

Autophagy flux is enhanced following adiponectin treatment in normoxic or hypoxic conditions

We used H9c2 cardiac myoblasts subjected to hypoxia (1% O_2) as an in vitro model relevant to myocardial ischemia and treated cells with or without adiponectin for up to 24 hours. First, we conducted temporal analyses via time-lapse microscopy using the probe DapRed to detect autophagosomes and autophagolysosomes (Figure 5.1 A), or DalGreen to detect autophagolysosomes (Figure 1B). An early increase in both autophagosome and autophagolysosome content was observed in hypoxic cells compared to control as shown by DapRed fluorescence, yet after 24h these levels were similar (Figure 5.1 A). The effect of adiponectin in cells under normoxic conditions was similar yet diverged after 12h toward enhanced autophagosome and autophagolysosome levels. Hypoxia elicited a rapid increase in autophagosome and autophagolysosome content which was further elevated in the presence of adiponectin (Figure 5.1 A). A similar pattern was observed when using DalGreen to detect autophagolysosomes (Figure 5.1 B). Based upon the above kinetic observations, autophagy markers were also assessed by western blotting after 12 hours of adiponectin treatment. Adiponectin, in normoxic conditions, increased LC3-II and decreased p62, indicating more autophagy flux (Figure 5.1 C-E). At the 12h of hypoxia, both with or without adiponectin, increased LC3-II and decreased p62 (Figure 5.1 C-E). Similarly, hypoxia reduced autophagy flux compared to normal cells as indicated by a reduced green to red ratio which was rescued following adiponectin treatment (Figure 5.1 F&G). Lysosomal cathepsin activity, measured using MagicRed, was increased after adiponectin treatment in both normoxia and hypoxia conditions compared to control (Figure 5.1 H&I).

Adiponectin mitigates hypoxia induced apoptosis in H9c2 cells

We measured temporal activation of caspase 3/7 in H9c2 cells using an activatable fluorescent probe in normoxia or hypoxia conditions with or without adiponectin treatment for up to 24h. As expected, hypoxia increased cleavage of caspase 3/7 compared to normoxia conditions, with the change manifest from 12h onwards. (Figure 5.2A). Adiponectin pretreatment attenuated this effect. Increased cleaved caspase 3 content after 24h hypoxia was also indicated by western blot (Figure 5.2 B&C). Again, cotreatment with adiponectin reduced cleavage of caspase 3 (Figure 5.2 B&C).

To further confirm our results, H9c2 cells stably expressing the caspase activity reporter VC3AI were used to monitor caspase 3 activity in real time. Cleaved caspase 3 was increased in hypoxic cells and attenuated in the presence of adiponectin (Figure 5.2 D&E). In addition, cell death measured using ReadyProbe Cell Viability kit specify was increased under hypoxia conditions and reduced in adiponectin treated cells (Figure 5.2 F&G). Alterations in oxidative stress under these conditions were assessed, first via examining the percentage of MitoSox positive cells to assess changes in mitochondrial ROS. We observed that hypoxia induced mitochondrial ROS in H9c2 cells was mitigated following adiponectin treatment as reflected by a decrease in the percentage of MitoSox positive cells (Figure 5.3 A&C). Similar findings were observed with mBBr staining which measures cellular glutathione levels. Together, analysis of ROS production indicated that adiponectin treatment alleviated elevated oxidative stress levels in hypoxic conditions (Figure 5.3 B &C). Therefore, under conditions of hypoxia, adiponectin treatment ameliorated apoptosis and reduced mitochondrial ROS and oxidative stress levels.

Adiponectin treatment does not limit apoptosis in autophagy deficient H9c2 cells

To determine whether adiponectin mitigates apoptosis through an autophagy-dependent mechanism, autophagy-deficient cells were generated using CRISPR mediated ATG7 deletion. First, to validate autophagy deficiency the cells were treated with rapamycin, an mTOR inhibitor well characterized to stimulate autophagy (Figure 5.4 A-D). Control cells responded to rapamycin treatment and had increased LC3-II and reduced p62 expression indicating enhanced autophagy flux (Figure 5.2 A-D). In contrast, in ATG7-KO cells there were no changes upon rapamycin treatment confirming impaired autophagy (Figure 5.5 A-D). Using western blot for cleaved caspase-3, cells grown under normoxic conditions showed no significant changes (Figure 5.5 A&B). After hypoxia treatment for 24h we observed activation of caspase-3, and this was reduced by adiponectin in WT but not ATG7-KO cells (Figure 5.5 A&B). To further investigate this, cell death was measured using fluorescence staining with ReadyProbe Cell Viability kit and similar findings were observed (Figure 5.5 C&D). Finally, flow cytometry using Annexin V, a marker for early apoptosis, and PI, a marker for necrosis or late apoptosis showed that in WT cells, hypoxia increased both early and late apoptosis (Figure 5.5 E&F). Importantly, adiponectin treatment mitigated these increases (Figure 5.5 E&F). In autophagy deficient cells, there was a significant increase in early and late apoptosis under hypoxia conditions, which was not attenuated by

adiponectin treatment (Figure 5.5 E&F). Collectively, these results indicate that adiponectin alleviates hypoxia induced apoptosis the stimulation of autophagy.

Adiponectin accumulation and signaling in the infarct zone is increased following 7 days of myocardial infarction in WT but not Ad-KO mice

To determine the role of adiponectin in cardiac autophagy during ischemia and explore its significance in cardiac remodeling, WT and Ad-KO mice at 12 weeks of age were subjected to coronary artery ligation surgery without reperfusion for 7 days. Western blot was performed on the ischemic zone of the LV heart tissue and adiponectin was expressed in WT but not Ad-KO mice as expected, and its expression was increased after 7 days of myocardial infarction in WT mice (Figure 5.6A&B). Immunofluorescence staining on heart tissue sections provided further qualitative evidence that adiponectin expression was increased following myocardial infarction in WT, with no expression observed in Ad-KO mice (Figure 5.6 C). To assess changes in mRNA expression, mRNA was isolated from heart tissues after 7 days of myocardial infarction. No changes were observed in adiponectin mRNA expression after inducing myocardial infarction in WT mice compared to sham mice, indicating that the changes observed in the protein level are not due to elevated adiponectin gene expression (Figure 5.6 D). Furthermore, ELISA quantification revealed no differences in serum adiponectin levels after 1 day or 7 days of myocardial infarction compared to sham treated mice (Figure 5.6 E). To observe whether downstream signaling pathways of adiponectin were altered, western blot was performed on heart tissue homogenates. As expected, the increased adiponectin expression observed in WT mice following 7 days of myocardial infarction was accompanied by higher phosphorylated ULK1, a protein kinase that is important in initiating autophagy (Figure 5.6 F&G). Basal ULK1 phosphorylation was reduced in Ad-KO mice and not increased upon myocardial infarction. Interestingly, AMPK was activated following myocardial infarction in both WT mice and Ad-KO mice (Figure 5.6 H) which suggests that AMPK could be activated by other signals in Ad-KO mice. Therefore, myocardial infarction increases adiponectin accumulation in the infarct zone, which then activates its downstream targets, including ULK1 and AMPK leading to the initiation of autophagy.

Validation of fluorescence molecular tomography detection of cathepin B (CatB 680) activity as a readout of myocardial autophagy in WT and autophagy-deficient mice.

To validate the use of cathepsin B activity analysis by FMT as a non-invasive indicator of myocardial autophagic flux we compared control mice and those with cardiomyocyte autophagy deficiency. Inducible cardiomyocyte-specific ATG7-deficient or WT mice were treated with rapamycin and starvation for 24h to induce autophagy. Representative ex vivo FMT images of hearts showed that cathepsin B activity was significantly induced by rapamycin and starvation treatment in wild type animals, but not in the autophagy-deficient group (Figure 5.7 A&B). Whole heart homogenates were analyzed by Western blotting for validated markers of autophagy, p62, LC3-I and LC3-II (Figure 5.7 C-G). Elevated LC3-II levels indicate increased autophagosome content, an observation which could arise due to elevated initiation or suppressed flux (Figure 5.7 C-E). Increased p62 levels in autophagy-deficient mice indicated that flux was reduced (Figure 5.7 C&F). This correlates with the data obtained using CatB as an indicator of autophagy flux. Finally, inducible cardiomyocyte-specific ATG7-deficiency was confirmed by the reduction of total ATG7 protein expression in heart homogenates (Figure 5.7 C&G). Residual levels of ATG7 and the small increase seen in ATG7-/- mice (Figure 5.7 A) could be explained as a result signals coming from other myocardial cell types. Overall, our data indicates that myocardial autophagy activation can be assessed not only by well-known autophagy markers, p62 and LC3-II conversion, but also by CatB activity. After we validated the use of CatB activity analysis by FMT, we also used this method to measure the effect of ischemia in WT and Ad-KO mice. Representative FMT images and four optical sections through the heart, are shown for each group (Figure 5.7 H). The increased fluorescence signal in the hearts of WT but not Ad-KO mice after myocardial infarction indicates augmented lysosomal CatB activity. Fluorescent molecular tomography imaging was also performed on hearts ex vivo (Figure 5.7 I) and data again revealed higher lysosomal activity in WT mice compared to Ad-KO mice (Figure 5.7 I&J). Hence, Ad-KO mice have disrupted autophagy flux when compared to WT after chronic myocardial ischemia.

Myocardial infarction-induced autophagy flux is attenuated in Ad-KO mice

Next, we explored whether loss of adiponectin expression disrupts autophagy related processes in mice following myocardial infarction. LC3B immunofluorescence efficacy was first validated in H9c2 rat embryonic cardiac myoblasts using Torin-1, an mTOR inhibitor used as a positive control to simulate autophagy. H9c2 cells displayed a red fluorescent punctate signal when treated with Torin-1 and stained with LC3B or probed with Cyto-ID, indicating autophagosome formation (Figure 5.8 A). To observe changes in key autophagy related proteins, western blot was performed

on infarct region homogenates (Figure 5.9 A-D). Beclin 1, an early marker of autophagy, was increased in both WT and Ad-KO mice subjected to myocardial infarction compared to their respective sham controls (Figure 5.9 A&B). LC3B-II levels were higher in Ad-KO versus WT mice and decreased after myocardial infarction (Figure 5.9 A&C). Myocardial infarction significantly increased p62 levels in Ad-KO but not WT mice (Figure 5.9 A&D).

Ad-KO mice had exaggerated infarction-induced cell death and cardiac dysfunction versus WT mice

We next determined whether loss of adiponectin expression can influence ischemia-induced apoptosis and cardiac dysfunction. To assess cell death, TUNEL staining was performed on heart sections and the extent of cell death was elevated in Ad-KO versus WT mice both before and after infarction (Figure 5.9 E&F). Western blot revealed that the infarction-induced decrease in Bcl2 (anti-apoptotic) to BAX (pro-apoptotic) ratio, an index of apoptosis, observed in WT mice was exacerbated in Ad-KO mice (Figure 5.10 G&H). In addition, the inflammatory and pro-apoptotic protein lipocalin-2 (Lcn2), was increased in Ad-KO mice to a greater extent than in WT mice after myocardial infarction (Figure 5.9 G&I). These data suggest that apoptosis due to prolonged ischemia was exacerbated in Ad-KO mice. The increased heart weight to tibia length found in Ad-KO mice with myocardial infarction compared to WT indicated exaggerated cardiac hypertrophy (Figure 5.9 J). In keeping with this, we also found increased cardiomyocyte hypertrophy (Figure 5.8 C-D). Echocardiography was used to examine cardiac function and myocardial strain in Ad-KO compared to WT mice. Myocardial infarction caused a small significant reduction in ejection fraction in both WT and Ad-KO compared to sham mice (Figure 5.9 K). Statistical analysis indicated the reduction in Ad-KO was significantly greater than in WT mice, suggesting that the presence of adiponectin is important for protecting cardiac function following ischemia (Figure 4.6 K). Speckle tracking echocardiography was used to examine radial and longitudinal strain, with data further confirming that Ad-KO mice had significant cardiac dysfunction compared to their respective WT controls after myocardial infarction (Figure 5.9 L-M). Consistent with impaired cardiac function, fibrosis was aggravated in Ad-KO compared to WT mice (Figure 5.10 A-B). These data confirm that presence of adiponectin reduced the impact of ischemia on cardiac function and cardiac remodeling.

Adiponectin stimulates autophagy in primary adult rat cardiomyocytes and H9c2 cardiac myoblasts

The previous results showed loss of adiponectin expression disrupts induction of autophagy in response to ischemia. We next determined whether adiponectin can directly stimulate autophagy in primary adult cardiomyocytes and H9c2 cardiac myoblasts. We found that the autophagy markers, pULK1, pAMPK and LC3-II were all increased following treatment of H9c2 cells with adiponectin for 30 min (Figure 5.11 A-D). To further examine direct effects of adiponectin on autophagy, the probe Cyto-ID was first validated in H9c2 cells treated with Torin-1 (Figure 5.11 E). Quantification of Cyto-ID in primary cardiomyocytes and H9c2 cells (Figure 5.11 E&F) revealed a higher number of autophagosomes per cell following adiponectin treatment. Similarly, lysosomal cathepsin activity measured by Magic Red in H9c2 cells was stimulated by adiponectin treatment (Figure 5.11 E&F). Therefore, adiponectin directly stimulated autophagy flux in cardiomyocytes.

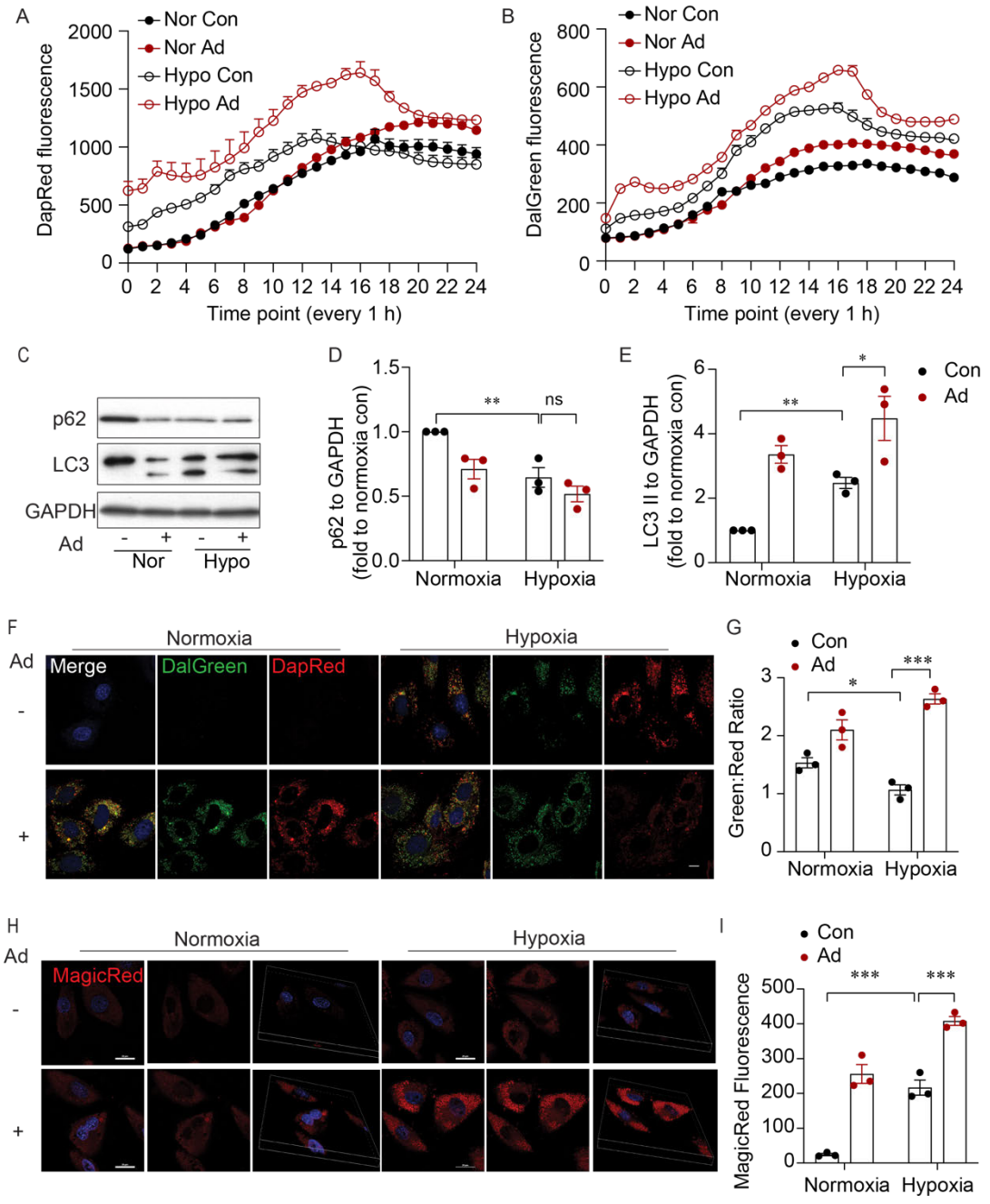

(Adapted from Sung HK, Tang J, et al. Clinical and Translational Science 2024; 17:e13758)

Figure 5.1 Adiponectin treatment enhanced autophagy flux in hypoxic cells in vitro

(A) DapRed fluorescence measured every hour in H9c2 cells during hypoxia or normoxia incubation with or without Ad (1 μg/mL). (B) DalGreen fluorescence measured every hour in H9c2 cells during hypoxia or normoxia incubation with or without Ad (1 μg/mL) for 24 h. (C)

Representative Western blot images of p62, LC3 and GAPDH after hypoxia incubation with Ad for 12 h. (D and E) Densitometry analysis of p62 and LC3B-II to GAPDH from 5C. (F) Representative confocal microscope images of H9c2 cells stained with DalGreen and DapRed in normoxia or hypoxia conditions with or without Ad for 12 h. (G) Quantification of the green to red ratio from 5F. (H) Representative confocal microscope images of H9c2 cells stained with MagicRed after hypoxia incubation with Ad for 12 h. (I) Quantification of MagicRed fluorescence from 5H. Results are presented as mean ± SEM (n = 3 per group). *$p < 0.05$, **$p < 0.01$, ***$p < 0.001$ versus control. Two-way ANOVA with Bonferroni correction was run for statistical analysis. Scale bar = 20 μm. Ad, adiponectin; ANOVA, analysis of variance; Con, control; Hypo, hypoxia; Nor, normoxia.

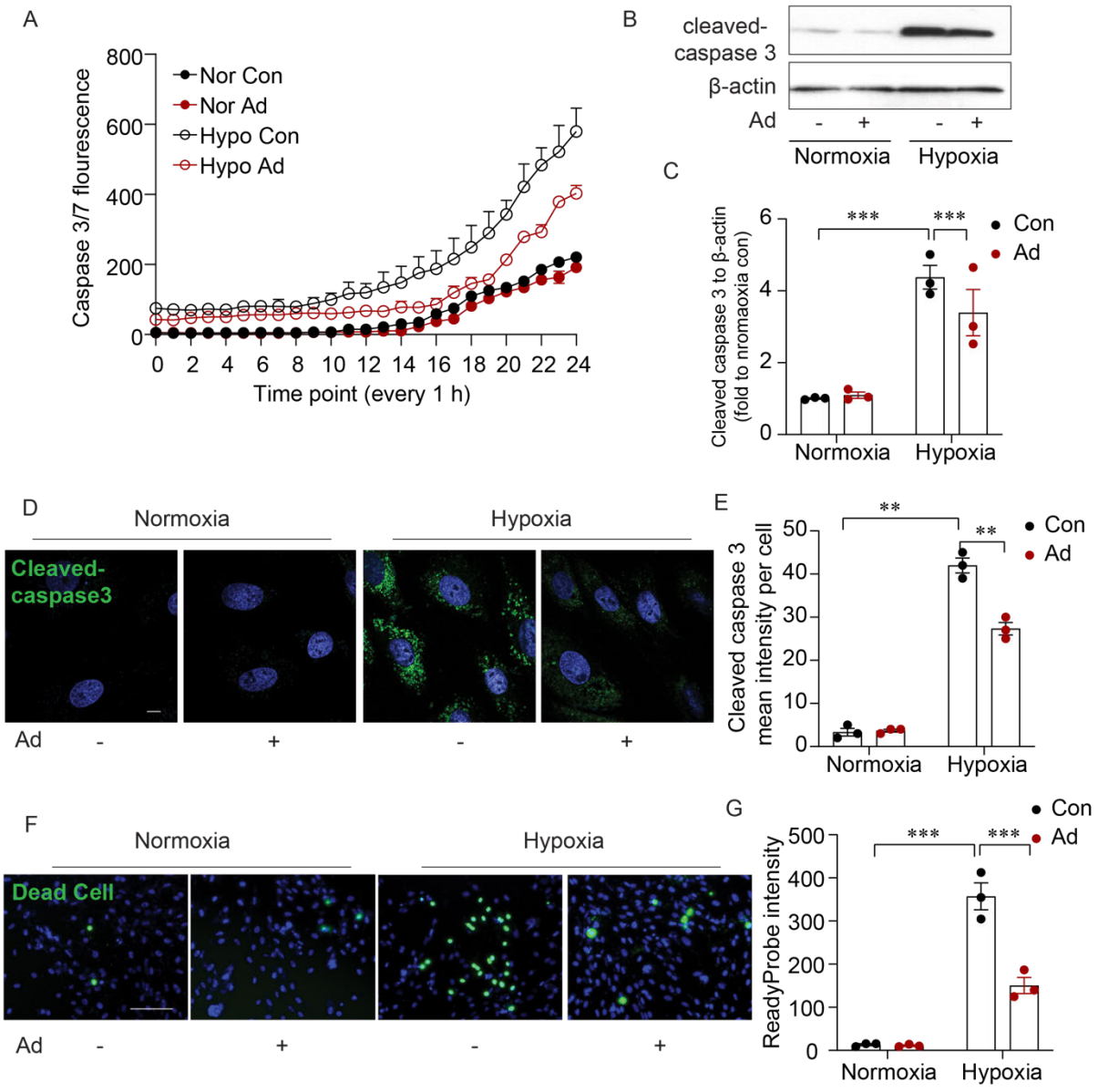

(Adapted from Sung HK, Tang J, et al. Clinical and Translational Science 2024; 17:e13758)

Figure 5.2 Adiponectin treatment enhanced autophagy flux in hypoxic cells in vitro

(A) Caspase 3/7 fluorescence measured for 24 h every 1 h innormoxia or hypoxia conditions with or without Ad treatment. (B) Representative Western blot images of cleaved caspase 3 and βactin expression in H9c2 cells after hypoxic incubation with Ad (1 μg/mL) for 24 h. (C) Densitometryanalysis of cleaved caspase 3 to β-actin expression in H9c2 cells from Figure 6b. (D) Representative confocal microscope images of H9c2 cells stably expressing VC3AI showing

cleaved caspase 3 (green) after hypoxia incubation with Ad (1 μg/mL) for 48 h. (E) Quantification of cleaved caspase 3 per cells from Figure 6d. (F) Representative confocal microscope images of H9c2 cells stained with ReadyProbe (green) after hypoxia incubation with or without Ad (1 μg/mL) for 24 h. (G) Quantification of cell death from Figure 6f. Results are presented as mean ± SEM (n = 3 per group for Figure 7 A-J). **$p < 0.01$, ***$p < 0.001$ versus control. Two-way ANOVA with Bonferroni correction was run for statistical analysis. Scale bar = 20 μm for Figure 6d and 5 μm for Figure 6f. Ad, adiponectin; ANOVA, analysis of variance; Con, control; Hypo, hypoxia; Nor, normoxia.

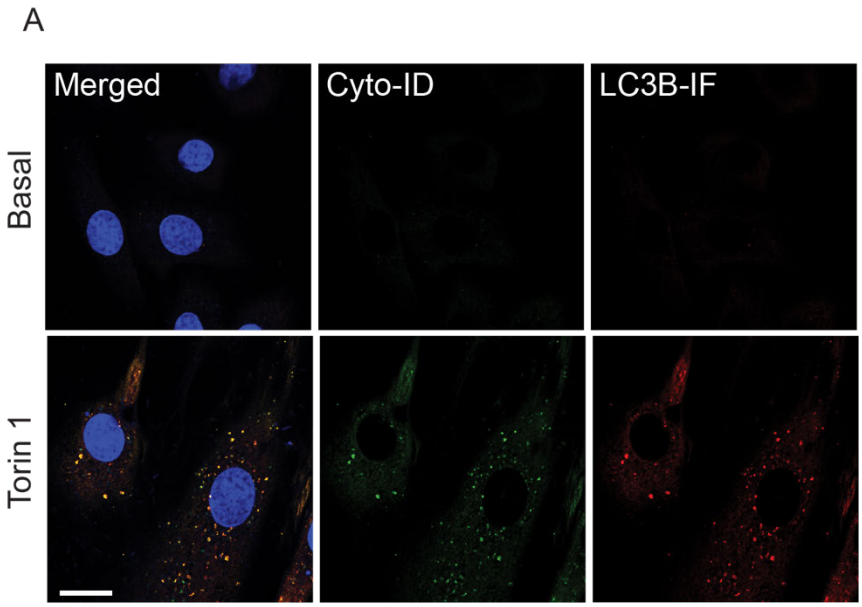

(Adapted from Sung HK, Tang J, et al. Clinical and Translational Science 2024; 17:e13758)

Figure 5.3 Validation of Cyto-ID and Magic Red assay to assess autophagy flux in H9c2 cells

(A) Representative confocal microscope images of H9c2 cells stained with Cyot-ID and LC3B IF after Torin-1 treatment (200 nM) for 1 hour. Scale bar = 10 μm

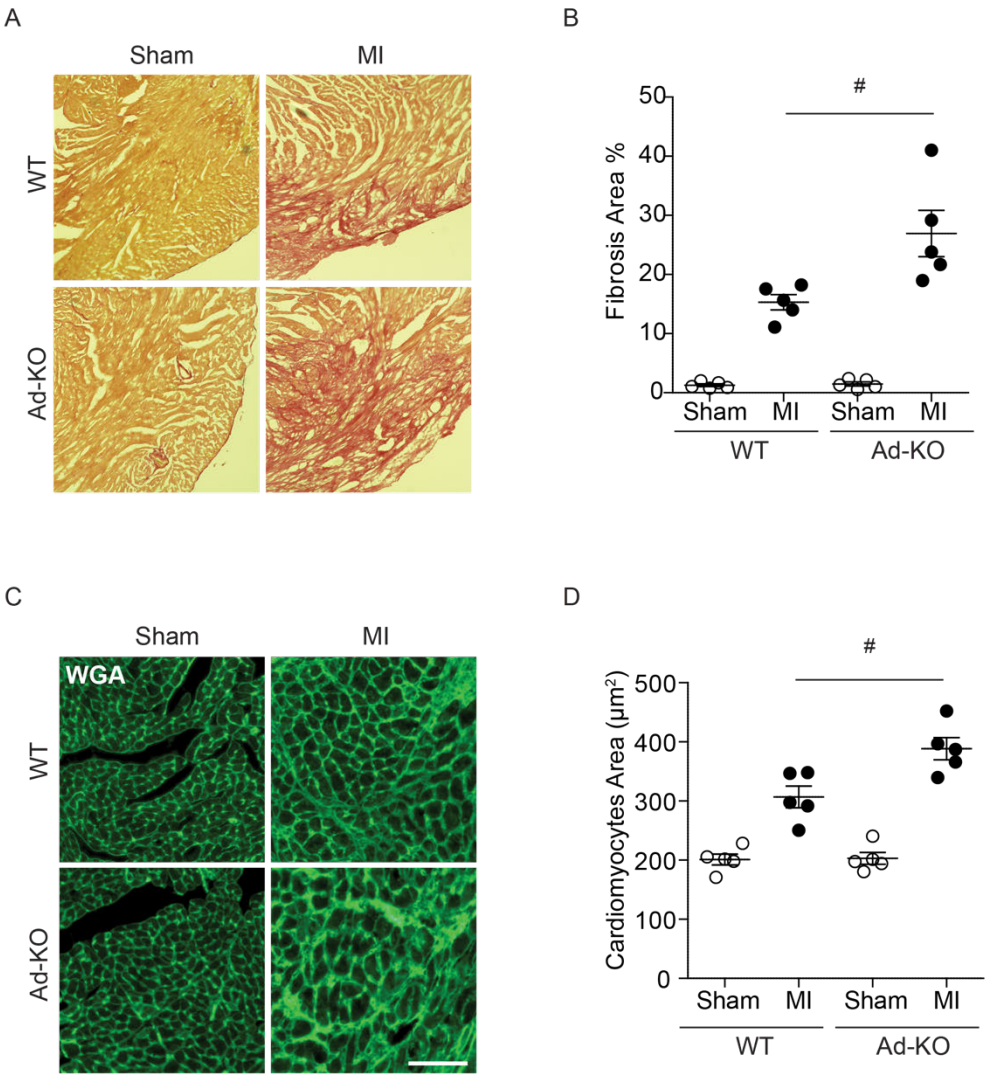

(Adapted from Sung HK, Tang J, et al. Clinical and Translational Science 2024; 17:e13758)

Figure 5.4 Exacerbated cardiac remodeling in Ad-KO mice after MI

(A) Representative paraffin embedded heart section stained with picosirius red staining after 7 days MI. (B) Quantification of fibrotic area at mid-ventricular section. (C) Representative images of WGA staining on paraffin embedded hearts after ischemia. (D) Quantification of cardiomyocyte cross sectional area at infarct zone. Results are presented as mean ± SEM (n=5 per group, biological replicates). *P<0.05 versus corresponding sham. #P<0.05 versus WT-MI. Two-way ANOVA test with Bonferroni correction was performed for statistical significance. Scale bar = 20 μm.

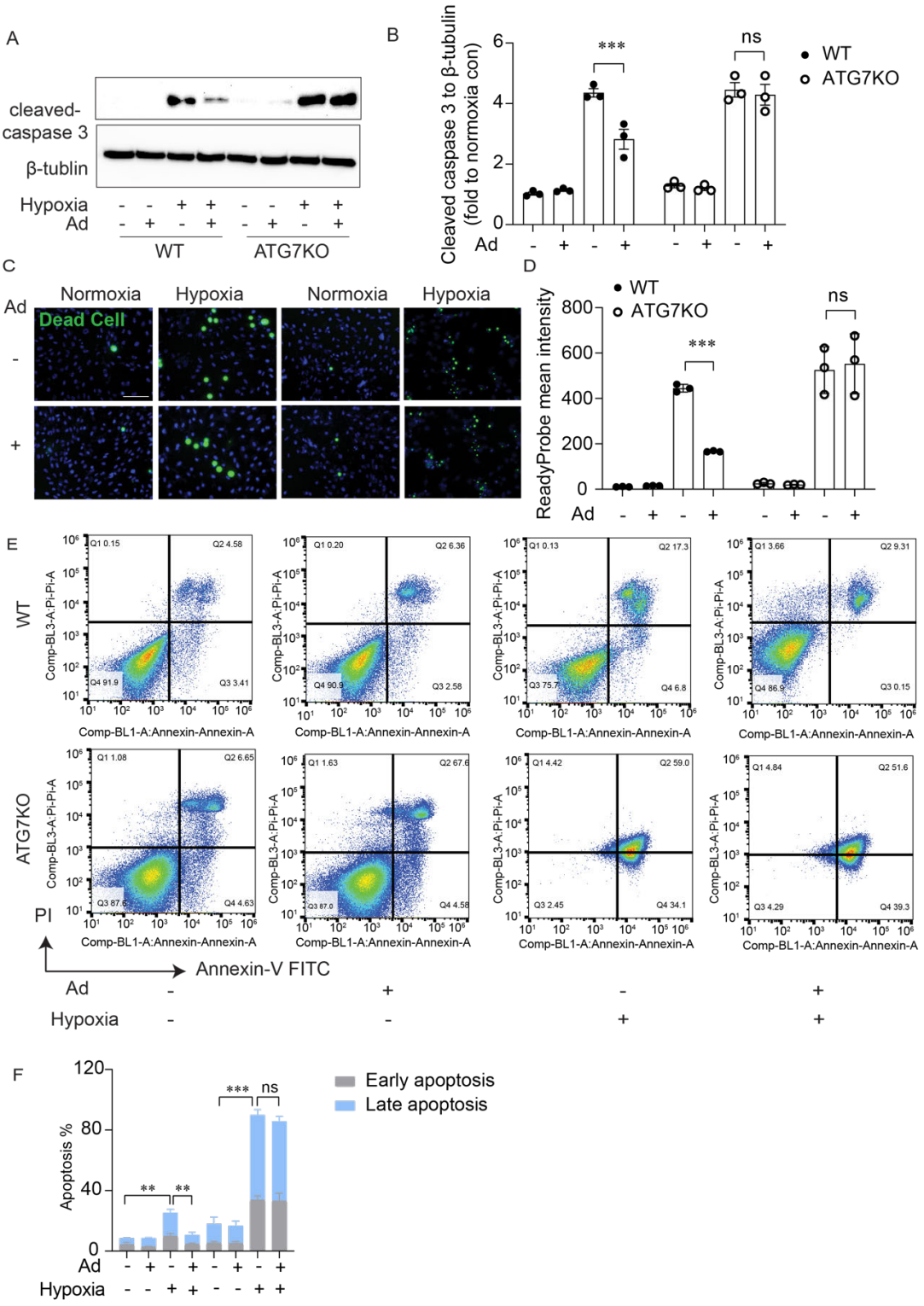

(Adapted from Sung HK, Tang J, et al. Clinical and Translational Science 2024; 17:e13758)

Figure 5.5 Hypoxia-induced apoptosis is alleviated by apoptosis through its effect on autophagy

(A) Representative Western blot image of cleaved caspase 3 and β-actin in WT or ATG7-KO H9c2 cells after hypoxia incubation or normoxia incubation with or without Ad for 24 h. (B) Densitometry analysis of cleaved caspase 3 to β-actin from Figure 7a. (C) Representative confocal microscope images of WT and ATG7-KO H9c2 cells after hypoxia incubation with Ad treatment for 24 h stained with ReadyProbe (green). (D) Quantification of cell death from 7C. (E) Flow cytometry in WT and ATG7-KO H9c2 cells after hypoxia or normoxia incubation with or without Ad treatment for 48 h stained with PI and annexin V. (F) Quantification of early and late apoptosis in WT and ATG7-KO H9c2 cells after hypoxia incubation with Ad for 48 h. Results are presented as mean ± SEM (n = 3 per group for Figure 6 A-C and H-J, n = 9 per group for Figure 6 F and G). *$p < 0.05$, **$p < 0.01$, ***$p < 0.001$ versus control. Two-way ANOVA with Bonferroni correction was run for statistical analysis. Scale bar = 5 μm. Ad, adiponectin; ANOVA, analysis of variance; KO, knock out; ns, not significant; PI, propidium iodide.

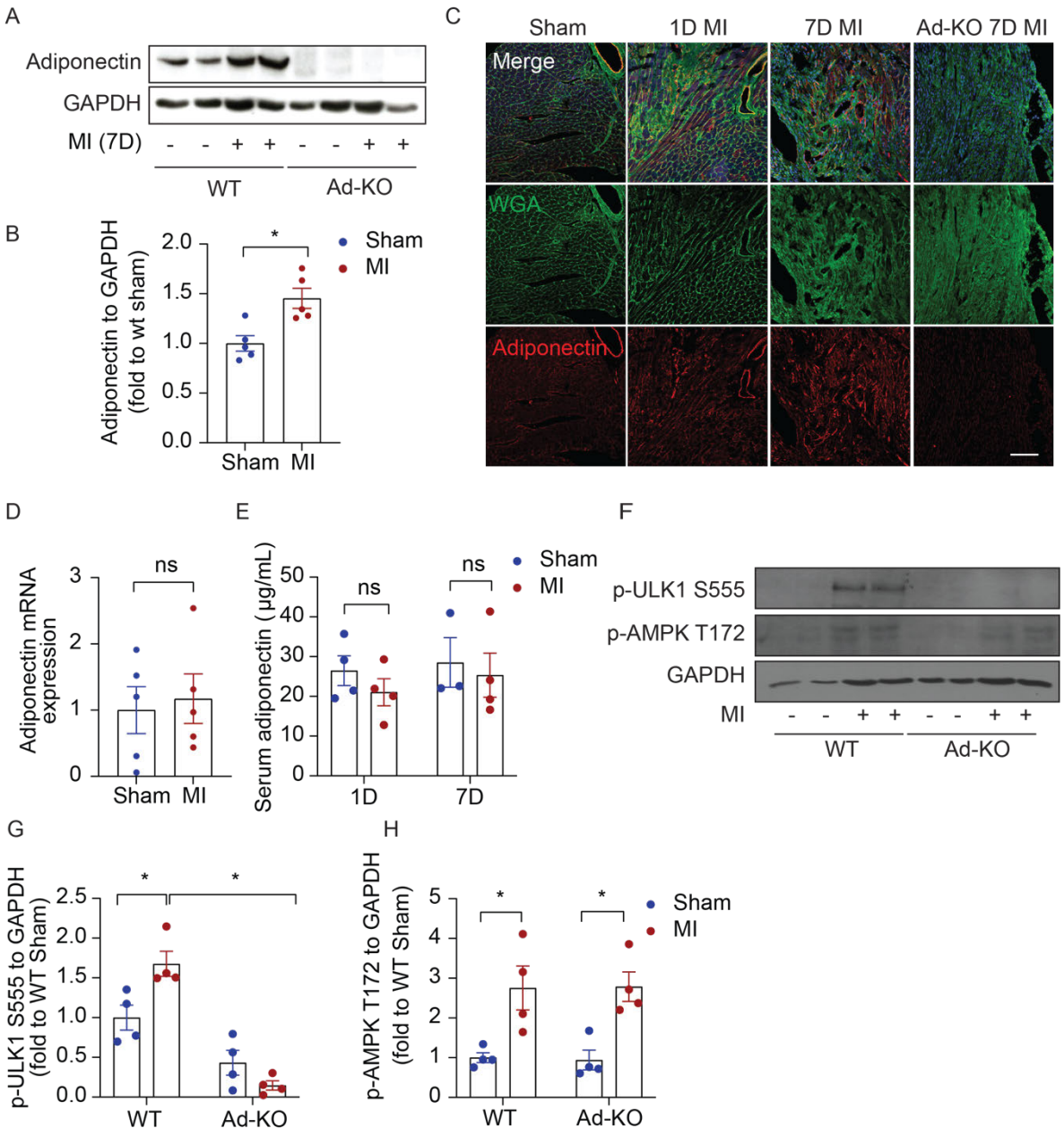

(Adapted from Sung HK, Tang J, et al. Clinical and Translational Science 2024; 17:e13758)

Figure 5.6 Accumulation of regional adiponectin at infarct zone after ischemia

(A) Representative western blot image of adiponectin and GAPDH in apex heart homogenates after 7 days (7D) MI. (B) Densitometry analysis of adiponectin over GAPDH in 1 day (1D) ischemia hearts. (C) Representative immunofluorescence images showing adiponectin (red) and WGA staining (green) in paraffin embedded heart after CAL. (D) Relative adiponectin mRNA expression over 18srRNA in heart apex after 7D MI. (E) ELISA quantification of adiponectin in

serum after 1 day or 7 days MI. (F) Representative Western blot images of p-AMPK T172, p-ULK1 S555, and GAPDH in apex heart homogenates after 1D MI. (G-I) Densitometry analysis of adiponectin, p-AMPK T172 and p-ULK1 S555 to GAPDH from Figure 1f. Results are presented as mean ± SEM (n = 5 per group for 7 days ischemia, n = 4 per group for 1 day ischemia, biological replicates). *p < 0.05 versus corresponding sham, #p < 0.05 versus WT MI. Two-way ANOVA with Bonferroni correction was performed in Figure 1G-I. Unpaired student t-test was run for statistical analysis in Figure 1B, D and E. Scale bar = 100 μm. Ad-KO, adiponectin-knock out; ANOVA, analysis of variance; CAL, coronary artery ligation; MI, myocardial infarction; ns, not significant; WGA, wheat germ agglutinin; WT, wild type.

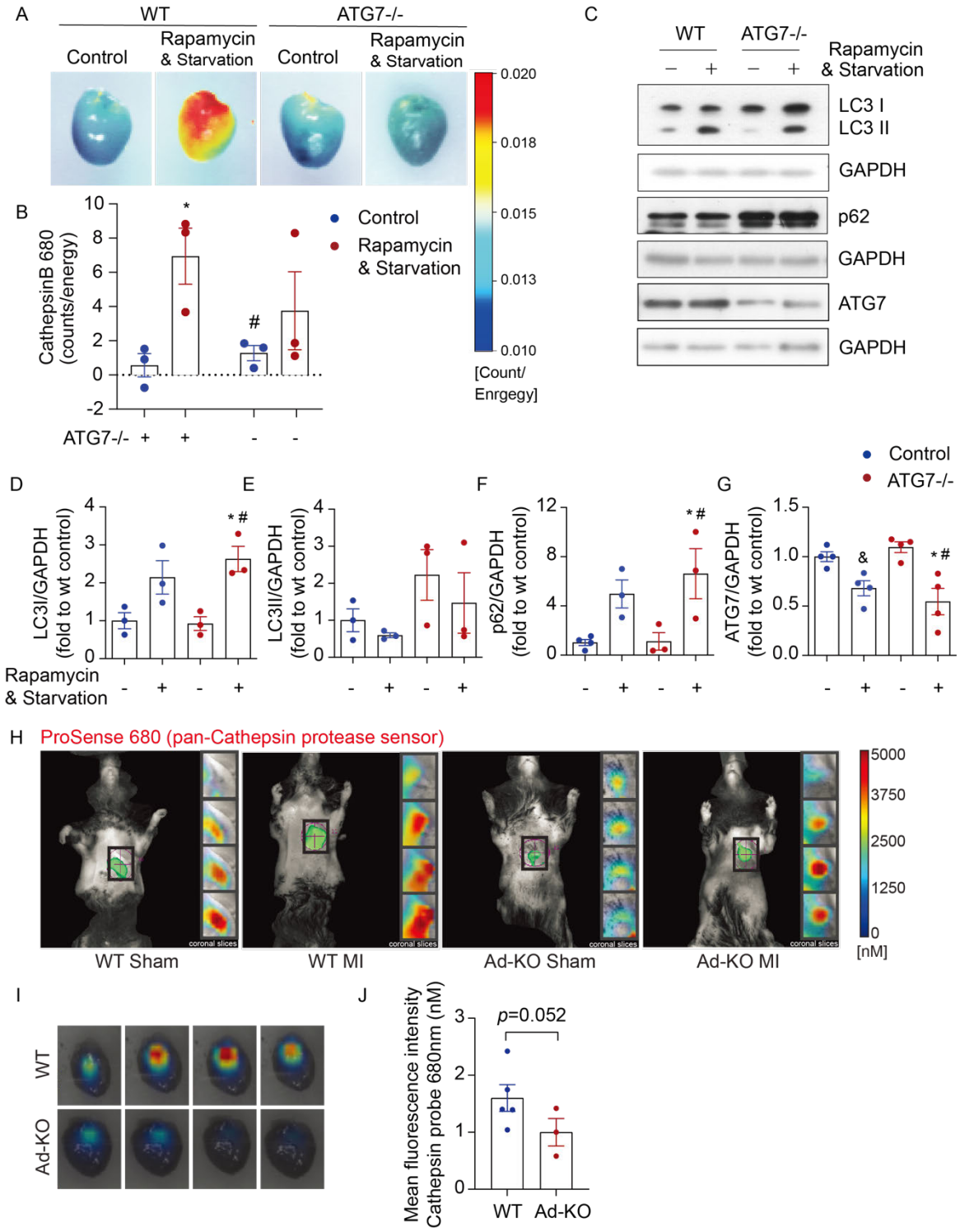

(Adapted from Sung HK, Tang J, et al. Clinical and Translational Science 2024; 17:e13758)

Figure 5.7 Validation of detection of myocardial autophagy flux via cathepsin B activity. Ischemia impairs the autophagy response in Ad-KO mice

(A) To elevate autophagy flux, Tamoxifen-induced cardiomyocyte specific ATG7-deficient and control mice were treated with rapamycin and starved for 24 h. All mice were infused with a cathepsin B 680 probe. Ex vivo FMT 2-dimensional analysis using isolated hearts is shown. * Indicates versus WT-control and # indicates versus WT-"rapamycin and starvation" condition and (B) quantification ($n = 3$, *,#$p < 0.05$). (C-G) Whole heart homogenates were analyzed by Western blotting with antibodies for validated autophagy markers, p62 and LC3. To confirm induction of cardiomyocyte-specific ATG7-deletion, ATG7 antibody was used for Western blotting. (C) The representative images shown with their own internal control, GAPDH and (D-G) quantitative analysis in graphs with folding over control. In (D-G), $n = 3$ and * indicates versus WT-control. # and & indicates versus WT-"rapamycin and starvation." ($^{*,\#,\&}P < 0.05$). (H) Representative live FMT (ProSense 680, pan-cathepsin protease sensor) in animals after MI. (I) Representative ex vivo FMT scan. (J) Quantification of Figure 2i. Results are presented as mean ± SEM ($n = 3$ per group for (h–k), biological replicates). *$p < 0.05$ versus corresponding sham. Two-way ANOVA with Bonferroni correction was run for statistical analysis. Ad-KO, adiponectin-knock out; ANOVA, analysis of variance; FMT, fluorescence molecular tomography; MI, myocardial infarction; WT, wild type.

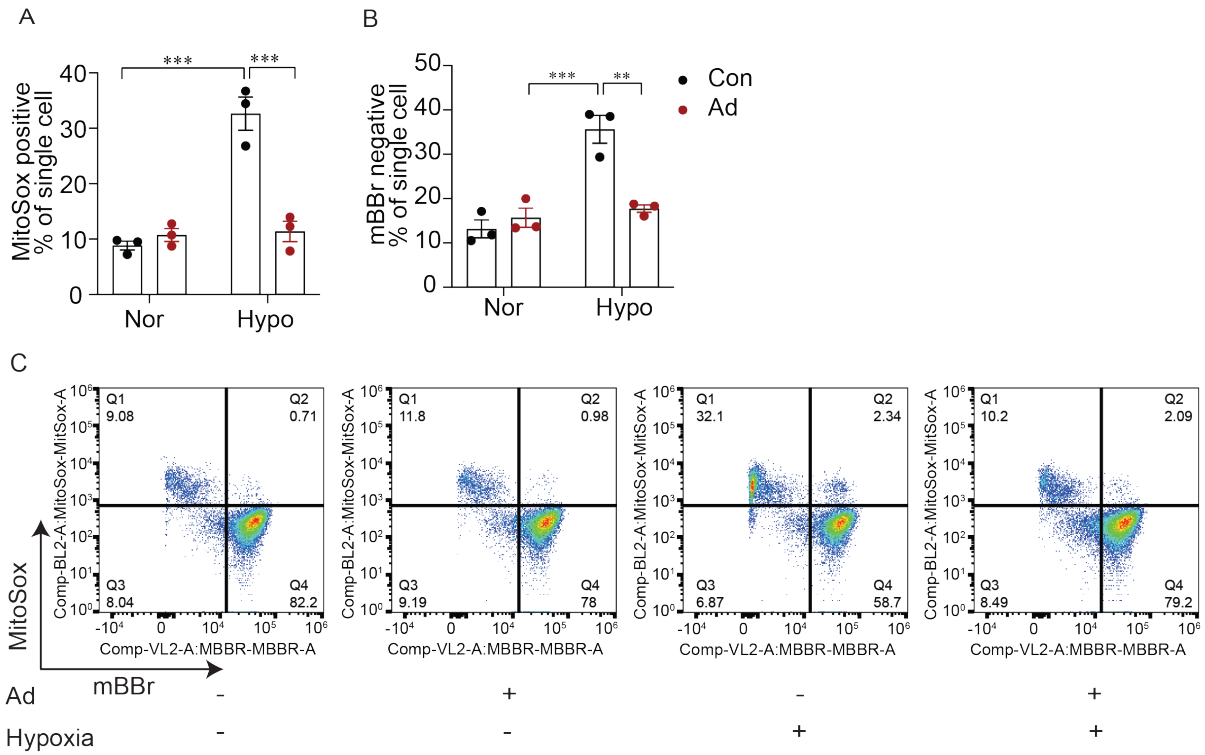

(Adapted from Sung HK, Tang J, et al. Clinical and Translational Science 2024; 17:e13758)

Figure 5.8 Adiponectin treatment alleviates oxidative stress in H9c2 cells during hypoxia.

(A) Quantification of MitoSox positive % of single cell. (B) Quantification of mBBR negative % of single cell. (C) Flow cytometry performed in H9c2 cells after hypoxic incubation with Ad for 24 hours using mitoSox and mBBr. Results are presented as mean ± SEM (n=3 per group for 7A-J). **P<0.01, ***P<0.001 versus control. Two-way ANOVA with Bonferroni correction was run for statistical analysis.

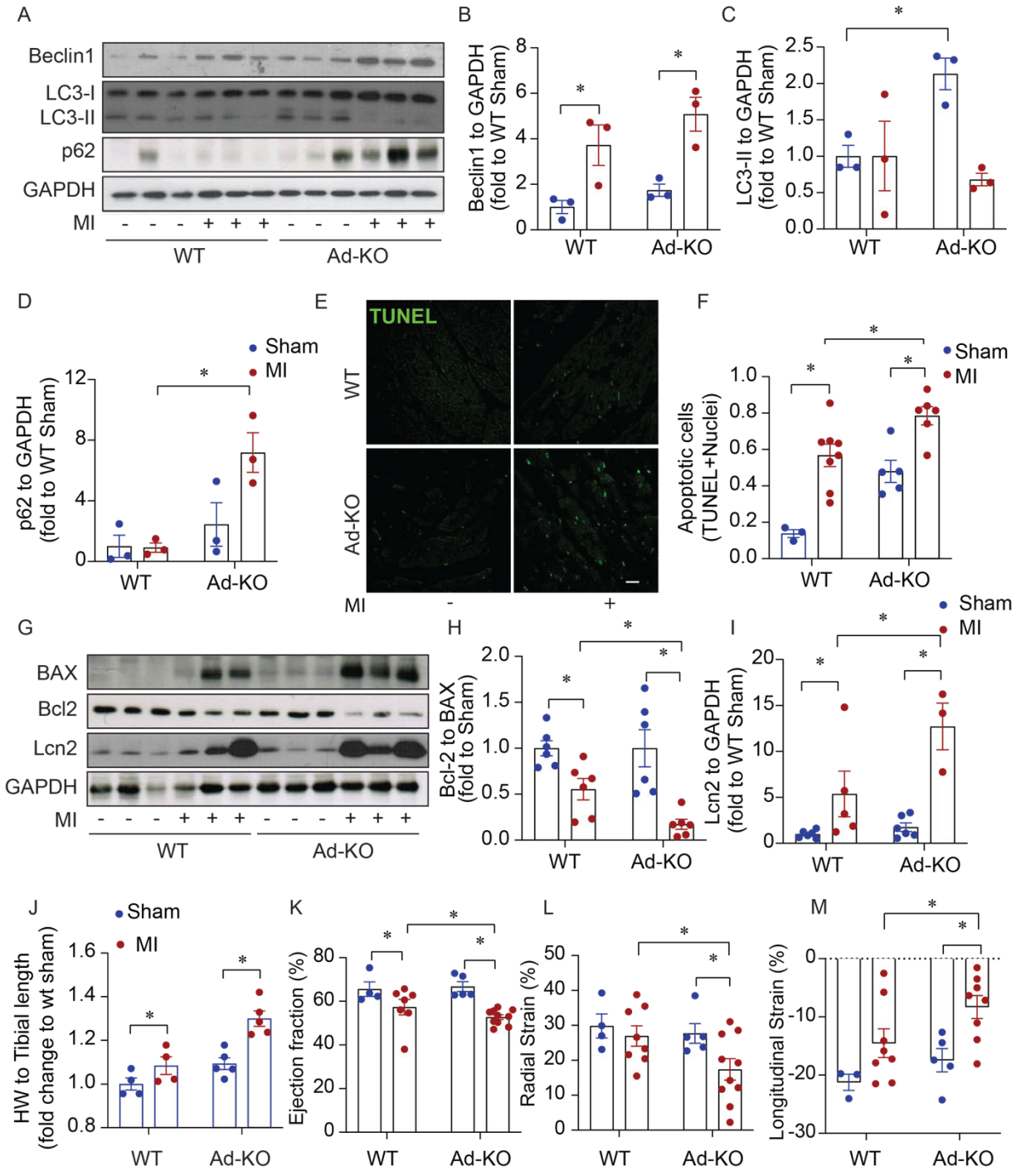

(Adapted from Sung HK, Tang J, et al. Clinical and Translational Science 2024; 17:e13758)

Figure 5.9 Ad-KO mice have reduced ejection fraction, impaired cardiac function, increased autophagy and apoptosis after ischemia

(A) Representative western blot images of Beclin-1, LC3B, p62, and GAPDH from apex heart homogenates after MI. (B-D) Densitometry analysis of Beclin-1, LC3-II, and p62 to GAPDH from Figure 2A. (E) Representative TUNEL staining images in heart sections from WT and Ad-KO mice with or without ischemia surgery. (F) Quantification of TUNEL positive nuclei from Figure 3g. (G) Representative western blot images of BAX, Bcl2, Lcn2 (lipocalin 2), and GAPDH from apex hearts after MI. (H-J) Densitometry analysis of Bcl2 over BAX and Lcn2 over GAPDH. (J) Gross heart weight to tibial length ratio in WT and Ad-KO mice after 7 days MI. (K) Representative M-mode images of heart after MI. (L) Ejection fraction measured from 3B. (M) Representative images of B-mode showing changes in strains over three cardiac cycles in radial and longitudinal directions from hearts with or without ischemia surgery. (N-O) Quantification of average strains from six segments in Figure 3d. Results are presented as mean ± SEM (n = 5 per group, biological replicates). *P < 0.05 versus corresponding sham. #P < 0.05 versus WT Ischemia. Two-way ANOVA with Bonferroni correction was run for statistical analysis. Scale bar = 50 μm. Ad-KO, adiponectin-knock out; ANOVA, analysis of variance; MI, myocardial infarction; WT, wild type.

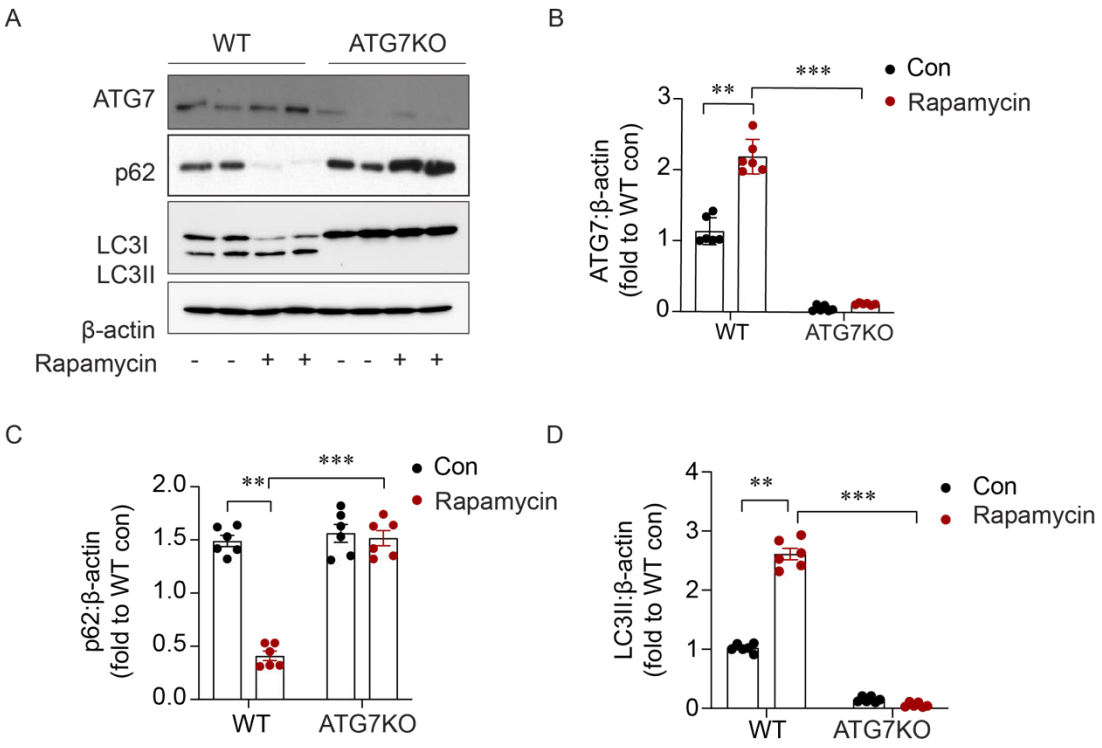

(Adapted from Sung HK, Tang J, et al. Clinical and Translational Science 2024; 17:e13758)

Figure 5.10 Expression of autophagy markers is not altered following adiponectin treatment in autophagy deficient cells

(A) Representative western blot images of ATG7, p62, LC3 and β-actin in WT and ATG7-KO H9c2 cells with or without Rapamycin (500nM) treatment for 16 hours. (B-D) Quantification of ATG7, p62, LC3 over β-actin from S3A. Results are presented as mean ± SEM (n=6 per group, biological replicates). *P<0.05, **P<0.01, ***P<0.001 versus respective controls. Two-way ANOVA test with Bonferroni correction was performed for statistical significance.

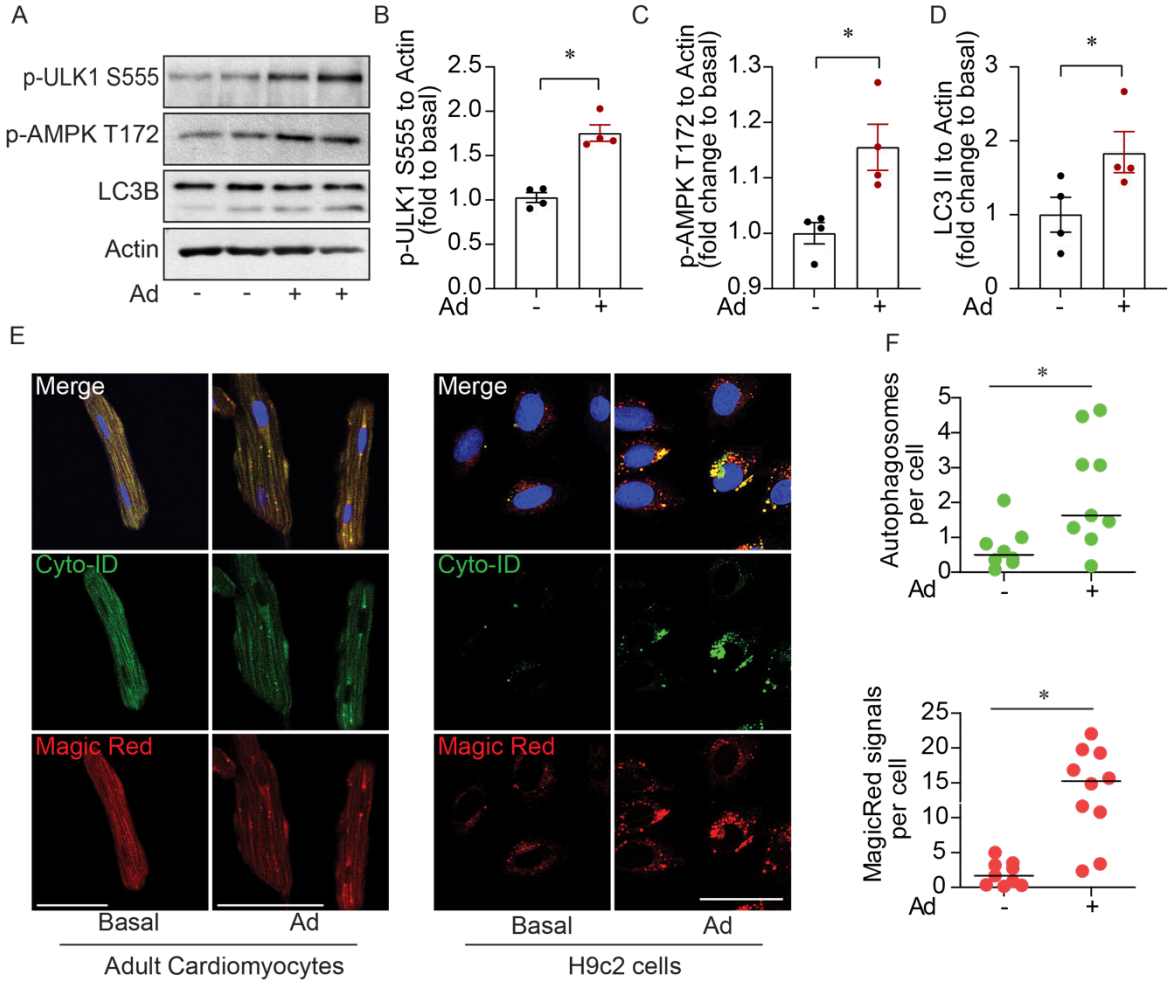

(Adapted from Sung HK, Tang J, et al. Clinical and Translational Science 2024; 17:e13758)

Figure 5.11 Autophagy is stimulated by adiponectin treatment in vitro in cardiomyocytes and H9c2 cells

(A) Representative Western blot images of p-ULK1 S555, p-AMPK T172, LC3B, and β-actin in H9c2 cells after adiponectin stimulation (1 μg/mL, 30 min). (B-D) Quantification of p-ULK1 S555, p-AMPK T172, LC3-l, and LC-ll over β-actin from Figure 4a. (E) Representative confocal microscope images of rat adult cardiomyocytes and H9c2 cells stained with Cyto-ID and Magic Red after Ad treatment (1 μg/mL) for 30 min. (F) Quantification of Cyto-ID and Magic Red puncta in 4E for H9c2 cells. Results are presented as mean ± SEM (n = 4 per group for a–d, n = 9 per group for e and f). *p < 0.05 versus control. One-way ANOVA with Dunnett post-test was performed for statistical analysis in Figure 4B-D. Unpaired student's t-test was performed for

statistical analysis in Figure 4f. Scale bar = 50 μm. Ad-KO, adiponectin-knock out; ANOVA, analysis of variance.

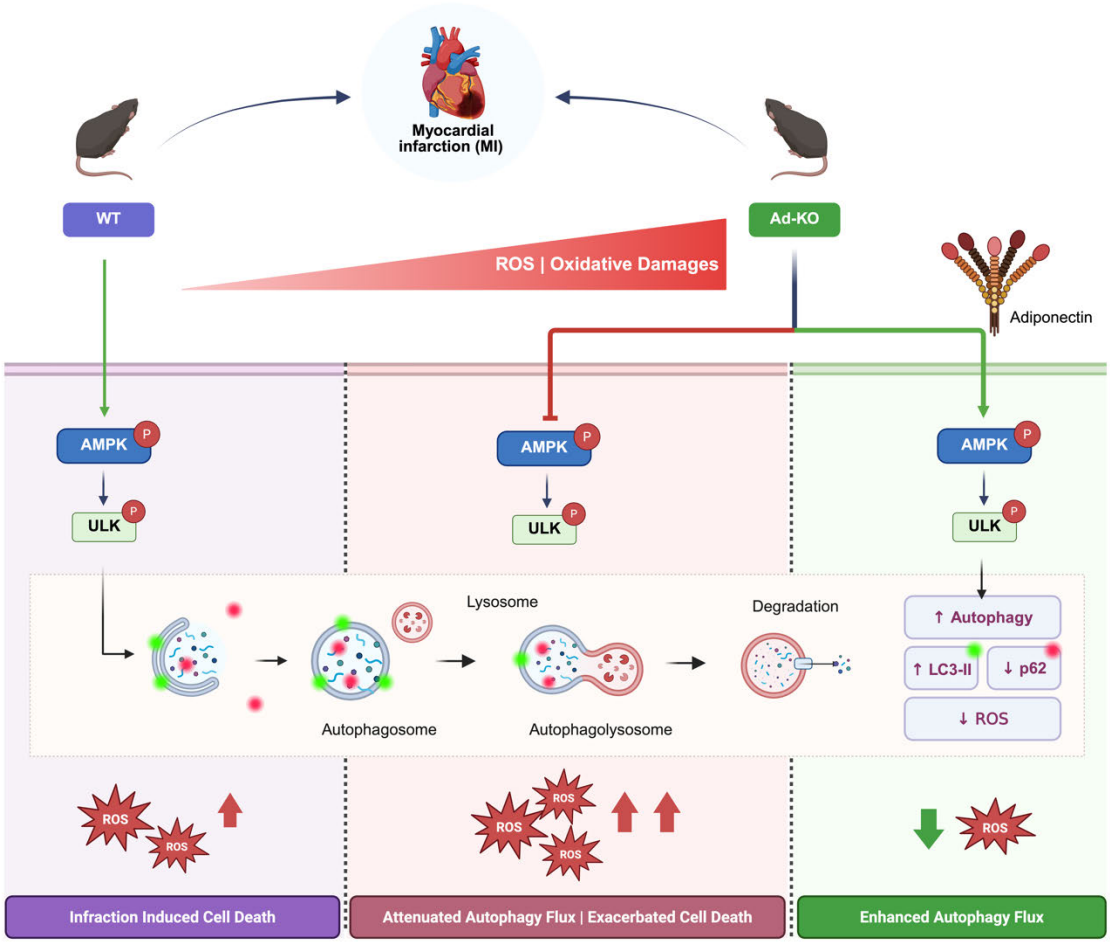

(Adapted from Sung HK, Tang J, et al. Clinical and Translational Science 2024; 17:e13758)

Figure 5.12 Graphical abstract

Adiponectin plays a pivotal role in protecting against ischemic injury via stimulating cardiac autophagy. In a permanent coronary artery ligation model, adiponectin-deficient mice exhibited an impaired autophagy response, measured via ULK1/AMPK phosphorylation and altered levels of autophagy markers LC3 (depicted as green dot) and p62 (red dot). In this way, adiponectin provided protective effects by mitigating ischemia/hypoxia-induced ROS production and cell death. Ad-KO, adiponectin-knock out; ROS, reactive oxygen species.

5.5 Discussion

Many clinical studies have demonstrated an inverse correlation of circulating adiponectin levels with the development and progression of various forms of cardiovascular diseases (349, 350). Ad-KO mice have exacerbated cardiac remodeling and dysfunction in various models of heart failure, which could be prevented by restoring normal adiponectin levels (267, 475-478). The mechanisms behind these effects remain to be fully defined. We and others have now demonstrated that adiponectin stimulates autophagy flux in cardiomyocytes (202) (479) (480). The link between autophagy and cell death in models of MI has been previously established (336, 481) and the majority of studies indicate that induction of autophagy is a protective mechanism that reduces the extent of ischemia-induced acute cell damage and also reduces the extent of postinfarction cardiac remodeling and dysfunction (463, 482). Nevertheless, it should also be noted that it has been demonstrated that cardiomyocytes can go through various forms of cell death during MI and that excess autophagy may in fact contribute to autophagic cell death (483). The present study was designed to examine the functional importance of adiponectin-stimulated myocardial cardiac autophagy in mice during ischemia. Parallel studies were conducted in a cellular model using hypoxia.

Here, we observed that in WT mice, adiponectin accumulates in the damaged myocardium. In keeping with our observation, previous work indicated that the adiponectin level was increased in LV post-MI in a rat model of heart failure (483). In that study, there was also a decreased adiponectin levels in plasma, which we did not observe in this study. Furthermore, another study in mice showed that adiponectin accumulates in the heart following ischemic damage and that it principally occurred via leakage from the vascular compartment (467). Our data supports this notion because we saw elevated adiponectin protein levels in the heart but did not observe any change in mRNA expression. It is also important to point out that the local production by cell types in the myocardium is orders of magnitude smaller than that from adipose tissue entering the circulation and thus circulating levels do not change significantly even though there is detectable local accumulation in the heart. This localized accumulation of adiponectin may be important in allowing enhanced local signaling leading to downstream consequences, such as stimulation of autophagy. Indeed, the accumulation of adiponectin was associated with significantly increased AMPK and ULK1 (Ser 555) phosphorylation in hearts after 7 days of ischemia, indicating activation of adiponectin targets.

We also developed a noninvasive fluorescent molecular tomography-based protocol using a near infrared (680 nm) activatable probe to assess lysosomal cathepsin activity as a surrogate for assessing autophagy flux in live mice. The concept for this approach is similar to a novel method which was published recently(484, 485). First, to validate the correlation between myocardial Cat-B 680 signal and autophagy, we began our study using mice with inducible cardiomyocyte autophagy-deficiency caused by deletion of Atg7. We believe that this approach represents a very useful step forward in allowing researchers to gauge temporal changes in autophagy flux via a noninvasive approach, whereas acknowledging that final conclusions should be supported by established biochemical approaches. This data indicated that hearts of Ad-KO mice had less lysosomal degradative activity compared with WT mice after ischemia. Ad-KO mice cannot accumulate adiponectin in damaged myocardium and have a disrupted autophagy flux when compared to WT after chronic myocardial ischemia. Other studies have also indicated that adiponectin can directly stimulate myocardial autophagy and consequently confer cardioprotection (202) (479, 480).

Using echocardiography, including strain analysis, we observed that mice lacking adiponectin had an enhanced degree of cardiac dysfunction. Correlated with this was a significant increase in indices of cell death, such as more TUNEL positive cells and increased Bcl2:BAX ratio in Ad-KO versus WT mice after ischemia. These data were expected because the ability of adiponectin to attenuate myocardial cell death, or adiponectin deletion to exacerbate cell death, is well-established (486-488). We also discovered in this study that induced ischemia led to increased lipocalin-2 accumulation in the heart, which was further elevated in Ad-KO mice. We previously reported that lipocalin-2, a pro-inflammatory cytokine mainly produced by neutrophils, causes cell death by enhancing oxidative stress and reducing autophagy flux in cardiomyocytes (471, 472, 489, 490). Hence, it is likely that adiponectin counteracts these effects of lipocalin-2 in WT mice. This represents one mechanism contributing to the anti-inflammatory effects of adiponectin and our data suggests that this emerging theme of crosstalk between adiponectin and lipocalin-2 in models of prolonged ischemia or ischemia–reperfusion should be further explored (491-493).

To further investigate our observations from studies in WT and Ad-KO mice, we also used the cellular models of primary adult rat cardiomyocytes or H9c2 cells subjected to hypoxia. Previous studies have indicated that adiponectin reduced apoptosis induced by chronic intermittent hypoxia and inhibited hypoxia/reoxygenation-induced necroptosis and intrinsic apoptosis via AdipoR1-

APPL1- AMPK signaling in H9c2 cells (494, 495). We found that autophagy flux was enhanced following adiponectin treatment in normoxic or hypoxic conditions. Importantly, to verify the functional significance of adiponectin-stimulated autophagy, we generated an autophagy-deficient cell model using CRISPR to delete Atg7. Whereas adiponectin reduced hypoxia-induced cell death in control cells, this effect was lost in Atg7-KO cells. A recent study also concluded that adiponectin induced ER-phagy to attenuate hypoxia-induced apoptosis in H9C2 cardiomyocytes (494). The same concept has been demonstrated in a model of resuscitation induced brain apoptosis, where adiponectin attenuated damage in an autophagy-dependent manner (479). Adiponectin was known reduce apoptosis caused by H_2O_2 in chondrocytes via stimulating autophagy (496). Furthermore, adiponectin protected hepatocytes from acetaminophen-induced cell via promoting autophagy (496). The verification of the functional significance of autophagy in the beneficial anti-apoptotic effects of adiponectin is an important result from this study.

In conclusion, our study demonstrates that adiponectin is an important mediator of cardiac autophagy. We first evaluated the role of adiponectin in regulating ischemic remodeling using a permanent coronary artery ligation model. We reported that mice lacking adiponectin subjected to MI have an impaired autophagy response, increased cellular apoptosis, and exacerbated cardiac dysfunction. Treatment of H9c2 cells with adiponectin increased autophagy flux and mitigated apoptosis under hypoxia conditions. Finally, lack of adiponectin's beneficial effect in the autophagy deficient cell line engineered by CRISPR-mediated ATG7 knockout, indicated that adiponectin mitigated hypoxia-induced apoptosis in an autophagy-dependent manner. Therefore, we demonstrated the importance of an adiponectin-autophagy axis in mitigating ischemia or hypoxia induced capase-3 activation and cell death. We have summarized these findings in a schematic diagram (Figure 4.8). This study further reinforces the potential of adiponectin as a therapeutic target to improve cardiac outcomes under ischemic conditions.

5.6 Statement of contribution

Animal experiments were performed by James Won Suk Jahng, Erfei Song. Fluorescence molecular tomography imaging in mice were done by James Won Suk Jahng. All animal associated analysis experiments were performed by James Won Suk Jahng, Erfei Song, and Hye Kyoung Sung. Genetic modification of H9c2 cells was performed by the Genome Editing and Molecular Biology Facility. Cell culture and associated experiments were done by Jialing Tang, and Hye Kyoung Sung. Flow cytometry wad done by Abdul Hadee Lone. Statistical analysis was performed by Jialing Tang, Hye Kyoung Sung and James Won Suk Jahng. The original manuscript draft was written by James Won Suk Jahng, and Hye Kyoung Sung. Funding was acquired by Gary Sweeney.

6. Chapter 6: Discussion

6.1 Summary

This thesis investigated the cardioprotective mechanisms of adiponectin receptor signaling in myocardial ischemia-reperfusion injury through comprehensive in vivo and in vitro experimental approaches. The overarching goal was to elucidate how ALY688, a synthetic adiponectin receptor agonist, mitigates ischemic cardiac injury and to identify novel therapeutic targets within the adiponectin signaling network. Four interconnected studies addressed complementary aspects of adiponectin-mediated cardioprotection, revealing mechanisms spanning direct cellular effects, extracellular vesicle-mediated intercellular communication, organellar metabolic coupling, and autophagy regulation (Figure 6.1).

6.1.1 Study 1: ALY688 Protects Against Myocardial Ischemia-Reperfusion Injury via Direct Effects and Rab8a-dependent Extracellular Vesicles

This study established a dual cardioprotective mechanism for ALY688 in a rat model of myocardial ischemia-reperfusion injury. ALY688 administration during ischemia or at reperfusion significantly preserved cardiac function over 28 days, reduced infarct size, and attenuated adverse ventricular remodeling, indicating a clinically relevant therapeutic window.

At the cellular level, ALY688 exerted direct protective effects in hypoxia-reoxygenation models using H9c2 and human iPSC-derived cardiomyocytes. ALY688 restored autophagic flux, reduced reactive oxygen species accumulation and apoptosis, and preserved mitochondrial function. Multiple autophagy flux assays demonstrated that ALY688 normalized impaired autophagosome-lysosome fusion during reperfusion, preventing accumulation of damaged organelles and excessive autophagic cell death.

Proteomic analysis of infarcted myocardium revealed downregulation of Rab8a following ischemia-reperfusion, which was restored by ALY688 treatment. Given Rab8a's role in extracellular vesicle biogenesis, we investigated EV dynamics and observed increased EV accumulation in ALY688-treated hearts. Serum EV analysis confirmed enhanced EV production and incorporation of Rab8a into EV cargo.

CRISPR-mediated Rab8a knockout in H9c2 cells abolished ALY688-induced EV biogenesis and eliminated the cytoprotective effects of ALY688-derived EVs against hypoxia-reoxygenation

injury. Proteomic profiling showed that ALY688 reprogrammed EV cargo toward pathways involved in protein homeostasis, glucose metabolism, and antioxidant defense while suppressing stress-related metabolic enzymes.

Together, these findings demonstrated that ALY688 confers cardioprotection through direct effects on cardiomyocytes and by enhancing Rab8a-dependent EV-mediated intercellular communication, establishing EVs as active therapeutic mediators rather than passive biomarkers of cardiac injury.

6.1.2 Study 2: Extracellular Vesicle Reprogramming by ALY688 Provides Novel Cardioprotective Therapy for Myocardial Infarction

Building on the role of ALY688 in EV modulation, this study characterized the therapeutic potential of ALY688-shaped EVs across different metabolic states. Using lean and high-fat diet-fed mice subjected to permanent myocardial infarction, we demonstrated that ALY688 improved cardiac function, reduced infarct size, and attenuated fibrosis in both groups, indicating preserved efficacy despite metabolic dysfunction.

Myocardial infarction markedly reduced circulating EV levels, which were restored by ALY688 treatment. ALY688 also enhanced adiponectin loading into EVs, suggesting coordinated regulation of EV quantity and cargo. Proteomic profiling revealed that ALY688-shaped EVs were enriched in proteins involved in metabolic pathways, including fructose and cholesterol metabolism, as well as autophagy-related proteins such as ATG3.

Functional studies showed that EVs derived from ALY688-treated mice conferred superior protection to hypoxia-challenged cardiomyocytes compared to control EVs. These EVs reduced apoptosis and oxidative stress, restored autophagic flux, preserved mitochondrial function, and improved mitochondrial respiratory capacity.

ALY688-shaped EVs also normalized mitochondrial dynamics by increasing fusion proteins and suppressing excessive fission. Systemic administration of these EVs to infarcted mice reduced circulating cardiac injury markers, decreased apoptosis, and improved mitochondrial organization, recapitulating many benefits of direct ALY688 treatment.

This study demonstrated that ALY688-mediated EV reprogramming is a major driver of cardioprotection and that pharmacologically modified EVs can function as effective cell-free therapeutics. The preservation of efficacy in obese models highlights strong translational relevance.

6.1.3 Study 3: Loss of Rab8a-Dependent Tethering of Lipid Droplets to Mitochondria Drives Hypoxia-Reoxygenation Injury

This study examined how hypoxia-reoxygenation disrupts metabolic coupling between lipid droplets and mitochondria and how ALY688 preserves this interface. Lipidomic analysis revealed accumulation of toxic lipid species and marked depletion of lipid droplets, accompanied by downregulation of lipid storage and mobilization genes. Using genetic and pharmacological approaches, we demonstrated that lipid droplet breakdown during hypoxia-reoxygenation occurs through both lipophagy and classical lipolysis. Despite increased lipid catabolism, long-chain fatty acid trafficking to mitochondria was severely impaired, resulting in lipotoxic intermediate accumulation, ATP depletion, and mitochondrial dysfunction.

Rab8a emerged as a critical mediator of lipid droplet-mitochondria tethering. Rab8a interacted with PLIN5 and the mitochondrial protein Tom20 under normoxic conditions, interactions that were disrupted during hypoxia-reoxygenation. Rab8a knockout exacerbated organellar uncoupling, impaired fatty acid transfer, and reduced mitochondrial respiratory capacity.

Notably, Rab8a did not regulate lipophagy itself but specifically controlled fatty acid trafficking to mitochondria. ALY688 preserved Rab8a expression through an AMPK-dependent mechanism, restored lipid droplet-mitochondria proximity, improved mitochondrial function, and reduced cell death. These effects were completely lost in Rab8a-deficient cells.

This study identified Rab8a as a key regulator of cardiac lipid metabolism and demonstrated that preserving Rab8a-dependent organellar tethering represents a novel strategy to prevent lipotoxic injury during ischemia-reperfusion.

6.1.4 Study 4: Ischemia-induced Cardiac Dysfunction Is Exacerbated In Adiponectin-knockout Mice Due To Impaired Autophagy Flux

This study used adiponectin knockout mice to define the physiological role of endogenous adiponectin in ischemic heart injury. Following myocardial infarction, adiponectin-deficient mice exhibited more severe cardiac dysfunction, exaggerated remodeling, increased fibrosis, and elevated apoptotic and inflammatory markers compared to wild-type controls.

Autophagy flux was markedly impaired in adiponectin knockout hearts, as evidenced by accumulation of LC3-II and p62 and reduced AMPK-ULK1 signaling. Using a newly developed

fluorescence molecular tomography approach with cathepsin B-activatable probes, we demonstrated reduced lysosomal activity and impaired autophagic degradation in vivo. In wild-type hearts, ischemia induced regional adiponectin accumulation accompanied by enhanced AMPK and ULK1 phosphorylation, a compensatory response absent in knockout mice. In vitro, adiponectin treatment enhanced autophagy flux and significantly reduced hypoxia-induced apoptosis in cardiomyocytes.

Genetic deletion of ATG7 abolished adiponectin-mediated cytoprotection, demonstrating that functional autophagy is required for adiponectin's anti-apoptotic effects. Pharmacological autophagy induction failed to rescue this phenotype in autophagy-deficient cells.

Collectively, this study established adiponectin as an essential endogenous regulator of autophagy during cardiac ischemia and identified impaired autophagy flux as a key mechanism underlying worsened injury in adiponectin deficiency. The FMT-based imaging strategy provides a valuable tool for longitudinal assessment of autophagy in preclinical models.

6.2 Discussion

The four studies presented in this thesis collectively reveal a multifaceted and hierarchically organized cardioprotective network activated by adiponectin receptor signaling. Rather than operating through a single linear pathway, adiponectin-mediated protection emerges from coordinated actions spanning multiple biological scales: intracellular signaling cascades, organellar metabolic coupling, intercellular communication via extracellular vesicles, and systemic inter-organ crosstalk. This section synthesizes the major mechanistic themes that emerged across studies and discusses their implications for understanding cardiovascular pathophysiology and developing novel therapeutics.

6.2.1 Rab8a as a central hub integrating vesicular trafficking and metabolic compartmentalization

A particularly striking discovery emerging from Studies 1 and 3 is the dual role of Rab8a in mediating both extracellular vesicle biogenesis and intracellular lipid droplet-mitochondria tethering. This functional pleiotropy positions Rab8a as a master regulator of membranous compartmentalization in cardiomyocytes under metabolic stress.

Rab GTPases constitutes the largest family of small GTPases and function as molecular switches that cycle between inactive GDP-bound and active GTP-bound states to coordinate vesicular trafficking, membrane fusion, and organellar positioning. Rab8a has been primarily studied in the context of post-Golgi trafficking, ciliogenesis, and exocytosis in polarized epithelial cells (412, 434). Our findings extend Rab8a's functional repertoire to cardiac metabolism and intercellular communication.

In Study 1, Rab8a was identified through unbiased proteomic screening as significantly downregulated in infarcted myocardium but restored by ALY688 treatment. Functional validation using CRISPR-mediated Rab8a knockout demonstrated that Rab8a is essential for ALY688-stimulated extracellular vesicle biogenesis. Mechanistically, Rab8a likely facilitates the docking and fusion of multivesicular bodies with the plasma membrane, enabling release of intraluminal vesicles (exosomes) into the extracellular space. This aligns with emerging literature demonstrating that Rab8a coordinates the final steps of secretory autophagy and EV release by interacting with the exocyst complex (261, 263, 319-321, 411, 413, 416, 418), a multi-protein tethering complex that mediates vesicle fusion at the plasma membrane.

In Study 3, Rab8a emerged as a critical mediator of lipid droplet-mitochondria tethering, enabling efficient long-chain fatty acid transfer for β-oxidation. Immunoprecipitation and proximity ligation assays revealed that Rab8a forms physical complexes with PLIN5 (a lipid droplet coat protein) and Tom20 (a mitochondrial outer membrane translocase), thereby bridging these organelles. This function is conceptually analogous to the role of other tethering proteins at membrane contact sites, such as PLIN5 itself, Mfn2, and VDAC1-PLIN5 interactions, which create nanoscale junctions enabling lipid and metabolite exchange (410, 430).

The convergence of Rab8a function at both the plasma membrane (for EV release) and at lipid droplet-mitochondria interfaces (for fatty acid trafficking) raises intriguing mechanistic questions. One plausible model is that Rab8a-mediated lipid droplet-mitochondria tethering enables selective packaging of lipid-derived metabolites or signaling lipids into EVs, thereby coupling intracellular lipid metabolism with extracellular lipid signaling. Alternatively, Rab8a may coordinately regulate both lipid droplet catabolism (via enhancing mitochondrial fatty acid oxidation) and lipid droplet-derived EV cargo loading. Supporting this hypothesis, recent lipidomic profiling of extracellular vesicles has revealed enrichment of ceramides, diacylglycerols, and other bioactive lipids, many

of which are derived from lipid droplet metabolism (497-499). Future studies employing Rab8a point mutants defective in specific protein-protein interactions (e.g., PLIN5 binding vs. exocyst binding) will be necessary to dissect whether these functions are mechanistically linked or represent independent roles of Rab8a in distinct subcellular compartments.

From a therapeutic perspective, Rab8a represents an attractive pharmacological target. Unlike global autophagy modulators, which carry risks of off-target effects, Rab8a-targeted interventions could selectively enhance both EV-mediated cardioprotective signaling and intracellular metabolic efficiency without perturbing basal cellular homeostasis. Small molecules that stabilize Rab8a in its GTP-bound active state or prevent its degradation during ischemia-reperfusion could recapitulate the beneficial effects of ALY688 observed in Studies 1 and 3.

6.2.2 Context-Dependent Autophagy Regulation: Balancing Cytoprotecting and Cell Death

Autophagy emerged as a recurring theme across all four studies, yet its role varied depending on the timing, magnitude, and cellular context of ischemic injury (500-503). This apparent complexity reflects the dual nature of autophagy as both a survival mechanism (when appropriately regulated) and a potential contributor to cell death (when excessive or dysregulated).

In Study 1, acute ischemia-reperfusion injury was associated with impaired autophagic flux, as evidenced by accumulation of both LC3-II and p62, indicating a block in autophagosome-lysosome fusion or lysosomal degradation capacity. ALY688 treatment restored autophagic flux by enhancing lysosomal cathepsin B activity and promoting autophagosome-lysosome fusion, as demonstrated using multiple orthogonal reporters (DapRed/DalGreen, tandem GFP-RFP-LC3, MagicRed). This restoration of flux enabled clearance of damaged mitochondria and misfolded proteins, reducing oxidative stress and preventing apoptosis.

In Study 3, hypoxia-reoxygenation triggered excessive lipophagy, the selective autophagic degradation of lipid droplets. While lipophagy can be adaptive by mobilizing stored fatty acids for energy generation, excessive lipophagy during ischemia-reperfusion became maladaptive when lipid droplet-mitochondria tethering was disrupted. Under these conditions, lipophagy released fatty acids that could not be efficiently transferred to mitochondria for β-oxidation, leading to cytoplasmic accumulation of lipotoxic intermediates (ceramides, diacylglycerols) and cellular injury. ALY688 mitigated this lipotoxicity not by inhibiting lipophagy per se, but by preserving

Rab8a-dependent metabolic coupling, ensuring that liberated fatty acids were efficiently channeled into mitochondrial oxidation pathways.

In Study 4, chronic ischemia (7 days post-ligation) in adiponectin-deficient mice was associated with impaired basal autophagy initiation and flux, as indicated by reduced cathepsin B activity, diminished AMPK-ULK1 signaling, and accumulation of both LC3-II and p62. This contrasts with the acute reperfusion scenario in Study 2, where autophagy initiation was relatively preserved but flux was blocked. The distinction likely reflects temporal dynamics: acute reperfusion injury involves sudden restoration of oxygen and nutrients, triggering rapid but uncoordinated autophagy induction that overwhelms lysosomal capacity, whereas chronic ischemia without reperfusion involves sustained energy stress that depletes cellular resources necessary for maintaining autophagy machinery.

Synthesis of these findings suggests a model of context-dependent autophagy regulation by adiponectin signaling. During acute reperfusion injury, adiponectin/ALY688 restores autophagic flux by enhancing lysosomal function and promoting efficient autophagosome-lysosome fusion, thereby preventing accumulation of damaged organelles and toxic protein aggregates. During chronic ischemia, adiponectin maintains basal autophagy through AMPK-ULK1 activation, enabling continuous turnover of damaged mitochondria (mitophagy) and sustaining cellular energy homeostasis. During lipid stress, adiponectin coordinates lipophagy with fatty acid oxidation by preserving organellar tethering, ensuring that autophagy-derived fatty acids are productively metabolized rather than accumulating as lipotoxic intermediates.

This context-dependent regulation likely reflects differential activation of upstream signaling nodes. AMPK, a key mediator of adiponectin signaling, phosphorylates multiple autophagy regulators including ULK1 (promoting initiation), Beclin-1 (enhancing autophagosome formation), and transcription factors controlling lysosomal biogenesis (TFEB/TFE3) (268, 479, 504, 505). Additionally, adiponectin activates p38 MAPK, which regulates autophagosome-lysosome fusion through phosphorylation of SNAP29 and syntaxin-17. The relative contribution of these pathways likely varies with the nature and duration of stress (181, 504).

From a therapeutic standpoint, these findings suggest that autophagy-targeted interventions for ischemic heart disease must account for disease stage and patient phenotype. Strategies that enhance autophagic flux (e.g., mTOR inhibitors like rapamycin or TFEB activators) may be

beneficial during acute reperfusion or chronic heart failure but could exacerbate injury during lipid overload states if not coupled with interventions that maintain metabolic coupling(94, 500, 506-508). In contrast, adiponectin receptor agonists like ALY688 may offer superior therapeutic profiles by coordinately regulating both autophagy and metabolic flux through integrated AMPK signaling.

6.2.3 Extracellular vesicles as mediators of yherapeutic reprogramming

A paradigm shift emerging from Studies 1 and 2 is the recognition that extracellular vesicles function not merely as passive carriers of cellular debris but as active therapeutic agents whose cargo and function can be pharmacologically reprogrammed. This concept has profound implications for cardiovascular therapeutics.

Traditional cardiovascular pharmacology has focused on small molecule drugs that directly modulate intracellular signaling pathways (115, 509, 510). However, this approach faces limitations including poor tissue penetration, off-target effects, and inability to deliver complex biological cargo (proteins, nucleic acids, organelles). Cell-based therapies (e.g., stem cell transplantation) offer potential advantages in delivering trophic factors and promoting tissue regeneration but are limited by poor engraftment, immune rejection, and logistical challenges in manufacturing and delivery.

Extracellular vesicles represent a convergence of these approaches, offering the advantages of biological cargo delivery without the complexities of live cell therapeutics (511). EVs are naturally occurring, membrane-enclosed particles (30-1000 nm) that mediate intercellular communication by transferring proteins, lipids, and nucleic acids between cells (212). In cardiovascular disease, EVs have been shown to play dual roles: pathological EVs released from injured or stressed cells can propagate inflammation and fibrosis, whereas EVs from regenerative cell types (e.g., mesenchymal stem cells, cardiac progenitor cells) exert cardioprotective effects.

Study 2 demonstrated that ALY688 administration shifts the balance toward cardioprotective EV phenotypes through two mechanisms: First, ALY688 enhances EV biogenesis. Myocardial infarction was associated with reduced circulating EV levels in both lean and obese mice, reflecting either decreased EV production or enhanced EV clearance. ALY688 treatment restored and even exceeded baseline EV levels, correlating with improved cardiac function. The mechanism involves ALY688-mediated preservation of Rab8a expression, which facilitates multivesicular

body fusion with the plasma membrane and exosome release. Second, ALY688 reprograms EV cargo composition. Proteomic analysis revealed that ALY688-derived EVs are enriched in bioactive adiponectin (confirming packaging of the ligand into EVs), metabolic enzymes (GAPDH, PKM, PGK1), autophagy-related proteins (ATG3), mitochondrial electron transport chain components (Complex I-V subunits), and stress-response chaperones, while showing reduced levels of ER stress markers (GRP78) and cytoskeletal proteins associated with cellular injury. Pathway enrichment analysis indicated that ALY688-EVs are particularly enriched in fructose metabolism and cholesterol homeostasis pathways.

Functional validation demonstrated that ALY688-derived EVs (EV^{ALY}) possess intrinsic cardioprotective properties when administered to naive cardiomyocytes or when systemically injected into mice with acute MI. EV^{ALY} reduced oxidative stress, restored autophagy flux, improved mitochondrial respiratory capacity, and promoted a balanced mitochondrial fusion-fission state favoring elongated, networked mitochondria. Notably, these effects were observed even in the absence of ongoing ALY688 treatment, indicating that EVs function as stable, transferable units of cardioprotective information.

The mechanistic basis for EV-mediated cargo transfer remains an active area of investigation. Upon uptake by recipient cardiomyocytes (confirmed by DiR-labeling studies), EVs can release their contents through several pathways: membrane fusion delivering cargo directly into the cytoplasm, endocytosis followed by endosomal escape, or receptor-mediated signaling at the plasma membrane without internalization. Proteomic cargo such as ATG3 and mitochondrial proteins likely exert effects after cytoplasmic delivery, whereas surface-exposed adiponectin may engage AdipoR1/R2 receptors. The relative contribution of these mechanisms requires further investigation using EV subtype-specific markers and selective uptake inhibitors.

A particularly compelling finding was that systemic administration of ALY688-derived EVs as a standalone therapeutic agent recapitulated many of the benefits of direct ALY688 treatment. This proof-of-concept experiment establishes EVs as viable therapeutic modalities for acute myocardial infarction. Compared to cell-based therapies, EV therapeutics offer several advantages: (1) they are non-replicative, eliminating concerns about tumorigenicity; (2) they have lower immunogenicity due to absence of MHC molecules; (3) they can be isolated, characterized, and stored, enabling off-the-shelf availability; (4) they can cross biological barriers including the

blood-brain barrier; and (5) they can be engineered to enhance targeting specificity or cargo loading.

Challenges remain in translating EV-based therapeutics to clinical application (512). Standardization of EV isolation, characterization, and dosing is critical, as EV populations are heterogeneous and isolation methods (ultracentrifugation, size exclusion chromatography, immunoaffinity capture) yield different subpopulations with potentially distinct functions. The International Society for Extracellular Vesicles has published guidelines (MISEV2023) to promote rigor and reproducibility in EV research. Additionally, scalable manufacturing of therapeutic EVs will require optimization of donor cell culture conditions, potentially through bioreactor-based systems.

Looking forward, the concept of pharmacological EV reprogramming opens new avenues for cardiovascular precision medicine. Beyond adiponectin receptor agonists, other classes of drugs (e.g., SGLT2 inhibitors, GLP-1 receptor agonists, metformin) may also exert part of their cardiovascular benefits through modulation of EV biogenesis and cargo. Combination strategies that pair pharmacological EV enhancers with engineered EVs loaded with specific therapeutic cargo (e.g., anti-inflammatory microRNAs, mitochondrial transfer) represent an exciting frontier.

6.2.4 Metabolic Flexibility and Lipid Droplet-Mitochondria Coupling as Determinants of Ischemic Tolerance

Study 3 revealed that disruption of lipid droplet-mitochondria tethering is a central mechanism underlying metabolic dysfunction during ischemia-reperfusion injury. This finding integrates with broader concepts of metabolic flexibility, the heart's ability to switch between fuel substrates (fatty acids, glucose, lactate, ketones) depending on substrate availability and workload.

Under physiological conditions, the adult mammalian heart derives approximately 60-70% of its ATP from fatty acid β-oxidation, with the remainder from glucose oxidation, lactate metabolism, and ketone oxidation (135). This metabolic flexibility is essential for matching energy supply to the heart's fluctuating energy demands, which can increase significantly from rest to maximal exercise. Metabolic inflexibility, defined as impaired capacity to switch between substrates, is a hallmark of heart failure, diabetic cardiomyopathy, and ischemic heart disease (91, 118, 513-515).

During acute ischemia, oxygen deprivation rapidly inhibits mitochondrial oxidative phosphorylation, causing accumulation of reducing equivalents and ATP depletion (516). Cardiomyocytes compensate by upregulating anaerobic glycolysis, but this yields only 2 ATP per glucose molecule and causes acidosis from lactate accumulation. Simultaneously, fatty acid oxidation is inhibited due to reduced NAD+ availability and accumulation of long-chain acyl-CoA esters, which inhibit adenine nucleotide translocase and further impair ATP synthesis (264, 517, 518).

Upon reperfusion, oxygen and nutrient supply are restored, but metabolic dysfunction persists and even worsens (365). Study 3 revealed a specific mechanism: hypoxia-reoxygenation disrupts the physical coupling between lipid droplets and mitochondria by downregulating Rab8a expression. Lipid droplets, once considered inert lipid storage depots, are now recognized as dynamic organelles that regulate cellular lipid homeostasis and energy metabolism. Contact sites between lipid droplets and mitochondria, mediated by tethering proteins including PLIN5, Mfn2, and (as shown in Study 3) Rab8a, enable direct channeling of fatty acids from lipid droplet TAG stores to mitochondrial β-oxidation machinery.

When this coupling is disrupted, lipolysis and lipophagy continue to release fatty acids from lipid droplets, but these fatty acids cannot be efficiently transferred to mitochondria (407, 519). Consequently, fatty acids accumulate in the cytoplasm where they are converted to toxic lipid intermediates (ceramides, diacylglycerols) that activate apoptotic signaling, impair insulin signaling, and generate reactive oxygen species through non-mitochondrial pathways (e.g., NADPH oxidase). Simultaneously, mitochondria become substrate-starved, further impairing ATP regeneration and Ca2+handling (404, 426, 450).

ALY688 preserved lipid droplet-mitochondria coupling during hypoxia-reoxygenation by maintaining Rab8a expression through AMPK-dependent mechanisms. This preserved coupling had several beneficial consequences: (1) efficient channeling of liberated fatty acids into mitochondrial oxidation, sustaining ATP production; (2) prevention of cytoplasmic lipid accumulation and lipotoxicity; (3) maintenance of mitochondrial respiratory capacity and membrane potential; (4) reduced production of reactive oxygen species from non-mitochondrial sources.

Interestingly, Study 3 also revealed that inhibition of mitochondrial fission with Mdivi-1 (an inhibitor of Drp1-mediated mitochondrial fragmentation) preserved mitochondrial morphology but did not restore lipid droplet-mitochondria coupling or fatty acid transfer, indicating that the structural integrity of individual mitochondria is insufficient for metabolic coupling if the tethering machinery is absent. This finding has important implications for therapeutic strategies targeting mitochondrial dynamics: while promoting mitochondrial fusion may prevent mitochondrial fragmentation and apoptosis, it does not address metabolic substrate supply unless organellar positioning and tethering are concurrently maintained.

The lipidomic changes observed in Study 3, which particularly accumulation of ceramides (Cer d18:1/16:0, Cer d18:1/18:0), that are consistent with clinical observations in patients with ischemic heart disease (94). Circulating ceramides are emerging as biomarkers for cardiovascular risk and predictors of adverse outcomes in MI patients (520, 521). Mechanistically, ceramides inhibit Akt signaling, thereby reducing glucose uptake and pro-survival pathways; promote mitochondrial outer membrane permeabilization, leading to cytochrome c release and apoptotic activation; and impair insulin receptor substrate phosphorylation, further exacerbating metabolic dysfunction. Adiponectin has been shown to activate ceramidases, enzymes that degrade ceramides into sphingosine and fatty acids, indicating that adiponectin signaling may mitigate ceramide-mediated lipotoxicity through both preventive mechanisms that preserve metabolic coupling and active clearance via ceramidase activation.

7.2.5 Limitations and Remaining Questions

While the studies in this thesis provide substantial mechanistic insights and proof-of-concept evidence for therapeutic potential, several important limitations and unanswered questions warrant discussion.

Animal model limitations

The rat and mouse models of myocardial infarction employed in these studies recapitulate key features of human ischemic injury including cardiomyocyte death, inflammatory infiltration, and progressive ventricular remodeling. However, important differences exist: rodents have higher heart rates (~400-600 bpm vs. ~60-80 bpm in humans), different ion channel expression profiles, greater regenerative capacity, and shorter lifespans that limit assessment of very long-term outcomes. Additionally, the permanent ligation model used in most studies does not fully replicate

clinical scenarios where reperfusion is achieved through primary PCI, which involves additional factors including microvascular obstruction, myocardial hemorrhage, and the effects of antiplatelet and anticoagulant therapies. Future studies should employ large animal models (pig, dog) that more closely approximate human cardiac physiology and use clinically relevant reperfusion protocols (transient ischemia followed by reperfusion) to better model the human condition.

Sex and age considerations

The studies predominantly used young adult female rats or young adult male mice, yet sex and age profoundly influence cardiovascular disease pathophysiology and response to therapy. Adiponectin levels are consistently higher in females than males, potentially due to suppressive effects of androgens on adiponectin transcription. This sex difference may explain, in part, the lower cardiovascular risk in premenopausal women compared to age-matched men. Post-menopausal women, in whom estrogen-mediated cardioprotection wanes, represent a particularly important population for adiponectin-based therapies. Aging is associated with reduced adiponectin levels, increased visceral adiposity, and "inflammaging" (chronic low-grade inflammation), all of which could influence adiponectin receptor agonist efficacy. Future preclinical studies should incorporate both sexes and aged animals to assess generalizability of findings and identify potential sex-specific or age-specific therapeutic strategies.

Mechanistic questions regarding EV cargo sorting

While Study 3 demonstrated that ALY688 reprograms EV cargo composition, the molecular mechanisms underlying selective cargo sorting into EVs remain incompletely understood. Proteins are sorted into intraluminal vesicles of multivesicular bodies through ESCRT-dependent and ESCRT-independent mechanisms involving tetraspanins, ceramides, and lipid raft domains. How ALY688-mediated signaling (via AMPK, p38 MAPK, or other pathways) influences these sorting mechanisms is unknown. Does AMPK directly phosphorylate ESCRT components or cargo proteins, thereby altering sorting efficiency? Does ALY688 alter the lipid composition of multivesicular body membranes, thereby influencing lipid raft-mediated sorting? Addressing these questions will require proteomic analysis of multivesicular bodies, lipidomic profiling of EV membranes, and functional studies using cargo proteins tagged with photoactivatable or pH-sensitive fluorophores to track sorting dynamics in real-time.

EV targeting and biodistribution

While systemic EV administration in Study 3 improved cardiac outcomes, the biodistribution and targeting specificity of EVs remain unclear. After intravenous injection, EVs are rapidly cleared by the liver, spleen, and lungs, with only a small fraction reaching the heart. Strategies to enhance cardiac targeting include: (1) engineering EV surfaces with cardiac-homing peptides (e.g., cardiac targeting sequences derived from atrial natriuretic peptide); (2) conjugating EVs with antibodies against cardiomyocyte surface markers; (3) administering EVs via intracoronary infusion during primary PCI to achieve high local concentrations; (4) exploiting passive targeting through enhanced permeability of inflamed/ischemic myocardium. Future studies should employ EVs labeled with radionuclides (¹¹¹In, ^{99m}Tc) or fluorescent dyes to quantitatively assess biodistribution and cardiac accumulation using PET/SPECT or intravital imaging.

Long-term cardiac remodeling and heart failure progression

The studies assessed outcomes at relatively early time points (acute phase: 2-7 days; subacute phase: 28 days). While these time points are appropriate for evaluating acute cardioprotection and early remodeling, the transition from compensated hypertrophy to overt heart failure typically occurs over months to years. Long-term studies (6-12 months in rodents, 6-24 months in large animals) are needed to assess whether the early benefits conferred by ALY688 translate into durable improvements in survival, prevention of heart failure hospitalization, and preservation of functional capacity. Equally important is assessing whether chronic adiponectin receptor agonism carries risks of desensitization, receptor downregulation, or unintended metabolic consequences (e.g., hypoglycemia, altered body composition).

7.2.6 Concluding Remarks

This thesis elucidates a multi-level cardioprotective network activated by adiponectin receptor signaling, encompassing direct cellular effects, extracellular vesicle-mediated communication, organellar metabolic coupling, and autophagy regulation. The therapeutic potential of adiponectin receptor agonists such as ALY688 derives from coordinated modulation of these interconnected pathways, providing redundancy and broad-spectrum cardioprotection against ischemia-reperfusion injury.

Several conceptual advances emerged from this body of work: Rab8a as a dual regulator of vesicular trafficking and metabolic compartmentalization, bridging extracellular communication

(EV biogenesis) with intracellular metabolism (lipid droplet-mitochondria coupling). This functional pleiotropy positions Rab8a as a master integrator of cellular stress responses and a promising therapeutic target. Context-dependent autophagy regulation by adiponectin, wherein autophagy flux enhancement, lipophagy coordination with fatty acid oxidation, and mitophagy collectively maintain cellular homeostasis. The ability of adiponectin signaling to fine-tune autophagy according to cellular context distinguishes it from generic autophagy inducers and may confer superior therapeutic profiles. Pharmacological reprogramming of extracellular vesicles as a novel therapeutic strategy, enabling drug-induced shifts toward cardioprotective EV phenotypes that can function as transferable units of protection. This concept extends cardiovascular pharmacology beyond traditional receptor agonism into the realm of intercellular communication engineering. Preservation of lipid droplet-mitochondria tethering as a mechanism for maintaining metabolic flexibility and preventing lipotoxicity during ischemic stress, highlighting the importance of subcellular spatial organization in determining metabolic outcomes.

Collectively, these findings provide a strong scientific rationale for clinical development of adiponectin receptor agonists for ischemic heart disease and establish a mechanistic framework for understanding how adiponectin deficiency contributes to cardiovascular risk. As cardiovascular medicine moves toward precision approaches that target specific pathophysiological mechanisms rather than relying solely on hemodynamic manipulation, adiponectin-based therapeutics, whether as receptor agonists, EV-modulating agents, or engineered EV therapeutics, representing a promising frontier with substantial translational potential.

Reference

Uncategorized References

1. N. Sattar, J. M. R. Gill, W. Alazawi, Improving prevention strategies for cardiometabolic disease. *Nat Med* **26**, 320-325 (2020).
2. J. W. O'Sullivan, E. A. Ashley, P. M. Elliott, Polygenic risk scores for the prediction of cardiometabolic disease. *Eur Heart J* **44**, 89-99 (2023).
3. U. A. Tahir, R. E. Gerszten, Omics and Cardiometabolic Disease Risk Prediction. *Annu Rev Med* **71**, 163-175 (2020).
4. E. D. Muse, E. J. Topol, Transforming the cardiometabolic disease landscape: Multimodal AI-powered approaches in prevention and management. *Cell Metab* **36**, 670-683 (2024).
5. F. B. Ortega, C. J. Lavie, S. N. Blair, Obesity and Cardiovascular Disease. *Circ Res* **118**, 1752-1770 (2016).
6. N. Esser, S. Legrand-Poels, J. Piette, A. J. Scheen, N. Paquot, Inflammation as a link between obesity, metabolic syndrome and type 2 diabetes. *Diabetes Res Clin Pract* **105**, 141-150 (2014).
7. F. H. Messerli, S. F. Rimoldi, S. Bangalore, The Transition From Hypertension to Heart Failure: Contemporary Update. *JACC Heart Fail* **5**, 543-551 (2017).
8. V. Ormazabal *et al.*, Association between insulin resistance and the development of cardiovascular disease. *Cardiovasc Diabetol* **17**, 122 (2018).
9. A. Di Pino, R. A. DeFronzo, Insulin Resistance and Atherosclerosis: Implications for Insulin-Sensitizing Agents. *Endocr Rev* **40**, 1447-1467 (2019).
10. A. Pirillo, M. Casula, E. Olmastroni, G. D. Norata, A. L. Catapano, Global epidemiology of dyslipidaemias. *Nat Rev Cardiol* **18**, 689-700 (2021).
11. Q. Xiang *et al.*, New insight into dyslipidemia-induced cellular senescence in atherosclerosis. *Biol Rev Camb Philos Soc* **97**, 1844-1867 (2022).
12. U. A. Tahir, R. E. Gerszten, Molecular Biomarkers for Cardiometabolic Disease: Risk Assessment in Young Individuals. *Circ Res* **132**, 1663-1673 (2023).
13. R. J. Henning, Obesity and obesity-induced inflammatory disease contribute to atherosclerosis: a review of the pathophysiology and treatment of obesity. *Am J Cardiovasc Dis* **11**, 504-529 (2021).
14. M. Zakkar, R. Ascione, A. F. James, G. D. Angelini, M. S. Suleiman, Inflammation, oxidative stress and postoperative atrial fibrillation in cardiac surgery. *Pharmacol Ther* **154**, 13-20 (2015).
15. W. J. Paulus, C. Tschöpe, A novel paradigm for heart failure with preserved ejection fraction: comorbidities drive myocardial dysfunction and remodeling through coronary microvascular endothelial inflammation. *J Am Coll Cardiol* **62**, 263-271 (2013).
16. T. Suganami *et al.*, Role of the Toll-like receptor 4/NF-kappaB pathway in saturated fatty acid-induced inflammatory changes in the interaction between adipocytes and macrophages. *Arterioscler Thromb Vasc Biol* **27**, 84-91 (2007).
17. H. Kolb, Obese visceral fat tissue inflammation: from protective to detrimental? *BMC Med* **20**, 494 (2022).
18. G. Solinas, B. Becattini, JNK at the crossroad of obesity, insulin resistance, and cell stress response. *Mol Metab* **6**, 174-184 (2017).

19. P. Bobbert *et al.*, High leptin and resistin expression in chronic heart failure: adverse outcome in patients with dilated and inflammatory cardiomyopathy. *Eur J Heart Fail* **14**, 1265-1275 (2012).
20. N. Panth, K. R. Paudel, K. Parajuli, Reactive Oxygen Species: A Key Hallmark of Cardiovascular Disease. *Adv Med* **2016**, 9152732 (2016).
21. N. Kaludercic, F. Di Lisa, Mitochondrial ROS Formation in the Pathogenesis of Diabetic Cardiomyopathy. *Front Cardiovasc Med* **7**, 12 (2020).
22. D. N. Granger, P. R. Kvietys, Reperfusion injury and reactive oxygen species: The evolution of a concept. *Redox Biol* **6**, 524-551 (2015).
23. Z. Bagi, A. Feher, J. Cassuto, Microvascular responsiveness in obesity: implications for therapeutic intervention. *Br J Pharmacol* **165**, 544-560 (2012).
24. A. Christodoulou *et al.*, Cardioprotective potential of oleuropein, hydroxytyrosol, oleocanthal and their combination: Unravelling complementary effects on acute myocardial infarction and metabolic syndrome. *Redox Biol* **76**, 103311 (2024).
25. S. Xu *et al.*, Endothelial Dysfunction in Atherosclerotic Cardiovascular Diseases and Beyond: From Mechanism to Pharmacotherapies. *Pharmacol Rev* **73**, 924-967 (2021).
26. J. Zhou, Y. S. Li, S. Chien, Shear stress-initiated signaling and its regulation of endothelial function. *Arterioscler Thromb Vasc Biol* **34**, 2191-2198 (2014).
27. Y. Gui, H. Zheng, R. Y. Cao, Foam Cells in Atherosclerosis: Novel Insights Into Its Origins, Consequences, and Molecular Mechanisms. *Front Cardiovasc Med* **9**, 845942 (2022).
28. M. O. J. Grootaert, M. R. Bennett, Vascular smooth muscle cells in atherosclerosis: time for a re-assessment. *Cardiovasc Res* **117**, 2326-2339 (2021).
29. J. Slysz *et al.*, Single-cell profiling reveals inflammatory polarization of human carotid versus femoral plaque leukocytes. *JCI Insight* **8** (2023).
30. H. C. Kenny, E. D. Abel, Heart Failure in Type 2 Diabetes Mellitus. *Circ Res* **124**, 121-141 (2019).
31. C. R. Chong, K. Clarke, E. Levelt, Metabolic Remodeling in Diabetic Cardiomyopathy. *Cardiovasc Res* **113**, 422-430 (2017).
32. B. A. Law *et al.*, Lipotoxic very-long-chain ceramides cause mitochondrial dysfunction, oxidative stress, and cell death in cardiomyocytes. *FASEB J* **32**, 1403-1416 (2018).
33. J. Zhao, R. Randive, J. A. Stewart, Molecular mechanisms of AGE/RAGE-mediated fibrosis in the diabetic heart. *World J Diabetes* **5**, 860-867 (2014).
34. H. J. Lu, N. Koju, R. Sheng, Mammalian integrated stress responses in stressed organelles and their functions. *Acta Pharmacol Sin* **45**, 1095-1114 (2024).
35. Y. Pu, D. Wu, X. Lu, L. Yang, Effects of GCN2/eIF2alpha on myocardial ischemia/hypoxia reperfusion and myocardial cells injury. *Am J Transl Res* **11**, 5586-5598 (2019).
36. Y. Zhang, J. Ren, Role of cardiac steatosis and lipotoxicity in obesity cardiomyopathy. *Hypertension* **57**, 148-150 (2011).
37. L. Chen, K. J. Sampson, R. S. Kass, Cardiac Delayed Rectifier Potassium Channels in Health and Disease. *Card Electrophysiol Clin* **8**, 307-322 (2016).
38. T. Shugg, A. Hudmon, B. R. Overholser, Neurohormonal Regulation of I(Ks) in Heart Failure: Implications for Ventricular Arrhythmogenesis and Sudden Cardiac Death. *J Am Heart Assoc* **9**, e016900 (2020).

39. T. Shugg *et al.*, Calcium/calmodulin-dependent protein kinase II regulation of I(Ks) during sustained beta-adrenergic receptor stimulation. *Heart Rhythm* **15**, 895-904 (2018).
40. X. Gou, W. Wang, S. Zou, Y. Qi, Y. Xu, Protein kinase C epsilon mediates the inhibition of angiotensin II on the slowly activating delayed-rectifier potassium current through channel phosphorylation. *J Mol Cell Cardiol* **116**, 165-174 (2018).
41. M. Albaghdadi, M. Gheorghiade, B. Pitt, Mineralocorticoid receptor antagonism: therapeutic potential in acute heart failure syndromes. *Eur Heart J* **32**, 2626-2633 (2011).
42. O. Polianska *et al.*, Neurohumoral Dysregulation in Acute Myocardial Infarction With Chronic Kidney Disease: Implications for Prognosis and Management. *Cureus* **17**, e93692 (2025).
43. L. Monzo *et al.*, Role of aldosterone in mid- and long-term left ventricular remodelling after acute myocardial infarction: The REMI study. *Eur J Heart Fail* **25**, 1742-1752 (2023).
44. N. S. Lee, L. B. Daniels, Current Understanding of the Compensatory Actions of Cardiac Natriuretic Peptides in Cardiac Failure: A Clinical Perspective. *Card Fail Rev* **2**, 14-19 (2016).
45. J. Hartupee, D. L. Mann, Neurohormonal activation in heart failure with reduced ejection fraction. *Nat Rev Cardiol* **14**, 30-38 (2017).
46. H. Nougue *et al.*, Effects of sacubitril/valsartan on neprilysin targets and the metabolism of natriuretic peptides in chronic heart failure: a mechanistic clinical study. *Eur J Heart Fail* **21**, 598-605 (2019).
47. N. Martin, K. Manoharan, J. Thomas, C. Davies, R. T. Lumbers, Beta-blockers and inhibitors of the renin-angiotensin aldosterone system for chronic heart failure with preserved ejection fraction. *Cochrane Database Syst Rev* **6**, CD012721 (2018).
48. M. Ksiazczyk, M. Lelonek, Angiotensin receptor/neprilysin inhibitor-a breakthrough in chronic heart failure therapy: summary of subanalysis on PARADIGM-HF trial findings. *Heart Fail Rev* **25**, 393-402 (2020).
49. M. Zhang *et al.*, Ischemia-reperfusion injury: molecular mechanisms and therapeutic targets. *Signal Transduct Target Ther* **9**, 12 (2024).
50. D. M. Yellon, D. J. Hausenloy, Myocardial reperfusion injury. *N Engl J Med* **357**, 1121-1135 (2007).
51. J. Kajstura *et al.*, Apoptotic and necrotic myocyte cell deaths are independent contributing variables of infarct size in rats. *Lab Invest* **74**, 86-107 (1996).
52. K. Konstantinidis, R. S. Whelan, R. N. Kitsis, Mechanisms of cell death in heart disease. *Arterioscler Thromb Vasc Biol* **32**, 1552-1562 (2012).
53. B. T. Cookson, M. A. Brennan, Pro-inflammatory programmed cell death. *Trends Microbiol* **9**, 113-114 (2001).
54. S. He *et al.*, Receptor interacting protein kinase-3 determines cellular necrotic response to TNF-alpha. *Cell* **137**, 1100-1111 (2009).
55. W. S. Yang, B. R. Stockwell, Synthetic lethal screening identifies compounds activating iron-dependent, nonapoptotic cell death in oncogenic-RAS-harboring cancer cells. *Chem Biol* **15**, 234-245 (2008).
56. S. Elmore, Apoptosis: a review of programmed cell death. *Toxicol Pathol* **35**, 495-516 (2007).
57. F. Eefting *et al.*, Role of apoptosis in reperfusion injury. *Cardiovasc Res* **61**, 414-426 (2004).

58. K. Wang *et al.*, Mitochondrial apoptosis in response to cardiac ischemia-reperfusion injury. *J Transl Med* **23**, 125 (2025).
59. M. Conrad, J. P. Angeli, P. Vandenabeele, B. R. Stockwell, Regulated necrosis: disease relevance and therapeutic opportunities. *Nat Rev Drug Discov* **15**, 348-366 (2016).
60. J. Karch, J. D. Molkentin, Regulated necrotic cell death: the passive aggressive side of Bax and Bak. *Circ Res* **116**, 1800-1809 (2015).
61. D. J. Robichaux, M. Harata, E. Murphy, J. Karch, Mitochondrial permeability transition pore-dependent necrosis. *J Mol Cell Cardiol* **174**, 47-55 (2023).
62. C. X. Zhang *et al.*, Mitochondria-targeted cyclosporin A delivery system to treat myocardial ischemia reperfusion injury of rats. *J Nanobiotechnology* **17**, 18 (2019).
63. H. Wu *et al.*, Programmed cardiomyocyte death in myocardial infarction. *Apoptosis* **30**, 597-615 (2025).
64. T. Zhang *et al.*, CaMKII is a RIP3 substrate mediating ischemia- and oxidative stress-induced myocardial necroptosis. *Nat Med* **22**, 175-182 (2016).
65. D. A. Rodriguez *et al.*, Characterization of RIPK3-mediated phosphorylation of the activation loop of MLKL during necroptosis. *Cell Death Differ* **23**, 76-88 (2016).
66. P. Zhu *et al.*, Ripk3 promotes ER stress-induced necroptosis in cardiac IR injury: A mechanism involving calcium overload/XO/ROS/mPTP pathway. *Redox Biol* **16**, 157-168 (2018).
67. S. A. Dabravolski *et al.*, Necroptosis in myocardial ischaemia-reperfusion injury: current update on mechanisms, therapeutic targets, and translational potential. *Apoptosis* **30**, 1216-1234 (2025).
68. A. Szobi *et al.*, Analysis of necroptotic proteins in failing human hearts. *J Transl Med* **15**, 86 (2017).
69. S. J. Dixon, J. A. Olzmann, The cell biology of ferroptosis. *Nat Rev Mol Cell Biol* **25**, 424-442 (2024).
70. W. Cai *et al.*, Alox15/15-HpETE Aggravates Myocardial Ischemia-Reperfusion Injury by Promoting Cardiomyocyte Ferroptosis. *Circulation* **147**, 1444-1460 (2023).
71. N. Shao *et al.*, Ferritinophagy and organ injury. *Autophagy* 10.1080/15548627.2026.2633246, 1-15 (2026).
72. W. Chan *et al.*, Effect of iron chelation on myocardial infarct size and oxidative stress in ST-elevation-myocardial infarction. *Circ Cardiovasc Interv* **5**, 270-278 (2012).
73. L. Timmers *et al.*, The innate immune response in reperfused myocardium. *Cardiovasc Res* **94**, 276-283 (2012).
74. G. Vilahur, L. Badimon, Ischemia/reperfusion activates myocardial innate immune response: the key role of the toll-like receptor. *Front Physiol* **5**, 496 (2014).
75. C. Peet, A. Ivetic, D. I. Bromage, A. M. Shah, Cardiac monocytes and macrophages after myocardial infarction. *Cardiovasc Res* **116**, 1101-1112 (2020).
76. I. Hilgendorf *et al.*, Ly-6Chigh monocytes depend on Nr4a1 to balance both inflammatory and reparative phases in the infarcted myocardium. *Circ Res* **114**, 1611-1622 (2014).
77. S. Sciarretta, Y. Maejima, D. Zablocki, J. Sadoshima, The Role of Autophagy in the Heart. *Annu Rev Physiol* **80**, 1-26 (2018).
78. S. Ljubojevic-Holzer *et al.*, Loss of autophagy protein ATG5 impairs cardiac capacity in mice and humans through diminishing mitochondrial abundance and disrupting Ca2+ cycling. *Cardiovasc Res* **118**, 1492-1505 (2022).

79. K. Mao, D. J. Klionsky, AMPK activates autophagy by phosphorylating ULK1. *Circ Res* **108**, 787-788 (2011).
80. Y. Zhang *et al.*, HIF-1alpha/BNIP3 signaling pathway-induced-autophagy plays protective role during myocardial ischemia-reperfusion injury. *Biomed Pharmacother* **120**, 109464 (2019).
81. Y. Matsui *et al.*, Distinct roles of autophagy in the heart during ischemia and reperfusion: roles of AMP-activated protein kinase and Beclin 1 in mediating autophagy. *Circ Res* **100**, 914-922 (2007).
82. L. Li, J. Tan, Y. Miao, P. Lei, Q. Zhang, ROS and Autophagy: Interactions and Molecular Regulatory Mechanisms. *Cell Mol Neurobiol* **35**, 615-621 (2015).
83. S. Xu *et al.*, Mitophagy in ischemic heart disease: molecular mechanisms and clinical management. *Cell Death Dis* **15**, 934 (2024).
84. J. M. Heo, A. Ordureau, J. A. Paulo, J. Rinehart, J. W. Harper, The PINK1-PARKIN Mitochondrial Ubiquitylation Pathway Drives a Program of OPTN/NDP52 Recruitment and TBK1 Activation to Promote Mitophagy. *Mol Cell* **60**, 7-20 (2015).
85. T. Kataura *et al.*, NDP52 acts as a redox sensor in PINK1/Parkin-mediated mitophagy. *EMBO J* **42**, e111372 (2023).
86. A. S. Titus, E. A. Sung, D. Zablocki, J. Sadoshima, Mitophagy for cardioprotection. *Basic Res Cardiol* **118**, 42 (2023).
87. Y. Liao, B. Ke, X. Long, J. Xu, Y. Wu, Abnormalities in the SIRT1-SIRT3 axis promote myocardial ischemia-reperfusion injury through ferroptosis caused by silencing the PINK1/Parkin signaling pathway. *BMC Cardiovasc Disord* **23**, 582 (2023).
88. H. Zhang *et al.*, The zinc transporter ZIP7 (Slc39a7) controls myocardial reperfusion injury by regulating mitophagy. *Basic Res Cardiol* **116**, 54 (2021).
89. X. Ding *et al.*, SIRT1 is a regulator of autophagy: Implications for the progression and treatment of myocardial ischemia-reperfusion. *Pharmacol Res* **199**, 106957 (2024).
90. N. Hariharan *et al.*, Deacetylation of FoxO by Sirt1 Plays an Essential Role in Mediating Starvation-Induced Autophagy in Cardiac Myocytes. *Circ Res* **107**, 1470-1482 (2010).
91. Q. G. Karwi, G. M. Uddin, K. L. Ho, G. D. Lopaschuk, Loss of Metabolic Flexibility in the Failing Heart. *Front Cardiovasc Med* **5**, 68 (2018).
92. S. Soni, R. J. Skow, S. Foulkes, M. J. Haykowsky, J. R. B. Dyck, Therapeutic potential of ketone bodies on exercise intolerance in heart failure: looking beyond the heart. *Cardiovasc Res* **121**, 230-240 (2025).
93. D. Shao, R. Tian, Glucose Transporters in Cardiac Metabolism and Hypertrophy. *Compr Physiol* **6**, 331-351 (2015).
94. A. C. Sletten, L. R. Peterson, J. E. Schaffer, Manifestations and mechanisms of myocardial lipotoxicity in obesity. *J Intern Med* **284**, 478-491 (2018).
95. A. Fukushima, G. D. Lopaschuk, Cardiac fatty acid oxidation in heart failure associated with obesity and diabetes. *Biochimica et biophysica acta* **1861**, 1525-1534 (2016).
96. R. R. Russell, 3rd *et al.*, AMP-activated protein kinase mediates ischemic glucose uptake and prevents postischemic cardiac dysfunction, apoptosis, and injury. *J Clin Invest* **114**, 495-503 (2004).
97. C. Mihl, W. R. Dassen, H. Kuipers, Cardiac remodelling: concentric versus eccentric hypertrophy in strength and endurance athletes. *Neth Heart J* **16**, 129-133 (2008).
98. M. J. Platt, J. S. Huber, N. Romanova, K. R. Brunt, J. A. Simpson, Pathophysiological Mapping of Experimental Heart Failure: Left and Right Ventricular Remodeling in

Transverse Aortic Constriction Is Temporally, Kinetically and Structurally Distinct. *Front Physiol* **9**, 472 (2018).
99. N. G. Frangogiannis, Fibroblasts and the extracellular matrix in right ventricular disease. *Cardiovasc Res* **113**, 1453-1464 (2017).
100. N. S. Ioakeimidis *et al.*, Periostin is overexpressed, correlated with fibrosis and differs among grades of cardiomyocyte hypertrophy in myectomy tissue of patients with hypertrophic cardiomyopathy. *PLoS One* **18**, e0293427 (2023).
101. A. D. Bradshaw *et al.*, Pressure overload-induced alterations in fibrillar collagen content and myocardial diastolic function: role of secreted protein acidic and rich in cysteine (SPARC) in post-synthetic procollagen processing. *Circulation* **119**, 269-280 (2009).
102. A. Weber *et al.*, Osteopontin as novel biomarker for reversibility of pressure overload induced left ventricular hypertrophy. *Biomark Med* **14**, 513-523 (2020).
103. B. K. Podesser *et al.*, Tenascin-C promotes chronic pressure overload-induced cardiac dysfunction, hypertrophy and myocardial fibrosis. *J Hypertens* **36**, 847-856 (2018).
104. S. Givvimani *et al.*, MMP-2/TIMP-2/TIMP-4 versus MMP-9/TIMP-3 in transition from compensatory hypertrophy and angiogenesis to decompensatory heart failure. *Arch Physiol Biochem* **116**, 63-72 (2010).
105. S. Givvimani *et al.*, TIMP-2 mutant decreases MMP-2 activity and augments pressure overload induced LV dysfunction and heart failure. *Arch Physiol Biochem* **119**, 65-74 (2013).
106. H. Ji *et al.*, Rho/Rock cross-talks with transforming growth factor-beta/Smad pathway participates in lung fibroblast-myofibroblast differentiation. *Biomed Rep* **2**, 787-792 (2014).
107. H. Khalil *et al.*, Fibroblast-specific TGF-beta-Smad2/3 signaling underlies cardiac fibrosis. *J Clin Invest* **127**, 3770-3783 (2017).
108. A. V. Villar *et al.*, Plasma levels of transforming growth factor-beta1 reflect left ventricular remodeling in aortic stenosis. *PLoS One* **4**, e8476 (2009).
109. Q. Liu *et al.*, Belumosudil, ROCK2-specific inhibitor, alleviates cardiac fibrosis by inhibiting cardiac fibroblasts activation. *Am J Physiol Heart Circ Physiol* **323**, H235-H247 (2022).
110. X. Liu, G. P. Shi, J. Guo, Innate Immune Cells in Pressure Overload-Induced Cardiac Hypertrophy and Remodeling. *Front Cell Dev Biol* **9**, 659666 (2021).
111. S. P. Levick, A. Widiapradja, Mast Cells: Key Contributors to Cardiac Fibrosis. *Int J Mol Sci* **19** (2018).
112. X. S. Revelo *et al.*, Cardiac Resident Macrophages Prevent Fibrosis and Stimulate Angiogenesis. *Circ Res* **129**, 1086-1101 (2021).
113. G. Bajpai *et al.*, Tissue Resident CCR2- and CCR2+ Cardiac Macrophages Differentially Orchestrate Monocyte Recruitment and Fate Specification Following Myocardial Injury. *Circ Res* **124**, 263-278 (2019).
114. S. Sankaralingam, G. D. Lopaschuk, Cardiac energy metabolic alterations in pressure overload-induced left and right heart failure (2013 Grover Conference Series). *Pulm Circ* **5**, 15-28 (2015).
115. Q. Sun, Q. G. Karwi, N. Wong, G. D. Lopaschuk, Advances in myocardial energy metabolism: metabolic remodelling in heart failure and beyond. *Cardiovasc Res* **120**, 1996-2016 (2024).

116. L. He *et al.*, Carnitine palmitoyltransferase-1b deficiency aggravates pressure overload-induced cardiac hypertrophy caused by lipotoxicity. *Circulation* **126**, 1705-1716 (2012).
117. I. M. E. Geraets, J. F. C. Glatz, J. Luiken, M. Nabben, Pivotal role of membrane substrate transporters on the metabolic alterations in the pressure-overloaded heart. *Cardiovasc Res* **115**, 1000-1012 (2019).
118. M. Makrecka-Kuka *et al.*, Altered mitochondrial metabolism in the insulin-resistant heart. *Acta Physiol (Oxf)* **228**, e13430 (2020).
119. R. H. Ritchie, E. D. Abel, Basic Mechanisms of Diabetic Heart Disease. *Circ Res* **126**, 1501-1525 (2020).
120. G. Jia, A. Whaley-Connell, J. R. Sowers, Diabetic cardiomyopathy: a hyperglycaemia- and insulin-resistance-induced heart disease. *Diabetologia* **61**, 21-28 (2018).
121. J. Gollmer, A. Zirlik, H. Bugger, Mitochondrial Mechanisms in Diabetic Cardiomyopathy. *Diabetes Metab J* **44**, 33-53 (2020).
122. W. Han *et al.*, Role of Adiponectin in Cardiovascular Diseases Related to Glucose and Lipid Metabolism Disorders. *Int J Mol Sci* **23** (2022).
123. S. Bernardi, A. Michelli, G. Zuolo, R. Candido, B. Fabris, Update on RAAS Modulation for the Treatment of Diabetic Cardiovascular Disease. *J Diabetes Res* **2016**, 8917578 (2016).
124. H. Tilg, G. Ianiro, A. Gasbarrini, T. E. Adolph, Adipokines: masterminds of metabolic inflammation. *Nat Rev Immunol* **25**, 250-265 (2025).
125. R. H. Choi, S. M. Tatum, J. D. Symons, S. A. Summers, W. L. Holland, Ceramides and other sphingolipids as drivers of cardiovascular disease. *Nat Rev Cardiol* **18**, 701-711 (2021).
126. J. Ke, J. Pan, H. Lin, J. Gu, Diabetic cardiomyopathy: a brief summary on lipid toxicity. *ESC Heart Fail* **10**, 776-790 (2023).
127. G. Daffu *et al.*, Radical roles for RAGE in the pathogenesis of oxidative stress in cardiovascular diseases and beyond. *Int J Mol Sci* **14**, 19891-19910 (2013).
128. Y. C. Yang *et al.*, Pkcdelta Activation is Involved in ROS-Mediated Mitochondrial Dysfunction and Apoptosis in Cardiomyocytes Exposed to Advanced Glycation End Products (Ages). *Aging Dis* **9**, 647-663 (2018).
129. Y. Zhao *et al.*, Ferroptosis: roles and molecular mechanisms in diabetic cardiomyopathy. *Front Endocrinol (Lausanne)* **14**, 1140644 (2023).
130. C. Cai *et al.*, Mitochondrial quality control in diabetic cardiomyopathy: from molecular mechanisms to therapeutic strategies. *Int J Biol Sci* **18**, 5276-5290 (2022).
131. J. C. Chatham, A. R. Wende, The role of protein O-GlcNAcylation in diabetic cardiomyopathy. *Biochem Soc Trans* **52**, 2343-2358 (2024).
132. X. Chang *et al.*, Mitochondrial quality control mechanisms as molecular targets in diabetic heart. *Metabolism* **137**, 155313 (2022).
133. J. Diaz-Juarez, J. A. Suarez, W. H. Dillmann, J. Suarez, Mitochondrial calcium handling and heart disease in diabetes mellitus. *Biochim Biophys Acta Mol Basis Dis* **1867**, 165984 (2021).
134. G. D. Lopaschuk, Q. G. Karwi, R. Tian, A. R. Wende, E. D. Abel, Cardiac Energy Metabolism in Heart Failure. *Circ Res* **128**, 1487-1513 (2021).
135. L. Da Dalt, A. G. Cabodevilla, I. J. Goldberg, G. D. Norata, Cardiac lipid metabolism, mitochondrial function, and heart failure. *Cardiovasc Res* **119**, 1905-1914 (2023).

136. Y. Xiong *et al.*, Decreased MFN2 activates the cGAS-STING pathway in diabetic myocardial ischaemia-reperfusion by triggering the release of mitochondrial DNA. *Cell Commun Signal* **21**, 192 (2023).
137. K. Nishida, K. Otsu, Inflammation and metabolic cardiomyopathy. *Cardiovasc Res* **113**, 389-398 (2017).
138. K. K. Wu, S. W. Cheung, K. K. Cheng, NLRP3 Inflammasome Activation in Adipose Tissues and Its Implications on Metabolic Diseases. *Int J Mol Sci* **21** (2020).
139. J. Yao, D. Wu, Y. Qiu, Adipose tissue macrophage in obesity-associated metabolic diseases. *Front Immunol* **13**, 977485 (2022).
140. D. Thomas, C. Apovian, Macrophage functions in lean and obese adipose tissue. *Metabolism* **72**, 120-143 (2017).
141. S. E. Hermansen, T. Kalstad, O. J. How, T. Myrmel, Inflammation and reduced endothelial function in the course of severe acute heart failure. *Transl Res* **157**, 117-127 (2011).
142. J. M. Cook-Mills, M. E. Marchese, H. Abdala-Valencia, Vascular cell adhesion molecule-1 expression and signaling during disease: regulation by reactive oxygen species and antioxidants. *Antioxid Redox Signal* **15**, 1607-1638 (2011).
143. D. De Nardo, E. Latz, NLRP3 inflammasomes link inflammation and metabolic disease. *Trends Immunol* **32**, 373-379 (2011).
144. C. S. Park, N. Shastri, The Role of T Cells in Obesity-Associated Inflammation and Metabolic Disease. *Immune Netw* **22**, e13 (2022).
145. K. Lingappan, NF-kappaB in Oxidative Stress. *Curr Opin Toxicol* **7**, 81-86 (2018).
146. Y. Zhang, P. Murugesan, K. Huang, H. Cai, NADPH oxidases and oxidase crosstalk in cardiovascular diseases: novel therapeutic targets. *Nat Rev Cardiol* **17**, 170-194 (2020).
147. J. N. Peoples, A. Saraf, N. Ghazal, T. T. Pham, J. Q. Kwong, Mitochondrial dysfunction and oxidative stress in heart disease. *Exp Mol Med* **51**, 1-13 (2019).
148. E. Lubos, D. E. Handy, J. Loscalzo, Role of oxidative stress and nitric oxide in atherothrombosis. *Front Biosci* **13**, 5323-5344 (2008).
149. S. Hamilton, D. Terentyev, ER stress and calcium-dependent arrhythmias. *Front Physiol* **13**, 1041940 (2022).
150. V. P. Singh, A. Bali, N. Singh, A. S. Jaggi, Advanced glycation end products and diabetic complications. *Korean J Physiol Pharmacol* **18**, 1-14 (2014).
151. J. Liu, S. Pan, X. Wang, Z. Liu, Y. Zhang, Role of advanced glycation end products in diabetic vascular injury: molecular mechanisms and therapeutic perspectives. *Eur J Med Res* **28**, 553 (2023).
152. N. D'Onofrio *et al.*, SIRT3 mediates the effects of PCSK9 inhibitors on inflammation, autophagy, and oxidative stress in endothelial cells. *Theranostics* **13**, 531-542 (2023).
153. D. L. Jennings *et al.*, PCSK9 inhibitors safely and effectively lower LDL after heart transplantation: a systematic review and meta-analysis. *Heart Fail Rev* **28**, 149-156 (2023).
154. K. Huang, X. Luo, B. Liao, G. Li, J. Feng, Insights into SGLT2 inhibitor treatment of diabetic cardiomyopathy: focus on the mechanisms. *Cardiovasc Diabetol* **22**, 86 (2023).
155. M. Packer, SGLT2 inhibitors: role in protective reprogramming of cardiac nutrient transport and metabolism. *Nat Rev Cardiol* **20**, 443-462 (2023).
156. V. Vallon, S. Verma, Effects of SGLT2 Inhibitors on Kidney and Cardiovascular Function. *Annu Rev Physiol* **83**, 503-528 (2021).

157. S. V. Badve *et al.*, Effects of GLP-1 receptor agonists on kidney and cardiovascular disease outcomes: a meta-analysis of randomised controlled trials. *Lancet Diabetes Endocrinol* **13**, 15-28 (2025).
158. J. R. Ussher, D. J. Drucker, Glucagon-like peptide 1 receptor agonists: cardiovascular benefits and mechanisms of action. *Nat Rev Cardiol* **20**, 463-474 (2023).
159. F. Costa *et al.*, Dual antiplatelet therapy duration after percutaneous coronary intervention in high bleeding risk: a meta-analysis of randomized trials. *Eur Heart J* **44**, 954-968 (2023).
160. G. N. Levine *et al.*, 2016 ACC/AHA Guideline Focused Update on Duration of Dual Antiplatelet Therapy in Patients With Coronary Artery Disease: A Report of the American College of Cardiology/American Heart Association Task Force on Clinical Practice Guidelines: An Update of the 2011 ACCF/AHA/SCAI Guideline for Percutaneous Coronary Intervention, 2011 ACCF/AHA Guideline for Coronary Artery Bypass Graft Surgery, 2012 ACC/AHA/ACP/AATS/PCNA/SCAI/STS Guideline for the Diagnosis and Management of Patients With Stable Ischemic Heart Disease, 2013 ACCF/AHA Guideline for the Management of ST-Elevation Myocardial Infarction, 2014 AHA/ACC Guideline for the Management of Patients With Non-ST-Elevation Acute Coronary Syndromes, and 2014 ACC/AHA Guideline on Perioperative Cardiovascular Evaluation and Management of Patients Undergoing Noncardiac Surgery. *Circulation* **134**, e123-155 (2016).
161. S. J. Hong *et al.*, Treat-to-Target or High-Intensity Statin in Patients With Coronary Artery Disease: A Randomized Clinical Trial. *Jama* **329**, 1078-1087 (2023).
162. S. V. Arnold *et al.*, Beyond medication prescription as performance measures: optimal secondary prevention medication dosing after acute myocardial infarction. *J Am Coll Cardiol* **62**, 1791-1801 (2013).
163. M. J. Korhonen *et al.*, Adherence Tradeoff to Multiple Preventive Therapies and All-Cause Mortality After Acute Myocardial Infarction. *J Am Coll Cardiol* **70**, 1543-1554 (2017).
164. A. Kastrati, J. J. Coughlan, G. Ndrepepa, Primary PCI, Late Presenting STEMI, and the Limits of Time. *J Am Coll Cardiol* **78**, 1306-1308 (2021).
165. P. Sinnaeve, F. Van de Werf, Primary PCI and the indistinct 120 min time limit. *Eur Heart J* **41**, 867-869 (2020).
166. G. M. Frohlich, P. Meier, S. K. White, D. M. Yellon, D. J. Hausenloy, Myocardial reperfusion injury: looking beyond primary PCI. *Eur Heart J* **34**, 1714-1722 (2013).
167. R. A. Guyton, M. E. Halkos, Benefit of Complete Anatomic Revascularization in ISCHEMIA: Reprise of a Familiar Theme. *J Am Coll Cardiol* **83**, e37 (2024).
168. G. Campo *et al.*, Complete Versus Culprit-Only Revascularization in Older Patients With ST-Segment-Elevation Myocardial Infarction: An Individual Patient Meta-Analysis. *Circulation* **150**, 1508-1516 (2024).
169. A. Argiro *et al.*, Applications of Gene Therapy in Cardiomyopathies. *JACC Heart Fail* **12**, 248-260 (2024).
170. J. S. Hulot, K. Ishikawa, R. J. Hajjar, Gene therapy for the treatment of heart failure: promise postponed. *Eur Heart J* **37**, 1651-1658 (2016).
171. T. A. McKinsey *et al.*, Emerging epigenetic therapies of cardiac fibrosis and remodelling in heart failure: from basic mechanisms to early clinical development. *Cardiovasc Res* **118**, 3482-3498 (2023).

172. C. G. Tocchetti, A. Ghigo, E. Hirsch, 'Circulating' RNA-based therapies in Cardio-Oncology. *Eur Heart J* **43**, 4512-4514 (2022).
173. R. Bolli, M. Solankhi, X. L. Tang, A. Kahlon, Cell therapy in patients with heart failure: a comprehensive review and emerging concepts. *Cardiovasc Res* **118**, 951-976 (2022).
174. A. Terzic, A. Behfar, Stem cell therapy for heart failure: Ensuring regenerative proficiency. *Trends Cardiovasc Med* **26**, 395-404 (2016).
175. P. E. Scherer, S. Williams, M. Fogliano, G. Baldini, H. F. Lodish, A novel serum protein similar to C1q, produced exclusively in adipocytes. *J Biol Chem* **270**, 26746-26749 (1995).
176. Z. V. Wang, P. E. Scherer, Adiponectin, the past two decades. *J Mol Cell Biol* **8**, 93-100 (2016).
177. X. Lei, S. Qiu, G. Yang, Q. Wu, Adiponectin and metabolic cardiovascular diseases: Therapeutic opportunities and challenges. *Genes Dis* **10**, 1525-1536 (2023).
178. M. Zhang *et al.*, Causal associations of circulating adiponectin with cardiometabolic diseases and osteoporotic fracture. *Sci Rep* **12**, 6689 (2022).
179. H. Fang, R. L. Judd, Adiponectin Regulation and Function. *Compr Physiol* **8**, 1031-1063 (2018).
180. H. Ruan, L. Q. Dong, Adiponectin signaling and function in insulin target tissues. *J Mol Cell Biol* **8**, 101-109 (2016).
181. E. Tam, M. Ouimet, G. Sweeney, Cardioprotective Effects of Adiponectin-Stimulated Autophagy. *J Lipid Atheroscler* **14**, 40-53 (2025).
182. Y. Luo, M. Liu, Adiponectin: a versatile player of innate immunity. *J Mol Cell Biol* **8**, 120-128 (2016).
183. K. Ohashi *et al.*, Adiponectin promotes macrophage polarization toward an anti-inflammatory phenotype. *J Biol Chem* **285**, 6153-6160 (2010).
184. F. Lovren *et al.*, Adiponectin primes human monocytes into alternative anti-inflammatory M2 macrophages. *Am J Physiol Heart Circ Physiol* **299**, H656-663 (2010).
185. F. Wang, Y. Liu, W. Yang, J. Yuan, Z. Mo, Adiponectin inhibits NLRP3 inflammasome by modulating the AMPK-ROS pathway. *Int J Clin Exp Pathol* **11**, 3338-3347 (2018).
186. Y. Yan, L. Wang, N. Zhong, D. Wen, L. Liu, Multifaced roles of adipokines in endothelial cell function. *Front Endocrinol (Lausanne)* **15**, 1490143 (2024).
187. P. Song, M. H. Zou, Regulation of NAD(P)H oxidases by AMPK in cardiovascular systems. *Free Radic Biol Med* **52**, 1607-1619 (2012).
188. H. Li *et al.*, Adiponectin ameliorates hyperglycemia-induced cardiac hypertrophy and dysfunction by concomitantly activating Nrf2 and Brg1. *Free Radic Biol Med* **84**, 311-321 (2015).
189. X. Wang *et al.*, Adiponectin abates atherosclerosis by reducing oxidative stress. *Med Sci Monit* **20**, 1792-1800 (2014).
190. Y. Qian *et al.*, AdipoRon ameliorates chronic ethanol induced cardiac necroptosis by reducing ceramide mediated mtROS. *Free Radic Biol Med* **229**, 237-250 (2025).
191. Z. Lin *et al.*, Adiponectin mediates the metabolic effects of FGF21 on glucose homeostasis and insulin sensitivity in mice. *Cell Metab* **17**, 779-789 (2013).
192. M. Abou-Samra, C. M. Selvais, N. Dubuisson, S. M. Brichard, Adiponectin and Its Mimics on Skeletal Muscle: Insulin Sensitizers, Fat Burners, Exercise Mimickers, Muscling Pills ... or Everything Together? *Int J Mol Sci* **21** (2020).

193. R. B. Ceddia *et al.*, Globular adiponectin increases GLUT4 translocation and glucose uptake but reduces glycogen synthesis in rat skeletal muscle cells. *Diabetologia* **48**, 132-139 (2005).
194. S. M. Ishtiaq, H. Rashid, Z. Hussain, M. I. Arshad, J. A. Khan, Adiponectin and PPAR: a setup for intricate crosstalk between obesity and non-alcoholic fatty liver disease. *Rev Endocr Metab Disord* **20**, 253-261 (2019).
195. M. Iwabu *et al.*, Adiponectin and AdipoR1 regulate PGC-1alpha and mitochondria by Ca(2+) and AMPK/SIRT1. *Nature* **464**, 1313-1319 (2010).
196. W. Yan *et al.*, Impaired mitochondrial biogenesis due to dysfunctional adiponectin-AMPK-PGC-1alpha signaling contributing to increased vulnerability in diabetic heart. *Basic Res Cardiol* **108**, 329 (2013).
197. C. Sun *et al.*, Adiponectin up-regulates the decrease of myocardial autophagic flux induced by beta(1) -adrenergic receptor autoantibody partly dependent on AMPK. *J Cell Mol Med* **25**, 8464-8478 (2021).
198. J. Guo, K. Zhu, Z. Li, C. Xiao, Adiponectin Protects Hypoxia/Reoxygenation-Induced Cardiomyocyte Injury by Suppressing Autophagy. *J Immunol Res* **2022**, 8433464 (2022).
199. W. Wang *et al.*, The role of mitophagy in the mechanism of genioglossal dysfunction caused by chronic intermittent hypoxia and the protective effect of adiponectin. *Sleep Breath* **25**, 931-940 (2021).
200. J. Nah *et al.*, Ulk1-dependent alternative mitophagy plays a protective role during pressure overload in the heart. *Cardiovasc Res* **118**, 2638-2651 (2022).
201. H. K. Sung *et al.*, Ischemia-induced cardiac dysfunction is exacerbated in adiponectin-knockout mice due to impaired autophagy flux. *Clinical and Translational Science* **17**, e13758 (2024).
202. Y. Wang *et al.*, Restoring diabetes-induced autophagic flux arrest in ischemic/reperfused heart by ADIPOR (adiponectin receptor) activation involves both AMPK-dependent and AMPK-independent signaling. *Autophagy* **13**, 1855-1869 (2017).
203. T. Ali *et al.*, Adiponectin-mimetic novel nonapeptide rescues aberrant neuronal metabolic-associated memory deficits in Alzheimer's disease. *Mol Neurodegener* **16**, 23 (2021).
204. L. Otvos, Jr., Potential Adiponectin Receptor Response Modifier Therapeutics. *Front Endocrinol (Lausanne)* **10**, 539 (2019).
205. M. Okada-Iwabu *et al.*, A small-molecule AdipoR agonist for type 2 diabetes and short life in obesity. *Nature* **503**, 493-499 (2013).
206. A. Tarkhnishvili *et al.*, Effects of Short Term Adiponectin Receptor Agonism on Cardiac Function and Energetics in Diabetic db/db Mice. *J Lipid Atheroscler* **11**, 161-177 (2022).
207. W. Tan *et al.*, AdipoRon ameliorates the progression of heart failure with preserved ejection fraction via mitigating lipid accumulation and fibrosis. *J Adv Res* **68**, 299-315 (2025).
208. Y. Kim *et al.*, Adiponectin receptor agonist ameliorates cardiac lipotoxicity via enhancing ceramide metabolism in type 2 diabetic mice. *Cell Death Dis* **13**, 282 (2022).
209. S. R. Choi *et al.*, Adiponectin receptor agonist AdipoRon decreased ceramide, and lipotoxicity, and ameliorated diabetic nephropathy. *Metabolism* **85**, 348-360 (2018).
210. H. O. Kalkman, An Explanation for the Adiponectin Paradox. *Pharmaceuticals (Basel)* **14** (2021).

211. S. Zhao, C. M. Kusminski, P. E. Scherer, Adiponectin, Leptin and Cardiovascular Disorders. *Circ Res* **128**, 136-149 (2021).
212. S. Fu *et al.*, Extracellular vesicles in cardiovascular diseases. *Cell Death Discov* **6**, 68 (2020).
213. C. Liu *et al.*, Therapeutic Applications of Extracellular Vesicles for Myocardial Repair. *Front Cardiovasc Med* **8**, 758050 (2021).
214. D. W. Yu, P. P. Ge, A. L. Liu, X. Y. Yu, T. T. Liu, HSP20-mediated cardiomyocyte exosomes improve cardiac function in mice with myocardial infarction by activating Akt signaling pathway. *Eur Rev Med Pharmacol Sci* **23**, 4873-4881 (2019).
215. M. T. Al-Omar *et al.*, Endothelial progenitor cell-derived small extracellular vesicles for myocardial angiogenesis and revascularization. *J Clin Transl Res* **8**, 476-487 (2022).
216. L. Bonanni, N. Ferri, Mesenchymal Stem Cell-Derived Extracellular Vesicles in Myocardial Ischemia-Reperfusion Injury: A Comprehensive Review. *Biology (Basel)* **15** (2026).
217. Z. Liao *et al.*, Cardiac telocytes inhibit cardiac microvascular endothelial cell apoptosis through exosomal miRNA-21-5p-targeted cdip1 silencing to improve angiogenesis following myocardial infarction. *Theranostics* **11**, 268-291 (2021).
218. D. Qin, X. Wang, J. Pu, H. Hu, Cardiac cells and mesenchymal stem cells derived extracellular vesicles: a potential therapeutic strategy for myocardial infarction. *Front Cardiovasc Med* **11**, 1493290 (2024).
219. A. C. M. Omoto, J. M. do Carmo, A. A. da Silva, J. E. Hall, A. J. Mouton, Immunometabolism, extracellular vesicles and cardiac injury. *Front Endocrinol (Lausanne)* **14**, 1331284 (2023).
220. L. Y. M. Michel, Extracellular Vesicles in Adipose Tissue Communication with the Healthy and Pathological Heart. *Int J Mol Sci* **24** (2023).
221. S. Le Lay, S. Rome, X. Loyer, L. Nieto, Adipocyte-derived extracellular vesicles in health and diseases: Nano-packages with vast biological properties. *FASEB Bioadv* **3**, 407-419 (2021).
222. H. Zhao *et al.*, Small Extracellular Vesicles From Brown Adipose Tissue Mediate Exercise Cardioprotection. *Circ Res* **130**, 1490-1506 (2022).
223. M. Monguio-Tortajada *et al.*, Acellular cardiac scaffolds enriched with MSC-derived extracellular vesicles limit ventricular remodelling and exert local and systemic immunomodulation in a myocardial infarction porcine model. *Theranostics* **12**, 4656-4670 (2022).
224. A. Łabędź-Masłowska *et al.*, Mesenchymal stem cell-derived extracellular vesicles exert pro-angiogenic and pro-lymphangiogenic effects in ischemic tissues by transferring various microRNAs and proteins including ITGa5 and NRP1. *J Nanobiotechnology* **22**, 60 (2024).
225. Z. Hou *et al.*, hUC-MSC-EV-miR-24 enhances the protective effect of dexmedetomidine preconditioning against myocardial ischemia-reperfusion injury through the KEAP1/Nrf2/HO-1 signaling. *Drug Deliv Transl Res* **14**, 143-157 (2024).
226. J. Zhao *et al.*, Mesenchymal stromal cell-derived exosomes attenuate myocardial ischaemia-reperfusion injury through miR-182-regulated macrophage polarization. *Cardiovasc Res* **115**, 1205-1216 (2019).
227. C. Liu *et al.*, From exosomes to mitochondria and myocardial infarction: Molecular insight and therapeutic challenge. *Pharmacol Res* **209**, 107468 (2024).

228. M. Y. Emmert *et al.*, Intracoronary delivery of extracellular vesicles from human cardiac progenitor cells reduces infarct size in porcine acute myocardial infarction. *Eur Heart J* **45**, 728-732 (2024).
229. H. R. Hocine *et al.*, Extracellular Vesicles Released by Allogeneic Human Cardiac Stem/Progenitor Cells as Part of Their Therapeutic Benefit. *Stem Cells Transl Med* **8**, 911-924 (2019).
230. L. Chen *et al.*, Cardiac progenitor-derived exosomes protect ischemic myocardium from acute ischemia/reperfusion injury. *Biochem Biophys Res Commun* **431**, 566-571 (2013).
231. P. Saha *et al.*, Circulating exosomes derived from transplanted progenitor cells aid the functional recovery of ischemic myocardium. *Sci Transl Med* **11** (2019).
232. Y. Tominaga *et al.*, Pleiotropic effects of extracellular vesicles from induced pluripotent stem cell-derived cardiomyocytes on ischemic cardiomyopathy: A preclinical study. *J Heart Lung Transplant* **43**, 85-99 (2024).
233. G. Senesi *et al.*, miR-24-3p secreted as extracellular vesicle cargo by cardiomyocytes inhibits fibrosis in human cardiac microtissues. *Cardiovasc Res* **121**, 143-156 (2025).
234. B. Lima Correa *et al.*, Extracellular vesicles from human cardiovascular progenitors trigger a reparative immune response in infarcted hearts. *Cardiovasc Res* **117**, 292-307 (2021).
235. M. Adamiak *et al.*, Induced Pluripotent Stem Cell (iPSC)-Derived Extracellular Vesicles Are Safer and More Effective for Cardiac Repair Than iPSCs. *Circ Res* **122**, 296-309 (2018).
236. L. Yap *et al.*, Pluripotent stem cell-derived committed cardiac progenitors remuscularize damaged ischemic hearts and improve their function in pigs. *NPJ Regen Med* **8**, 26 (2023).
237. R. Gallet *et al.*, Exosomes secreted by cardiosphere-derived cells reduce scarring, attenuate adverse remodelling, and improve function in acute and chronic porcine myocardial infarction. *Eur Heart J* **38**, 201-211 (2017).
238. E. Lopez *et al.*, The Immunomodulatory Signature of Extracellular Vesicles From Cardiosphere-Derived Cells: A Proteomic and miRNA Profiling. *Front Cell Dev Biol* **8**, 321 (2020).
239. G. de Couto *et al.*, Exosomal MicroRNA Transfer Into Macrophages Mediates Cellular Postconditioning. *Circulation* **136**, 200-214 (2017).
240. J. R. Lin *et al.*, Brown Adipocyte ADRB3 Mediates Cardioprotection via Suppressing Exosomal iNOS. *Circ Res* **131**, 133-147 (2022).
241. R. Garcia-Martin, B. B. Brandao, T. Thomou, E. Altindis, C. R. Kahn, Tissue differences in the exosomal/small extracellular vesicle proteome and their potential as indicators of altered tissue metabolism. *Cell Rep* **38**, 110277 (2022).
242. M. Yadid *et al.*, Endothelial extracellular vesicles contain protective proteins and rescue ischemia-reperfusion injury in a human heart-on-chip. *Sci Transl Med* **12** (2020).
243. G. Wei *et al.*, Extracellular vesicle-derived CircWhsc1 promotes cardiomyocyte proliferation and heart repair by activating TRIM59/STAT3/Cyclin B2 pathway. *J Adv Res* **53**, 199-218 (2023).
244. N. Akbar *et al.*, Rapid neutrophil mobilization by VCAM-1+ endothelial cell-derived extracellular vesicles. *Cardiovasc Res* **119**, 236-251 (2023).
245. G. Jia, J. R. Sowers, Targeting endothelial exosomes for the prevention of cardiovascular disease. *Biochim Biophys Acta Mol Basis Dis* **1866**, 165833 (2020).

246. S. P. Ashcroft, B. Stocks, B. Egan, J. R. Zierath, Exercise induces tissue-specific adaptations to enhance cardiometabolic health. *Cell Metab* **36**, 278-300 (2024).
247. L. Gan *et al.*, Ischemic Heart-Derived Small Extracellular Vesicles Impair Adipocyte Function. *Circ Res* **130**, 48-66 (2022).
248. J. Wang *et al.*, Extracellular vesicles mediate the communication of adipose tissue with brain and promote cognitive impairment associated with insulin resistance. *Cell Metab* **34**, 1264-1279 e1268 (2022).
249. S. Zheng, M. Gong, J. Chen, Extracellular vesicles enriched with miR-150 released by macrophages regulates the TP53-IGF-1 axis to alleviate myocardial infarction. *Am J Physiol Heart Circ Physiol* **320**, H969-h979 (2021).
250. L. Li *et al.*, M2 Macrophage-Derived sEV Regulate Pro-Inflammatory CCR2(+) Macrophage Subpopulations to Favor Post-AMI Cardiac Repair. *Adv Sci (Weinh)* **10**, e2202964 (2023).
251. S. Graf *et al.*, Macrophage-derived extracellular vesicles alter cardiac recovery and metabolism in a rat heart model of donation after circulatory death. *J Cell Mol Med* **28**, e18281 (2024).
252. L. Weiss, H. Macleod, P. B. Maguire, Platelet-derived extracellular vesicles in cardiovascular disease and treatment - from maintaining homeostasis to targeted drug delivery. *Curr Opin Hematol* **32**, 4-13 (2025).
253. Q. Li *et al.*, Engineering extracellular vesicles with platelet membranes fusion enhanced targeted therapeutic angiogenesis in a mouse model of myocardial ischemia reperfusion. *Theranostics* **11**, 3916-3931 (2021).
254. C. Jung *et al.*, Circulating endothelial and platelet derived microparticles reflect the size of myocardium at risk in patients with ST-elevation myocardial infarction. *Atherosclerosis* **221**, 226-231 (2012).
255. D. Livkisa *et al.*, Extracellular vesicles purified from serum-converted human platelet lysates offer strong protection after cardiac ischaemia/reperfusion injury. *Biomaterials* **306**, 122502 (2024).
256. J. Jiang *et al.*, Platelet Membrane-Fused Circulating Extracellular Vesicles Protect the Heart from Ischemia/Reperfusion Injury. *Adv Healthc Mater* **12**, e2300052 (2023).
257. Y. Obata *et al.*, Adiponectin/T-cadherin system enhances exosome biogenesis and decreases cellular ceramides by exosomal release. *JCI Insight* **3** (2018).
258. Y. Nakamura *et al.*, Adiponectin Stimulates Exosome Release to Enhance Mesenchymal Stem-Cell-Driven Therapy of Heart Failure in Mice. *Mol Ther* **28**, 2203-2219 (2020).
259. A. Blandin *et al.*, Extracellular vesicles are carriers of adiponectin with insulin-sensitizing and anti-inflammatory properties. *Cell Rep* **42**, 112866 (2023).
260. J. Cherfils, M. Zeghouf, Regulation of small GTPases by GEFs, GAPs, and GDIs. *Physiol Rev* **93**, 269-309 (2013).
261. T. Wu *et al.*, Klotho-beta attenuates Rab8a-mediated exosome regulation and promotes prostate cancer progression. *Oncogene* **42**, 2801-2815 (2023).
262. B. Wu *et al.*, Stiff matrix induces exosome secretion to promote tumour growth. *Nat Cell Biol* **25**, 415-424 (2023).
263. S. Q. Hu *et al.*, Scutellarin-mediated autophagy activates exosome release of rat nucleus pulposus cells by positively regulating Rab8a via the PI3K/PTEN/Akt pathway. *Cell Biol Int* **46**, 1588-1603 (2022).

264. G. Heusch, Molecular basis of cardioprotection: signal transduction in ischemic pre-, post-, and remote conditioning. *Circ Res* **116**, 674-699 (2015).
265. D. J. Hausenloy, D. M. Yellon, Ischaemic conditioning and reperfusion injury. *Nat Rev Cardiol* **13**, 193-209 (2016).
266. R. Dharmakumar *et al.*, Reperfused Myocardial Infarction. *JACC: Advances* **4**, 101528 (2025).
267. T. Pischon *et al.*, Plasma adiponectin levels and risk of myocardial infarction in men. *Jama* **291**, 1730-1737 (2004).
268. R. Shibata *et al.*, Adiponectin protects against myocardial ischemia-reperfusion injury through AMPK- and COX-2-dependent mechanisms. *Nat Med* **11**, 1096-1103 (2005).
269. M. Dębiński *et al.*, Intracoronary adiponectin at reperfusion reduces infarct size in a porcine myocardial infarction model. *Int J Mol Med* **27**, 775-781 (2011).
270. H. Yue *et al.*, Adiponectin protects against myocardial ischemia-reperfusion injury: a systematic review and meta-analysis of preclinical animal studies. *Lipids Health Dis* **23**, 51 (2024).
271. Y. Liu *et al.*, Adiponectin stimulates autophagy and reduces oxidative stress to enhance insulin sensitivity during high-fat diet feeding in mice. *Diabetes* **64**, 36-48 (2015).
272. S. Cho *et al.*, Cardioprotection by the adiponectin receptor agonist ALY688 in a preclinical mouse model of heart failure with reduced ejection fraction (HFrEF). *Biomed Pharmacother* **171**, 116119 (2024).
273. J. Tang *et al.*, Development of a non-invasive bioassay for adiponectin target engagement in mice. *iScience* **27**, 110994 (2024).
274. J. Tang *et al.*, Potent anti-inflammatory effects of the adiponectin receptor agonist, ALY688. *Physiology* **38**, 5733710 (2023).
275. H. Li *et al.*, Unlocking the Potential of Extracellular Vesicles in Cardiovascular Disease. *J Cell Mol Med* **29**, e70407 (2025).
276. L. Cheng, A. F. Hill, Therapeutically harnessing extracellular vesicles. *Nat Rev Drug Discov* **21**, 379-399 (2022).
277. S. Hu, Y. Hu, W. Yan, Extracellular vesicle-mediated interorgan communication in metabolic diseases. *Trends Endocrinol Metab* **34**, 571-582 (2023).
278. P. Sun *et al.*, Extracellular vesicle-packaged mitochondrial disturbing miRNA exacerbates cardiac injury during acute myocardial infarction. *Clin Transl Med* **12**, e779 (2022).
279. X. Ge *et al.*, Myocardial ischemia-reperfusion induced cardiac extracellular vesicles harbour proinflammatory features and aggravate heart injury. *J Extracell Vesicles* **10**, e12072 (2021).
280. K. Fukuoka *et al.*, ER stress decreases exosome production through adiponectin/T-cadherin-dependent and -independent pathways. *J Biol Chem* **299**, 105114 (2023).
281. F. A. Ran *et al.*, Genome engineering using the CRISPR-Cas9 system. *Nat Protoc* **8**, 2281-2308 (2013).
282. N. E. Sanjana, O. Shalem, F. Zhang, Improved vectors and genome-wide libraries for CRISPR screening. *Nat Methods* **11**, 783-784 (2014).
283. R. Velagapudi *et al.*, Induction of Autophagy and Activation of SIRT-1 Deacetylation Mechanisms Mediate Neuroprotection by the Pomegranate Metabolite Urolithin A in BV2 Microglia and Differentiated 3D Human Neural Progenitor Cells. *Mol Nutr Food Res* **63**, e1801237 (2019).

284. M. R. Hildebrandt *et al.*, Precision Health Resource of Control iPSC Lines for Versatile Multilineage Differentiation. *Stem Cell Reports* **13**, 1126-1141 (2019).
285. J. Tang *et al.*, Impaired autophagy flux contributes to enhanced ischemia reperfusion injury in the diabetic heart. *Autophagy Reports* **3**, 2330327 (2024).
286. M. Ouimet *et al.*, MicroRNA-33-dependent regulation of macrophage metabolism directs immune cell polarization in atherosclerosis. *J Clin Invest* **125**, 4334-4348 (2015).
287. S. Lebek *et al.*, Ablation of CaMKIIdelta oxidation by CRISPR-Cas9 base editing as a therapy for cardiac disease. *Science* **379**, 179-185 (2023).
288. Q. Xiang, X. Yi, X. H. Zhu, X. Wei, D. S. Jiang, Regulated cell death in myocardial ischemia-reperfusion injury. *Trends Endocrinol Metab* **35**, 219-234 (2024).
289. X. Ma *et al.*, Impaired autophagosome clearance contributes to cardiomyocyte death in ischemia/reperfusion injury. *Circulation* **125**, 3170-3181 (2012).
290. P. Sanchez-Perez *et al.*, Energy substrate metabolism, mitochondrial structure and oxidative stress after cardiac ischemia-reperfusion in mice lacking UCP3. *Free Radic Biol Med* **205**, 244-261 (2023).
291. M. Litvinukova *et al.*, Cells of the adult human heart. *Nature* **588**, 466-472 (2020).
292. X. Bi *et al.*, Endoplasmic Reticulum Chaperone GRP78 Protects Heart From Ischemia/Reperfusion Injury Through Akt Activation. *Circ Res* **122**, 1545-1554 (2018).
293. Z. Liu *et al.*, ER chaperone GRP78/BiP translocates to the nucleus under stress and acts as a transcriptional regulator. *Proc Natl Acad Sci U S A* **120**, e2303448120 (2023).
294. W. Cao *et al.*, The Role of PGK1 in Promoting Ischemia/Reperfusion Injury-Induced Microglial M1 Polarization and Inflammation by Regulating Glycolysis. *Neuromolecular Med* **25**, 301-311 (2023).
295. X. Li *et al.*, Mitochondria-Translocated PGK1 Functions as a Protein Kinase to Coordinate Glycolysis and the TCA Cycle in Tumorigenesis. *Mol Cell* **61**, 705-719 (2016).
296. T. Xu *et al.*, Git1-PGK1 interaction achieves self-protection against spinal cord ischemia-reperfusion injury by modulating Keap1/Nrf2 signaling. *Redox Biol* **62**, 102682 (2023).
297. C. Y. Chen *et al.*, Suppression of detyrosinated microtubules improves cardiomyocyte function in human heart failure. *Nat Med* **24**, 1225-1233 (2018).
298. A. M. Manso *et al.*, Talin1 has unique expression versus talin 2 in the heart and modifies the hypertrophic response to pressure overload. *J Biol Chem* **288**, 4252-4264 (2013).
299. A. Y. Li, Q. Yang, K. Yang, miR-133a mediates the hypoxia-induced apoptosis by inhibiting TAGLN2 expression in cardiac myocytes. *Mol Cell Biochem* **400**, 173-181 (2015).
300. S. M. Hwang *et al.*, Transgelin 2 guards T cell lipid metabolism and antitumour function. *Nature* **635**, 1010-1018 (2024).
301. M. Asada *et al.*, ADIP, a novel Afadin- and alpha-actinin-binding protein localized at cell-cell adherens junctions. *J Biol Chem* **278**, 4103-4111 (2003).
302. C. Maillard *et al.*, Tubulin mutations in human neurodevelopmental disorders. *Semin Cell Dev Biol* **137**, 87-95 (2023).
303. P. Holmager *et al.*, Galectin-3 and fibulin-1 in systolic heart failure - relation to glucose metabolism and left ventricular contractile reserve. *BMC Cardiovasc Disord* **17**, 22 (2017).

304. M. Liu, B. López de Juan Abad, K. Cheng, Cardiac fibrosis: Myofibroblast-mediated pathological regulation and drug delivery strategies. *Adv Drug Deliv Rev* **173**, 504-519 (2021).
305. M. Cao *et al.*, Role of CyPA in cardiac hypertrophy and remodeling. *Biosci Rep* **39** (2019).
306. F. Canonico *et al.*, GLUT-1/PKM2 loop dysregulation in patients with non-ST-segment elevation myocardial infarction promotes metainflammation. *Cardiovasc Res* **119**, 2653-2662 (2023).
307. M. A. Lorenzana-Carrillo *et al.*, TRIM35-mediated degradation of nuclear PKM2 destabilizes GATA4/6 and induces P53 in cardiomyocytes to promote heart failure. *Sci Transl Med* **14**, eabm3565 (2022).
308. M. Rihan, S. S. Sharma, Role of Pyruvate Kinase M2 (PKM2) in Cardiovascular Diseases. *J Cardiovasc Transl Res* **16**, 382-402 (2023).
309. C. E. Molina *et al.*, Identification of optimal reference genes for transcriptomic analyses in normal and diseased human heart. *Cardiovascular research* **114**, 247-258 (2018).
310. L. Ansani *et al.*, F13A1 Gene Variant (V34L) and Residual Circulating FXIIIA Levels Predict Short- and Long-Term Mortality in Acute Myocardial Infarction after Coronary Angioplasty. *Int J Mol Sci* **19** (2018).
311. S. Q. Wang *et al.*, Targeting GSTP1 as Therapeutic Strategy against Lung Adenocarcinoma Stemness and Resistance to Tyrosine Kinase Inhibitors. *Adv Sci (Weinh)* **10**, e2205262 (2023).
312. T. Gautier *et al.*, New therapeutic horizons for plasma phospholipid transfer protein (PLTP): Targeting endotoxemia, infection and sepsis. *Pharmacol Ther* **236**, 108105 (2022).
313. J. Huuskonen, V. M. Olkkonen, M. Jauhiainen, C. Ehnholm, The impact of phospholipid transfer protein (PLTP) on HDL metabolism. *Atherosclerosis* **155**, 269-281 (2001).
314. B. Y. Hsiao *et al.*, Human Costars Family Protein ABRACL Modulates Actin Dynamics and Cell Migration and Associates with Tumorigenic Growth. *Int J Mol Sci* **22** (2021).
315. Z. Zheng, L. Yu, Y. Wu, H. Wu, FGL2 knockdown improves heart function through regulation of TLR9 signaling in the experimental autoimmune myocarditis rats. *Immunol Res* **66**, 52-58 (2018).
316. X. Zhang, S. Wang, S. Fang, B. Yu, Prognostic Role of High Sensitivity C-Reactive Protein in Patients With Acute Myocardial Infarction. *Front Cardiovasc Med* **8**, 659446 (2021).
317. C. U. Lorentz *et al.*, Factor XI contributes to myocardial ischemia-reperfusion injury in mice. *Blood Adv* **2**, 85-88 (2018).
318. D. J. Hausenloy, D. M. Yellon, Myocardial ischemia-reperfusion injury: a neglected therapeutic target. *J Clin Invest* **123**, 92-100 (2013).
319. M. J. Kim, H. X. Deng, Y. C. Wong, T. Siddique, D. Krainc, The Parkinson's disease-linked protein TMEM230 is required for Rab8a-mediated secretory vesicle trafficking and retromer trafficking. *Hum Mol Genet* **26**, 729-741 (2017).
320. Y. D. Chen *et al.*, Exophagy of annexin A2 via RAB11, RAB8A and RAB27A in IFN-γ-stimulated lung epithelial cells. *Sci Rep* **7**, 5676 (2017).
321. M. Essid, N. Gopaldass, K. Yoshida, C. Merrifield, T. Soldati, Rab8a regulates the exocyst-mediated kiss-and-run discharge of the Dictyostelium contractile vacuole. *Mol Biol Cell* **23**, 1267-1282 (2012).

322. C. Horvath *et al.*, Inhibition of Cardiac RIP3 Mitigates Early Reperfusion Injury and Calcium-Induced Mitochondrial Swelling without Altering Necroptotic Signalling. *Int J Mol Sci* **22** (2021).
323. S. Gao *et al.*, Intervention of Tanshinone IIA on the PGK1-PDHK1 Pathway to Reprogram Macrophage Phenotype After Myocardial Infarction. *Cardiovasc Drugs Ther* **38**, 1359-1373 (2024).
324. M. K. Nayak *et al.*, The metabolic enzyme pyruvate kinase M2 regulates platelet function and arterial thrombosis. *Blood* **137**, 1658-1668 (2021).
325. L. Gan *et al.*, Small Extracellular Microvesicles Mediated Pathological Communications Between Dysfunctional Adipocytes and Cardiomyocytes as a Novel Mechanism Exacerbating Ischemia/Reperfusion Injury in Diabetic Mice. *Circulation* **141**, 968-983 (2020).
326. A. A. Salybekov *et al.*, Extracellular Vesicles Derived From Regeneration Associated Cells Preserve Heart Function After Ischemia-Induced Injury. *Front Cardiovasc Med* **8**, 754254 (2021).
327. J. Xiao *et al.*, Cardiac progenitor cell-derived exosomes prevent cardiomyocytes apoptosis through exosomal miR-21 by targeting PDCD4. *Cell Death Dis* **7**, e2277 (2016).
328. Q. Wu *et al.*, Extracellular vesicles from human embryonic stem cell-derived cardiovascular progenitor cells promote cardiac infarct healing through reducing cardiomyocyte death and promoting angiogenesis. *Cell Death Dis* **11**, 354 (2020).
329. J. Li *et al.*, Inhalable Stem Cell Exosomes Promote Heart Repair After Myocardial Infarction. *Circulation* **150**, 710-723 (2024).
330. A. Huang *et al.*, Intravenously transplanted mesenchymal stromal cells: a new endocrine reservoir for cardioprotection. *Stem Cell Res Ther* **13**, 253 (2022).
331. R. T. Morales, J. Ko, Future of Digital Assays to Resolve Clinical Heterogeneity of Single Extracellular Vesicles. *ACS Nano* **16**, 11619-11645 (2022).
332. S. Wendt *et al.*, Evaluation of the cardioprotective potential of extracellular vesicles - a systematic review and meta-analysis. *Sci Rep* **8**, 15702 (2018).
333. C. W. Tsao *et al.*, Heart Disease and Stroke Statistics-2022 Update: A Report From the American Heart Association. *Circulation* **145**, e153-e639 (2022).
334. G. Heusch *et al.*, Cardiovascular remodelling in coronary artery disease and heart failure. *Lancet* **383**, 1933-1943 (2014).
335. P. S. Azevedo, B. F. Polegato, M. F. Minicucci, S. A. Paiva, L. A. Zornoff, Cardiac Remodeling: Concepts, Clinical Impact, Pathophysiological Mechanisms and Pharmacologic Treatment. *Arq Bras Cardiol* **106**, 62-69 (2016).
336. G. Heusch, Myocardial ischaemia-reperfusion injury and cardioprotection in perspective. *Nat Rev Cardiol* **17**, 773-789 (2020).
337. M. Tkach, C. Thery, Communication by Extracellular Vesicles: Where We Are and Where We Need to Go. *Cell* **164**, 1226-1232 (2016).
338. S. Hartwig *et al.*, Exosomal proteins constitute an essential part of the human adipose tissue secretome. *Biochim Biophys Acta Proteins Proteom* **1867**, 140172 (2019).
339. S. Kita, N. Maeda, I. Shimomura, Interorgan communication by exosomes, adipose tissue, and adiponectin in metabolic syndrome. *J Clin Invest* **129**, 4041-4049 (2019).
340. C. Crewe, Energetic Stress-Induced Metabolic Regulation by Extracellular Vesicles. *Compr Physiol* **13**, 5051-5068 (2023).

341. F. Mitani *et al.*, Asteltoxin inhibits extracellular vesicle production through AMPK/mTOR-mediated activation of lysosome function. *Sci Rep* **12**, 6674 (2022).
342. Y. You *et al.*, Extracellular vesicle-mediated VEGF-A mRNA delivery rescues ischaemic injury with low immunogenicity. *Eur Heart J* **46**, 1662-1676 (2025).
343. X. Liu *et al.*, Cardiac-derived extracellular vesicles improve mitochondrial function to protect the heart against ischemia/reperfusion injury by delivering ATP5a1. *J Nanobiotechnology* **22**, 385 (2024).
344. J. Zhang *et al.*, Exosomes Derived from Human Endothelial Progenitor Cells Accelerate Cutaneous Wound Healing by Promoting Angiogenesis Through Erk1/2 Signaling. *Int J Biol Sci* **12**, 1472-1487 (2016).
345. X. Loyer *et al.*, Intra-Cardiac Release of Extracellular Vesicles Shapes Inflammation Following Myocardial Infarction. *Circ Res* **123**, 100-106 (2018).
346. V. Biemmi *et al.*, Inflammatory extracellular vesicles prompt heart dysfunction via TRL4-dependent NF-kappaB activation. *Theranostics* **10**, 2773-2790 (2020).
347. S. Tacconi *et al.*, M1-derived extracellular vesicles polarize recipient macrophages into M2-like macrophages and alter skeletal muscle homeostasis in a hyper-glucose environment. *Cell Commun Signal* **22**, 193 (2024).
348. R. Almeida Paiva *et al.*, Ischaemia alters the effects of cardiomyocyte-derived extracellular vesicles on macrophage activation. *J Cell Mol Med* **23**, 1137-1151 (2019).
349. M. Park, G. Sweeney, Direct effects of adipokines on the heart: focus on adiponectin. *Heart Fail Rev* **18**, 631-644 (2013).
350. R. Shibata *et al.*, Adiponectin-mediated modulation of hypertrophic signals in the heart. *Nat Med* **10**, 1384-1389 (2004).
351. A. Xu, P. M. Vanhoutte, Adiponectin and adipocyte fatty acid binding protein in the pathogenesis of cardiovascular disease. *Am J Physiol Heart Circ Physiol* **302**, H1231-1240 (2012).
352. L. Woodward, I. Akoumianakis, C. Antoniades, Unravelling the adiponectin paradox: novel roles of adiponectin in the regulation of cardiovascular disease. *British journal of pharmacology* **174**, 4007-4020 (2017).
353. R. Shibata *et al.*, Adiponectin protects against the development of systolic dysfunction following myocardial infarction. *J Mol Cell Cardiol* **42**, 1065-1074 (2007).
354. H. K. Sung *et al.*, Ischemia-induced cardiac dysfunction is exacerbated in adiponectin-knockout mice due to impaired autophagy flux. *Clin Transl Sci* **17**, e13758 (2024).
355. K. Kulaj *et al.*, Adipocyte-derived extracellular vesicles increase insulin secretion through transport of insulinotropic protein cargo. *Nat Commun* **14**, 709 (2023).
356. L. Otvos, Jr. *et al.*, Design and development of a peptide-based adiponectin receptor agonist for cancer treatment. *BMC Biotechnol* **11**, 90 (2011).
357. H. K. Sung, P. L. Mitchell, S. Gross, A. Marette, G. Sweeney, ALY688 elicits adiponectin-mimetic signaling and improves insulin action in skeletal muscle cells. *Am J Physiol Cell Physiol* **322**, C151-c163 (2022).
358. D. Da Eira, S. Jani, H. Sung, G. Sweeney, R. B. Ceddia, Effects of the adiponectin mimetic compound ALY688 on glucose and fat metabolism in visceral and subcutaneous rat adipocytes. *Adipocyte* **9**, 550-562 (2020).
359. S. Maji *et al.*, Exosomal Annexin II Promotes Angiogenesis and Breast Cancer Metastasis. *Mol Cancer Res* **15**, 93-105 (2017).

360. E. Zubkova, A. Kalinin, A. Bolotskaya, I. Beloglazova, M. Menshikov, Autophagy-Dependent Secretion: Crosstalk between Autophagy and Exosome Biogenesis. *Curr Issues Mol Biol* **46**, 2209-2235 (2024).
361. C. Global Burden of Metabolic Risk Factors for Chronic Diseases *et al.*, Metabolic mediators of the effects of body-mass index, overweight, and obesity on coronary heart disease and stroke: a pooled analysis of 97 prospective cohorts with 1.8 million participants. *Lancet* **383**, 970-983 (2014).
362. M. M. Dann *et al.*, Quantification of murine myocardial infarct size using 2-D and 4-D high-frequency ultrasound. *Am J Physiol Heart Circ Physiol* **322**, H359-H372 (2022).
363. M. E. Kranendonk *et al.*, Extracellular vesicle markers in relation to obesity and metabolic complications in patients with manifest cardiovascular disease. *Cardiovasc Diabetol* **13**, 37 (2014).
364. C. Han, J. Yang, J. Sun, G. Qin, Extracellular vesicles in cardiovascular disease: Biological functions and therapeutic implications. *Pharmacol Ther* **233**, 108025 (2022).
365. L. Zhu, Y. Liu, K. Wang, N. Wang, Regulated cell death in acute myocardial infarction: Molecular mechanisms and therapeutic implications. *Ageing Res Rev* **104**, 102629 (2025).
366. E. T. Chouchani *et al.*, Ischaemic accumulation of succinate controls reperfusion injury through mitochondrial ROS. *Nature* **515**, 431-435 (2014).
367. B. Y. Liu *et al.*, Baicalein attenuates cardiac hypertrophy in mice via suppressing oxidative stress and activating autophagy in cardiomyocytes. *Acta Pharmacol Sin* **42**, 701-714 (2021).
368. Y. Xing *et al.*, Blunting TRPML1 channels protects myocardial ischemia/reperfusion injury by restoring impaired cardiomyocyte autophagy. *Basic Res Cardiol* **117**, 20 (2022).
369. I. E. Bank *et al.*, The diagnostic and prognostic potential of plasma extracellular vesicles for cardiovascular disease. *Expert Rev Mol Diagn* **15**, 1577-1588 (2015).
370. S. H. Han, M. J. Quon, J. A. Kim, K. K. Koh, Adiponectin and cardiovascular disease: response to therapeutic interventions. *J Am Coll Cardiol* **49**, 531-538 (2007).
371. M. B. Nielsen *et al.*, Plasma adiponectin levels and risk of heart failure, atrial fibrillation, aortic valve stenosis, and myocardial infarction: large-scale observational and Mendelian randomization evidence. *Cardiovasc Res* **120**, 95-107 (2024).
372. S. Kim-Mitsuyama *et al.*, Total adiponectin is associated with incident cardiovascular and renal events in treated hypertensive patients: subanalysis of the ATTEMPT-CVD randomized trial. *Sci Rep* **9**, 16589 (2019).
373. T. Yamauchi, T. Kadowaki, Adiponectin receptor as a key player in healthy longevity and obesity-related diseases. *Cell Metab* **17**, 185-196 (2013).
374. Y. Wang, X. L. Ma, W. B. Lau, Cardiovascular Adiponectin Resistance: The Critical Role of Adiponectin Receptor Modification. *Trends Endocrinol Metab* **28**, 519-530 (2017).
375. T. C. Lai *et al.*, MicroRNA-221/222 Mediates ADSC-Exosome-Induced Cardioprotection Against Ischemia/Reperfusion by Targeting PUMA and ETS-1. *Front Cell Dev Biol* **8**, 569150 (2020).
376. D. Zhu *et al.*, Exosomes from adipose-derived stem cells alleviate myocardial infarction via microRNA-31/FIH1/HIF-1alpha pathway. *J Mol Cell Cardiol* **162**, 10-19 (2022).
377. Y. Ding *et al.*, Brown adipose tissue-derived FGF21 mediates the cardioprotection of dexmedetomidine in myocardial ischemia/reperfusion injury. *Sci Rep* **14**, 18292 (2024).

378. K. Fujii *et al.*, Pharmacological HIF-1 activation upregulates extracellular vesicle production synergistically with adiponectin through transcriptional induction and protein stabilization of T-cadherin. *Sci Rep* **14**, 3620 (2024).
379. Y. Zhang *et al.*, miR-155 down-regulation protects the heart from hypoxic damage by activating fructose metabolism in cardiac fibroblasts. *J Adv Res* **39**, 103-117 (2022).
380. M. A. Herman, M. J. Birnbaum, Molecular aspects of fructose metabolism and metabolic disease. *Cell Metab* **33**, 2329-2354 (2021).
381. H. Yamamoto, S. Zhang, N. Mizushima, Autophagy genes in biology and disease. *Nat Rev Genet* **24**, 382-400 (2023).
382. M. Jin *et al.*, Inhibiting the Histone Demethylase Kdm4a Restrains Cardiac Fibrosis After Myocardial Infarction by Promoting Autophagy in Premature Senescent Fibroblasts. *Adv Sci (Weinh)* **12**, e2414830 (2025).
383. Q. Zhang *et al.*, Inhibiting CD36 palmitoylation improves cardiac function post-infarction by regulating lipid metabolic homeostasis and autophagy. *Nat Commun* **16**, 6602 (2025).
384. J. M. Alam *et al.*, Complete set of the Atg8-E1-E2-E3 conjugation machinery forms an interaction web that mediates membrane shaping. *Nat Struct Mol Biol* **31**, 170-178 (2024).
385. C. J. A. Ramachandra, S. Hernandez-Resendiz, G. E. Crespo-Avilan, Y. H. Lin, D. J. Hausenloy, Mitochondria in acute myocardial infarction and cardioprotection. *EBioMedicine* **57**, 102884 (2020).
386. R. A. Kloner *et al.*, New and revisited approaches to preserving the reperfused myocardium. *Nat Rev Cardiol* **14**, 679-693 (2017).
387. R. Guo, S. Zong, M. Wu, J. Gu, M. Yang, Architecture of Human Mitochondrial Respiratory Megacomplex I(2)III(2)IV(2). *Cell* **170**, 1247-1257 e1212 (2017).
388. I. Vercellino, L. A. Sazanov, The assembly, regulation and function of the mitochondrial respiratory chain. *Nat Rev Mol Cell Biol* **23**, 141-161 (2022).
389. D. A. Brown *et al.*, Expert consensus document: Mitochondrial function as a therapeutic target in heart failure. *Nat Rev Cardiol* **14**, 238-250 (2017).
390. S. Ranjbarvaziri *et al.*, Altered Cardiac Energetics and Mitochondrial Dysfunction in Hypertrophic Cardiomyopathy. *Circulation* **144**, 1714-1731 (2021).
391. B. J. Floyd *et al.*, Mitochondrial Protein Interaction Mapping Identifies Regulators of Respiratory Chain Function. *Mol Cell* **63**, 621-632 (2016).
392. S. Hernandez-Resendiz *et al.*, Targeting mitochondrial fusion and fission proteins for cardioprotection. *J Cell Mol Med* **24**, 6571-6585 (2020).
393. T. Wai *et al.*, Imbalanced OPA1 processing and mitochondrial fragmentation cause heart failure in mice. *Science* **350**, aad0116 (2015).
394. J. M. Quiles, A. B. Gustafsson, The role of mitochondrial fission in cardiovascular health and disease. *Nat Rev Cardiol* **19**, 723-736 (2022).
395. W. D. Watson *et al.*, Retained Metabolic Flexibility of the Failing Human Heart. *Circulation* **148**, 109-123 (2023).
396. S. Neubauer, The failing heart--an engine out of fuel. *N Engl J Med* **356**, 1140-1151 (2007).
397. B. Zhou, R. Tian, Mitochondrial dysfunction in pathophysiology of heart failure. *J Clin Invest* **128**, 3716-3726 (2018).

398. Q. Liu, J. C. Docherty, J. C. Rendell, A. S. Clanachan, G. D. Lopaschuk, High levels of fatty acids delay the recovery of intracellular pH and cardiac efficiency in post-ischemic hearts by inhibiting glucose oxidation. *J Am Coll Cardiol* **39**, 718-725 (2002).
399. S. C. Kolwicz, Jr., L. Liu, I. J. Goldberg, R. Tian, Enhancing Cardiac Triacylglycerol Metabolism Improves Recovery From Ischemic Stress. *Diabetes* **64**, 2817-2827 (2015).
400. I. J. Goldberg, C. M. Trent, P. C. Schulze, Lipid metabolism and toxicity in the heart. *Cell Metab* **15**, 805-812 (2012).
401. A. Zadoorian, X. Du, H. Yang, Lipid droplet biogenesis and functions in health and disease. *Nat Rev Endocrinol* **19**, 443-459 (2023).
402. J. A. Olzmann, P. Carvalho, Dynamics and functions of lipid droplets. *Nat Rev Mol Cell Biol* **20**, 137-155 (2019).
403. P. C. Schulze, K. Drosatos, I. J. Goldberg, Lipid Use and Misuse by the Heart. *Circulation Research* **118**, 1736-1751 (2016).
404. Y. Getiye, T. A. Rice, B. D. Phillips, D. F. Carrillo, G. He, Dysregulated lipolysis and lipophagy in lipid droplets of macrophages from high fat diet-fed obese mice. *J Cell Mol Med* **26**, 4825-4836 (2022).
405. U. Kintscher, A. Foryst-Ludwig, G. Haemmerle, R. Zechner, The Role of Adipose Triglyceride Lipase and Cytosolic Lipolysis in Cardiac Function and Heart Failure. *Cell Rep Med* **1**, 100001 (2020).
406. I. J. Goldberg *et al.*, Deciphering the Role of Lipid Droplets in Cardiovascular Disease: A Report From the 2017 National Heart, Lung, and Blood Institute Workshop. *Circulation* **138**, 305-315 (2018).
407. R. Zechner, F. Madeo, D. Kratky, Cytosolic lipolysis and lipophagy: two sides of the same coin. *Nat Rev Mol Cell Biol* **18**, 671-684 (2017).
408. M. Boutant *et al.*, Mfn2 is critical for brown adipose tissue thermogenic function. *Embo j* **36**, 1543-1558 (2017).
409. B. Kien *et al.*, Lipid droplet-mitochondria coupling via perilipin 5 augments respiratory capacity but is dispensable for FA oxidation. *J Lipid Res* **63**, 100172 (2022).
410. L. Hu *et al.*, Mfn2/Hsc70 Complex Mediates the Formation of Mitochondria-Lipid Droplets Membrane Contact and Regulates Myocardial Lipid Metabolism. *Advanced Science* **11**, 2307749 (2024).
411. Q. Ouyang *et al.*, Rab8a as a mitochondrial receptor for lipid droplets in skeletal muscle. *Dev Cell* **58**, 289-305.e286 (2023).
412. X. Ao, L. Zou, Y. Wu, Regulation of autophagy by the Rab GTPase network. *Cell Death & Differentiation* **21**, 348-358 (2014).
413. L. Wu *et al.*, Rab8a-AS160-MSS4 regulatory circuit controls lipid droplet fusion and growth. *Dev Cell* **30**, 378-393 (2014).
414. A. Bezawork-Geleta *et al.*, Proximity proteomics reveals a mechanism of fatty acid transfer at lipid droplet-mitochondria- endoplasmic reticulum contact sites. *Nature Communications* **16**, 2135 (2025).
415. B. Schroeder *et al.*, The small GTPase Rab7 as a central regulator of hepatocellular lipophagy. *Hepatology* **61** (2015).
416. K. Kanerva *et al.*, LDL cholesterol recycles to the plasma membrane via a Rab8a-Myosin5b-actin-dependent membrane transport route. *Dev Cell* **27**, 249-262 (2013).

417. K. M. Holzem *et al.*, Mitochondrial structure and function are not different between nonfailing donor and end-stage failing human hearts. *The FASEB Journal* **30**, 2698-2707 (2016).
418. Q. Chen *et al.*, Rab8a Deficiency in Skeletal Muscle Causes Hyperlipidemia and Hepatosteatosis by Impairing Muscle Lipid Uptake and Storage. *Diabetes* **66**, 2387-2399 (2017).
419. Y. Zhang *et al.*, Adiponectin inhibits oxidative/nitrative stress during myocardial ischemia and reperfusion via PKA signaling. *Am J Physiol Endocrinol Metab* **305**, E1436-1443 (2013).
420. Y. Kim *et al.*, Adiponectin receptor agonist ameliorates cardiac lipotoxicity via enhancing ceramide metabolism in type 2 diabetic mice. *Cell Death & Disease* **13**, 282 (2022).
421. D. Qi, L. H. Young, AMPK: energy sensor and survival mechanism in the ischemic heart. *Trends Endocrinol Metab* **26**, 422-429 (2015).
422. K. Zhang *et al.*, FGF21 protects against HFpEF by improving cardiac mitochondrial bioenergetics in mice. *Nature Communications* **16**, 1661 (2025).
423. L. Yang *et al.*, Metformin Inhibits Lipid Droplets Fusion and Growth via Reduction in Cidec and Its Regulatory Factors in Rat Adipose-Derived Stem Cells. *Int J Mol Sci* **23** (2022).
424. A. J. Valente, L. A. Maddalena, E. L. Robb, F. Moradi, J. A. Stuart, A simple ImageJ macro tool for analyzing mitochondrial network morphology in mammalian cell culture. *Acta Histochem* **119**, 315-326 (2017).
425. S. Zhang *et al.*, The regulation, function, and role of lipophagy, a form of selective autophagy, in metabolic disorders. *Cell Death Dis* **13**, 132 (2022).
426. T. Laval, M. Ouimet, A role for lipophagy in atherosclerosis. *Nat Rev Cardiol* **20**, 431-432 (2023).
427. C. J. Rosado, D. Mijaljica, I. Hatzinisiriou, M. Prescott, R. J. Devenish, Rosella: a fluorescent pH-biosensor for reporting vacuolar turnover of cytosol and organelles in yeast. *Autophagy* **4**, 205-213 (2008).
428. T. Laval *et al.*, A Rosella-PLIN2 Knock-in Mouse Reveals Lipophagy and Immunometabolic Interplay in Atherosclerosis. *bioRxiv* 10.1101/2025.04.15.647781, 2025.2004.2015.647781 (2025).
429. I. Y. Benador, M. Veliova, M. Liesa, O. S. Shirihai, Mitochondria Bound to Lipid Droplets: Where Mitochondrial Dynamics Regulate Lipid Storage and Utilization. *Cell Metab* **29**, 827-835 (2019).
430. G. E. Miner *et al.*, PLIN5 interacts with FATP4 at membrane contact sites to promote lipid droplet-to-mitochondria fatty acid transport. *Dev Cell* **58**, 1250-1265.e1256 (2023).
431. V. I. Gallardo-Montejano *et al.*, Perilipin 5 links mitochondrial uncoupled respiration in brown fat to healthy white fat remodeling and systemic glucose tolerance. *Nat Commun* **12**, 3320 (2021).
432. H. Wang *et al.*, Perilipin 5, a lipid droplet-associated protein, provides physical and metabolic linkage to mitochondria. *Journal of Lipid Research* **52**, 2159-2168 (2011).
433. A. S. Rambold, S. Cohen, J. Lippincott-Schwartz, Fatty acid trafficking in starved cells: regulation by lipid droplet lipolysis, autophagy, and mitochondrial fusion dynamics. *Dev Cell* **32**, 678-692 (2015).
434. H. Stenmark, Rab GTPases as coordinators of vesicle traffic. *Nature Reviews Molecular Cell Biology* **10**, 513-525 (2009).

435. A. Herms *et al.*, AMPK activation promotes lipid droplet dispersion on detyrosinated microtubules to increase mitochondrial fatty acid oxidation. *Nat Commun* **6**, 7176 (2015).
436. J. Du *et al.*, CircNFIB inhibits tumor growth and metastasis through suppressing MEK1/ERK signaling in intrahepatic cholangiocarcinoma. *Mol Cancer* **21**, 18 (2022).
437. X. Chen *et al.*, Metabolic Reprogramming: A Byproduct or a Driver of Cardiomyocyte Proliferation? *Circulation* **149**, 1598-1610 (2024).
438. L. Han *et al.*, Lipid droplet-associated lncRNA LIPTER preserves cardiac lipid metabolism. *Nature Cell Biology* **25**, 1033-1046 (2023).
439. J. Ke *et al.*, Targeting Rab7-Rilp Mediated Microlipophagy Alleviates Lipid Toxicity in Diabetic Cardiomyopathy. *Adv Sci (Weinh)* **11**, e2401676 (2024).
440. W. Du *et al.*, HIF drives lipid deposition and cancer in ccRCC via repression of fatty acid metabolism. *Nat Commun* **8**, 1769 (2017).
441. R. C. Sun, N. C. Denko, Hypoxic regulation of glutamine metabolism through HIF1 and SIAH2 supports lipid synthesis that is necessary for tumor growth. *Cell Metab* **19**, 285-292 (2014).
442. K. Bensaad *et al.*, Fatty acid uptake and lipid storage induced by HIF-1alpha contribute to cell growth and survival after hypoxia-reoxygenation. *Cell Rep* **9**, 349-365 (2014).
443. J. Krishnan *et al.*, Activation of a HIF1alpha-PPARgamma axis underlies the integration of glycolytic and lipid anabolic pathways in pathologic cardiac hypertrophy. *Cell Metab* **9**, 512-524 (2009).
444. G. L. Semenza, Hypoxia-inducible factors in physiology and medicine. *Cell* **148**, 399-408 (2012).
445. G. F. Grabner, H. Xie, M. Schweiger, R. Zechner, Lipolysis: cellular mechanisms for lipid mobilization from fat stores. *Nat Metab* **3**, 1445-1465 (2021).
446. Y. Gao *et al.*, Exercise and dietary intervention ameliorate high-fat diet-induced NAFLD and liver aging by inducing lipophagy. *Redox Biol* **36**, 101635 (2020).
447. D. Das *et al.*, VPS4A is the selective receptor for lipophagy in mice and humans. *Mol Cell* **84**, 4436-4453.e4438 (2024).
448. J. Chung *et al.*, The Troyer syndrome protein spartin mediates selective autophagy of lipid droplets. *Nat Cell Biol* **25**, 1101-1110 (2023).
449. M. Pu *et al.*, ORP8 acts as a lipophagy receptor to mediate lipid droplet turnover. *Protein Cell* **14**, 653-667 (2023).
450. Y. Li *et al.*, CD36 plays a negative role in the regulation of lipophagy in hepatocytes through an AMPK-dependent pathway. *J Lipid Res* **60**, 844-855 (2019).
451. T. B. Nguyen *et al.*, DGAT1-Dependent Lipid Droplet Biogenesis Protects Mitochondrial Function during Starvation-Induced Autophagy. *Developmental Cell* **42**, 9-21.e25 (2017).
452. A. M. Valm *et al.*, Applying systems-level spectral imaging and analysis to reveal the organelle interactome. *Nature* **546**, 162-167 (2017).
453. Q. Wu *et al.*, Acetylcholine reduces palmitate-induced cardiomyocyte apoptosis by promoting lipid droplet lipolysis and perilipin 5-mediated lipid droplet-mitochondria interaction. *Cell Cycle* **20**, 1890-1906 (2021).
454. Y. Meng *et al.*, Glycolytic enzyme PFKL governs lipolysis by promoting lipid droplet-mitochondria tethering to enhance β-oxidation and tumor cell proliferation. *Nat Metab* **6**, 1092-1107 (2024).

455. I. Y. Benador *et al.*, Mitochondria Bound to Lipid Droplets Have Unique Bioenergetics, Composition, and Dynamics that Support Lipid Droplet Expansion. *Cell Metab* **27**, 869-885.e866 (2018).
456. N. K. Talari *et al.*, Lipid-droplet associated mitochondria promote fatty-acid oxidation through a distinct bioenergetic pattern in male Wistar rats. *Nat Commun* **14**, 766 (2023).
457. Z. Nichtová *et al.*, Enhanced Mitochondria-SR Tethering Triggers Adaptive Cardiac Muscle Remodeling. *Circulation Research* **132**, e171-e187 (2023).
458. Y. Guo *et al.*, Enhancing fatty acid utilization ameliorates mitochondrial fragmentation and cardiac dysfunction via rebalancing optic atrophy 1 processing in the failing heart. *Cardiovascular Research* **114**, 979-991 (2018).
459. Y. Xu *et al.*, Characteristics of different lipid droplet-mitochondrial contacts patterns during lipid droplet metabolism in T2DM-induced MASLD. *Scientific Reports* **15**, 3399 (2025).
460. L. G. Straub, P. E. Scherer, Metabolic Messengers: Adiponectin. *Nat Metab* **1**, 334-339 (2019).
461. G. Heusch, B. J. Gersh, The pathophysiology of acute myocardial infarction and strategies of protection beyond reperfusion: a continual challenge. *Eur Heart J* **38**, 774-784 (2017).
462. M. V. Basalay, D. M. Yellon, S. M. Davidson, Targeting myocardial ischaemic injury in the absence of reperfusion. *Basic Res Cardiol* **115**, 63 (2020).
463. L. M. D. Delbridge, K. M. Mellor, D. J. Taylor, R. A. Gottlieb, Myocardial stress and autophagy: mechanisms and potential therapies. *Nat Rev Cardiol* **14**, 412-425 (2017).
464. A. Nakai *et al.*, The role of autophagy in cardiomyocytes in the basal state and in response to hemodynamic stress. *Nat Med* **13**, 619-624 (2007).
465. J. M. Bravo-San Pedro, G. Kroemer, L. Galluzzi, Autophagy and Mitophagy in Cardiovascular Disease. *Circ Res* **120**, 1812-1824 (2017).
466. S. S. Nandi *et al.*, Induction of autophagy markers is associated with attenuation of miR-133a in diabetic heart failure patients undergoing mechanical unloading. *Am J Transl Res* **7**, 683-696 (2015).
467. R. Shibata *et al.*, Adiponectin accumulates in myocardial tissue that has been damaged by ischemia-reperfusion injury via leakage from the vascular compartment. *Cardiovasc Res* **74**, 471-479 (2007).
468. J. Ren *et al.*, Permissive role of AMPK and autophagy in adiponectin deficiency-accentuated myocardial injury and inflammation in endotoxemia. *J Mol Cell Cardiol* **93**, 18-31 (2016).
469. J. W. Jahng *et al.*, Pressure Overload-Induced Cardiac Dysfunction in Aged Male Adiponectin Knockout Mice Is Associated With Autophagy Deficiency. *Endocrinology* **156**, 2667-2677 (2015).
470. N. Maeda *et al.*, Diet-induced insulin resistance in mice lacking adiponectin/ACRP30. *Nat Med* **8**, 731-737 (2002).
471. H. K. Sung *et al.*, Lipocalin-2 (NGAL) Attenuates Autophagy to Exacerbate Cardiac Apoptosis Induced by Myocardial Ischemia. *J Cell Physiol* **232**, 2125-2134 (2017).
472. E. Song *et al.*, Holo-lipocalin-2-derived siderophores increase mitochondrial ROS and impair oxidative phosphorylation in rat cardiomyocytes. *Proc Natl Acad Sci U S A* **115**, 1576-1581 (2018).

473. Y. Liu *et al.*, Adiponectin corrects high-fat diet-induced disturbances in muscle metabolomic profile and whole-body glucose homeostasis. *Diabetes* **62**, 743-752 (2013).
474. J. Zhang *et al.*, Visualization of caspase-3-like activity in cells using a genetically encoded fluorescent biosensor activated by protein cleavage. *Nat Commun* **4**, 2157 (2013).
475. M. Kumada *et al.*, Association of hypoadiponectinemia with coronary artery disease in men. *Arterioscler Thromb Vasc Biol* **23**, 85-89 (2003).
476. R. S. Khan *et al.*, Adipose tissue inflammation and adiponectin resistance in patients with advanced heart failure: correction after ventricular assist device implantation. *Circ Heart Fail* **5**, 340-348 (2012).
477. T. Tsutamoto *et al.*, Total and high molecular weight adiponectin, haemodynamics, and mortality in patients with chronic heart failure. *Eur Heart J* **28**, 1723-1730 (2007).
478. M. G. Karas *et al.*, Relations of plasma total and high-molecular-weight adiponectin to new-onset heart failure in adults ≥65 years of age (from the Cardiovascular Health study). *Am J Cardiol* **113**, 328-334 (2014).
479. Y. He *et al.*, Adiponectin inhibits cardiac arrest/cardiopulmonary resuscitation-induced apoptosis in brain by increasing autophagy involved in AdipoR1-AMPK signaling. *Mol Med Rep* **22**, 870-878 (2020).
480. C. Sun *et al.*, Adiponectin up-regulates the decrease of myocardial autophagic flux induced by β(1) -adrenergic receptor autoantibody partly dependent on AMPK. *J Cell Mol Med* **25**, 8464-8478 (2021).
481. D. P. Del Re, D. Amgalan, A. Linkermann, Q. Liu, R. N. Kitsis, Fundamental Mechanisms of Regulated Cell Death and Implications for Heart Disease. *Physiol Rev* **99**, 1765-1817 (2019).
482. G. Takemura *et al.*, Anti-apoptosis in nonmyocytes and pro-autophagy in cardiomyocytes: two strategies against postinfarction heart failure through regulation of cell death/degeneration. *Heart Fail Rev* **23**, 759-772 (2018).
483. M. Kalisz *et al.*, Total and high molecular weight adiponectin levels in the rat model of post-myocardial infarction heart failure. *J Physiol Pharmacol* **66**, 673-680 (2015).
484. H. H. Chen *et al.*, A nanoparticle probe for the imaging of autophagic flux in live mice via magnetic resonance and near-infrared fluorescence. *Nat Biomed Eng* **6**, 1045-1056 (2022).
485. H. H. Chen *et al.*, Fluorescence tomography of rapamycin-induced autophagy and cardioprotection in vivo. *Circ Cardiovasc Imaging* **6**, 441-447 (2013).
486. D. Zhao *et al.*, Adiponectin agonist ADP355 ameliorates doxorubicin-induced cardiotoxicity by decreasing cardiomyocyte apoptosis and oxidative stress. *Biochem Biophys Res Commun* **533**, 304-312 (2020).
487. Y. Sun *et al.*, Adiponectin exerts cardioprotection against ischemia/reperfusion injury partially via calreticulin mediated anti-apoptotic and anti-oxidative actions. *Apoptosis* **22**, 108-117 (2017).
488. Y. Zhang *et al.*, AdipoRon, the first orally active adiponectin receptor activator, attenuates postischemic myocardial apoptosis through both AMPK-mediated and AMPK-independent signalings. *Am J Physiol Endocrinol Metab* **309**, E275-282 (2015).
489. E. Song *et al.*, Cardiac Autophagy Deficiency Attenuates ANP Production and Disrupts Myocardial-Adipose Cross Talk, Leading to Increased Fat Accumulation and Metabolic Dysfunction. *Diabetes* **70**, 51-61 (2021).

490. Y. K. Chan *et al.*, Lipocalin-2 inhibits autophagy and induces insulin resistance in H9c2 cells. *Mol Cell Endocrinol* **430**, 68-76 (2016).
491. F. A. Scheer *et al.*, Day/night variations of high-molecular-weight adiponectin and lipocalin-2 in healthy men studied under fed and fasted conditions. *Diabetologia* **53**, 2401-2405 (2010).
492. B. Al-Absi, M. Al-Habori, R. Saif-Ali, Plasma Lipocalin-2 and Adiponectin are Affected by Obesity Rather Than Type 2 Diabetes Mellitus per se. *Diabetes Metab Syndr Obes* **14**, 4547-4556 (2021).
493. N. Siri-Angkul, S. C. Chattipakorn, N. Chattipakorn, Roles of lipocalin 2 and adiponectin in iron overload cardiomyopathy. *J Cell Physiol* **233**, 5104-5111 (2018).
494. Q. Zhang *et al.*, Globular adiponectin alleviates chronic intermittent hypoxia-induced H9C2 cardiomyocytes apoptosis via ER-phagy induction. *Cell Cycle* **19**, 3140-3153 (2020).
495. K. Zhu *et al.*, Polypeptide Globular Adiponectin Ameliorates Hypoxia/Reoxygenation-Induced Cardiomyocyte Injury by Inhibiting Both Apoptosis and Necroptosis. *J Immunol Res* **2021**, 1815098 (2021).
496. J. Hu *et al.*, Globular Adiponectin Attenuated H2O2-Induced Apoptosis in Rat Chondrocytes by Inducing Autophagy Through the AMPK/ mTOR Pathway. *Cell Physiol Biochem* **43**, 367-382 (2017).
497. S. Ghadami, K. Dellinger, The lipid composition of extracellular vesicles: applications in diagnostics and therapeutic delivery. *Front Mol Biosci* **10**, 1198044 (2023).
498. N. Nishida-Aoki *et al.*, Lipidomic Analysis of Cells and Extracellular Vesicles from High- and Low-Metastatic Triple-Negative Breast Cancer. *Metabolites* **10** (2020).
499. T. Skotland, N. P. Hessvik, K. Sandvig, A. Llorente, Exosomal lipid composition and the role of ether lipids and phosphoinositides in exosome biology. *J Lipid Res* **60**, 9-18 (2019).
500. M. Xie *et al.*, Activation of Autophagic Flux Blunts Cardiac Ischemia/Reperfusion Injury. *Circ Res* **129**, 435-450 (2021).
501. K. Przyklenk, Y. Dong, V. V. Undyala, P. Whittaker, Autophagy as a therapeutic target for ischaemia /reperfusion injury? Concepts, controversies, and challenges. *Cardiovasc Res* **94**, 197-205 (2012).
502. S. Lavandero, M. Chiong, B. A. Rothermel, J. A. Hill, Autophagy in cardiovascular biology. *J Clin Invest* **125**, 55-64 (2015).
503. A. B. Gustafsson, R. A. Gottlieb, Autophagy in ischemic heart disease. *Circ Res* **104**, 150-158 (2009).
504. K. He *et al.*, Adiponectin alleviated Alzheimer-like pathologies via autophagy-lysosomal activation. *Aging Cell* **20**, e13514 (2021).
505. M. Shimano *et al.*, Adiponectin deficiency exacerbates cardiac dysfunction following pressure overload through disruption of an AMPK-dependent angiogenic response. *J Mol Cell Cardiol* **49**, 210-220 (2010).
506. A. Das, F. N. Salloum, D. Durrant, R. Ockaili, R. C. Kukreja, Rapamycin protects against myocardial ischemia-reperfusion injury through JAK2-STAT3 signaling pathway. *J Mol Cell Cardiol* **53**, 858-869 (2012).
507. S. Wundersitz *et al.*, The Transcription Factor EB (TFEB) Sensitizes the Heart to Chronic Pressure Overload. *Int J Mol Sci* **23** (2022).

508. T. Saito *et al.*, Autophagy regulates lipid metabolism through selective turnover of NCoR1. *Nat Commun* **10**, 1567 (2019).
509. G. W. Reed, J. E. Rossi, C. P. Cannon, Acute myocardial infarction. *Lancet* **389**, 197-210 (2017).
510. G. Savarese *et al.*, Global burden of heart failure: a comprehensive and updated review of epidemiology. *Cardiovasc Res* **118**, 3272-3287 (2023).
511. L. Ohayon, X. Zhang, P. Dutta, The role of extracellular vesicles in regulating local and systemic inflammation in cardiovascular disease. *Pharmacol Res* **170**, 105692 (2021).
512. G. Xu *et al.*, Extracellular vesicle-based drug overview: research landscape, quality control and nonclinical evaluation strategies. *Signal Transduct Target Ther* **10**, 255 (2025).
513. S. C. Kolwicz, Jr., S. Purohit, R. Tian, Cardiac metabolism and its interactions with contraction, growth, and survival of cardiomyocytes. *Circ Res* **113**, 603-616 (2013).
514. A. T. Turer, C. R. Malloy, C. B. Newgard, M. V. Podgoreanu, Energetics and metabolism in the failing heart: important but poorly understood. *Curr Opin Clin Nutr Metab Care* **13**, 458-465 (2010).
515. S. N. Vallerie, K. E. Bornfeldt, Metabolic Flexibility and Dysfunction in Cardiovascular Cells. *Arterioscler Thromb Vasc Biol* **35**, e37-42 (2015).
516. G. D. Lopaschuk, J. R. Ussher, C. D. Folmes, J. S. Jaswal, W. C. Stanley, Myocardial fatty acid metabolism in health and disease. *Physiol Rev* **90**, 207-258 (2010).
517. N. S. Dhalla, A. K. Shah, A. Adameova, M. Bartekova, Role of Oxidative Stress in Cardiac Dysfunction and Subcellular Defects Due to Ischemia-Reperfusion Injury. *Biomedicines* **10** (2022).
518. S. Cadenas, ROS and redox signaling in myocardial ischemia-reperfusion injury and cardioprotection. *Free Radic Biol Med* **117**, 76-89 (2018).
519. W. Cui *et al.*, Lipophagy-derived fatty acids undergo extracellular efflux via lysosomal exocytosis. *Autophagy* **17**, 690-705 (2021).
520. A. Mantovani, C. Dugo, Ceramides and risk of major adverse cardiovascular events: A meta-analysis of longitudinal studies. *J Clin Lipidol* **14**, 176-185 (2020).
521. R. Klingenberg *et al.*, Ceramides in cardiovascular disease: emerging role as independent risk predictors and novel therapeutic targets. *Cardiovasc Res* **121**, 1345-1358 (2025).

Appendix A: List of research outcomes

Publication

1. **Tang J**, Tam E, Song E, Xu A, Sweeney G. Crosstalk between myocardial autophagy and sterile inflammation in the development of heart failure. Autophagy Reports 2024; 3:2320605.
2. **Tang J**, Lei Y, Pignalosa A, Hsu HH, Abdul-Sater AA, Sweeney G. Development of a non-invasive bioassay for adiponectin target engagement in mice. iScience 2024:110994.
3. **Tang J**, Yoon N, Dadson K, Sung HK, Lei Y, Dang TQ, et al. Impaired autophagy flux contributes to enhanced ischemia reperfusion injury in the diabetic heart. Autophagy Reports 2024; 3:2330327.
4. **Tang J***, Sung HK*, Lei Y, et al. ALY688 protects against myocardial ischemia reperfusion injury via direct effects and Rab8a-dependent extracellular vesicles. Journal of Extracellular Vesicles. (Under revision, Manuscript ID JEXV-2025-11-1002)
5. **Tang J**, Wing C, Lei Y, et al. ALY688 induced interorgan transport of adipocyte-derived extracellular vesicle mediates cardio protection in myocardial ischemic mice. All experiments are complete, and the manuscript is currently in preparation. Advanced Healthcare Material (Under revision, Manuscript ID ADHM.202505837)
6. **Tang J**, Joyce N, Laval T, et al. Loss of Rab8a-Dependent Tethering of Lipid Droplets to Mitochondria Drives Hypoxia-Reoxygenation Injury. MedComms. (Under revision, Manuscript ID MCO2-2025-4663)
7. **Tang J**, Crewe C, Sweeney G, et al. Extracellular vesicle mediated crosstalk between cardiometabolic tissues: mechanisms, pathophysiological significance and therapeutic potential. Physiological Review. Forthcoming, 2026
8. **Tang J***, Sung HK*, Lei Y, et al. Gut integrity-IL-17 axis stimulated by ALY688 orchestrates ischemia reperfusion injury protection. All experiments are complete, and the manuscript is currently in preparation. Target journal: iMeta. *Forthcoming*, 2026.
9. Nguyen K, **Tang J**, Gatica D, Russell RC, Sung HK, Sweeney G. ALY688 Attenuates Iron-Induced ER Stress and Insulin Resistance via Activation of ER-Phagy. Diabetes 2025; 74:1761-74.

10. Lone AH, **Tang J**, Pignalosa A, Hsu HH, Abdul-Sater AA, Sweeney G. A novel blood-based bioassay to monitor adiponectin signaling. International Immunopharmacology 2024; 132:111890.

11. Nguyen K, **Tang J**, Cho S, Ying F, Sung HK, Jahng JW, et al. Salubrinal promotes phospho-eIF2α-dependent activation of UPR leading to autophagy-mediated attenuation of iron-induced insulin resistance. Molecular Metabolism 2024; 83:101921.

12. Sung HK, **Tang J**, Jahng JWS, Song E, Chan YK, Lone AH, et al. Ischemia-induced cardiac dysfunction is exacerbated in adiponectin-knockout mice due to impaired autophagy flux. Clinical and Translational Science 2024; 17:e13758.

13. Xu Y, **Tang J**, Guo Q, Xu Y, Yan K, Wu L, et al. Traditional Chinese Medicine formula FTZ protects against polycystic ovary syndrome through modulating adiponectin-mediated fat-ovary crosstalk in mice. Journal of Ethnopharmacology 2021; 268:113587

14. Wang C, **Tang J**, Xu P, Li W. Effect of Effective Fractions of Huangqi San on mRNA Expression of SREBP-1c and Its Target Genes in Insulin-resistant HepG2 Cells. Chinese Journal of Experimental Traditional Medical Formulae 2018,24(16):96-102

15. Wang C, Gao Y, Li Y, **Tang J**, Li W, Gao Y. Effects of Huangqi San Effective Fractions on Hepatic Glycogen Content and Gluconeogenesis Enzymes in Type 2 Diabetes Mellitus Rats, Traditional Chinese Drug Research and Clinical Pharmacology 2018,29(01):1-7.

16. Tang Y, Aleithan F, Madahar SS, Mirzaesmaeili A, Saran S, **Tang J**, et al. Selective disruption of Traf1/cIAP2 interaction attenuates inflammatory responses and rheumatoid arthritis. J Autoimmun 2025; 152:103377.

Abstract

1. **Tang J**, Sung HK, Wu J, Li R-K, Pignalosa A, Hsu H, et al. Abstract P2118: Intervention With The Adiponectin Mimetic Peptide ALY688 Protects Against Cardiac Dysfunction Induced By Ischemia Reperfusion Injury. Circulation Research 2023; 133:AP2118-AP.

2. **Tang J**, Lone AH, Pignalosa A, Crawford K, Abdul-Sater AA, Sweeney G. Potent anti-inflammatory effects of the adiponectin receptor agonist, ALY688. Physiology 2023; 38:5733710.

Patent

1. Sweeney G, Sung H, **Tang J**, et al. Extracellular vesicle comprising adiponectin or cargo induced by adiponectin signaling and method of use, NO 63/755,401, US Provisional Patent